PREPARATION, CHARACTERIZATION AND CATALYTIC ACTIVITY OF METAL - DOPED COCONUT SHELL BIOCHAR

BY

EJIMADU, MAXIMUS CHIMA

B.Sc., M.Sc. (Benin)

(PG/PSC0807072)

DEPARTMENT OF CHEMISTRY

FACULTY OF PHYSICAL SCIENCES

UNIVERSITY OF BENIN, BENIN CITY

FEBRUARY, 2026

PREPARATION, CHARACTERIZATION AND CATALYTIC ACTIVITY OF METAL - DOPED COCONUT SHELL BIOCHAR

BY

EJIMADU, MAXIMUS CHIMA

B.Sc., M.Sc. (Benin)

(PG/PSC0807072)

A THESIS WRITTEN IN THE DEPARTMENT OF CHEMISTRY AND SUBMITTED TO COLLEGE OF POSTGRADUATE STUDIES IN PARTIAL FULFILMENT OF THE REQUIREMENT(S) FOR THE AWARD OF THE DEGREE OF DOCTOR OF PHILOSOPHY (Ph.D.) IN CHEMISTRY OF THE UNIVERSITY OF BENIN, BENIN CITY, NIGERIA.

FEBRUARY, 2026

CERTIFICATION

This is to certify that this work was done by **Chima Maximus EJIMADU** with matriculation number PG/PSC0807072, in the Department of Chemistry, Faculty of Physical Sciences, University of Benin, Benin City, Edo State.

....

Ejimadu Maximus Chima **Date**

....
Professor F.E. Okieimen **Date**
(Supervisor)

....
Professor J. M. Okuo **Date**
(Supervisor)

....
Professor E.E.I. Irabor **Date**
(Head of Department)

DEDICATION

This project work is dedicated to God Almighty the giver of life wisdom, knowledge and understanding. I give Him all the Praise and Glory for seeing me throughout my academic journey.

I also dedicate this work to my beloved mother Mrs Cordelia Chidi Ejimadu, whose love, sacrifices, passion for education and unwavering support inspired and encouraged me throughout this research.

And to the memory of my Late Father Dr. Ignatius Ejimadu. May his memory continues to be a blessing.

ACKNOWLEDGEMENT

I wish to express my profound gratitude to Almighty God for His grace, mercy, and unfailing guidance throughout the course of this research.

My sincere and utmost appreciation goes to my amiable Supervisors, Emeritus Prof. F. E. Okieimen and Prof. J. M. Okuo, for their continuous support, guidance, and invaluable mentorship throughout this research. I am deeply grateful for the time, resources, and expertise they devoted, despite their busy schedules, to review the study, provide corrections, and offer insightful suggestions from the beginning to the end. Their commitment and encouragement significantly improved the quality and completion of this research. May God bless and keep you both. Amen.

My appreciation also goes to the Head of the Department of Chemistry, Prof. E. E. I. Irabor; the Postgraduate Coordinator, Dr. O. K. Ogbeide; and to all Professors, Doctors, and Lecturers in the Department of Chemistry for their constant encouragement and academic support. I also appreciate Dr. Achibong, Dr. Agho and Dr. (Mrs) Emeribe for their contributions. To all the technologists, I express my special thanks for your assistance, cooperation, and encouragement throughout the experimental work. I am deeply grateful to my precious mother, Mrs. C.C. Ejimadu, for her prayers, financial support, and unwavering encouragement during the course of this study. I also fondly remember my late father, Dr. I.M. Ejimadu, whose love for education, discipline, and moral guidance laid the foundation upon which my academic journey was built; his memory continues to inspire me.

To my lovely wife, thank you for your constant prayer, understanding, and emotional support your love gave me the strength to keep pushing.

Finally, to everyone who contributed in one way or another to the success of this work, I say thank you. May God bless you all.

TABLE OF CONTENTS

Title Page	i
Certification	ii
Dedication	iii
Acknowledgements	iv
Table of Contents	v
List of Tables	ix
List of Figures	xi
List of Plates	xiv
Abstract	xv
CHAPTER ONE	**1**
1.0 Introduction	1
1.2 Background of Study	2
1.3 Background of Study	3
1.4 Justification of Study	3
1.5 Scope of Study	3
1.6 Aim and Objectives	4
CHAPTER TWO	**5**
2.0 Literature Review	5
2.1 Biomass	5
2.1.1 Categories of Biomass Materials	5
2.1.2 Lignocellulosic Biomass	6
2.1.2.1 Coconut	8
2.1.3 Biochar	9
2.1.3.1 Biochar Preparation Methods	9
2.1.4 Modification of Biochar	14
2.1.4.1 Physical Modification	15
2.1.4.2 Chemical Modification	15
2.1.4.3 Oxidizing-Agents Modification	17
2.1.4.4 Metal Salts or Metal Oxides Modification	17
2.1.5 Factors Affecting Biochar Properties	18
2.1.5.1 Feedstocks	18
2.1.5.2 Carbonization Temperature	19
2.1.5.3 Residence Time	19

2.1.5.4 Pre-Treatment of Biomass 20
2.1.6 Characterization of Biochar 20
2.1.6.1 Fourier Transform Infrared Spectroscopy (FTIR) 20
2.1.6.2 Scanning Electron Microscopy (SEM) and Energy Dispersive X-Ray (EDX) 21
2.1.6.3 Brunauer-Emmett-Teller Analysis (BET) 21
2.1.6.4 Atomic H/C and O/C Ratios 22
2.1.6.5 Calorific Value 24
2.1.7 Applications of Biochar 24
2.1.8 Biochar as Support 26
2.1.8.1 Synthesis of Metal Doped Biochar 27
2.2 Friedel-Crafts Reaction 31
2.2.1 Catalysis 32
2.2.1.1 Homogeneous Catalysis 33
2.2.1.2 Heterogeneous Catalysis 34
2.3 Optimization and Design of Experiment 38
2.3.1 Response Surface Methodology 38
2.3.2 Theory of RSM 39
2.3.2.1 Preliminary Investigation – Determination of Independent Variables and Their Levels 40
2.3.2.2 Selection of Experimental Design, and Prediction and Verification of Model Equation 41
2.3.2.3 Graphical Presentation of the Model Equation and Determination of Optimal Operating Conditions 43
2.3.3 Advantages and Disadvantages of RSM 44
CHAPTER THREE **46**
3.0 Materials and Methods 46
3.1 Materials 46
3.1.1 Reagents 46
3.1.2 Apparatus/Equipment 47
3.2 Methods 48
3.2.1 Collection of Materials / Sampling of Materials 48
3.2.2 Preparation of Biochar 48
3.2.3 Preparation of Metal-Doped Biochar 49
3.2.4 Characterization of Biochar and the Metal - Doped Biochar 50

3.2.4.1 pH Determination - 50
3.2.4.2 Electrical Conductivity 51
3.2.4.3 Bulk Density 51
3.2.4.4 Cation Exchange Capacity (CEC) 51
3.2.4.5 Surface Morphology and Elemental Composition 52
3.2.4.6 Determination of Surface Area 52
3.2.4.7 Fourier Transform Infrared Spectroscopy 52
3.2.4.8 Surface Acid Functional Groups 53
3.3 Ultimate Analysis 53
3.4 Chemical Oxidation Stability 55
3.4 Estimation of High Heating Value (HHV) of Coconut Shell Biochar 55
3.5 Statistical Approach for the Production of Metal Doped Biochar 56
3.6 Catalytic Activity 58
3.7 Statistical Approach of Friedel Crafts Benzylation of Toluene 59
CHAPTER FOUR **61**
4.0 Results and Discussion 58
4.1 Physicochemical Properties 58
4.2 Surface Oxygen Functional Groups 60
4.3 Fourier Transform Infra-Red Spectroscopy 61
4.4 Textural Properties of Coconut Shell Biochar 65
4.5 Surface Morphology / Elemental Composition of Coconut Shell Biochars 66
4.6 Ultimate Composition of Biochar Samples 73
4.7 Higher Heating Rate of Coconut Shell Biochar 75
4.8 Carbon Sequestration 77
4.9 Chemical Oxidation Stability of Coconut Shell Biochar 79
4.10 Optimization Process for the Preparation of Metal Doped Coconut Shell Biochar 81
4.10.1 Regression Analysis 93
4.10.2 Optimization of Process Parameters 106
4.10.3 Validation of the Model 107
4.11 Physicochemical Properties of the Metal Doped Coconut Shell Biochar Materials 108
4.12 Surface Oxygen Functional Group 109
4.13 Functional Group 110
4.14 Scanning Electron Microscopy 112
4.15 Textural Properties 115

4.16 Catalytic Performance of Metal-Doped Biochar in Friedel Crafts Alkylation Reaction 116
4.16.1 Effect of Mole Ratio of Reactants 117
4.16.2 Effect of Temperature 118
4.16.3 Effect of Catalyst Loading 119
4.17 Kinetic Study 120
4.18 Optimization of Process Parameters for Friedel Crafts Alkylation Reaction 125
4.18.1 Regression Analysis 137
4.18.2 Optimization of Process Parameters 150
4.18.3 Validation of the Model 151
CHAPTER FIVE **152**
5.0 Conclusion 152
5.2 Findings 154
5.3 Contribution to Knowledge 155
5.4 Recommendation for Further Studies 155
LIST OF PUBLICATIONS **156**
REFERENCES **157**

LIST OF TABLES

PAGE

Table 2.1: Classification of Biomass Feedstocks and Their Representative Materials 5

Table 2.2: Cellulose, Hemicellulose and Lignin Contents in Common Agricultural Residues and Wastes 7

Table 2.3: Pyrolysis Processes in a Variety of Conditions 12

Table 2.4: Advantages and Limitations of Different Applications of Biochar 25

Table 3.1: Range and Levels of Independent Variables for Preparation of Metal Doped Biochar Samples 55

Table 3.2: Central Composite Design Experimental Conditions for the Friedel Crafts Reaction 57

Table 4.1: Variation of the Physicochemical Properties of Coconut Shell Biochar with Pyrolysis Temperatures 58

Table 4.2: Surface Oxygen Functional Groups of Coconut Shell Biochar Prepared at Different Pyrolysis Temperatures 60

Table 4.3: Textural Properties (surface area, porosity and pore volume) of Coconut Shell Biochar Prepared at Different Pyrolysis Temperatures 65

Table 4.4: Effect of Pyrolysis Temperature of Ultimate Composition of Coconut Shell Biochar 73

Table 4.5: Higher Heating Value (HHV) of coconut shell and coconut shell Biochars 75

Table 4.6: Atomic Mass Ratios in Coconut Shell Biochar Pyrolysed at Different Temperatures 77

Table 4.7: Experimental Runs for Specific Surface Area Determination of Fe^{3+} - Doped Biochar 81

Table 4.8: Experimental Runs for Specific Surface Area Determination of Zn^{2+} - Doped Biochar 82

Table 4.9: Experimental runs for specific surface area determination of Fe^{3+} / Zn^{2+} - doped Biochar 83

Table 4.10: Fit Statistics for Metal and Bimetallic-Doped Biochar 87

Table 4.11: Summary of Model Statistics of Specific Surface Area of Fe^{3+} - Doped Biochar 88

Table 4.12: Summary of Model Statistics of Specifics Surface Area of Zn^{2+} - Doped Biochar 88

Table 4.13: Summary of Model Statistics of Specifics Surface Area of Fe^{3+}/Zn^{2+} - Doped Biochar 88

Table 4.14: Anova of Specific Surface Area of Fe^{3+} - Doped Biochar 90

Table 4.15: Anova of Specific Surface Area of Zn^{2+} - Doped Biochar 91
Table 4.16: Anova of Specific Surface Area of Fe^{3+}/Zn^{2+} - Doped Biochar 92
Table 4.17: Optimization of Process Parameters for Single and Bimetallic-Doped Biochar 106
Table 4.18: Validation of Model Equation: Comparison of the Values of Surface Area 107
Table 4.19: Physicochemical Properties of Metal Doped Coconut Shell Biochars 108
Table 4.20: Surface Oxygen Functional Groups of Metal Doped Biochars 109
Table 4.21: Textural Properties of Metal Doped Biochar Samples 115
Table 4.22: Variation of First-Order Rate Constant and Half-Life with Reaction Temperature for Metal-Doped Biochar Catalysts 121
Table 4.23: Experimental Runs for Friedel–Crafts Benzylation Reaction over Fe^{3+}-Doped Biochar 126
Table 4.24: Experimental Runs for Friedel–Crafts Benzylation Reaction over Zn^{2+}-Doped Biochar 127
Table 4.25: Experimental Runs for Friedel–Crafts Benzylation Reaction over Fe^{3+} / Zn^{2+} - Doped Biochar 128
Table 4.26: Fit Statistics for Benzyl Chloride Conversion on Metal - Doped Biochar 131
Table 4.27: Summary of Model Statistics of Benzyl Chloride Conversion Using Fe^{3+} - Doped Biochar 132
Table 4.28: Summary of Model Statistic of Benzyl Chloride Conversion Using Zn^{2+} - Doped Biochar 132
Table 4.29: Summary of Model Statistic of Benzyl Chloride Conversion Using Fe^{3+}/Zn^{2+} - Doped Biochar 133
Table 4.30: Anova of Benzyl Chloride Conversion Using Fe^{3+}- Doped Biochar 134
Table 4.31: Anova of Benzyl Chloride Conversion Using Zn^{2+} - Doped Biochar 135
Table 4.32: Anova of Benzyl Chloride Conversion Using Fe^{3+}/Zn^{2+} - Doped Biochar 136
Table 4.33: Optimization of Process Parameters for the Friedel Crafts alkylation Reaction 150
Table 4.34: Validation of model equation 151

LIST OF FIGURES

PAGE

Fig. 2.1: Mechanism of Pyrolysis 10

Fig. 2.2: Hydrothermal Carbonization Procedure 13

Fig. 2.3: Process of Gasification 14

Fig. 2.4: Van Krevelen's diagram of the H/C to O/C ratio 23

Figure 2.5: A Porous Biochar Model with Multiple Functional Groups 26

Fig. 2.6: Schematic Diagram of: One-step and Two-Step Methodologies to Metal Supported Biochar Preparation 28

Fig. 2.8: A Typical Friedel Acylation Reaction 31

Figure 2.9: Schematic diagram of main steps of reaction in heterogeneous catalyst 35

Fig 3.1a: Flow Chart of the Preparation of Biochar 49

Fig. 3.1b: Flowchart for the Preparation of Metal Doped Biochar Preparation 50

Fig. 4.1: FTIR Results of CSB350 61

Fig. 4.2: FTIR Results of CSB400 62

Fig. 4.3: FTIR Results of CSB450 62

Fig. 4.4: FTIR Results of CSB500 63

Fig. 4.5: FTIR Results of CSB600 63

Fig. 4.6: FTIR Results of CSB600 64

Fig. 4.7: SEM/EDX of CSB350 67

Fig. 4.8: SEM/EDX of CSB400 68

Fig. 4.9: SEM/EDX of CSB450 69

Fig. 4.10: SEM/EDX of CSB500 70

Fig. 4.11: SEM/EDX of CSB600 71

Fig. 4.12: SEM/EDX of CSB700 72

Fig. 4.13: Variation of carbon content and HHV of coconut shell biochars with pyrolysis temperature 76

Fig. 4.14: A plot of H/C Versus O/C as a Function of Pyrolysis Temperature 78

Fig 4.15: Chemical Oxidation Stability of Coconut Shell Biochar Produced at Different Pyrolysis Temperatures 79

Fig. 4.16: Correlation of Indicators of Biochar Stability 80

Fig. 4.17: Line Plot of the Actual and Predicted Value of Fe^{3+} - Doped Biochar 84

Fig. 4.18: Line Plot of the Actual and Predicted Value of Zn^{2+} - Doped Biochar 85

Fig. 4.19: Line Plot of the Actual and Predicted Value of Fe^{3+}/Zn^{2+} - Doped Biochar 86

Fig. 4.20A: Interaction of (i) 3D and, (ii) Contour Plots for Fe^{3+} - Loading and Pyrolysis Temperature on the Specific Surface Area of the Fe^{3+} - Doped Biochar 95
Fig. 4.20B: Interaction of (i) 3D and, (ii) Contour Plots for Fe^{3+} - Loading and Pyrolysis Time on the Specific Surface Area of the Fe^{3+} - Doped Biochar 96
Fig. 4.20C: Interaction of (i) 3D and, (ii) Contour Plots for Pyrolysis Temperature and Pyrolysis Time on the Specific Surface Area of the Fe^{3+} - Doped Biochar 97
Fig. 4.21A: Interaction of (i) 3D and, (ii) Contour Plots for Zn^{2+} - Loading and Pyrolysis Temperature on the Specific Surface Area of the Zn^{2+} - Doped Biochar 99
Fig. 4.21B: Interaction of (i) 3D and, (ii) Contour plots for Zn^{2+} - Loading and Pyrolysis Time on the Specific Surface Area of the Zn^{2+} - Doped Biochar 100
Fig. 4.21C: Interaction of (i) 3D and, (ii) Contour Plots for Pyrolysis Temperature and Pyrolysis Time on the Specific Surface Area of the Zn^{2+} - Doped Biochar 101
Fig. 4.22A: Interaction of (i) 3D and, (ii) Contour Plots for Fe^{3+}/Zn^{2+} - Loading and Pyrolysis Temperature on the Specific Surface Area 103
Fig. 4.22B: Interaction of (i) 3D and, (ii) Contour Plots for Fe^{3+}/Zn^{2+} - Loading and Pyrolysis Time on the Specific Surface Area 104
Fig. 4.22C: Interaction of (i) 3D and, (ii) Contour Plots for Pyrolysis Temperature and Pyrolysis Time on the Specific Surface Area 105
Fig. 4.23: FTIR of Fe^{3+} -Doped Biochar 110
Fig. 4.24: FTIR of Zn^{2+} -Doped Biochar 110
Fig. 4.25: FTIR of Fe^{3+}/Zn^{2+} -Doped Biochar 111
Fig. 4.26: SEM/EDX of Fe^{3+}-Doped Biochar 112
Fig. 4.27: SEM/EDX of Zn^{2+}-Doped Biochar 113
Fig. 4.28: SEM/EDX of Fe^{3+}/Zn^{2+}- Doped Biochar 114
Fig. 4.29: Effect of Mole Ratio of T:BC on Benzylation of Toluene over Metal Doped Catalyst (Catalyst Loading 8.2 wt% BC, Temperature 70ºC) 117
Fig. 4.30: Effect of Reaction Temperature on Benzylation of Toluene over Metal Doped Catalyst (catalyst loading 8.2 wt% CSB, mole ratio T:BC, 15:1) 118
Fig. 4.31: Effect of Catalyst Dose on Benzylation of Toluene over Metal Doped Catalyst (Mole Ratio, T:BC, 10:1, Reaction Temperature, 70º C) 119
Fig. 4.32: Arrhenius plot of the Friedel Crafts alkylation reaction on of (a) Fe^{3+}- doped biochar, (b) Zn^{2+}- doped biochar and (c) Fe^{3+}/Zn^{2+} - doped biochar 123
Figure 4.33: Schematic Diagram of Main Steps of Reaction in Heterogeneous Catalyst 125
Fig. 4.34: Line Plot of the Actual and Predicted Values of Benzyl Chloride Conversion over

of Fe^{3+} - Doped Biochar 129
Fig. 4.35: Line Plot of the Actual and Predicted Values of Benzyl Chloride Conversion over Zn^{2+} - Doped Biochar 130
Fig. 4.36: Line Plot of the Actual and Predicted Values of Benzyl Chloride Conversion over Fe^{3+}/Zn^{2+} - Doped Biochar 130
Fig. 4.37A: Interaction of (i)3D, (ii) Contour Plots of Mole Ratio and Temperature of BC conversion on Fe^{3+} - doped biochar 139
Fig. 4.37B: Interaction of (i)3D, (ii) Contour Plots of Mole Ratio and Time of BC conversion on Fe^{3+} - doped biochar 140
Fig. 4.37C: Interaction of (a)3D, (b) Contour Plots of Temperature and Time of BC conversion on Fe^{3+} - doped biochar 141
Fig. 4.38A: Interaction of (i)3D, (ii) Contour Plots of Mole Ratio and Temperature of BC conversion on Zn^{2+} - doped biochar 143
Fig. 4.38B: Interaction of (i)3D, (ii) Contour Plots of Mole Ratio and Time of BC conversion on Zn^{2+} - doped biochar 144
Fig. 4.38C: Interaction of (i)3D, (ii) Contour Plots of Temperature and Time of BC conversion on Zn^{2+} - doped biochar 145
Fig. 4.39A: Interaction of (i)3D, (ii) Contour Plots of Mole Ratio and Temperature of BC conversion on Fe^{3+}/Zn^{2+} - doped biochar 146
Fig. 4.39B: Interaction of (i)3D, (ii) Contour Plots of Mole Ratio and Time of BC conversion on Fe^{3+}/Zn^{2+} - doped biochar 147
Fig. 4.39C: Interaction of (i)3D, (ii) Contour Plots of Temperature and Time of BC conversion on Fe^{3+}/Zn^{2+} - doped biochar 148

LIST OF PLATES

	PAGE
Plate 2.1: Coconut fruit Layers of the coconut fruit	8

ABSTRACT

Chemical industries increasingly rely on catalytic processes, and more than 90% of large scale chemical transformations depend on catalysts. Some of the commonly used homogeneous catalysts in Fridel Crafts alkylation reaction are; BF_3, H_2SO_4, HF, $AlCl_3$. Though, readily available at low cost, they have several limitations and these include toxicity, difficulty in separation and recovery and disposal problems. These limitations have intensified the demand for sustainable, efficient, and environmentally benign heterogeneous catalysts.

This study focuses on the development of metal-doped coconut-shell biochars as robust heterogeneous catalysts for the Friedel Crafts benzylation of toluene. Biochars derived from the coconut shell produced at different pyrolysis temperatures (350, 400, 450, 500, 600 and 700 °C) were characterized in terms of their physicochemical and textural properties, surface oxygen functional groups and surface morphology using standard methods. The coconut shell biochar (CSB) sample with the optimal textural properties (CSB450) was then co-pyrolysed with Fe^{3+}, Zn^{2+}, and Fe^{3+}/Zn^{2+} ions to produce metal doped biochars (Fe^{3+} - doped, Zn^{2+}- doped, and Fe^{3+}/Zn^{2+}-doped biochar). Central Composite Design (CCD) of the Response Surface Methodology (RSM) was employed to optimize the process variables (metal loading, pyrolysis temperature and pyrolysis time) for the co-pyrolysis reaction. Similarly, RSM was used to optimized the process variables (mole ratio of toluene: benzyl chloride (T:BC), reaction temperature and reaction time) on benzyl chloride conversion to benzylated toluenes with the metal doped biochars.

RSM-derived optimal conditions resulted in enhanced specific surface areas of 2098.04 $m^2.g^{-1}$ for the Fe^{3+}-doped biochar, 1721.40 $m^2.g^{-1}$ for the Zn^{2+}-doped biochar, and 2124.5 $m^2.g^{-1}$ for the Fe^{3+}/Zn^{2+}-doped biochar. Compared with the pristine biochar (CSB450), the metal doped biochars (MBCs) showed improved physicochemical properties and textural properties. In addition, surface elemental analysis confirmed the successful incorporation of the Fe (10.09%), Zn (5.17%) and Fe/Zn (9.44/6.51%) on the MBCs. The results of the conversion process showed that the reaction temperature, mole ratio, and reaction time significantly affected benzyl chloride conversion with the metal doped biochar. Three novel models were developed for benzyl chloride conversion process. From the models, we predicted optimized process conditions; optimum benzyl chloride conversion of 93% was found for Fe^{3+}/Zn^{2+} - doped biochar, with values of 87 and 81% for the Fe^{3+} - and Zn^{2+} - doped biochar respectively. This research established metal doped coconut shell biochar as an effective, low-cost, and environmentally friendly heterogeneous catalysts for organic transformations, presenting a viable alternative to conventional corrosive and non-recyclable catalysts in industrial alkylation processes.

CHAPTER ONE

1.0 Introduction

Chemical reactions play a vital role in the field of science and they are extensively applied in different areas including health, pharmacy, environment, chemical industry, and nutrition (Shi *et al.,* 2020). Catalysis is considered as a significant aspect in chemical reactions as the rate or outcome of the reaction is greatly influence by the presence of a substance (homogeneous or heterogeneous catalyst) that is not consumed during the reaction (Richard, 2001).

The Friedel Crafts reactions in particular are versatile route for the synthesis of substituted aromatic compounds (Iqbal *et al*., 2020). The Friedel Crafts alkylation reactions in particular involve the interaction between alkyl halides and aromatic compounds in the presence of homogeneous acid catalysts leading to the production of benzylated product, which are valuable commodity chemicals in fragrance, fine chemicals, and other high value industrial materials. (Rueping and Nachtsheim, 2010; Sun *et al*., 2017).

The reactions involving conventional (homogeneous) catalyst ($AlCl_3$, BF_3, HF, and H_2SO_4) in synthesis of high added value chemicals have been used for decades in industrially relevant processes (Luque *et al.,* 2011). However, several limitations including toxicity, difficulty in separation and recovery, corrosion and disposal problem and others, restricted their use. In addition, its very high moisture sensitivity demands a moisture free atmosphere, solvent, and substrates for the reaction (Luque *et al.,* 2011; Lachter *et al*., 2024).

Consequently, there is a growing need to replace such homogeneous systems with environmentally friendly alternatives. The adoption of solid acid catalysts (heterogeneous catalysts) presents a promising solution due to their advantages such as environmental compatibility, reusability, ease of separation, and high catalytic activity even in the presence of moisture (Choudhary *et al.,* 2002; Saber *et al.,* 2003).

1.2 Background of Study

The development of efficient, sustainable, and low-cost heterogeneous catalysts has become a key focus in green chemistry (Vinu *et al*., 2005). Several solid acids catalyst have been reportedly used in Friedel Crafts alkylation reactions including; Fe_2O_3 or $FeCl_3$ supported on micro-, meso- and macroporous materials, lewis acids supported clays and silicas, $NiCl_2$ or $ZnCl_2$ supported aluminas and heteropolyacids supported catalysts as well as Fe or Zn supported montmorillonite, Fe supported graphite and Ga-Mg/ hydrotalcite, (Saber *et al.,* 2003; Luque *et al.,* 2011). Although these catalysts showed good selectivity in alkylation reaction, their mode of preparation process are usually complex and expensive. which limits their large-scale industrial application.

Over the years, carbon-based materials have emerged as attractive supports for heterogeneous catalysis. Carbon materials such as biomass and metal - organic frameworks (MOFs) derived porous carbons, carbon nanotubes, graphene and graphene oxide, including graphitic carbon nitride have been extensively used as catalyst supports due to their well-defined and custom-tailored properties such as large surface area, high thermal and chemical stability in acid or basic media, good electronic conductivity, easy recovery from the reaction mixture, easy heteroatom doping and controllable defect structure (Pérez-Mayoral *et al.,* 2016; Gawande *et al.,* 2020; Chen *et al.,* 2019; Li *et al.,* 2019; Luque *et al.,* 2011). Interestingly, they can be prepared from low cost precursors such as agricultural or industrial biowaste, and their mode of preparation is simple which represents a huge advantage (Pérez-Mayoral *et al.,* 2016).

Among this carbon based material, biochar, a carbon rich solid produced from the thermochemical conversion (e.g., pyrolysis) of biomass has attracted increasing attention on account of its intrinsic nature (Lee *et al.,* 2019). Traditionally used as a soil amendment and environmental remediation (Agegnehu *et al.,* 2017; Lam *et al.,* 2019), biochar exhibit tunable physicochemical properties, making it an excellent candidate as catalyst support. Recent studies have demonstrated its application in various catalytic systems due to its

stability, porosity, and ability to disperse active metal sites (Wang *et al*. 2015; Lee *et al.,* 2020).

1.3 STATEMENT OF PROBLEM

Heterogeneous catalysts have been developed to replace homogeneous catalysts in many synthetic industrial applications and this is on account of the challenges including; difficult in separating and recovery of catalyst, concerns about its disposal as well as issues related to corrosion and toxicity associated with homogeneous catalytic process (Brahmi *et al*., 2016). Furthermore, the high cost and complex preparation routes of many heterogeneous catalysts limit their accessibility and large-scale application, highlighting the need for low-cost, sustainable catalytic materials.

1.4 JUSTIFICATION OF STUDY

Developing a catalyst from biomass waste material will provide an advantage of added value to the low-cost material. Utilizing the biomass materials may reduce the overall cost of catalyst production compared to using more conventional and costly materials. The preparation of heterogeneous catalysts from biochar aligns with the principles of green chemistry, as it promotes the use of renewable resources, reduces waste generation, and supports the development of environmentally sustainable chemical processes(Noman *et al*., 2024).

1.5 SCOPE OF STUDY

This study is limited to the feedstock collection, pyrolysis of coconut shell at different temperatures, characterization of the resulting biochars, doping the biochars with metals of interest, characterization of the doped biochars and their application in the Friedel Crafts catalytic reactions.

1.6 AIM AND OBJECTIVES

The aim of this study is to prepare, characterize metal - doped biochar and evaluate its catalytic activity on Friedel Crafts benzylation reaction.

The objectives of this study are to:

i. prepare and characterize biochar from coconut shell at 350, 400, 450, 500, 600 and 700^{o}C respectively.

ii. dope the obtained biochar with the metals of interest (Fe^{3+}, Zn^{2+} and Fe^{3+} / Zn^{2+}) and characterize the resulting metal-doped biochar in terms of the physicochemical properties, surface acid functional groups, textural properties, surface morphology and functional groups.

iii. determine the variables for attaining optimum specific area of metal - doped biochar

iv. optimize the process variables for the Friedel Crafts benzylation reaction .

CHAPTER TWO

2.0 LITERATURE REVIEW

2.1 BIOMASS

Every organic substance derived directly or indirectly from the photosynthesis process is considered biomass (Jacobsson and Johnson, 2000). Due to the complex nature of the materials, biomass refers to any organic materials that are derived from plants or animals such as the products, byproducts, residues and wastes from agriculture, forestry, industrial and municipal wastes. (Parmar, 2017). Biomass also includes gases and liquids recovered from the decomposition of non-fossilized and biodegradable organic materials (McKendry, 2002b; Basu, 2013).

2.1.1 Categories of biomass materials

Table 2.1: Classification of Biomass Feedstocks and Their Representative Materials

Biomass Type	Typical Materials
Agricultural	Food grains, bagasse (crushed sugarcane), corn stalks, straw, seed hulls, nutshells, cattle/poultry/hog manure
Forest	Trees, wood waste, bark, sawdust, timber slash, mill residues
Municipal	Sewage sludge, refuse-derived fuel (RDF), food waste, waste paper, yard clippings
Energy Crops	Switchgrass, alfalfa, prairie bluestem, corn, soybean, canola, other plant oils
Biological	Animal waste, aquatic organisms, other biological residues

Source: Sikarwar et al., 2017

2.1.2 Lignocellulosic Biomass

Lignocellulose, the fibrous, non-starch component of plant biomass, forms the bulk of plant material. Its three main constituents are cellulose, hemicellulose, and lignin. Unlike starch or other carbohydrates, lignocellulose cannot be readily broken down by the human digestive system. For example, while humans can eat rice grains, which are rich in carbohydrates, the rice husk or straw made largely of lignocellulosic material cannot be digested. Lignocellulosic biomass does not belong to the human food chain, thus using it for biogas or bio-oil production does not compete with global food supplies

Woody plants, a primary source of lignocellulosic biomass, are vascular plants with perennial stems above ground, covered by thick bark. They are mainly composed of cellulose and lignin. Woody plants include trees, shrubs, cacti, and perennial vines, which can be classified into herbaceous and non-herbaceous types (Zhang *et al*., 2022). Herbaceous plants have leaves and stems that die annually, such as wheat and rice, and develop hard stems with vascular bundles but lack the thick bark of non-herbaceous plants. Non-herbaceous plants, including trees, shrubs, and vines, survive year-round, with above ground stems that remain alive during dormancy and regrow shoots the following season. Among the various biomass sources, tree trunks and leaves constitute the largest fraction and are classified as lignocellulosic materials due to their cellulose, hemicellulose, and lignin content, as summarized for selected agricultural residues in Table 2.2 (Kumar *et al*., 2009 and Boonmee, 2012).

Interest is growing in cultivating plants specifically for energy production, known as energy crops. These lignocellulosic crops generally have short growing periods, high yields, and low fertilizer requirements, offering quick returns on investment. Woody energy crops commonly used include miscanthus, willow, switchgrass, and poplar, which are typically planted densely to maximize biomass production. They have high-energy yield per unit of land area and require much less energy for cultivation (Basu, 2013).

Table 2.2: Cellulose, Hemicellulose, and Lignin Contents in Common Agricultural Residues and Wastes.

Lignocellulosic Material	Cellulose (%)	Hemicellulose (%)	Lignin (%)
Bagasse	44	23	20
Peanut shell	22.1	12.1	35.2
Rice hull	49.1	9.6	12.9
Rice straw	33	26	7
Sugarcane leaf & stalk	40	29	13
Sorghum leaf & stalk	31	30	11
Hardwood stems	40-55	24-40	18-25
Softwood stems	45-50	25-35	25-35
Nut shells	25-30	25-30	30-40
Corn cobs	45	35	15
Grasses	25-40	35-50	10-30
Paper	85-99	0	0-15
Wheat straw	30	50	15
Sorted refuse	60	20	20
Leaves	15-20	80-85	0
Cotton seed hairs	80-95	5-20	0
Newspaper	40-55	25-40	18-30
Waste papers from chemical pulps	60-70	10-20	05-10
Solid cattle manure	1.6-4.7	1.4-3.3	2.7-5.7
Coastal bermudagrass	25	35.7	6.4
Switch grass	45	31.4	12

Source: Kumar *et al*. (2009) and Boonmee, (2012)

2.1.2.1 Coconut

Coconut waste is one of the most abundant forms of biomass found in many regions of the world. It is estimated that about 124 million tons of coconut husk are generated by the coconut industry annually (Ajien *et al*., 2022). Coconut (*Cocos nucifera*) is cultivated extensively in tropical countries such as Thailand, India, Nigeria, and a host of other African countries (Azeta *et al*., 2021). *Cocos nucifera* is a large palm, growing up to 30 meters (98 ft) tall, with pinnate leaves 4–6 meters (13–20 ft) long, and pinnae 60–90 cm long; old leaves break away cleanly, leaving the trunk smooth (Emojevwe *et al.,* 2013). The coconut fruit consists of several distinct components; the pith (the exocarp), which forms the outer protective covering of the seed; the husk (mesocarp), which contains fibers of varying sizes embedded in a matrix and contained about 30% fiber and 70% pith on a dry weight basis; and the shell, a hard endocarp that encloses and protects the endosperm, which contains water (Reddy, 2015). Like most plant-derived biomass, coconut is primarily composed of lignocellulosic materials. The main constituents of this type of material are water, ash, and dry ash-free parts consisting of cellulose, hemicellulose, and lignin (Khan *et al.,* 2023). Nigeria ranked on the 18th position on the world coconut production country and only about 265 thousand tonnes is generated annually (Owoyemi *et al*., 2022).

Plate 2.1: Layers of the coconut fruit:(1) Exocarp/Epicarp, (2) Mesocarp, (3) Endocarp, (4) Endosperm, (5) Embryo

The processing of coconut for food, fuel, and fiber generate a large amount of residues biomass, including coconut shells among others (Azeta *et al.,* 2021). These coconut shell are often prodigiously discarded, occupying landfill space and emitting greenhouse gases or by open-air burning causes considerable environmental and public health concerns; thus finding alternative ways to utilize coconut shell is critical for sustainable development (Ajien *et al*., 2022).

2.1.3 Biochar

Biochar is the carbon-rich material produced from organic feedstock under certain thermal combustion with limited oxygen (Lehmann and Joseph, 2015). Organic wastes, such as agricultural residues and municipal solid waste, can be used as feedstocks for biochar production, as they are particularly promising due to their high carbon content and the presence of nutrients such as calcium, potassium, nitrogen, and phosphorus, which enhances soil fertility and support microbial activity (Sepehri and Mohammad-Hossein, 2018; Shoudho *et al*., 2024). Biochar has gained attention of many researchers due to its versatile nature that allows its utilization in a wide range of applications, including catalysts, catalyst support, soil amendment, water treatment, carbon sequestration, and renewable energy production (Varkolu *et al*., 2025). The process parameters such as; temperature, types of biomass, residence time and heating rate are mainly responsible for determining the yield of biochar (Babu and Chaurasia, 2003; Sharma *et al*., 2015).

2.1.3.1 Biochar preparation methods

The preparation of biochar involves various methods including pyrolysis, hydrothermal carbonization, and gasification, of which pyrolysis remains the most frequently used (Amalina *et al*., 2022). Pyrolysis as the thermal degradation of biomass at a temperature of 350–900 °C in an oxygen-deprived environment, converts waste materials into valuable

products, including biochar, pyrolysis gas, and bio-oil (Deng *et al*., 2017). During pyrolysis, lignocellulosic materials namely cellulose, hemicellulose, and lignin decompose through processes such as dehydration, depolymerization, carboxylation, fragmentation, and cross-linking at defined temperatures thereby promoting the formation of solid, liquid, and gaseous fractions, where the solid and liquid products are biochar and bio-oil, and the gaseous products (pyrolysis gas) comprise CO_2, CO, H_2, and light C_1–C_2 hydrocarbons (syngas) (Pandit *et al*., 2023). The amount of biochar obtained is strongly influenced by the nature and properties of the biomass feedstock, pyrolysis temperature and residence time with pyrolysis temperature being the most critical operational parameter governing product yield (Wei *et al*., 2019). In general, increasing the pyrolysis temperature leads to a reduction in biochar yield while enhancing pyrolysis gas formation (Amalina *et al*., 2022). The pyrolysis pathway is illustrated in Fig. 2.1.

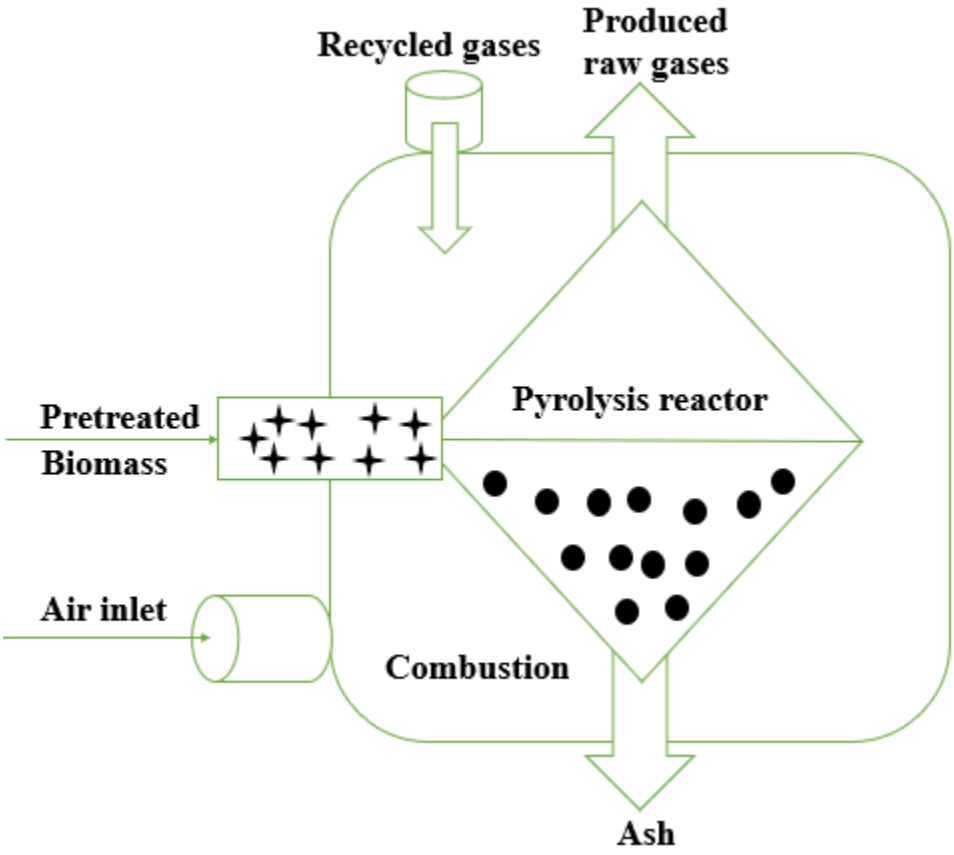

Fig. 2.1: Mechanism of pyrolysis

Based on operating parameters such as heating rate, temperature, and residence time, and pressure, pyrolysis is broadly categorized into slow and fast processes (Amenaghawon *et al*., 2021). Slow pyrolysis is a process that converts recalcitrant carbon into valuable products while reducing atmospheric CO_2 levels through the production of biochar from various biomass feedstocks (Mohamed Noor *et al*., 2012). In slow pyrolysis, the temperature operation is between 350 - 800 °C, with a heating rate of 5 °C min^{-1} and possesses a longer residence time of more than 1 h (Tomczyk *et al*., 2020; Liu *et al*., 2015). The solid product of biochar is maximized through slow pyrolysis, which can be done in a laboratory setting with a slow pyrolysis apparatus (Yu *et al*., 2017; Mohamed Noor *et al*., 2012). About 30–35% biochar, 40–45% of liquid product and 20–25% of gaseous product are derived from slow pyrolysis from a 1 kg of wood (Mohamed Noor *et al*., 2012). Retorts, converters, and kilns are examples of reactors used in slow pyrolysis (Sakhiya *et al*., 2020). Many researchers have used slow pyrolysis techniques to produce biochar from agricultural wastes such as wood sawdust, rice waste (Gupta *et al*., 2018), and corn stover (Karimi *et al*., 2020).

Fast pyrolysis of biomass is a thermal decomposition process carried out at a high temperature of 500 ◦C to 1300 ◦C at a heat rate of 200 ◦C/min for no more than 10 s in the absence of oxygen (Elkhalifa *et al*., 2019). The final products of fast pyrolysis typically consist of approximately 60–75% liquid (bio-oil), 10–20% gases, and 10–20% solid residue (biochar), with bio-oil as the main product, and the rapid heating and cooling rates enhance liquid yields, making the process an efficient route for producing renewable biofuels and chemicals (Yu *et al*., 2017; Elkhalifa *et al*., 2019). Fast pyrolysis is widely regarded as an efficient and sustainable energy conversion approach as it convert diverse biomass feedstocks into products with added value. This approach uses circulating beds, ablative reactors, rotating cone reactors, and bubbling fluidized beds as reactors (Zhang *et al*., 2019). The most liquid product is produced when softwood is used, together with hardwood, grass, and other agricultural wastes (Torri *et al*., 2016). Table 2.3 Shows the various pyrolysis processes.

Table 2.3: Pyrolysis Processes in a Variety of Conditions

Process	Pyrolysis Temperature (°C)	Pressure	Residence Time	Bio-oil (%)	Synthetic Gas (%)	Biochar (%)
Fast Pyrolysis	500 – 1300	Atmospheric	2 – 5 Sec.	60 - 75	10 – 20	10 - 20
Slow Pyrolysis	350 – 800	Atmospheric	Min – Hr	40 - 45	20 – 25	30 - 35

Source: Elkhalifa *et al*. (2019)

Hydrothermal carbonization is considered to be a cost-effective method for biochar production as the process can be performed at a low temperature around 180 - 250 ^{o}C (Lee *et al*., 2018). It is also known as wet pyrolysis (Zhou *et al*., 2019) and the obtained biochar is named as hydrochar to differentiate the product produced from dry processes such as pyrolysis and gasification (Fang *et al*., 2018). In this process, the biomass is mixed with water and transferred into an airtight reactor, after which the temperature is gradually increased to ensure stable reaction (Lee *et al*., 2018; Zhang *et al*., 2017). At different temperatures, the products are produced as follows: biochar at a temperature below 250^{o}C referred to as hydrothermal carbonization (Zhang *et al*., 2017), bio-oil between 250 - 400 ^{o}C known as hydrothermal liquefaction and gaseous products syngas such as CO, CO_2, H_2 and CH_4 produced at a temperature above 400 ^{o}C referred as hydrothermal gasification (Khorram *et al*., 2016). Fig. 2 illustrates the hydrothermal carbonization process.

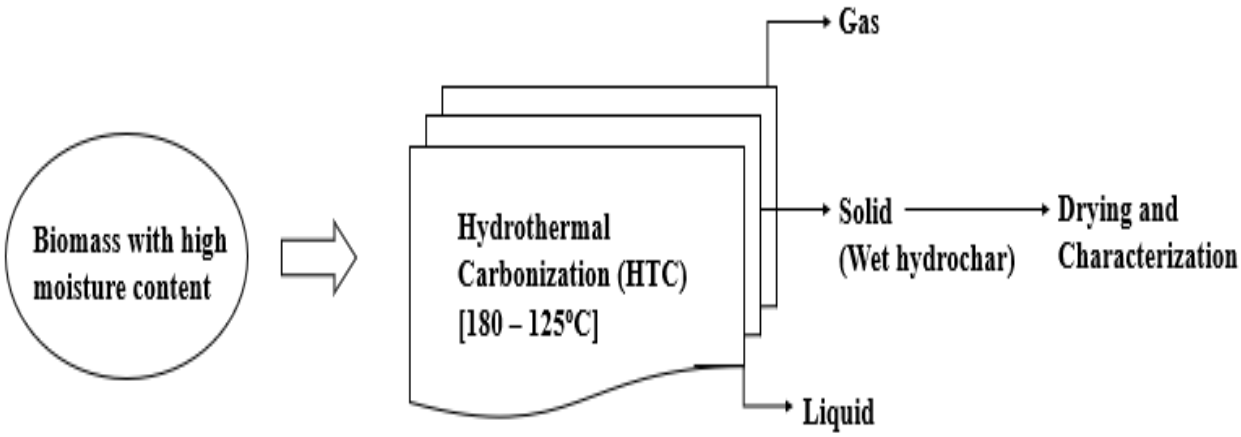

Fig. 2.2: Hydrothermal Carbonization Procedure

During this process, the hydrolyzed products undergo successive reactions including dehydration, fragmentation, and isomerization forming intermediate compounds such as 5-hydroxymethylfurfural and its derivatives, which further react through condensation, polymerization, and intramolecular dehydration to yield hydrochar (Bakraoui *et al*., 2020). The lignin decomposition starts through dealkylation and hydrolysis reaction producing phenolic products like phenols, catechols, syringols, etc (Jain *et al*., 2016).

Gasification is a thermochemical technique that decomposes carbon-rich materials into gaseous products, known as syngas, which mainly consists of CO, CO_2, CH_4, H_2, and trace hydrocarbons as shown in Fig. 2.3 (Zhang *et al*. 2023). This process takes place at high temperatures in the presence of gasification agents such as oxygen, air, or steam. Reaction temperature being the most critical factor influencing the composition and yield of syngas (Ferreiro *et al*., 2024). It was found that as temperature increased carbon monoxide, hydrogen production increased while other contents such as methane, carbon dioxide and hydrocarbons were decreased (Prabakar *et al*., 2018). The major product of this process is syngas and the char are referred to as the by-product with less yield (Zhang *et al*. 2023).

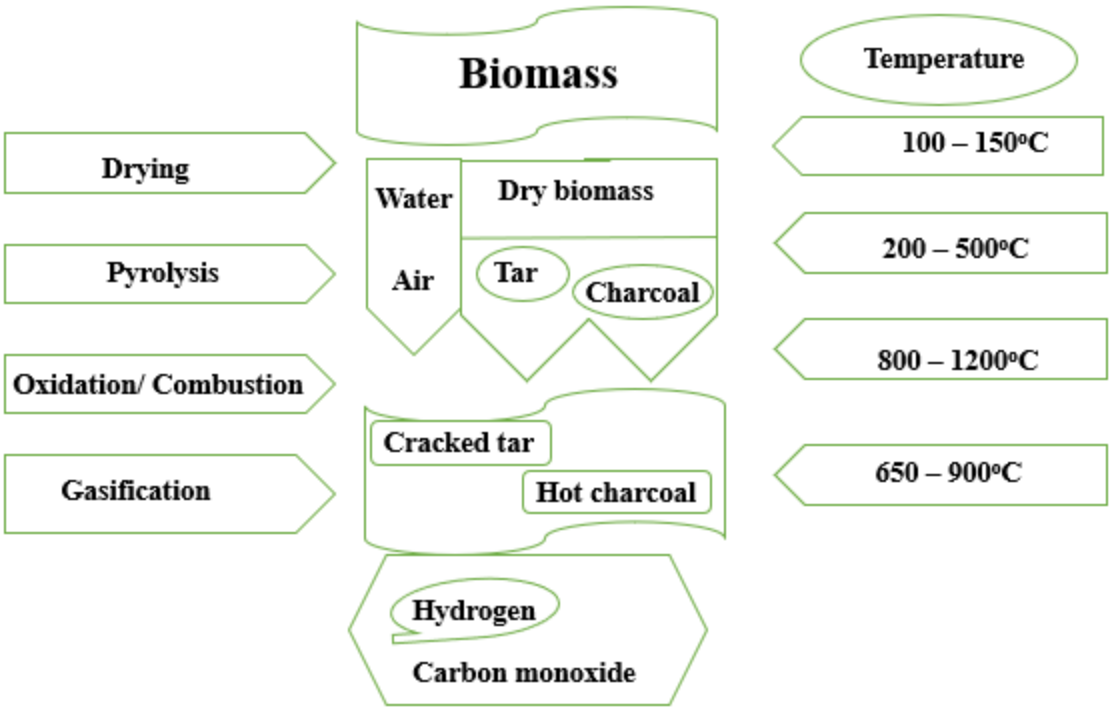

Fig. 2.3: Process of Gasification

The gasification process can be divided into two main stages: drying and oxidation/combustion (Shadle *et al*., 2025). In the drying stage, the moisture in the biomass is completely evaporated, typically without energy recovery (Chen *et al*., 2023). The moisture content differs depending on the type of biomass, and drying may be conducted as a separate step when the biomass has high moisture levels (Chen *et al*., 2023). While oxidation and combustion reactions are between gasification agents and the combustible components of biomass supply the primary energy for the process, leading to the formation of CO_2, CO, and H_2O (Couto *et al*., 2013).

2.1.4 Modification of Biochar

To tailor biochar properties for environmental applications, various modification methods have been employed (Zhang *et al*., 2025). The most common approaches are chemical and physical modifications. Chemical modification comprises the acid treatment, alkaline treatment, oxidation, and incorporation of metal salts. Physical modification primarily involves steam treatment or gas purging.

2.1.4.1 Physical modification

Physical modification enhances the surface pores of biochar and can also modify its chemical properties (e.g., surface functional groups, hydrophobicity, and polarity) (Erdem and Dogru, 2021). During physical modification, biochar is exposed to a required amount of oxidizing agents, such as steam, ozone, carbon dioxide, or air, at temperatures typically above 500 °C (Rangabhashiyam and Balasubramanian, 2019). These oxidizing chemicals enter the biochar structure and gasify the carbon atoms, opening and expanding previously inaccessible pores (Sajjadi *et al*., 2019). This type of activation can produce a biochar with larger surface areas and generate a large amount of surface oxygen functional groups, which frequently serve as active adsorption sites for pollutant removal (Sajjadi *et al*., 2019). Another physical process, like steam activation, is gas purging, in which gases (such as carbon dioxide) are mixed with the accessible amorphous carbon at the biochar surface in a restricted oxygen environment to produce carbon monoxide, consequently increase the biochar surface area as well as improving its microporous structure and pore volume (Bushra and Remya, 2020). Zhang *et al*. (2019) have reported sludge-based pyrolysis to produce biochar, which was modified using a physical activator (CO_2) to enhance its adsorption capacity of Pb^{2+} from an aqueous solution. The results revealed that the physical modification with CO_2 enhanced the specific surface area by more than ten folds, and its Pb^{2+} adsorption capacity increased from 7.6 mg/g to 22.4 mg/g with simultaneous introduction of oxygen-containing functional groups on the biochar (Zhang *et al*., 2019).

2.1.4.2 Chemical modification

Chemical modification is the most widely used method involving impregnating the materials (biomass) with chemical agent and the combination is subsequently thermally treated to obtain a biochar-doped material (Sajjadi *et al*., 2019). During the process, the chemical agent can act as an activator, which favors sample dehydration and prevents the generation of tar and volatile chemicals, thus increasing the yield of the carbonization process (Timur *et al*., 2006). This method of chemical modification is widely applied to tailor both the nature and surface functional groups on biochar, while simultaneously

improving its textural properties and porosity (Tomczyk *et al*., 2023). Common chemical modification techniques include acid treatment, alkaline treatment, oxidation using chemical agents, and modification with metal salts or oxidizing agents.

- **Acid Modification**

Metals present on the biochar surface are usually remove during the acid treatment and acid functional groups are introduced onto the surface of biochar. The common acids include hydrochloric acid, sulphuric acid, nitric acid, phosphoric acid, oxalic acid and citric acid (Rajapaksha *et al*., 2016; Peng *et al*., 2016; Li *et al*., 2014). Acid modification can also alters the surface area of biochar, and the effect on the surface area varied with the concentration and types of acids, feedstock, and preparation conditions (Yakout *et al*., 2015; Peng *et al*., 2016; Taha *et al*., 2014).

- **Alkaline modification**

The main purpose of alkaline modification is to enhance the surface area while introducing more oxygen-containing functional groups onto the biochar surface. The common alkaline agents used include potassium hydroxide (KOH) and sodium hydroxide (NaOH) (Jin *et al*., 2014;Sun *et al*., 2015). The effectiveness of the alkaline treatment on biochar properties depends on several factors, such as the concentration of the activating agent, the type of feedstock used, and the preparation conditions (Cazette *et al*., 2011; Feng and Zhu 2018). Compared to potassium hydroxide, sodium hydroxide is less corrosive and more economical (Cazetta *et al*., 2011). Furthermore, the ratio of base to biochar also plays a crucial role in determining the final textural and surface characteristics of the modified biochar (Shen and Zhang, 2019).

2.1.4.3 Oxidizing-agents modification

This approach increases oxygen-containing functional groups on the biochar surface and the hydrogen peroxide is the common oxidizing agent utilized (Wang *et al*., 2015; Tan *et al*., 2011). The carboxyl group is the oxygen containing functional group that is usually increased with these type of modification, which increases the sorption capacity of the material (Xue *et al*., 2012). Huff and Lee (2016) reported that the modification using hydrogen peroxide decreased the pH value of the pine wood derived biochar from 7.16 to 5.66, and increased the oxygen containing functional groups. However, when the hydrogen peroxide content exceeded 10%, the modified biochar exhibited a lower adsorption capacity for methylene blue compared with the unmodified biochar and this suggests that the adsorption performance of modified biochar depends on concentration of the oxidizing agent (Huff and Lee, 2016). The modification of biochar by potassium permanganate have also shown to enhanced the adsorption capacity to Pb(II), Cu(II) and Cd(II) for hickory wood derived biochar (Wang *et al*., 2015).

2.1.4.4 Metal salts or metal oxides modification

Modification of biochar with metal salts or metal oxides can significantly alter its adsorption, catalytic, as well as its magnetic properties and this approach is motivated by three main objectives: (1) to improve the adsorption of specific pollutants for example, unmodified biochar has limited capacity for anionic dyes due to its negatively charged surface, but metal modification can enhance its affinity and adsorption capacity; (2) to facilitate biochar recovery, as the small particle size of biochar makes it difficult to separate from water or wastewater, whereas incorporation of iron salts or iron oxides imparts magnetic properties that allow easy separation and recycling; and (3) to enhance the catalytic performance of biochar for various chemical reactions (Lamberti *et al*., 2024). To enhance the catalytic characteristic of biochar during the persulfate activation process, metal salts or metal oxides could be employed to synthesize the metal-biochar composite (Wang and Wang, 2018).

Metal incorporation into biochar commonly employed to tailor the physicochemical properties of biochar can be achieved through two main routes: (i) blending the metal salts or metal oxides along with the raw biomass and subjecting it to heat treatment temperature (pyrolysis) to produce biochar; (ii) biomass is converted to biochar through pyrolysis before impregnation with the desired metal salts or metal oxides under certain conditions (Zhang *et al*., 2025). The common metals include iron, zinc, magnesium, aluminum and manganese (Tan *et al*., 2016). The modification of rice husk-derived biochar by Fe(III) enhanced the removal of As(III) and As(V) (Samsuri *et al*., 2013). Similarly, the modification of swine manure-derived biochar by MnO_2 could enhance the removal of Pb (II) and Cd (II) (Liang *et al*., 2017). To increase the magnetism of marine macroalgae-derived biochar, nano-composite Fe_3O_4 was used to modify biochar (Jung *et al*., 2016). To enhance the catalytic characteristic of biochar, nano-scale zerovalent iron was used to modify the rice hull-derived biochar (Yan *et al*., 2015). Liu *et al*. (2015) modified corn straw biochar using iron and found that the surface of the modified biochar was covered by small granules of Fe_3O_4, which improved the removal efficiency of phosphorus from aqueous solutions.

2.1.5 Factors Affecting Biochar Properties

The production of biochar via pyrolysis is largely influenced by conditions such as the type of feedstock, pyrolysis temperature and residence time which determine both the biochar yield and its properties. Hence understanding these factors in detail is essential for assessing the potential applications of the resulting biochar (Amalina *et al*., 2022).

2.1.5.1 Feedstocks

Biomass is considered as a complex material, consisting of biological and organic components derived from living organisms such as plants and animals (Parmar, 2017). Biomass is generally classified into two categories: (i) woody biomass and (ii) non-woody biomass, with woody biomass primarily comprising tree and forestry residues (Tripathi *et al*., 2016). Wood and non-wood biomass differ in their properties. Woody biomass is generally distinguished by its low moisture and ash content, compact structure, and high

energy value, while non-woody biomass, including animal waste and agricultural or industrial residues, is characterized by higher moisture and ash levels, lower density, and reduced calorific value (Yaashikaa *et al*., 2020). Among these characteristics, moisture content plays a particularly important role in biochar formation. Moisture in biomass can exist in various forms, including liquid water, water vapor, and water adsorbed within the pores (Yaashikaa *et al*., 2020). Higher moisture content in biomass majorly inhibits formation of char and raises amount of energy needed to attain the pyrolysis temperature (Jafri *et al*., 2018). Low moisture content in biomass is preferred for biochar production, as it significantly reduces the energy required and shortens the pyrolysis time thereby making biochar production more economically feasible compared to using biomass with high moisture content (Yaashikaa *et al*., 2020).

2.1.5.2 Carbonization Temperature

Pyrolysis is the most adopted method for converting biomasses to biochar through thermochemical process under an oxygen-limited environment (Yaashikaa *et al*., 2020). Based on thermal conditions, it can be grouped into three fundamental classifications: (i) Slow pyrolysis (temperatures of 300–500 ^{o}C) and (iii) Fash pyrolysis (temperatures more prominent than 500 ^{o}C) (Tomczyk *et al*., 2020; Liu *et al*., 2015; Yu *et al*., 2017; Elkhalifa *et al*., 2019). Pyrolysis temperature influences properties and structure of biochar, for example, elemental components, pore structure, surface area and functional groups (Dhyani *et al*., 2018). The impact of pyrolysis temperature on such properties can be attributed to the evolution of volatiles at high temperatures (Elnour *et al*., 2019).

2.1.5.3 Residence Time

Increasing the residence time at low pyrolysis temperature (300 ^{o}C) brought about a slow decrease in biochar yield and progressive expansion in pH and iodine adsorption number of biochars (Sun *et al*., 2017). Nonetheless, increasing residence time at high pyrolysis temperature (600 ^{o}C) had little impact on biochar yield or pH, while it diminished iodine adsorption number of biochars (Liang *et al*., 2016).

2.1.5.4 Pre-treatment of Biomass

Pretreating biomass prior to pyrolysis significantly affects the characteristics of the resulting biochar and common pretreatment techniques include soaking the raw material in a solution and reducing the particle size of the biomass, with smaller particle sizes generally yielding higher biochar amounts (You *et al*., 2018). For instance, pine wood has been pretreated by immersion in dilute acidic solutions. Other pretreatment methods involving nitrogen or metal doping, can alter biochar production, while soaking or steaming can modify its elemental composition and properties (Zhang *et al*., 2025b; Qu *et al*., 2025) . Baking the biomass can increase carbon content while decreasing oxygen and moisture levels. Biochar quality depends on both the biomass feedstock and production method, as high moisture or mineral contents (e.g., chlorine or soluble metals) can induce unfavorable reactions during pyrolysis. During this process, volatile elements including H, O, N, and S are largely released, while minerals such as P, K, Ca, Mg, and Si are retained and become enriched in the resulting biochar (Joseph *et al*., 2021; Duwiejuah *et al*., 2020). The occurrence of harmful compounds or components in biochar can either be an outcome of polluted biomass during pyrolysis/gasification (You *et al*., 2018).

2.1.6 Characterization of Biochar

Biochar characterization is performed to determine its utilization in various applications and the structural and elemental analysis also help to predict the impact of biochar on the environment (Brewer *et al*., 2014).

2.1.6.1 Fourier Transform Infrared Spectroscopy (FTIR)

FTIR spectroscopy is a non-destructive vibrational analytical technique used to identify functional groups present on the surface of biochar, as significant structural and compositional changes occur on biochar surface at different pyrolysis temperature (Amalina *et al*., 2022). In DRIFTS (Diffuse Reflectance Infrared Fourier Transform Spectroscopy), the biochar sample is typically prepared in pellet form using potassium bromide (KBr) for analysis which is brought into contact with an ATR crystal to enable the identification of surface functional groups using ATR-FTIR spectroscopy (Berrazoum

et al., 2015). The essential functional groups present at surface of biochar that increase its sorption properties include carboxylic (-COOH), hydroxyl (-OH), amine, amide and lactonic groups, which are primarily influenced by the type of biomass and the pyrolysis temperature (Li *et al*., 2017). Moreover, an increase in physicochemical properties such as pH, specific surface area, and pore structure may be accompanied by a decrease in the abundance of surface functional groups on biochar (Tomczyk *et al*., 2020). Biochars prepared at varying pyrolysis temperatures exhibited pronounced variations in the types and intensities of their surface functional groups and increasing the pyrolysis temperature (650–800 °C) led to a gradual loss of aromatic functional groups (Janu *et al*., 2021).

2.1.6.2 Scanning Electron Microscopy (SEM) and Energy Dispersive X-ray (EDX)

The physical morphology of solid substance can be examined using SEM, which are mainly influenced by the preparation method and temperature, while the overall shape of the particles remains mostly unchanged (Zaitun *et al*., 2022). In addition, biochar produced at higher temperatures exhibit enhanced pore development, resulting in significant improvement in its pore structure and overall textural properties (Fellet *et al.,* 2014). Scanning Electron Microscopy (SEM) provides detailed insights into the microporous and mesoporous structures as well as the pore arrangements within the biochar (Zaitun *et al*., 2022). Furthermore, SEM can be used to examine changes in surface morphology before and after adsorption, and when coupled with Energy Dispersive X-ray Spectroscopy (EDX), it enables the identification of the elemental composition of biochar surfaces. Many studies on biochar applications employ SEM-EDX to evaluate surface characteristics after contaminant adsorption. However, a limitation of SEM-EDX is that it is not suitable for detecting organic contaminants.

2.1.6.3 Brunauer-Emmett-Teller Analysis (BET)

The specific surface area of biochar can be examined using BET analysis which is crucial on account of its responsibility for pollutant removal from soil and aqueous environment (Amalina *et al*., 2022). The BET surface area and porosity of biochar tend to increase after pyrolysis, as crude feedstocks initially lack significant micropores, which are newly formed

during the pyrolysis process (Dougherty *et al*., 2014; Xu *et al*., 2019). For both feedstock types, textural properties (specific surface area), as well as porosity (micropore volume) increased with an increased temperature, which is attributed to the faster release of unstable volatiles and the enhanced development of micropores at higher heating rates (Liu *et al*., 2014). Elnour *et al.* (2019) investigated the effect of pyrolysis temperature on date palm biomass and reported that the BET surface area increased from 2.04 m^2/g to 249.13 m^2/g when the pyrolysis temperature was raised from 300 °C to 700 °C which they attributed to the intense release of volatiles at higher temperatures, leading to the formation of pores in the resulting biochar structure.

2.1.6.4 Atomic H/C and O/C Ratios

The atomic hydrogen/carbon (H/C) and oxygen/carbon (O/C) ratios are indicators of biochar's chemical stability and degree of aromaticity of which a low H/C ratio suggests a material with high stability and fixed carbon content suitable for long-term carbon sequestration (Xie *et al*., 2022; Igalavithana *et al*., 2017). The O/C ratio is important for assessing biochar's surface reactivity, polarity and hydrophilicity influencing its ability to adsorb polar compounds in remediation applications (Igalavithana *et al*., 2017). The atomic H/C ratios of biochar is usually used to evaluate aromaticity and predict its longevity (Wijitkosum and Sriburi. 2023; Xiao *et al*., 2016). The classification based on H/C is preferable due to H's direct experimental determination, whereas O is indirectly determined (Klasson, 2017). IBI classifies biochar samples based on organic carbon contents (OC), being Class 1: OC ≥ 60%, Class 2: 30% ≤ OC < 60%, Class 3: 10% ≤ OC < 30%, and non-biochars OC < 10% (Klasson, 2017). The half-life of an O/C < 0.2 biochar, would be >1000 years; for an O/C 0.2–0.6 biochar sample, the half-life would be 100–1000 years and for O/C > 0.6 the half-life would be <100 years (Spokas, 2010). The Van Krevelen diagram illustrating the standard regions of biomass and derived biochars is presented in Fig. 2.4 (Silveira *et al*., 2023).

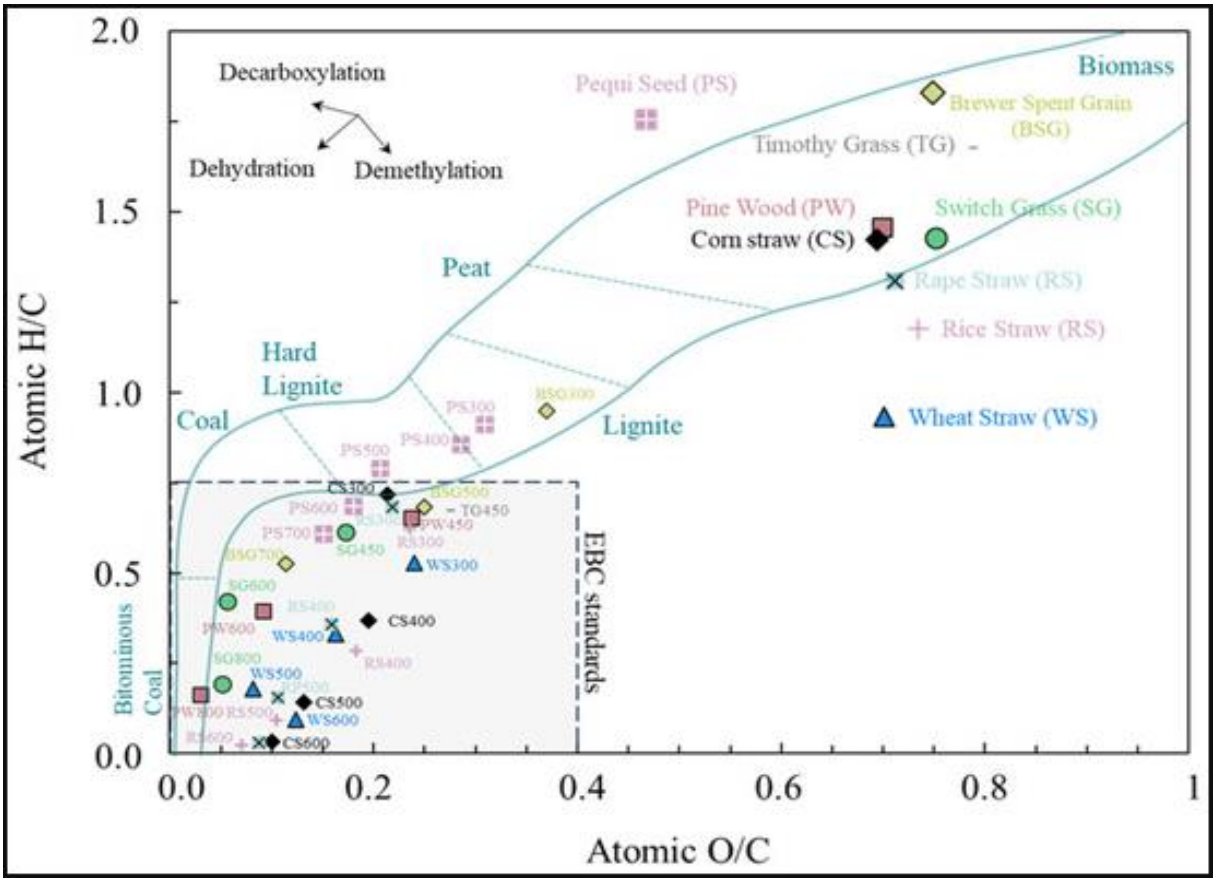

Fig. 2.4: Van Krevelen's diagram of the H/C to O/C ratio(Source: Silveira *et al*., 2023).

Fig. 2.4 proves valuable in assessing the coalification and reaction pathways of the modified products (Silveira *et al*., 2023). It offers valuable insights into the reduction of polarity (O/C) and aromaticity (H/C), as well as the extent of reactivity (degradation of carboxyl and hydroxyl groups) (Ivanovski *et al*., 2022; McKendry, 2002a). The conversion of hemicelluloses (at temperatures ranging from 200 to 350 °C) involves a process of dehydration combined with the cleavage of weak linkages between small substituents and the leading polymer chains, while in the case of cellulose, dehydration reactions start at approximately 200 °C, releasing water as the primary product (González Martínez *et al*., 2022).

2.1.6.5 Calorific value

Calorific value, also known as higher heating value (HHV), is one of the most important properties to consider when evaluating biochar for energy applications, such as a solid fuel. It represents the amount of energy released during combustion and reflects the energy efficiency of biochar (Xie *et al*., 2022; Igalavithana *et al*., 2017). The higher heating value indicates an upper limit for the available thermal energy produced on a given combustion and stands as the main comparison parameter for the combustion of biochar samples (Xie *et al*., 2022). Furthermore, the caloric value of biochar can be estimated from the proximate analysis and ultimate analysis (Qian *et al*., 2020). The production method of biochar, particularly the pyrolysis temperature, plays a crucial role in determining its elemental composition, specifically in terms of hydrogen, carbon, nitrogen, and oxygen content, directly influencing the higher heating value (HHV) (Kim *et al*., 2011). This transformation is reflected in the reduction of the O/C and H/C ratios, which are strongly correlated with an increase in the higher heating value (HHV) (Zhang *et al*., 2020; Kim *et al*., 2011). As a result, the biochar becomes more suitable as an energy source and these characteristics make it ideal for energy applications requiring high fuel efficiency (Zhang *et al*., 2020).

2.1.7 Applications of Biochar

Biochar has attracted significant research interest due to its eco-friendly nature, low cost, and ease of preparation from various biomass sources via thermochemical techniques for a wide range of environmental applications (Jha *et al*., 2023). It is particularly effective in removing contaminants from soil and water, with its performance influenced by the type of biomass and pyrolysis temperature (Amalina *et al*., 2022). Biochar produced at high pyrolysis temperatures is carbon-rich and exhibits enhanced removal of organic pollutants due to properties such as high porosity, large surface area, elevated pH, low dissolved carbon content, and hydrophobicity (Yaashikaa *et al*., 2020). In contrast, biochar prepared at lower temperatures contains more oxygen-containing functional groups, higher dissolved organic carbon, and lower porosity, making it more suitable for removing inorganic pollutants (Jha *et al*., 2023). Additional factors such as pH and contact time also affect its removal efficiency (Luo *et al*., 2021). Beyond pollutant removal, biochar finds

applications as a catalyst, in wastewater treatment, composting, energy storage, carbon sequestration, and soil amendment (Yaashikaa *et al*., 2020). The advantages and limitations of these applications are summarized in Table 2.4.

Table 2.4: Advantages and Limitations of Different Applications of Biochar

Applications	Aim	Benefits	Limitations	References
Catalyst	Act as supporting materials for direct catalysis	Low cost, more functional groups, large surface area	Efficiency may be less	(Dehkhoda *et al*., 2010; Kastner *et al*., 2012; Mani *et al*., 2013)
Energy storage	Utilized as electrode materials	Low cost, highly porous, large surface area	Performance is low	(Qian and Kumar, 2015)
Soil amendment	Enhancing soil fertility and quality and carbon sequestration	Low cost, minimizes emission of greenhouse gases, helps to retain nutrients and water, controls nutrient loss	Contamination of heavy metals and polyaromatic hydrocarbons may persist	(Sohi *et al*., 2010; Varjani *et al*., 2019)
Adsorbents	Removal of organic and inorganic pollutants in soil and aqueous system	Low cost and more oxygen groups present in biochar enhance adsorption of pollutants	Removal efficiency of pollutants is undetermined and heavy metals retain in soil	(Houben *et al*., 2012)
Composting	Improving structure of microbial population and carbon mineralization	Porous, reduces emission of greenhouse gases, large surface area and retains nutrients	There may be a chance of heavy metals and other contaminants invading into soil	(Zhang and Sun, 2014)

2.1.8 Biochar as support

Biochar can serve as catalyst support due to its porosity and the presents of functional groups (such as $^{-}$OH, -COOH, -NH_2), which is more favorable for surface functionalization, anchoring of metal nanoparticles (Creamer *et al*., 2014; Gao *et al*., 2016). Fig. 2.5 present the pore structure as well as the typical functional groups present on the

biochar surface. Biochar has been shown to act as an effective support for metal catalysts by facilitating the loading of metal precursors onto its surface, enabling the synthesis of biochar-supported metal catalysts (Wang et al., 2020). Biochar's mesoporous structure enhances the proper dispersion of immobilized metal particles while also preventing particle aggregation owing to intra-particle interaction (Hervy *et al.,* 2017). The incorporation or fixing of metal elements, for example, Mn, Cu, Co, and Fe into biochar pores (Biochar-based solid-acid catalysts) result in no or minimal metal escape into the aqueous phase thereby providing more accessible active sites for chemical reactants (Xiong *et al.,* 2017). Biochar-based solid acid catalysts can perform well in some reactions when they have certain functional groups on their surface. For instants, sulfonated carbon has been shown to be more effective for the hydrolysis of cellohexaose than SO_3H-functionalized resins, with the catalytic adsorption sites primarily associated with carboxylic (–COOH) and phenolic hydroxyl (–OH) groups on the carbon surface (Kitano *et al.*, 2009).

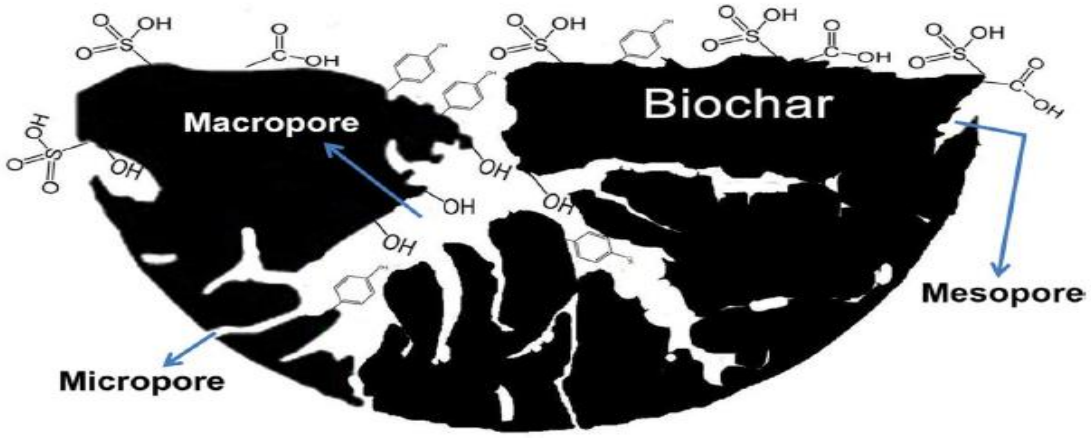

Figure 2.5: A Porous Biochar Model with Multiple Functional Groups (Source: Yang *et al.*, 2019).

Biochar, for instance, is catalytically active in cracking tar because it has presence of inorganic elements including Fe and K (Hervy *et al.,* 2017). Furthermore, several processes can be used to activate feedstocks, control synthesis conditions, functionalize materials on the surfaces and form composites with other materials (Chellappan *et al.,* 2018).

2.1.8.1 Synthesis of Metal - Doped Biochar

Biochar itself has little catalytic activity, and thus loading the biochar with active substances helps to enhance its physicochemical properties, leading to enhanced reactivity in a range of processes and applications (Xiong *et al*., 2017). The two most frequently used procedures for the preparation of metal-doped biochar are impregnation-pyrolysis and co-precipitation, both of which involve the loading of the desired active substance onto the surface of the biochar (Xiao *et al*., 2023).

- **Impregnation-Pyrolysis**

These methods comprise of the one-step (*in-situ*) and the two-step (step-by-step) method. The *insitu* method involved impregnating the biomass carbon precursor with a metal solution, consequently depositing metal ions onto the surface or interior of the biomass matrix (Liu *et al*., 2025). After drying, the metal ions on the biomass matrix is pyrolysed (usually from 400^{o}C to 800^{o}C) converting metal ions to metal oxide nanoparticles or zero-valent metals (due to the release of strong reducing volatile compounds during activation pyrolysis such as CO_2) (Bombuwala Dewage *et al*., 2019). This method presents several advantages for the synthesis of biochar-supported metal nanoparticles (NPs) such as: (i) the activation/production of biochar and the reduction of metal NPs proceed simultaneously in one-step method, thus eliminating the use of additional reducing agents; (ii) the metal precursors may have some catalytic effects on the pyrolysis process itself, thus reducing the required activation conditions (temperature and pressure) and improving the porous structure of the final biochar; and (iii) the entire preparation process involves only one pyrolysis step, making it easy to scale up (Liu *et al.,* 2015).

In the two-step method, the biochar (BC) is firstly mixed with active phase metal salts and later calcined at the desired temperature in an inert atmosphere (Wang *et al*., 2021). Compared with the two-step method, the in-situ synthesis method (one-step method) is more convenient in operation; however, the two-step pyrolysis process is usually chosen over the one-step process due to the fact that it allows for more controlled and efficient conversion of biomass into biochar, leading to the formation of larger, and more uniform

pores including higher specific surface area (Mahmoud *et al*., 2024). During the impregnation method, metal ions are adsorbed onto the biochar surface through coordination and electrostatic interactions. During the subsequent pyrolysis process, these metals interact with various oxygen-containing functional groups, leading to the formation of highly dispersed and firmly anchored metal or metal oxide nanoparticles on the biochar surface (Longo *et al*., 2025).

The successful integration of metals onto biochar has led to the development of metal-doped biochar catalysts and has significantly advanced biomass-based catalytic processes. The key characteristics of the two principal synthesis routes are illustrated in Fig. 2.6.

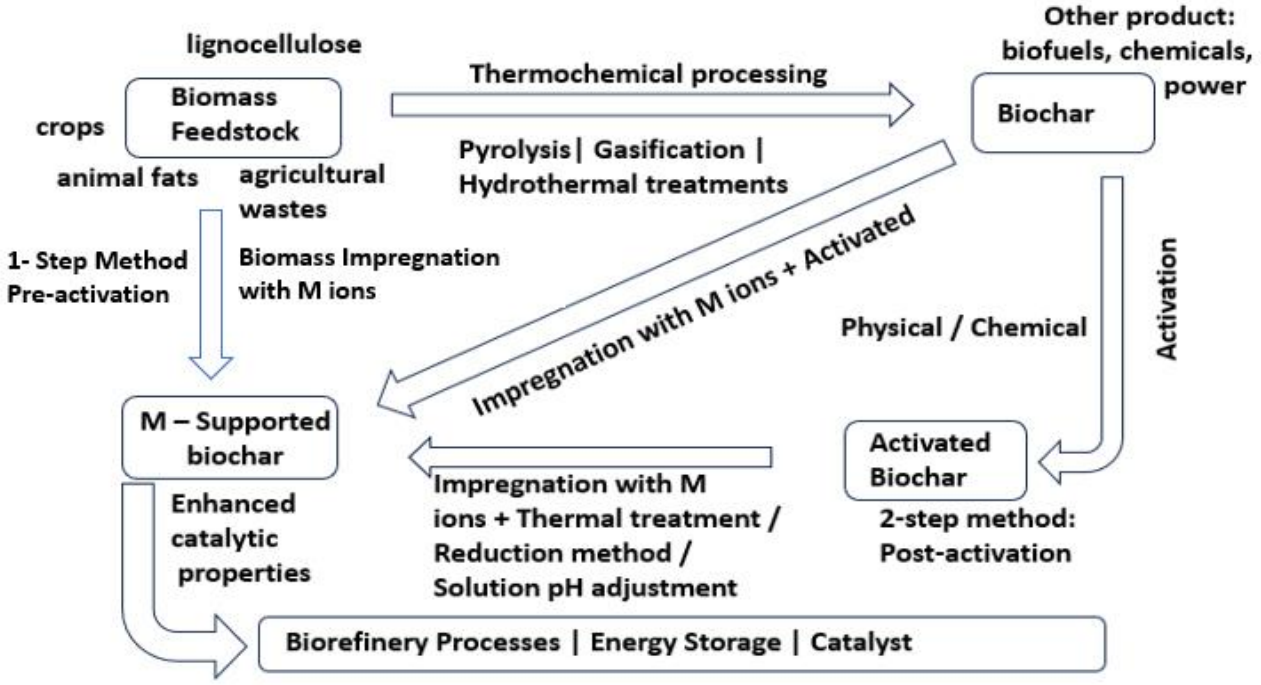

Fig. 2.6: Schematic Diagram of: One-step and Two-Step Methodologies to Metal Supported Biochar Preparation

The impregnation pyrolysis method is the most widely used method at present (Du *et al*., 2020; Ma *et al*., 2020; Wang *et al*., 2020; Yi *et al*., 2020). According to some previous studies, using ferric iron salt as a metal precursor enhances the dispersion of iron species on the carbon matrix, thereby improving the catalytic activity and stability of the resulting biochar-based catalysts (Zarate-Guzman *et al.,* 2020; Masud *et al.,* 2025). The reaction of

metal - doped biochar (MBC) prepared by impregnation-pyrolysis is summarized as follows (Bombuwala Dewage *et al*., 2019; Collard *et al*., 2012; Gan *et al*., 2020; Hu *et al*., 2019):

$$Fe\,(III) + Biochar \rightarrow Fe(?)—Biochar \quad (2.1)$$

$$BC \xrightarrow{\Delta,\ oxygen-limited} CO_2 + CO + H_2 + CH_4 + Other\ products \quad (2.2)$$

$$Fe(III)—Biochar + CO + H_2 \rightarrow Fe_3O_4/(\gamma - Fe_2O_3)/Fe^0—Biochar + CO_2 + H_2O \quad (2.3)$$

Pyrolysis temperature, pyrolysis time, and the ratio of impregnated metal precursor to biomass/biochar all affect the preparation of MBC, among which pyrolysis temperature is the most important. Wang *et al*. (2019) found that when the pyrolysis temperature increases from 300 to 450℃, α-Fe_2O_3 will be transformed into Fe_3O_4, and the magnetism of MBC will increase greatly. Generally, as the pyrolysis temperature continues to increase (≥ 600°C), iron oxides will gradually transfer to zero-valent iron (Jiang *et al*., 2019; Liu *et al*., 2019).

Shen *et al*. (2014) investigated the catalytic conversion of tar during co-pyrolysis with biomass using nickel-rich rice husk char (RHC–Ni) and nickel-rich rice husk ash (RHA–Ni). These catalysts were prepared from rice husk and a nickel salt through a one-step impregnation method, yielding silica-rich carbonaceous materials with highly dispersed nickel species. Both catalysts exhibited excellent catalytic performance, achieving tar conversion efficiencies of 96.9% and 98.6%, respectively.

Zhu *et al*. (2019) synthesized a bimetallic Cu-Ni carbon catalysts by loading Ni and Cu onto biochar through the impregnation method at mild conditions. The catalysts demonstrated excellent performance in the conversion of 5-hydroxymethylfurfural (HMF) to 2,5-dimethylfurfural (DMF), a promising liquid fuel/fuel additive with 93.5% yield under optimized conditions.

- **Co-precipitation**

The co-precipitation method involves dispersing biochar (BC) into metal salt solution (solution containing metals such as Fe, Co, Ni etc.), and adding alkaline solutions, such as NaOH, NH_4OH to adjust the pH, or reducing agents as $NaBH_4$ and KBH_4, at a fixed

temperature (Mohan *et al*., 2015). The process allows the magnetic precursor generates magnetic precipitation on the surface of the BC resulting in magnetic biochar (MBC) (Mohan *et al*., 2015). This method is more complicated than the impregnation-pyrolysis method but it is more controllable, enabling the magnetic medium to be stably adhered to the biochar matrix, however, the addition of alkali will increase the cost (Alchouron *et al*., 2020; Tong *et al*., 2020). The metal precursor commonly used in chemical co-precipitation is Fe^{3+} and Fe^{2+} with a molar ratio of 2:1, and the reaction in the preparation process is represented by eqns 2.4 and 2.5 (Wu *et al*., 2018):

$$Fe^{2+} + 2Fe^{3+} + 8OH^{-} \rightarrow Fe_3O_4 + 4H_2O \qquad (2.4)$$

The Fe_3O_4 is unstable and prone to the following reactions (Qambrani *et al*., 2017):

$$Fe_3O_4 + 2H^{+} \rightarrow \gamma - Fe_2O_3 + Fe^{2+} + H_2O \qquad (2.5)$$

Guel-Nájar *et al*. (2023) synthesized iron doped corncob biochar by co-precipitation method and reported that it effectively immobilized methylene blue, achieving a maximum adsorption capacity (q_m) of 39.66 mg/g higher than 23.17 mg/g obtained for the unmodified corncob biochar. Geetha *et al*. (2024) incorporated metal ions onto biochar surface by co-precipitation method to produce metal - doped biochar (MBC). The MBC was effective in adsorbing more than 90 % of crystal violet from aqueous solution.

As a catalyst support, biochar offers many advantages including large surface area, lower cost, functional group tailoring, etc., which makes it highly beneficial for many catalytic applications (Shetty *et al*., 2023). There are several intrinsic properties of biochar – based catalyst that contribute to its effectiveness as a catalyst support including (i) heterogeneity, i.e., the reaction mixture can be easily isolated from other reactants; (ii) bifunctionality, i.e., transesterification and esterification are involved; (iii) recyclable; (iv) porous; (v) non-graphiṭable, i.e., it does not form crystal at high temperatures (Jitjamnong *et al.,* 2021; Dehkhoda and Ellis, 2013). In addition, the properties of metal - doped biochar catalysts including particle size and dispersion, etc., can affect the breakage of C-C, C-O and C-H bonds, resulting in selectively controlling the pyrolytic reaction process (Wang *et al*., 2025).

Comparing biochar-based catalysts with other solid-based catalysts, biochar has the advantages of being cost-effective, eco-friendly, easy to produce, reusable, and sustainable (Jitjamnong *et al.,* 2021).

Furthermore, biochar – based catalyst can be used in many different fields, including agriculture, environment, and energy, for biodiesel production, tar removal, waste management, production of syngas, production of chemicals, and removal of contaminants (Jose *et al.,* 2011; Guo *et al*., 2019).

2.2 Friedel-Crafts Reaction

Friedel-Crafts (FCs) reaction involve introducing an alkyl or acyl group into an aromatic ring in the presence of a catalyst (Ohata, 2024). The alkylation and acylation are two basic type of Friedel Craft reaction, and both reactions proceed *via* the same mechanism, which is the typical reaction of aromatic compounds known as electrophilic aromatic substitution (Heravi and Zadsirjan, 2021). FCs alkylation in particular comprise of the alkylation of an appropriate aromatic ring using an alkyl halide, conventionally in the presence of a strong Lewis acid ($AlCl_3$, $FeCl_3$, BF_3, $BeCl_2$, $TiCl_4$, etc.) as the catalyst (Rueping and Nachtsheim, 2010). Commonly, anhydrous ferric chloride act as a lewis acid catalyst by interacting with the alkyl halide to generate a carbocation (electrophile). This electrophile then attacks the aromatic ring (nucleophile), leading to the substitution of a hydrogen atom via a process known as electrophilic aromatic substitution (Smith and March, 2007). In addition, strong Brønsted acids such as H_2SO_4 and HF, or super acids, such as $HF{\cdot}SbF_5$ and $HSO_3F{\cdot}SbF_5$, have also been used successfully and proven to accelerate the FCs alkylation reaction (Heravi *et al*., 2018). A reaction involving alkylation and acylation are presented in Fig. 2.7 and 2.8.

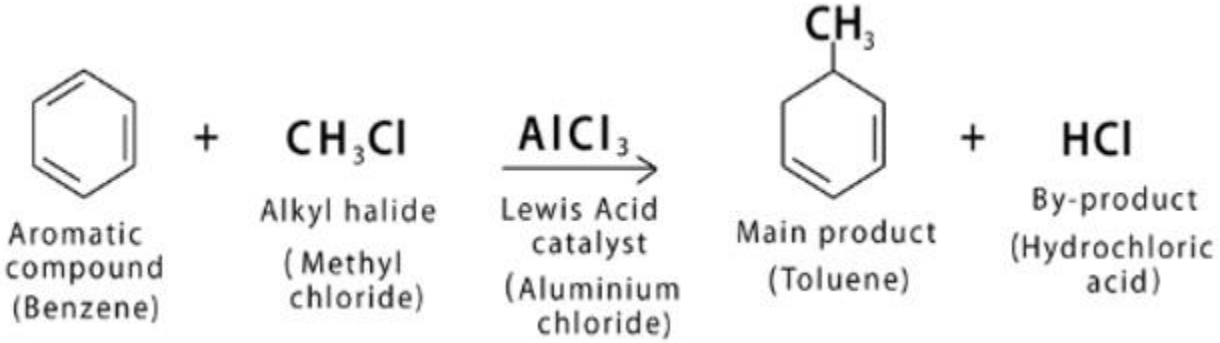

Fig. 2.7: A Typical Friedel Alkylation Reaction

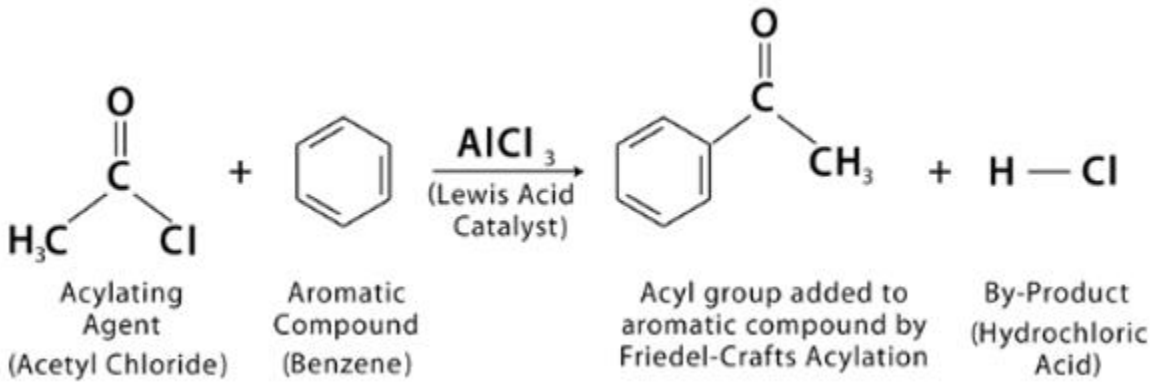

Fig. 2.8: A Typical Friedel Acylation Reaction

Friedel–Crafts reaction is one of the oldest carbon– carbon bond forming processes, and is still an attractive method to introduce substituents on aromatic rings. Although effective, this method often suffers from over-alkylation because the products are more nucleophilic than the starting materials. It is also limited to secondary or tertiary alkylating agents to avoid carbocation rearrangements (Prajapati *et al*., 2012). Notably, the reaction typically relies on stoichiometric or excess quantities of Lewis or Brønsted acid catalysts. For example, the FCs alkylation reaction requires stoichiometric or super stoichiometric amounts of a Lewis acid or Brønsted acid (Heravi *et al*., 2018). Despite the importance of Friedel–Crafts alkylation in organic synthesis, several limitations remain that need to be addressed, including the use of corrosive and non-recyclable homogeneous catalysts, poor selectivity, catalyst deactivation, formation of polyalkylated by-products, harsh reaction conditions, and environmental concerns associated with waste generation and catalyst disposal. Thus, developing greener, more economical alternatives therefore remains a major research priority.

2.2.1 Catalysis

Catalysis is simply a process whereby the rate of chemical reaction is enhanced by the adding of a substance (catalyst), which supposedly does not take part or simply does not undergo any chemical change (Dev *et al*., 2018; Yunes *et al*., 2023). The catalyst is a substance that accelerates the rate of a chemical reaction without being consumed or permanently changed in the process. Catalytic materials promote reactions by decreasing

the activation energy required for overcoming the energy barrier, resulting in faster kinetics without altering the thermodynamic feasibility of the process. Catalysts also enhance reaction selectivity, enabling processes that would normally yield multiple products to form predominantly a single or desired product, thereby minimizing environmentally harmful by-products (Kumar *et al*., 2020). Catalysts can be classified as homogeneous and heterogeneous according to their physical state or according to the environment in which the reaction takes place.

2.2.1.1 Homogeneous Catalysis

The catalyst and reactants are present in the same phase, which is often liquid or gaseous, in homogeneous catalysis. Homogeneous reaction media containing homogeneous catalysts are highly effective for liquid-phase organic reactions due to their evenly dispersed discrete molecules (Diallo *et al*., 2025). Conversely, several limitations including toxicity, large stoichiometric amounts, difficulty in separation and recovery, equipment corrosion as well as disposal problems etc, are accompanied with these catalysts (Devi *et al*., 2014; Li *et al*., 2013). The two major types of homogeneous catalyst include Lewis acids or Bronsted acid. In organic chemistry most especially in Friedel Crafts alkylation, reactions occur with reactants in solution, in the presence of Lewis acids or Bronsted acid which are equally soluble.

Lewis acid catalysis

Lewis acids are chemical species that act as electron pair acceptors. The process of accepting an electron pair by a Lewis acid results in the formation of a Lewis complex or a new coordinate covalent bond. Lewis acidity is closely linked and intertwined with electrophilicity. Thus, due to their electron deficiency, electrophiles with positive or partially positive characters as a result of electronic effects (inductive and electronic) manifest themselves as electron pair acceptors (Al Mamari, 2023). Lewis acids have long been used as catalysts and played significant roles in various chemical transformations, particularly in Friedel-Crafts alkylation of organic reactions. Lewis acids including boranes

(BR_3), such as BH_3 and BF_3, aluminum compounds (AlR_3)such as $AlCl_3$. Other examples include alkali (M^+) metal ions, such as K^+ and alkaline earth metal ions (M^{2+}), such as Ca^{2+} and transition metal ions, such as Mn^{2+}, Fe^{3+}, etc. have been described as catalysts for the FC alkylation (Al Mamari, 2023; Lachter *et al*., 2024). For instance, ferric nitrate serves as an influential Lewis acid that efficiently catalyzes Friedel–Crafts alkylation of indoles with electron-rich olefins at room temperature. The reaction is highly regioselective and iron(III) ion was found to activate the electron-rich C=C bond with collaboration of the carbonyl group in the catalytic processing which produced about 83% of the alkylated indoles (Jiang *et al*., 2010).

Bronsted acid catalysis

Brønsted acid catalyst plays a key role in the catalytic system by protonation of nucleophilic substrates. The resulting complex proceeds to undergo a reaction, then product and the catalyst are liberated to enable repetition of the catalytic cycle. Brønsted-acids including HF, H_2SO_4, and H_3PO_4 have also been shown to accelerate this transformation (You *et al*., 2009). Brønsted acids are highly effective in promoting water-assisted Friedel–Crafts alkylation reactions. In this process, benzyl and propargyl alcohols were coupled with *N*-substituted indoles and naphthols using a calix[n]arene sulfonic acid catalyst bearing suspended aliphatic chains, operating under mild temperature conditions. The catalyst was found to promotes the nucleophilic substitution in aqueous medium, generating the alkylated products of up to 60–94% yields. Furthermore, it exhibited excellent stability, maintaining high catalytic performance after seven recycling cycles, with product yields remaining between 92% and 96% (Liu *et al*., 2008). The first asymmetric aza-Friedel‑Crafts alkylation catalyzed by Bronsted acids was reported by Uraguchi *et al*. (2004), where 2-methoxyfuran was used as the nucleophilic donor in the presence of 2 mol% of the phosphoric acid as catalyst and at 35°C. The aza-Friedel‑Crafts reaction of 2-methoxyfuran with N-tert-butoxycarbonylaldimines proceeded smoothly affording furan-2-ylamine (2-aminofuran) in 80‑96% yields.

2.2.1.2 Heterogeneous Catalysis

Catalysis is heterogeneous when the catalyst and the reactant(s) are not in the same phase. Heteropolyacids (HPAs) and their salts, zeolite, clay montmorillonite, and mesoporous oxides are commonly used heterogeneous catalysts (Alzeer et al., 2022). These catalysts exhibit advantages including, comparatively easy separation from the product and high recycling ability (Kokel *et al*., 2019). In addition, they also possess high thermal and chemical stability, making them suitable for a wide range of reaction (Anekwe *et al*., 2025). The vast majority of cases of heterogeneous catalysis involve a catalyst in solid form (bulk), the reactants being gaseous and/or liquid (Králik *et al*., 2025). Adsorption takes place when reactant molecules attach to the surface of a catalyst, allowing the reaction to occur. The specific location on the catalyst surface where the reactants bind is known as the active site. Generally, the larger the contact area between the catalyst and the reactants, the faster the reaction proceeds. Indeed, the greater the contact surface between the catalyst and the reactants, the faster the reaction (Králik, 2014).

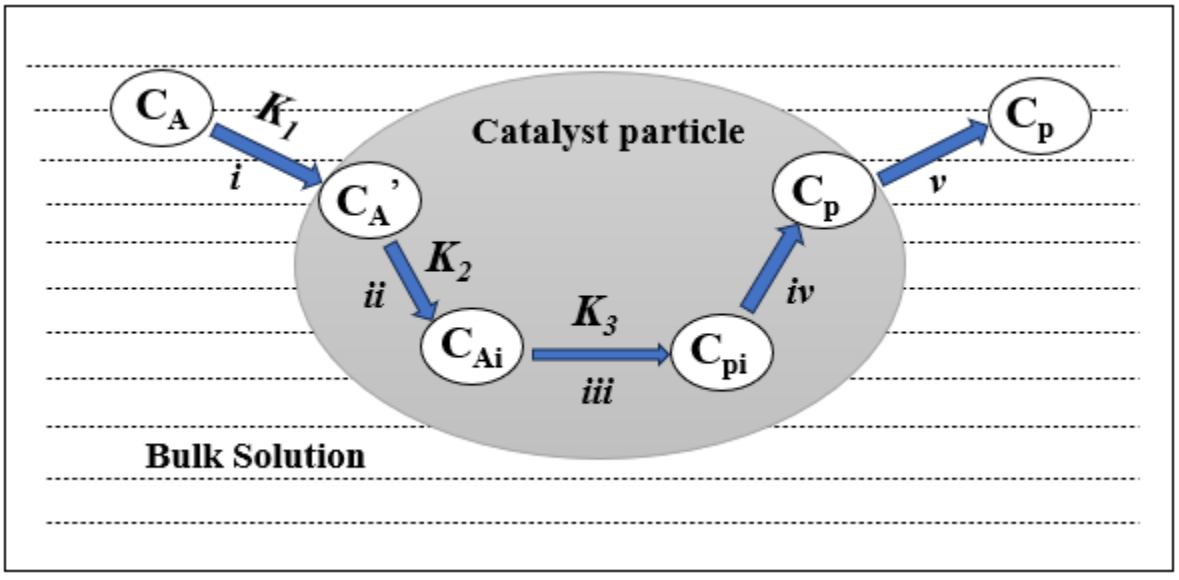

Figure 2.9: Schematic diagram of main steps of reaction in heterogeneous catalyst

The main steps in the mechanism of heterogeneous catalysis as describe in Fig. 2.9 are as follows: (i) diffusion of reactant A from the bulk solution to the catalyst external surface,

(ii) diffusion of reactant A from the catalyst external surface to its internal reactional surface, (iii) chemical reaction between reactants A and B on the catalyst internal surface to produce product (P) (iv) desorption of P from the catalyst internal surface, (v) diffusion of P away from the surface to the bulk solution (Dung *et al*., 2017). The first step is called external diffusion, where the reactants move from the solution to the surface of the catalyst. This step is explained using the mass transfer coefficient (k_1). The second step is internal diffusion, where the reactants move inside the catalyst pores, and this is described by the adsorption equilibrium constant (k_2). The third step is the surface reaction, where the actual chemical reaction takes place on the catalyst surface, and it depends on the reaction rate constant. The fourth and fifth steps have very little effect on the reaction. Hence, steps (i), (ii), and (iii) are typically considered when determining the rate-controlling step of the catalytic reaction (Dung *et al*., 2017).

Heterogeneous catalyst possess high relevance in Friedel Crafts alkylation reaction on account of their strong acidity and redox characteristics. Heteropoly acids (HPAs) are a broad class of compounds composed of nanometer-sized transition metal–oxygen octahedral anions, which create a stable, compact framework of polymeric oxoanions as their basic structural units. HPAs exhibit a wide variety of structures, but those with a Keggin-type structure are the most studied and widely used, particularly as acid catalysts, due to their chemical stability and ready availability (Luo et al., 2020). Bhure *et al*. (2007) demonstrated that phosphotungstic acid (PTA) could be used as a solid catalyst for the rearrangement of benzyl phenyl ether in toluene to give 2-benzyl phenol as a major product. A complete conversion of benzyl phenyl ether with 52% selectivity to 2-benzyl phenol was achieved at reflux conditions of 0.1% PTA catalyst, 110^{o}C and at 0.5hr. In addition, the PTA catalyst could be easily recovered and reused without the loss of activity.

Zeolites are crystalline microporous aluminosilicates with uniform 3D pore structures, high surface area, tunable acidity and strong thermal stability, making them excellent heterogeneous catalysts (Alotaibi, 2025; Yu *et al*., 2019; Cai *et al*., 2020; Masoumifard et al., 2018). Their dense network of active sites supports efficient molecular-level reactions (Kordala and Wyszkowski, 2024; Yang and Zhou, 2017; Zhang *et al*., 2022). However,

their commercial adoption remains limited, primarily because of challenges in stability under moisture, synthetic cost, and scalability (Zormpa *et al*., 2025; Alotaibi, 2025). Leng *et al*. (2022) evaluated hierarchical (M-HM, M-HBeta) and pristine (HM and HBeta) zeolites for benzylation of benzene with benzyl alcohol at 120 °C, forming mainly diphenylmethane and dibenzyl ether. HM and HBeta catalyst showed low initial conversions of about 30% at 60 min and deactivated rapidly, while M-HBeta achieved a much higher initial conversion of 93% at the same time but also deactivated quickly. M-HM showed the same 30% conversion at 60 min, however increased to 80% at 120 min, and then gradually decreased to 41% at 300 min, maintaining >90% selectivity to diphenylmethane. Candu *et al*. (2011) investigated the catalytic liquid-phase benzylation of benzene with benzyl alcohol (BnOH) to produce diphenylmethane (DPM) over several zeolite catalyst types; HSZ 600 mordenite, CBV 20A mordenite, and H-beta zeolites with Si/Al ratios of 10.8 and 35.8 at 80 – 150^{o} C and atmospheric pressure, using three reaction approaches: (A) adding all benzyl alcohol at the start, (B) dropwise addition, and (C) continuous-flow operation. They found that both conversion and product distribution depended strongly on the reaction method and the zeolite type. Under optimal conditions, the H-beta zeolite (Si/Al = 10.8) in the continuous-flow method (C) gave the best performance, achieving 99.2% BnOH conversion with 88.9% selectivity to DPM.

Clay montmorillonite has shown good catalytic activity in Friedel–Crafts alkylation. It is an abundant, low-cost aluminosilicate clay with layered SiO_4/AlO_6 sheets that give it useful 2D structures and strong catalytic properties (Fajrina, and Tahir, 2019). Its flexibility, swelling, ion-exchange ability, acidity, reusability and low cost make it valuable in many applications, and its performance is further enhanced when modified with metals, nanoparticles or polymers (Akinwunmi *et al*., 2020; Upadhyay and Srivastava, 2016). For instance, the aromatics benzene, toluene, o-xylene, p-xylene, mesitylene and anisole were efficiently alkylated with cyclohexanol and cyclo-pentanol in 1,2-dichloroethane using Fe^{3+}-montmorillonite as the catalyst, consistently gave high yields under both p-toluene sulfonic acid (TsOH) and methanesulfonic acid (MsOH) conditions.

Metal oxides are widely applied in catalysis, especially in Friedel–Crafts alkylation, since they are more resistant to catalyst poisoning. These materials consist of metal–oxygen structural units and may be derived from either transition metals or main-group metals. Their surface properties, morphology, and solid-state characteristics play key roles in enabling complex heterogeneous catalytic reactions (Peña and Fierro, 2001). Common examples include the oxides of chromium, aluminum, manganese, zinc, iron, and nickel, which often possess stable high oxidation states and intermediate stability, making them particularly effective in catalytic processes (Pirkanniemi and Sillanp, 2002). Nguyen *et al*. (2018), synthesized three Cu-Mg-Al mixed metal oxides (MMO) and evaluated their catalytic efficiency for the synthesis of bis(indolyl)methanes via the Friedel–Crafts alkylation of indoles with aromatic aldehydes under solvent-free microwave irradiation. The Cu-Al MMO showed the best catalytic activity to produce the expected products up to 98% yield and 100% selectivity for only 20 min.

2.3 Optimization and Design of experiment

Optimization is used to improve chemical process performance by adjusting process variables to achieve the best operating conditions. The Design of Experiments (DOE) is a systematic approach that quantifies and optimizes the effects of multiple input variables (factors) on one or more output variables (responses). Design of experiment (DOE) is a controlled experiment in which the experimenter is interested in both quantifying and optimizing the effect of a number of input variables on one or more output variables. By quantification we mean estimating the size of the effect of each input variable.

DOE helps to:

- Identify key factors affecting the response(s)
- Determine interactions between factors
- Establish optimal factor settings for desired outcomes

The main steps in DOE include identifying factors and responses, designing the experiment, conducting it, analyzing results, and optimizing outcomes (Hardwick, 2011).

2.3.1 Response surface methodology

Response surface methodology (RSM) is a collection of mathematical and statistical techniques used for the modelling and analysis of problems in which a response of interest is influenced by several variables. The objective is to optimize the response (output variable) which is influenced by several independent variables (input variables or factors) (Montgomery, 2001). Different levels or values of the operating conditions comprise the factors in each experiment (Jurado-Alameda, 2003). Some independent variables may be categorical, such as the supplier of the raw material, while others are quantitative, like feed rates, temperature, or time. In practice, categorical variables are treated separately by evaluating the optimal conditions of the quantitative variables across the different levels or combinations of the categorical variables. The fundamental methods for quantitative variables involve fitting first-order (linear) or second-order (quadratic) functions of the predictors to one or more response variables, and then examining the characteristics of the fitted surface to decide what action is appropriate (Jurado-Alameda, 2003).

2.3.2 Theory of RSM

Response Surface Methodology (RSM) is a collection of mathematical and statistical techniques used to describe the relationship between a response and its independent variables. It evaluates the effects of individual variables as well as their interactions on a process. Beyond analyzing these effects, RSM also produces a predictive mathematical model. The term "Response Surface Methodology" arises from the graphical representation of this model, which depicts the response as a surface over the independent variable space. The relationship between the response and the input is given in Eq. (2.6):

$$\eta = f(x_1, x_2, \dots, x_n) + \varepsilon \qquad (2.6)$$

Here, η represents the response, while f denotes an unknown function relating the response to the independent variables. The terms x_1, x_2, … , x_n are the independent (natural) variables, with n indicating their total number. The symbol ε corresponds to the random error term, which accounts for variations not explained by the function f, including factors

such as experimental and measurement errors. This error term is commonly assumed to follow a normal distribution with a mean of zero and a constant variance.

An optimization study based on response surface methodology (RSM) can generally be divided into three main phases. The first phase involves preliminary investigations, during which the relevant independent variables and their operating ranges are identified. The second phase focuses on choosing an appropriate experimental design, followed by model development and validation. The final phase involves generating response surface and contour plots to illustrate how the response varies with the independent variables and to locate the optimal operating conditions. Further details of each phase are discussed in the subsequent sections.

2.3.2.1 Preliminary Investigation – Determination of Independent Variables and Their Levels

Chemical and biochemical processes are influenced by numerous parameters. Since it is impractical to study the effects of all parameters simultaneously, it becomes necessary to select those that have the most significant influence. Screening experiments are therefore employed to identify the independent variables (factors) that most strongly affect the process. Factorial designs are often useful for this purpose.

Once the important parameters have been identified, the next step is to determine the direction in which improvements occur and to define appropriate levels for each parameter. The success of the optimization process strongly depends on the correct choice of these parameter levels; incorrectly chosen levels may result in an unsuccessful optimization outcome.

The independent variables usually differ in their measurement units and ranges. Even when some parameters share the same units, they may not be examined over identical ranges. Therefore, direct regression analysis cannot be performed using the natural variables. To eliminate this inconsistency, the variables must first be normalized or coded to a dimensionless scale prior to regression analysis.

Each coded variable is typically scaled to range between –1 and +1 so that all parameters contribute comparably to the response, regardless of their original units or ranges. The commonly used equation for coding is given by:

$$X = \frac{x-[x_{max}+x_{min}]/2}{[x_{max}-x_{min}]/2} \quad (2.7)$$

where

x= natural variable,

X= coded variable,

$x_{\max}$and $x_{\min}$= maximum and minimum values of the natural variable, respectively.

2.3.2.2 Selection of Experimental Design, and Prediction and Verification of Model Equation

According to Myers and Montgomery (1995), ten important properties should be considered when choosing an appropriate response surface design. Many statistical software packages are capable of generating optimal designs based on specific criteria and user-defined inputs. These designs differ in their selection of experimental points, number of runs, and the inclusion of blocks.

After the design is selected, the model equation is formulated and the corresponding coefficients are estimated. In most RSM studies, the model is expressed as a second-order polynomial (quadratic model), which can be written as:

$$y = \beta_0 + \sum_{j=1}^{n} \beta_j X_j + \sum_{j=1}^{n} \beta_{jj} X_j^2 + \sum_{i<j}^{n} \beta_{ij} X_i X_j + \varepsilon \quad (2.8)$$

where

β_0= intercept,

β_j= linear coefficients,

β_{jj}= quadratic coefficients,

β_{ij}= interaction coefficients,

and X_i, $X_j$are coded independent variables.

In matrix form, the model can be expressed as:

$$y = X\beta + \varepsilon \quad (2.9)$$

The coefficients (β) are estimated using the method of least squares (MLS), which minimizes the sum of squared residuals (errors). Assuming that random errors are independently and identically distributed with zero mean and constant variance, the residual for the *i*th observation is given by:

$$\varepsilon_i = y_i - \hat{y}_i \quad (2.10)$$

and the sum of squared errors (SSE) is:

$$\text{SSE} = \varepsilon^T \varepsilon = (y - X\beta)^T (y - X\beta) \quad (2.11)$$

Differentiating SSE with respect to $\beta$and setting it to zero gives:

$$X^T X\beta = X^T y \quad (2.12)$$

The least squares solution is therefore:

$$\beta = (X^T X)^{-1} X^T y \quad (2.13)$$

where $C = (X^T X)^{-1}$is a square matrix (Penny and Lindfield, 1999).

After estimating the regression coefficients, the predicted responses can be calculated using the model equation. Since the true system behavior is often unknown, model adequacy verification is necessary. Common techniques include residual analysis, scaled residuals, prediction error sum of squares (PRESS) residuals, and lack-of-fit tests.

The coefficient of determination (R^2) is frequently used to express the model's predictive capability. However, a high R^2 alone does not necessarily indicate a good model, as adding more variables always increases R^2, even when those variables are not statistically significant. Therefore, a model with a high R^2 value can still perform poorly when predicting new observations (Myers and Montgomery, 1995).

Plotting the experimental results against the model predictions should ideally yield a 45° straight line through the origin (y = x). However, a line of the form y = a + bx with R^2 = 1.000 may still be meaningless if a ≠ 0 or b ≠ 1.

To address this limitation, absolute average deviation (AAD) analysis is often used to describe the deviations directly. AAD is given by:

$$\text{AAD} = \frac{1}{p}\sum_{i=1}^{p} \left| \frac{y_{i,\text{exp}} - y_{i,\text{cal}}}{y_{i,\text{exp}}} \right| \times 100 \qquad (2.14)$$

where

$y_{i,\text{exp}}$ and $y_{i,\text{cal}}$ are the experimental and calculated responses, respectively, and p is the number of experimental runs.

The combination of high R^2 (close to 1.0) and low AAD indicates a highly accurate model capable of describing the true system behavior within the studied range. However, caution must be exercised when applying the model beyond the range of the experimental data, as it may not remain valid outside this region.

2.3.2.3 Graphical presentation of the model equation and determination of optimal operating conditions

The predicted model can be graphically interpreted using response surface and contour plots. A response surface plot is a three-dimensional representation that illustrates how the response varies with changes in the independent variables. Its two-dimensional projection is known as the contour plot, in which lines corresponding to constant response values are plotted on the plane of the process variables. Contour plots are useful for revealing the overall geometry of the response surface. Elliptical or circular contour patterns generally indicate the presence of a maximum or minimum response at the center of the design space. In some cases, the contours may appear hyperbolic or parabolic, signifying a saddle point where the response is neither maximized nor minimized. Although these plots provide valuable insight into the fitted model and variable interactions, they may not always fully capture the actual behavior of the system. One must not forget that the contours (or

surfaces) represent contours of estimated response and the general nature of the system arises as a result of a fitted model, not the true structure (Myers and Montgomery, 1995). The stationary point (minimum or maximum point) of a second order equation is the point where the first derivative of the function equals to zero:

Let $y = f(x_1, x_2) = \beta_0 + \beta_1 x_1 + \beta_2 x_2 + \beta_{11} x_1^2 + \beta_{22} x_2^2 + \beta_{12} x_1 x_2$ (2.15)

The stationary point is found by computing $\partial y/\partial x_1$ and $\partial y/\partial x_2$ and setting to zero:

$$\frac{\partial y}{\partial x_1} = \beta_1 + 2\beta_{11} x_1 + \beta_{12} x_2 = 0 \quad (2.16)$$

The resulting set of equations is solved to obtain the values of x_1 and x_2. These computed values represent the coded levels of the independent variables at which the response reaches either a maximum or a minimum. For process optimization, it is necessary to locate the stationary point within the experimental domain of the independent variables. However, in certain cases, studies may focus solely on assessing the influence of process parameters rather than performing optimization, or physical constraints may prevent the existence of a stationary point within the investigated range.

2.3.3 Advantages and disadvantages of RSM

Response Surface Methodology (RSM) provides several clear benefits over conventional experimental or optimization approaches that rely on varying one factor at a time. To begin with, RSM generates extensive and meaningful information using a relatively limited number of experiments, whereas traditional methods are labor-intensive, time-consuming, and require many experimental runs to adequately describe system behavior. In addition, RSM enables the evaluation of interaction effects among independent variables on the response. This feature is particularly important in biochemical systems, where interactions such as synergistic, antagonistic, or additive effects can strongly influence outcomes. These interactions are readily interpreted through the developed model equations, especially for

paired variables. Furthermore, the empirical model linking the response to the process variables provides valuable insight into the overall behavior and optimization potential of the system. Based on these considerations, RSM can be regarded as an effective approach for optimizing chemical and biochemical processes. However, a key limitation of RSM lies in its reliance on second-order polynomial models to describe system behavior. Not all systems that exhibit curvature can be adequately represented by such models. For instance, simple enzyme kinetics are more accurately described by the Michaelis–Menten equation rather than a quadratic polynomial. In fact, Michaelis – Menten equation defines a curve which is a rectangular hyperbola through the origin, with asymptotes S = - K_m and v = V (Cornish-Bowden, 1999). Furthermore, temperature effects in biochemical processes are often characterized by symmetric or asymmetric bell-shaped profiles. Such behavior cannot be adequately captured using a second-order polynomial, particularly in cases where the response curve is asymmetric. To address this limitation, experimental data may be transformed into alternative forms that are more suitably represented by a quadratic model. Common approaches include logarithmic transformations and other linearization techniques. An example of a logarithmic transformation applied to the response and independent variable is presented in the following equation:

$$\ln y = \beta_0 + \beta_1 x_1 + \beta_2 x_2 + \beta_{12} x_1 x_2 \quad (2.17)$$

$$y = \beta_0 + \beta_1 (ln x_1) + \beta_2 (ln x_2) \quad (2.18)$$

Although such transformations can be helpful, they do not necessarily produce satisfactory results for every system. Moreover, transforming either the response or the input variables can be time-intensive, and selecting the most appropriate transformation is often challenging. As an alternative, when a system cannot be adequately described by a second-order model, reducing the range of the independent variables may be more suitable. Operating within a narrower parameter range can improve the accuracy of the fitted model; however, this approach also limits the ability to identify the true stationary point of the response surface. Preliminary work becomes more critical for the determination of the independent parameter range (Bas and Boyacı, 2007).

CHAPTER THREE

3.0 MATERIALS AND METHODS

3.1 MATERIALS

All reagents used in this research work are of analytical grade. They were used without further purification.

3.1.1 Reagents

Acetic acid (CH_3COOH)

Ammonium acetate ($NH_4CH_3CO_2$)

Benzyl Chloride ($C_6H_5CH_2Cl$)

Ethanol (CH_3CH_2OH)

Ferric Chloride ($FeCl_3$)

Hydrochloric acid (H_2SO_4)

Phenolphthalein

Potassium permanganate ($KMnO_4$)

Sodium acetate trihydrate ($NaCH_3CO_2.3H_2O$)

Sodium carbonate (Na_2CO_3)

Sodium hydrogen carbonate ($NaHCO_3$)

Sodium hydroxide ($NaOH$)

Sulphuric acid (H_2SO_4)

Toluene ($C_6H_5CH_3$)

Zinc chloride ($ZnCl_2$)

3.1.2 Apparatus/ Equipment

Digital weighing balance (Ohaus Adventurer AR-2130)

FTIR (BRUKER)

Magnetic stirrer(STILOGES MLX H280 PRO)

Muffle furnace (Carbolite AAF-1100)

Oven (DHG-9023A)

pH Meter (Jenway 3020)

Surface Analyser (Quantachrome, NOVA 4200e)

Surface morphology (PHENOM PROX)

3.2 METHODS

3.2.1 Collection of Materials / Sampling of Materials

Coconut shelsl were obtained from a coconut seller at Oba market, Oredo L.G.A, Benin City, Edo state. The coconut shells were washed with water and air-dried for 7 days. The dried coconut shells were crushed, milled to particle size of 2mm and kept for further processing.

3.2.2 Preparation of Biochar

The biochar was prepared according to the method described by Yeboah *et al.* (2020). Coconut shells were carbonized at different temperatures (350, 400, 450,500,600 and 700^{O} C) for 3 hr respectively under limited oxygen atmosphere in a Muffle furnace. The obtained biochars were allowed to cool in the furnace and further reduced to a particle size of 150µm, stored in an air-tight container and labelled as CSB350, CSB400, CSB450, CSB500, CSB600 and CSB700, respectively.

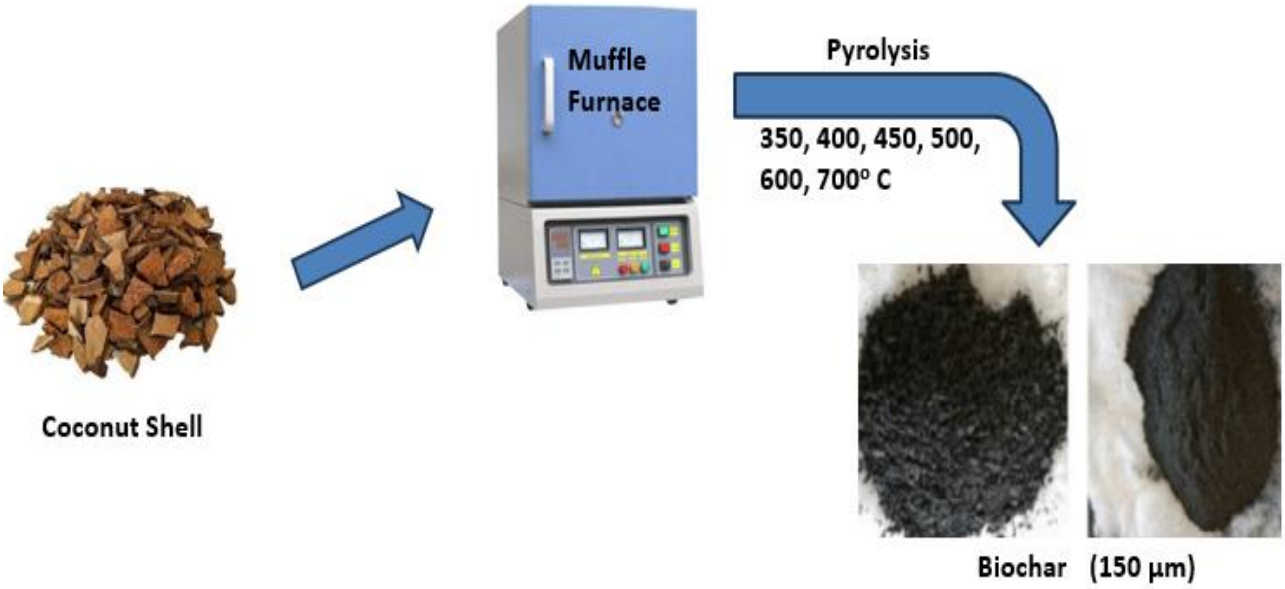

Fig 3.1a: Flow Chart of the Preparation of biochar

3.2.3 Preparation of Metal-Doped Biochar

The preparation of metal-doped biochar followed the method described by Tomin and Yazdani (2022). A known amount of the biochar with optimal BET surface area was slurred in an aqueous solution of known concentration of the metal ions ($FeCl_3$, $ZnCl_2$ and $FeCl_3$ + $ZnCl_2$) and stirred for 6hr at room temperature. The slurry was oven-dried at 80 °C for 6 hours before being transferred to a muffle furnace and subjected to a co-pyrolysis process at the desired temperature and time. The obtained metal-doped biochar was allowed to cool in the muffle furnace and then washed repeatedly with distilled water until a neutral pH was achieved. It was subsequently dried in an oven at 80 °C for 6 hours and thereafter transferred to an airtight container, labelled according to the metal ion used, and preserved for further analysis.

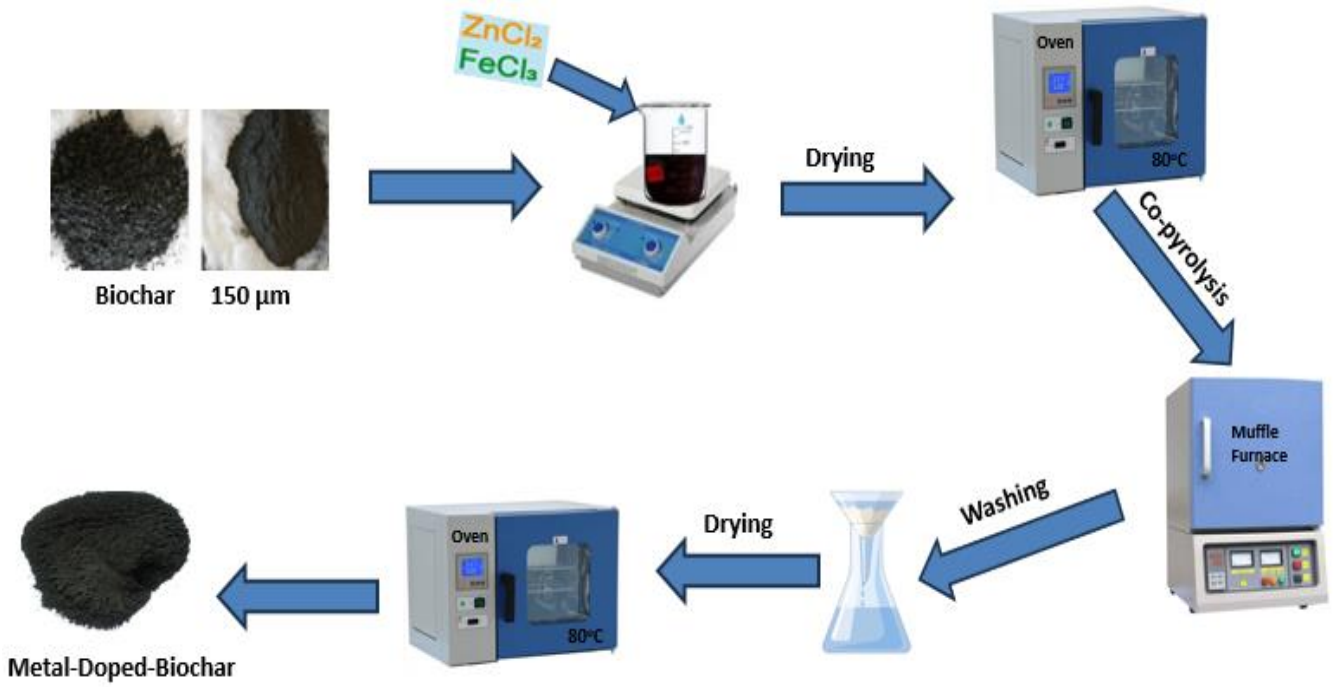

Fig. 3.1b: Flowchart for the Preparation of Metal - Doped Biochar

3.2.4 Characterization of Biochar and the Metal - Doped Biochar

The biochar and the metal-doped biochar were characterized using several analytical instruments including; Brunaeur-Emmett-Teller (BET), Scanning Electron Microscope, Energy Dispersive X-ray (EDX), Fourier Transform Infrared Spectroscopy (FTIR).

3.2.4.1 pH Determination

The pH was measured in deionized water using 1:5 ratio of biochar : deionized water. Samples were thoroughly mixed and allowed to stand for 1hr (Singh *et al*., 2017). The pH was measured with a precalibrated digital pH meter (Jenway 3020, DUNMOW ESSEX, JENWAY LTD., England).

3.2.4.2 Electrical Conductivity

A slurry of the biochar and deionized water in a 1:10 w/v ratio was agitated for 1 hr. Afterward, the samples were allowed to stand for 30 minutes, and the EC of the suspension was measured using a precalibrated conductivity meter (DDS-307, SearchTech Instrument, No. X619070942) (Singh *et al*., 2017).

3.2.4.3 Bulk Density

10 ml tubes were filled with dry biochar and capped. The tubes were tamped to a constant (minimum) volume by the tapping on a table, and weighed. The bulk density of the biochars were calculated thus (Ahmedna *et al*., 1997):

$$\text{Bulk density (g.cm}^{-3}) = \frac{\text{Weight of dry sample (g)}}{\text{Volume of packed dry material } (cm^3)} \quad (3.1)$$

3.2.4.4 Cation Exchange Capacity (CEC):

Samples (0.2g each) were leached five times with 20 mL deionized water to reduce interference from soluble salts. The samples were then leached five times with 20 mL of 1M sodium acetate (pH 7), to remove or extract exchangeable cations. The samples were later washed with 20ml of ethanol five times to remove the excess sodium ion (Na^+). The Na^+ on the exchangeable sites of the material was then displaced five times using 100ml of 1M Ammonium acetate (pH 7). The CEC was calculated from the Na^+ displaced by NH_4^+, measured using a flame photometer (Othugile *et al*., 2022).

3.2.4.5 Surface Morphology and Elemental Composition

The Scanning Electron Microscope (SEM, Hitachi SU 3500 scanning microscope, Tokyo) and an Energy Dispersive X-ray Spectrometer (EDX) were used in combination to analyze the surface morphology and surface elemental composition of the biochar samples and determine their elemental composition (Li *et al.,* 2021).

3.2.4.6 Determination of Surface Area

The surface area of the samples was analyzed using the nitrogen adsorption-desorption method based on the Brunauer–Emmett–Teller (BET) theory. Approximately 0.3 g of each sample was placed in a BET glass tube and weighed before and after loading. The samples were degassed at 473 K for 3 hours using a Micromeritics FlowPrep 060 system under a flow of nitrogen gas to remove physically adsorbed moisture and gases (Aimikhe *et al*., 2022). After degassing, the samples were reweighed and the analysis was carried out in micromeritics Tristar 3000 V4.02 under liquid nitrogen temperature where BET surface area and pore volume/size of the samples were automatically calculated by the instrument using Nitrogen adsorption-desorption isotherms and the results were recorded on the computer attached to the instrument (Aimikhe *et al*., 2022; Shoaib *et al*., 2022).

3.2.4.7 Fourier Transform Infrared Spectroscopy

A BRUKER FTIR (USA) Spectrometer was used to identify the functional groups attached to the catalyst, by detecting the bonding of the elements. It was carried out by using KBr pellet technique at wavelength range of 4000–650cm^{-1}, where a small amount of the sample

was mixed with KBr powder, pressed into a pellet using a hydraulic press, and placed in the FTIR sample holder for analysis (Chi *et al*., 2019).

3.2.4.8 Surface Acid Functional Groups

About 0.50 g of coconut shell biochar (CSB) and metal-doped biochar (MBC) were each mixed with 50 mL of 0.05M each of the three different basic solutions: sodium bicarbonate ($NaHCO_3$), sodium carbonate (Na_2CO_3), and sodium hydroxide (NaOH). A control solution without biochar was also prepared. All the mixtures were shaken for 24 hours and then filtered to remove solid particles. After filtration, 1 mL of each solution was mixed with 10 mL of excess acid (0.05M HCl) to neutralize the base completely. The remaining acid was then measured by titrating with 0.05 M NaOH using phenolphthalein as an indicator and the total surface acidity was calculated as moles neutralized by NaOH, the carboxylic acid fraction as the moles neutralized by $NaHCO_3$, and the lactonic group fraction as those neutralized by Na_2CO_3, while difference between the moles of NaOH and Na_2CO_3 was assumed to represent the phenolic functional group content.

The equation used to determine the quantity of surface acidic groups on biochar are expressed in Eqs. 3.2 and 3.3:

$$n_{CSF} = \frac{n_{HCl}}{n_B}[B]V_B - ([HCl V_{HCl} - [NaOH]\, V_{NaOH})\frac{V_B}{V_a} \quad (3.2)$$

$$n_{CSF} = \frac{n_{CSF}}{m_c} \quad (3.3)$$

where [B] and V_B are the concentration and volume of the reaction base mixed with the carbon, providing the number of moles of reaction base that was available to the carbon

surface for reaction with the surface functionalities. V_a is the volume of the aliquot taken from the V_B, and [HCl] and V_{HCl} are the concentration and volume of the acid added to the aliquot taken from the original sample. This gives the number of moles of acid added to the aliquot, and available for reaction with the remaining reaction base. The remaining moles of acid are then determined through the titration using [NaOH] and V_{NaOH}, the concentration and volume of the titrant in the back-titration. Thus, through the knowledge of the remaining moles of acid, leading to the amount of reaction base remaining after reaction, and by difference (knowing the total amount of reaction base available initially) the amount of base reacted with the surface functionalities, the surface functionalities can be quantified. The n_{CSF} denotes the moles of carbon surface functionalities on the surface of the biochar that reacted with the base during the mixing step. The carbon surface functionalities calculated is denoted as n_{CSF}, in moles. η_{CSF}, in mol g^{-1}, represents the CSF per unit mass, which is n_{CSF} divided by the weight of carbon used in the preparation of each sample (Mukherjee *et al.,* 2011: Ren *et al.,* 2019).

3.3 Ultimate analysis

The percentages of C, H, S, and N contents of the biochars were determined with an elemental analyzer (Elemental Vario EL III, Germany), and the O content was calculated by subtracting C, H, N, S, and ash contents from the total (Gazulla *et al*., 2016).

3.4 Chemical oxidation stability

The $KMnO_4$ method (Tirol-Padre and Ladha, 2004), was used to assess the easily oxidizable fraction of the studied biochars. Biochar samples were acid pretreated to remove inorganic carbonates following the method described by Fidel *et al.* (2017). Typically, the biochar was added to a solution of $KMnO_4$ (33mM, pH 7.2) in a 1:50 w/v biochar: KMnO4 ratio. It was agitated for 60 min, heated at about 60°C for 60 min and thereafter left overnight at 25°C. The solid residue was separated, thoroughly rinsed with distilled water, and dried at 80°C for 4 days. The mass loss from the oxidation treatment was measured gravimetrically, and the dried sample was subsequently analyzed for its elemental composition (C, H, N, O, and S). An indication of the stability of biochar to oxidative degradation, AE may be obtained from Eq. 3.4:

$$\text{AE (\%)} = \frac{\text{Br x BrC}}{\text{Bt x BrC}} \text{ x } 100 \qquad (3.4)$$

Where, BrC and BtC represent the carbon content in the residual and total biochar, respectively, and Br and Bt are the mass after and before treatment (Cross and Sohi, 2013).

3.5 Estimation of Higher Heating Value (HHV) of coconut shell biochar

There are many empirical formulae in the literature for estimating the fuel value (higher heating value) of biomass fuel from basic analysis data such as ultimate analysis (elemental composition wt % C, H, O, N and S). These formulae were statistically evaluated based on a large number of data of biomass from the literature. Some of the more frequently used and generally accepted formulae for estimating higher heating value that have been shown

to have high accuracy (with up to 90% prediction in the range of ± 12%, (Sheng and Azevedo, 2005) are given as equations (3.5 – 3.9):

HHV ($KJ.kg^{-1}$) = 357.8C + 1135.6H + 54.9N + 119.5S – 85.4Oxygen – 974 Cordero *et al*. (2001) ---------- (3.5)

HHV ($MJ.kg^{-1}$)= 0.3403C + 1.2432H + 0.0628N + 0.1909S – 0.0984O Channiwala and Parikh (2002) -------- (3.6)

HHV ($MJ.kg^{-1}$) = 0.3259C + 3.4597 Sheng and Azevedo (2005) ---------- (3.7)

HHV ($KJ.kg^{-1}$) = $3.55C^2$ – 232C – 2230H + 51.2C * H + 131N + 20600 Friedl *et al*. (2005) ---------- (3.8)

HHV ($MJ.kg^{-1}$) = 0.4373C – 1.6701 Tilman *et al*. (1978) ----------(3.9)

3.5 Statistical Approach for the Production of Metal - Doped Biochar

A statistical approach, response surface methodology (RSM) (Design Expert 11, Stat-ease, Inc., Minneapolis, USA) was adopted to optimize the second stage co-pyrolysis step for the preparation of metal - doped biochar samples. A three-factor, five-level Central Composite Design (CCD) under response surface methodology was employed to optimize the process variables for the production of metal-doped biochar with enhanced textural properties (surface area). For each dopant system, a total of 19 experimental runs were conducted, comprising 8 factorial points, 6 axial points (two for each variable), and 5 replicated central points, as generated using Design-Expert software (Version 11.1.2.0, Stat-Ease, Minneapolis, USA). The selected process variables and their corresponding ranges are presented in Table 3.1. The response obtained from each experimental run was

subsequently subjected to statistical analysis using the software to identify the optimum operating conditions.

Table 3.1: Range and Levels of Independent Variables for Preparation of Metal - doped Biochar Samples.

Metal System	Independent Variables	Coding	-1	0	+1
Fe^{3+} (single)	Fe^{3+} loading (wt %)	A	0.558	3.071	5.584
	Temperature (°C)	B	250	375	500
	Time (hr)	C	1	2.5	4
Zn^{2+} (single)	Zn^{2+} loading (wt %)	A	0.654	3.597	6.54
	Temperature (°C)	B	250	375	500
	Time (hr)	C	1	2.5	4
Fe^{3+}/Zn^{2+} (bimetallic)	(Fe^{3+} wt% of 10% wt of CSB)	A	5	50	95
	Temperature (°C)	B	250	375	500
	Time (hr)	C	1	2.5	4

CSB – Coconut Shell Biochar

To predict the optimal conditions and the existence of interaction, experimental data was fitted to a second and polynomial regression model as given by Equation (3.10) containing three linear, three interaction and three quadratic terms.

$$Y = \beta o + \sum \beta i Xi + \sum \beta ii\, X^2 + \sum \beta ij Xi Xj \quad (3.10)$$

where βo is the constant coefficient, βi is the slope or linear effect of the input factor Xi, βij is the linear by linear interaction effect between the input factor Xi and, βii is the quadratic effect of input factor Xi. The effects of process variables and their possible interaction effects on the response in the response surface regression procedure was estimated using analysis of variance (ANOVA) in which the level of significance (p-value) of all coefficients was < 0.05. Regression coefficient, R^2 was used to evaluate the goodness

and best fit of the model and the response surface and contour plots were obtained using the fitted quadratic polynomial equation generated from regression analysis by keeping one of the independent variables at central value (0) and varying the other two (Mourabet *et al*., 2014; Kalu *et al.,* 2021).

3.6 CATALYTIC ACTIVITY

The benzylation of toluene by benzyl chloride was used as model reaction to evaluate the catalytic activity of metal-doped coconut shell biochar in Friedel Crafts alkylation process. The reaction was carried out in a magnetic stirred batch reactor, fitted with a reflux condenser, having a low dead volume mercury thermometer and an arrangement for the continuous bubbling of moisture free nitrogen (N_2) gas maintained at a constant flow rate through the liquid reaction mixture. The reaction was started by introducing benzyl chloride into the reactor containing toluene and the metal-doped biochar catalyst, without the addition of solvent. The hydrogen chloride (HCl) gas evolved was carried by the N_2 gas into standard sodium hydroxide (NaOH) solution, and aliquots of the solution were titrated back-titrated with standard HCl solution to determine the extent of reaction.

The benzylation reaction was studied under various reaction conditions of stoichiometric toluene : benzyl chloride (T:BC) ratios of 5:1, 10:1, and 15:1; catalyst amounts (metal-doped biochar) of 4.1, 8.2, and 16.4 wt% relative to BC; and reaction temperatures of 50, 60, and 70 °C, all conducted for 180 minutes.

The benzyl chloride (BC) conversion was calculated using Eq. 3.11 (Fogler, 2006):

$$\text{BC conversion (\%)} = \frac{\text{mole of HCl}}{\text{mole of BC}} \text{ x } 100 \qquad (3.11)$$

Where BC represents benzyl chloride and HCl denotes hydrogen chloride gas.

3.7 Statistical Approach of Friedel Crafts Benzylation of Toluene

A statistical approach, response surface methodology (RSM) (Design Expert 11, Stat-ease, Inc., Minneapolis, USA) was adopted to optimize the Friedel Crafts benzylation of toluene in the present of the three catalysts (Fe^{3+} - doped, Zn^{2+} - doped and Fe^{3+}/Zn^{2+} - doped biochars). Central composite design (CCD) of response surface methodology, was employed for the optimization of process variables for maximum benzyl chloride conversion in the present of the metal - doped biochars catalysts. A total of 20 experimental trials for each catalyst were generated that included 8 trials for factorial design, 6 trials for axial points (two for each variable) and 6 trials for replication of the central points were performed using the experimental designed by the Design Expert Software (Version 11.1.2.0, Stat-ease, Mineapolis, USA). The process variables considered and their corresponding ranges are presented in Table 3.2. All experiments were conducted at a constant catalyst dose of 8.20 wt% benzyl chloride. The responses for each run based on the conversion of benzylchloride were further statistically analyzed by the statistical software to determine the optimum reaction condition.

Table 3.2: Central Composite Design Experimental Conditions for the Friedel Crafts Reaction using Metal - Doped Biochar (Fe^{3+}, Zn^{2+}, Fe^{3+}/Zn^{2+}) at Constant Catalyst Dose of 8.2wt%.

Independent variables	**Coding**	**Level**		
		-1	0	+1
Mole ratio (T:BC)(mol/mol)	A	5.0	10.0	20.0
Reaction Temperature (^oC)	B	55.0	67.5	80.0
Reaction Time (min)	C	30.0	105.0	180.0

T – Toluene
BC – Benzyl Chloride

CHAPTER FOUR

4.0 RESULTS AND DISCUSSION

4.1 PHYSICOCHEMICAL PROPERTIES

This chapter discusses the results obtained from the study or research work. The effect of pyrolysis temperature on the physicochemical properties of the coconut shell biochars are given in Table 4.1. The yield of biochars depend on the pyrolysis temperature. It decreases with increase in pyrolysis temperature. The yield decreased by about 47.17% from 67.70% at 350^{o} C to 35.76% at 700^{o} C. The decrease in biochar yield with increase in pyrolysis temperature could be attributed to the decomposition of the biomass at high temperatures (Mimmo *et al*., 2014) and to secondary decomposition of biochar residue that involved the charring and devolatilization reactions at higher pyrolysis temperature (Claoston *et al*., 2014). The results are consistent with the reports of Chen *et al*. (2014) and Noor *et al*. (2019).

The pH of the coconut shell biochar samples increased by 2.8 pH units within the range of pyrolysis temperatures (350 - 700°C) used in this study. The increase in pH of biochar samples with pyrolysis temperature may be related to the observed high degree of carbonization and accumulation of inorganic salts (carbonates) in the biochar samples (Yuan *et al*., 2011). High pH is generally considered to have ameliorative effect on the soil properties relevant to agronomic benefits. The electrical conductivity (EC) (mS.cm^{-1}) of the biochar samples were observed to increase progressively from 5.12 at 350 °C to 25.60 at 700 °C. This trend is linked to the increased ash content at higher pyrolysis temperatures, where the buildup of inorganic minerals such as K^{+}, Na^{+}, Ca^{2+}, and Mg^{2+} contributed to improved conductivity (Roshan *et al.,* 2023).

Table 4.1: Variation of the Physicochemical Properties of Coconut Shell Biochar with Pyrolysis Temperatures

Properties	Pyrolysis Temperature (°C)					
	350°C	**400°C**	**450°C**	**500°C**	**600°C**	**700°C**
Yield (%)	67.70 ± 0.50	53.30 ± 0.35	46.50 ± 0.10	41.67 ± 0.55	39.44 ± 0.64	35.76 ± 0.42
pH	7.90 ± 0.90	8.25 ± 1.20	9.73 ±1.11	10.01 ± 0.50	10.25 ± 0.36	10.70 ± 0.77
EC(ms.cm^{-1})	5.12 ± 1.50	7.58 ± 1.22	12.18 ± 1.07	15.3 ± 1.00	18.54 ± 0.95	25.60 ± 1.11
Bulk Density (g.cm^{-3})	1.12 ± 0.22	0.97 ± 0.09	0.91 ± 0.18	0.75 ± 0.30	0.70 ± 0.11	0.59 ± 0.15
CEC (cmol.kg^{-1})	11.47 ± 2.43	23.06 ± 2.59	28.03 ± 2.00	19.66 ± 2.26	19.01 ± 1.95	14.11 ± 2. 50

EC – Electrical Conductivity
CEC - Cation Exchange Capacity

Cation exchange capacity (CEC cmol.kg^{-1}) is the amount of exchangeable cation such as Na^+, K^+, NH_4^+, Ca^{2+} and Mg^{2+} that a material is capable of holding. It is a result of negative surface charges attracting cations and it is used as an indicator of soil fertility (Roberston *et al*., 1999). Therefore CEC depends directly on this surface structure with functional groups providing surface charges and surface area, making surface charges accessible (Liang *et al*., 2006). At 450ºC more than 100% increase in CEC was observed. This was followed by about 49.66% decrease in CEC result obtained. At low to moderate pyrolysis temperatures, these functional groups are abundant and readily deprotonate, generating negatively charged sites that enhance the cation exchange capacity. However, as the pyrolysis temperature increases further, these functional groups are progressively degraded or volatilized leading to a reduction in the number of negatively charged sites on the biochar surface (Banik *et al.,* 2018; Tomczyk *et al.*, 2020).

The bulk density (g.cm^{-3}) of the biochar samples (Table 4.1) decreased by about 47% within the pyrolysis temperatures used in this study. The decrease in the values of bulk density (g.cm^{-3}) with pyrolysis temperature from 1.12 at 350° C to 0.59 at 700° C representing a decrease of about 96% is as expected (Weber and Quicker, 2018). During pyrolysis and as gases are devolatilized from the biomass with increase in pyrolysis temperature, the solid mass becomes porous. The higher the porosity, the lighter the mass becomes and the smaller the mass of the char per unit volume (bulk density) (Novotný *et al.,* 2023).

4.2 Surface oxygen functional groups

The results of the quantitative determination of the surface oxygen functional groups on the coconut shell biochar samples are given in Table 4.2.

Table 4.2: Surface Oxygen Functional Groups of Coconut Shell Biochar Prepared at Different Pyrolysis Temperatures

Functional Groups	Biochar Samples					
	CSB350	CSB400	CSB450	CSB500	CSB600	CSB700
Phenolic (mmol.g^{-1})	1.65	1.58	1.27	1.81	1.27	0.50
Lactonic (mmol.g^{-1})	1.51	1.30	0.39	1.15	0.80	0.43
Carboxylic (mmol.g^{-1})	1.78	1.23	1.81	0.65	0.41	1.24
Total (mmol.g^{-1})	4.94	4.11	3.47	3.61	2.48	2.17

CSB – Coconut Shell Biochar

There is no apparent trend in the levels of the various functional groups with the pyrolysis temperature with respect to phenolic, lactonic and carboxylic; however the total surface oxygen functional groups decreased from 4.94 mmol.g^{-1} at CSB350 to 2.17 mmol.g^{-1} at CSB700. a change of about 56%. The decrease in surface oxygen functional groups are considered to be due to volatilization of the surface groups during pyrolytic decomposition of biomass (Yang *et al*., 2004; Ogede *et al*., 2024). Surface oxygen functional groups in biochar are important due to it sorptive capacities and biochar surface modification processes are aimed at enhancing the sorptive properties for environmental benefits.

4.3 FOURIER TRANSFORM INFRA-RED SPECTROSCOPY

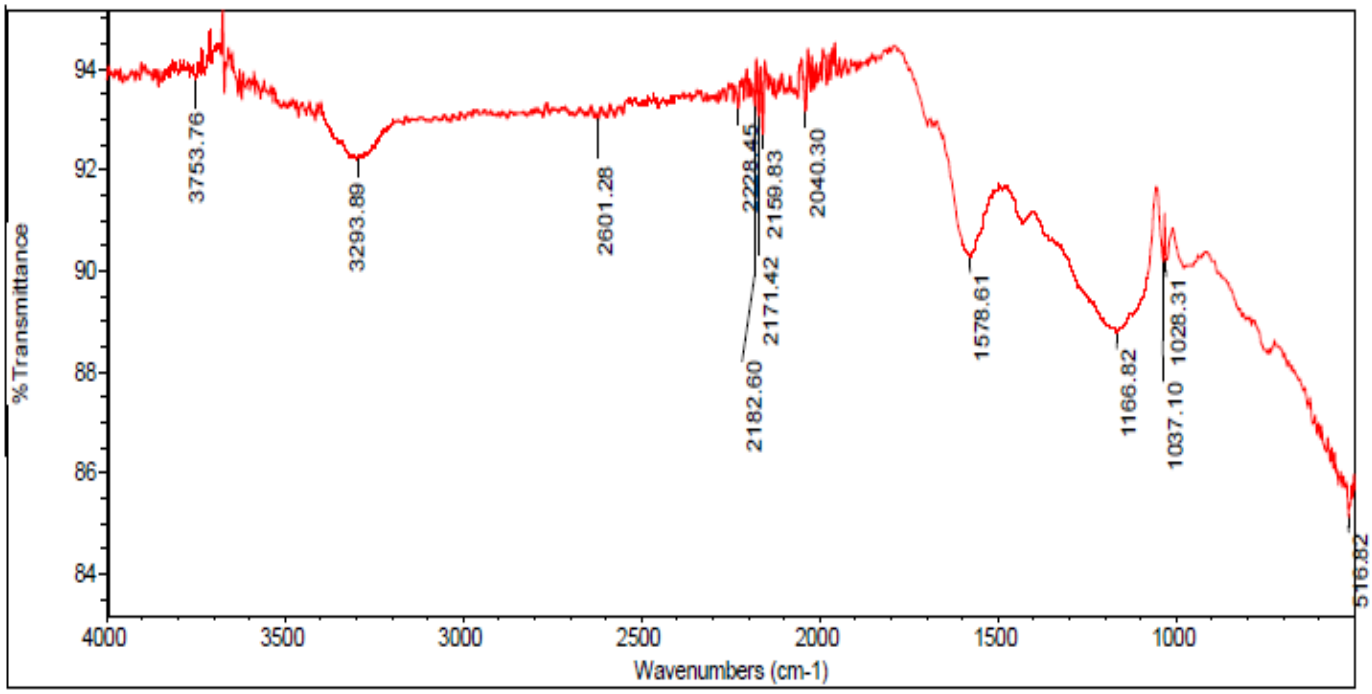

Fig. 4.1: FTIR Results of CSB350

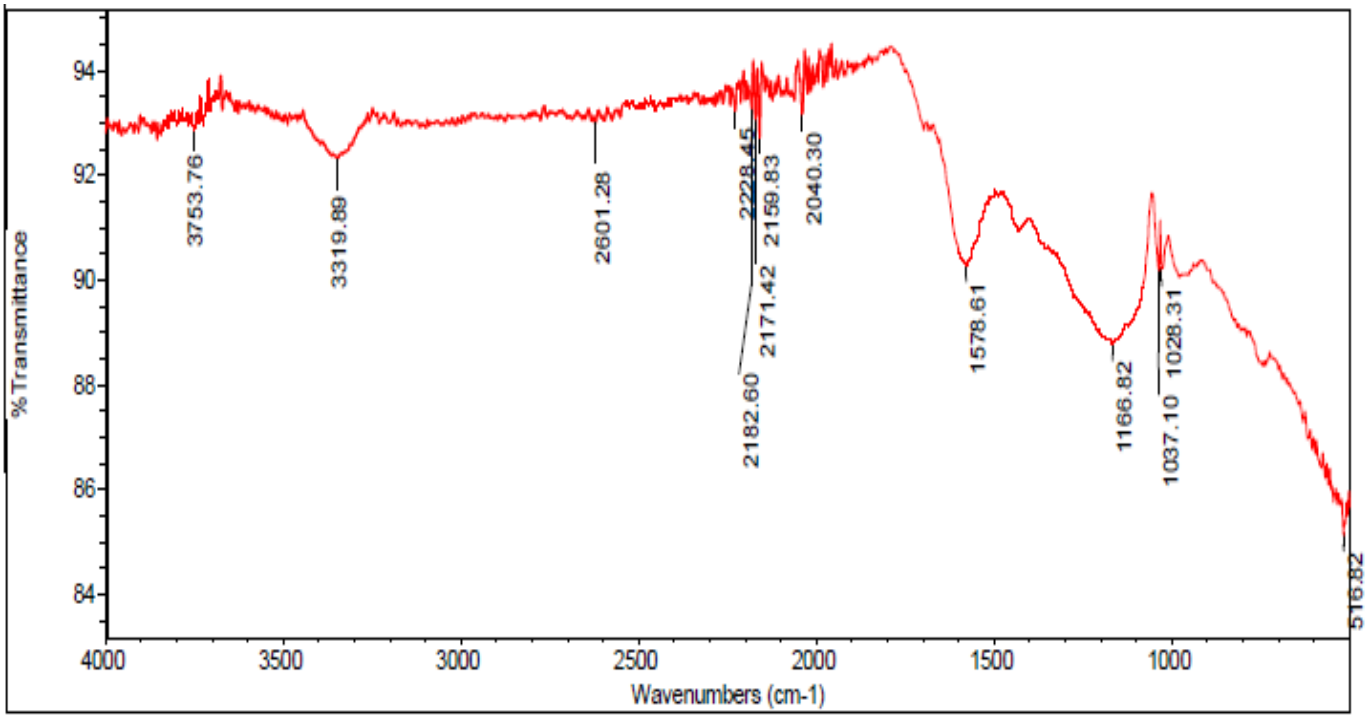

Fig. 4.2: FTIR Results of CSB400

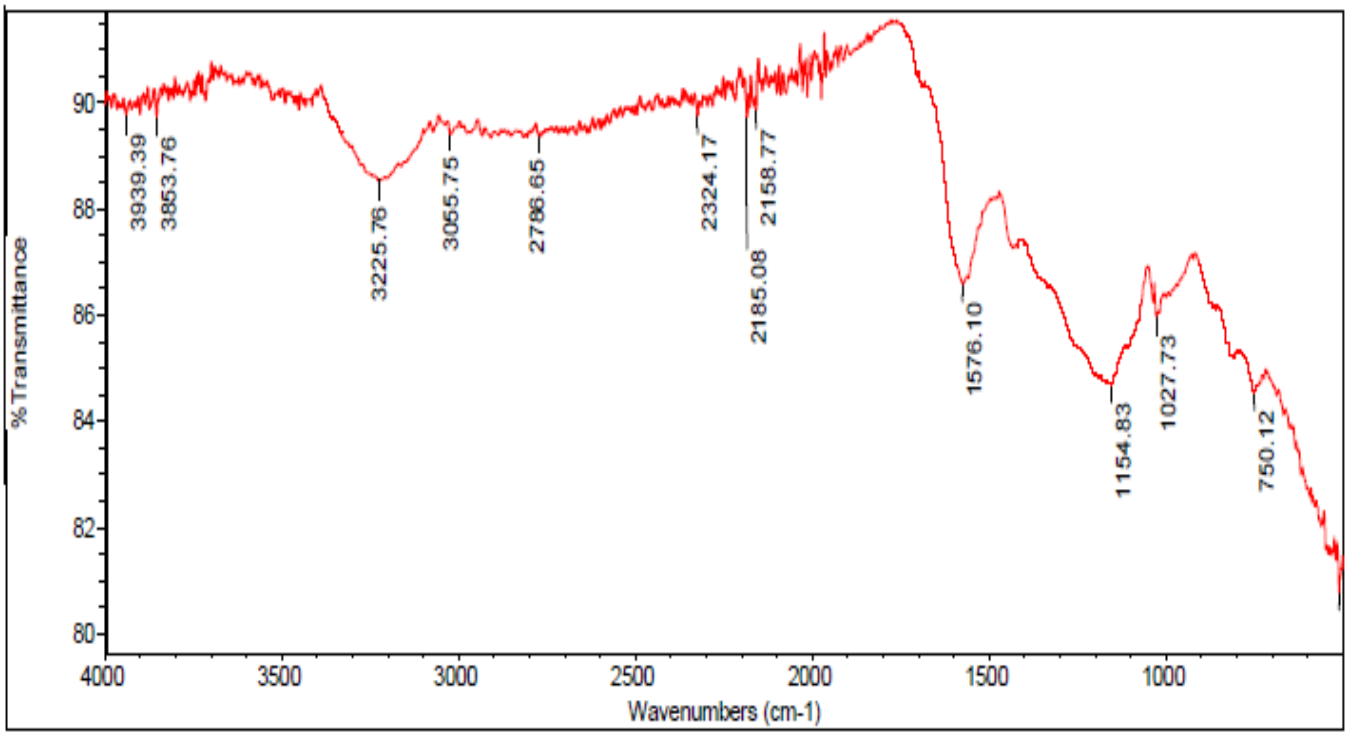

Fig. 4.3: FTIR Results of CSB450

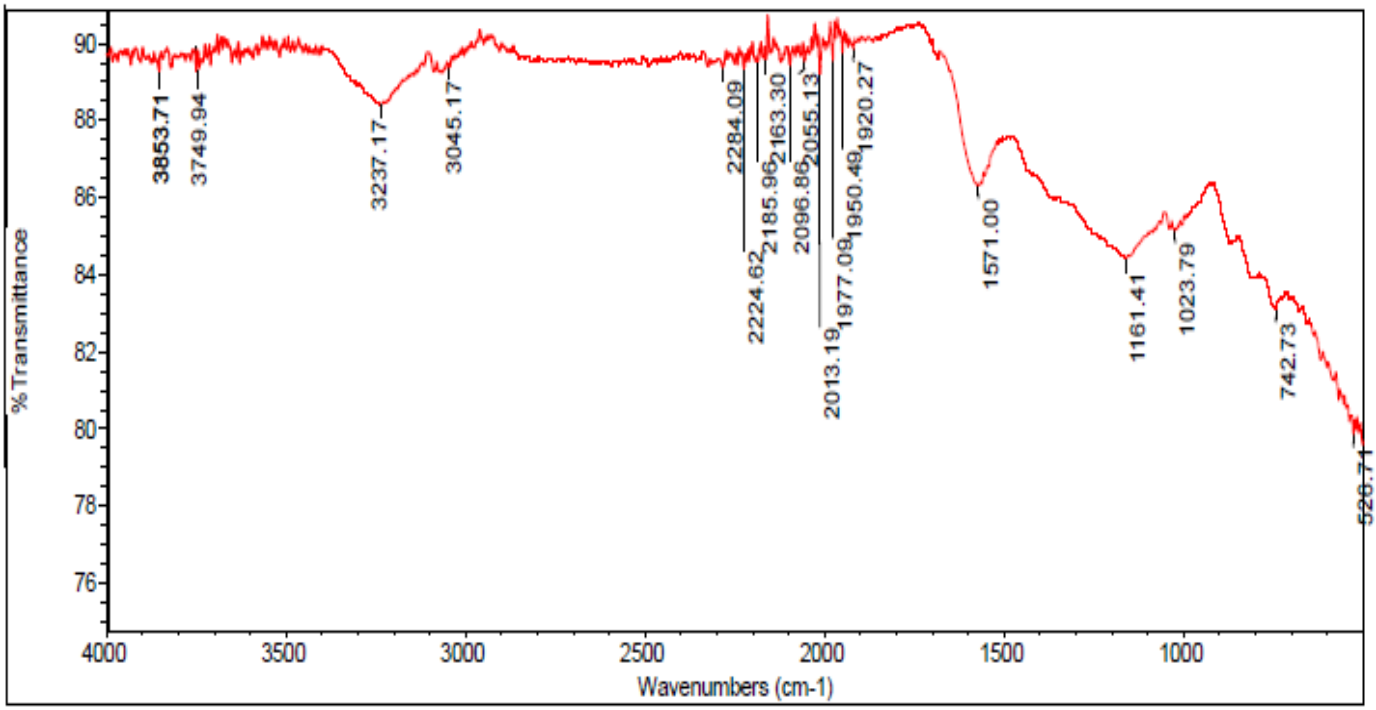

Fig. 4.4: FTIR Results of CSB500

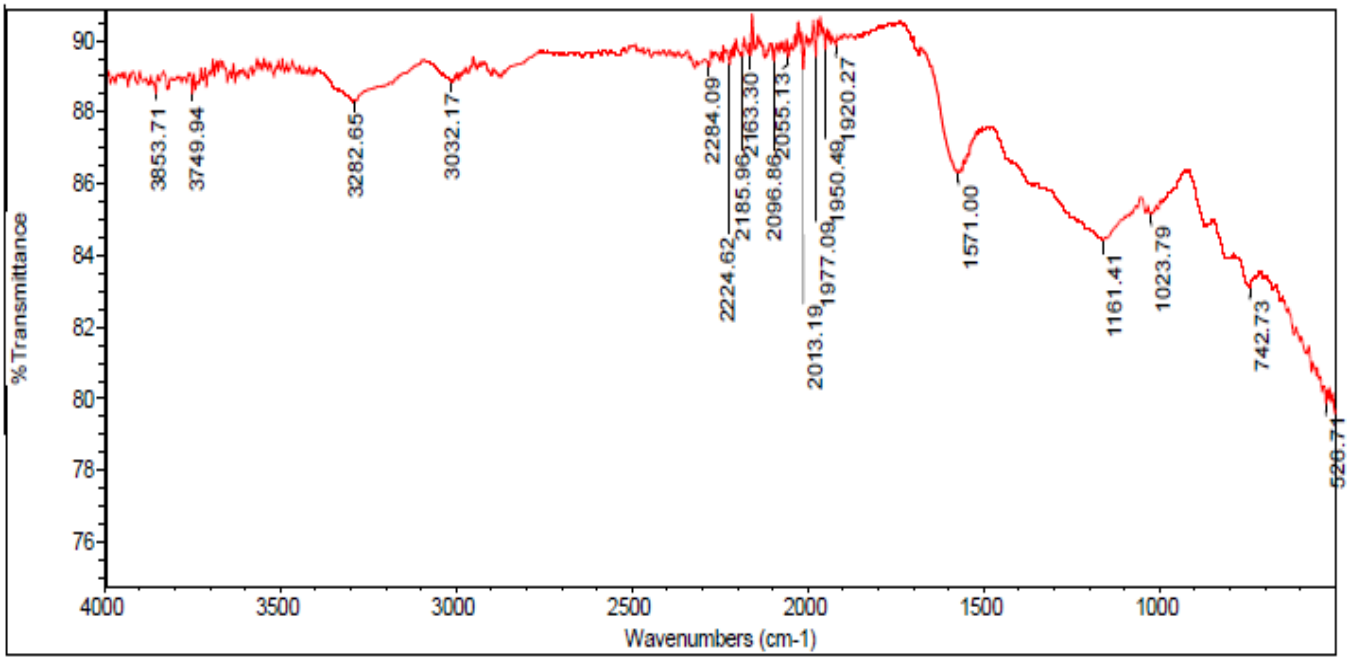

Fig. 4.5: FTIR Results of CSB600

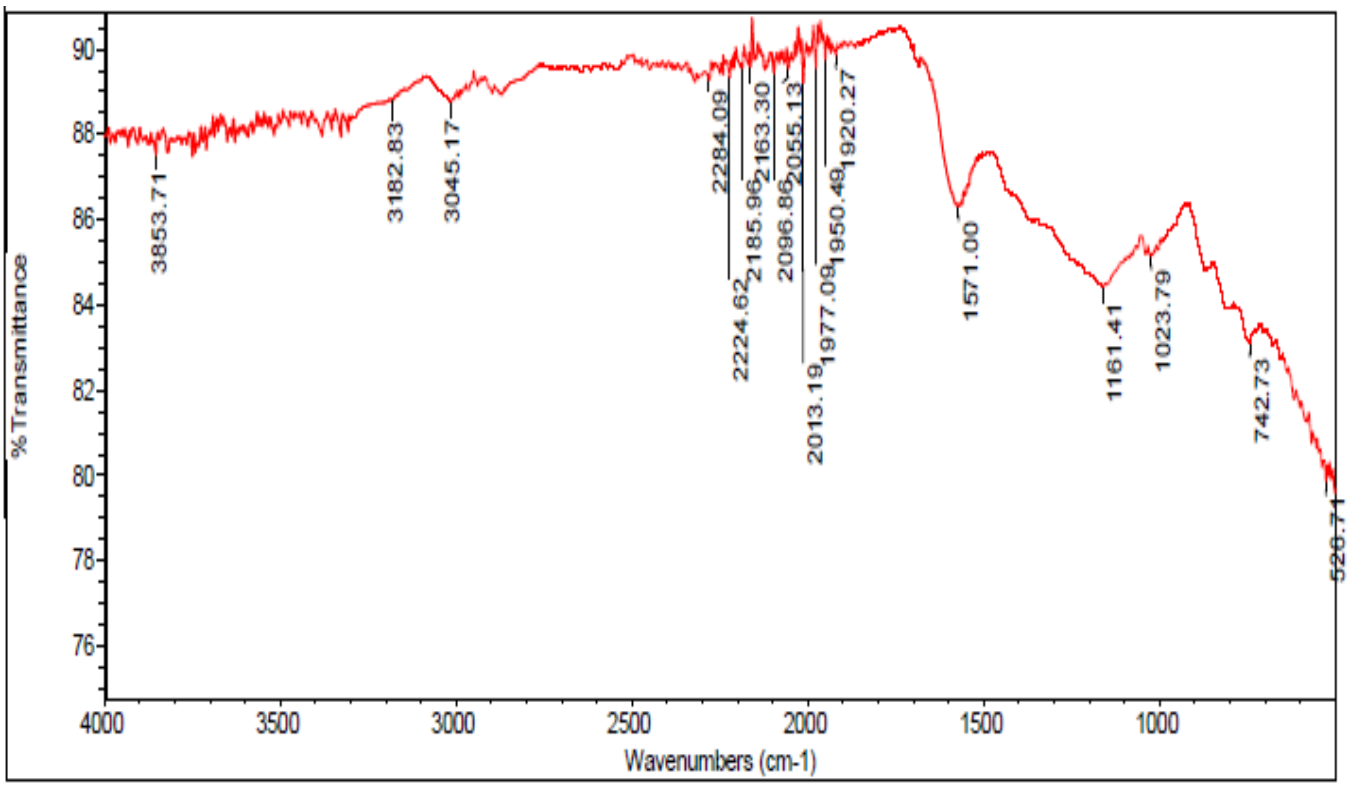

Fig. 4.6: FTIR Results of CSB700

The functional groups present in the biochars samples were evaluated by fourier transform infra-red spectroscopy. As depicted in Fig. 4.1 – 4.6, the absorption bands at 3500 – 3200 cm^{-1} corresponds to O-H vibration relating to phenolic group (Theivandran *et al*., 2015), absorption bands at 3200 – 2500 cm^{-1} also represent the stretching vibration of O-H associated with carboxylic acid in all samples (Theivandran *et al*., 2015). In addition, absorption bands in the range of 2300 – 1900 cm^{-1} and 1710 – 1550 cm^{-1} are assigned to CO_2 molecules and C = C vibrations respectively (Babu *et al.,* 2024; Chintala *et al*., 2017; Mishra *et al*., 2020). The spectral region between 1500 and 1000 cm^{-1} exhibited bands corresponding to C–O and C–H vibrational modes, which are associated with the presence of polysaccharides (Pertile et al., 2025).

4.4 TEXTURAL PROPERTIES OF COCONUT SHELL BIOCHAR

The specific (BET) surface area, porosity and pore volume of the coconut shell biochars prepared at different pyrolysis temperatures are given in Table 4.3.

Table 4.3: Textural Properties (surface area, porosity and pore volume) of Coconut Shell Biochar Prepared at Different Pyrolysis Temperatures.

	Biochar Samples					
Properties	**CSB350**	**CSB400**	**CSB450**	**CSB500**	**CSB600**	**CSB700**
S_{BET} ($m^2.g^{-1}$)	282.00	314.00	712.00	618.30	572.10	320.70
Pore diameter (nm)	2.80	2.13	2.11	3.51	3.94	4.85
Pore volume ($cm^3.g^{-1}$)	0.17	0.17	0.36	0.29	0.18	0.10

CSB – Coconut Shell Biochar
S_{BET} – Specific Surface Area

The specific surface area ($m^2.g^{-1}$) of the coconut shell biochars range from 282.00 for CSB350 through 712.00 for CSB 450 to 320.70 for CSB700 indicating an initial marked

increase of about two and a half folds, followed by a decrease thenceforth to CSB700 with specific surface area of 320.70. This trend is similar to the report of Brown *et al*. (2006) for biochar produced by the slow pyrolysis of wood. The reports of the effect of pyrolysis temperature on the evolution of porous structures on biochar derived from different biomass suggest that increase in specific surface area of biochar occurred by the release of volatiles from the biomass components and from the crack resulting from the fusion of benzene rings and possible graphic microcrystals in the biochar (Yang and Sheng, 2012; Yang *et al*., 2016). Increase in pyrolysis temperature resulted in increase of about 1.7 folds, (72%), in the pore size (nm) of the biochar samples, and the values suggested that the biochar samples were largely mesoporous. The pore volume ($cm^3.g^{-1}$) of the biochar samples followed an opposite trend and decreased in an order of 1.74 folds, and about (41%), with the range of pyrolysis temperature used in this study. The porous structures of biochar are important in many applications; sorptive capacity (i) relevant for the removal of pollutants from wastewaters (ii) mitigating the dispersion of pollutant molecules in soil, and (iii)in industrial applications related to catalytic activity, etc.

4.5 Surface Morphology / Elemental Composition of Coconut Shell Biochars

The scanning electron micrographs and surface elemental composition determined by energy dispersive x-ray (SEM/EDX) of the coconut shell biochar samples obtained at different pyrolysis temperatures are given in Figs. 4.7 – 4.12.

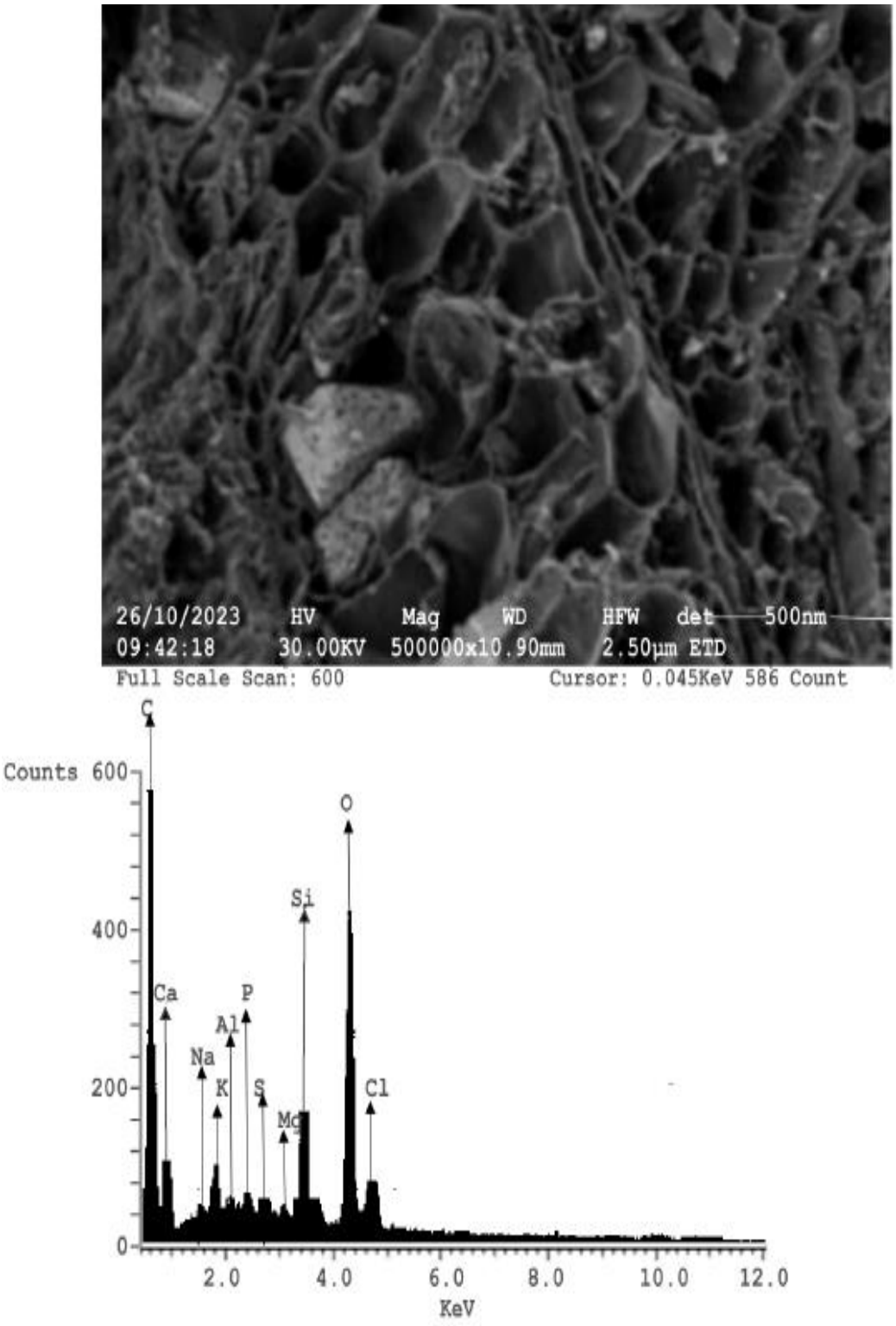

Elements	Composition (%)
C	60.50
O	29.72
Ca	1.15
Si	3.01
Al	0.20
K	1.76
Na	0.78
Mg	0.56
P	1.04
Cl	1.16
S	0.11

Fig. 4.7: SEM/EDX of CSB350

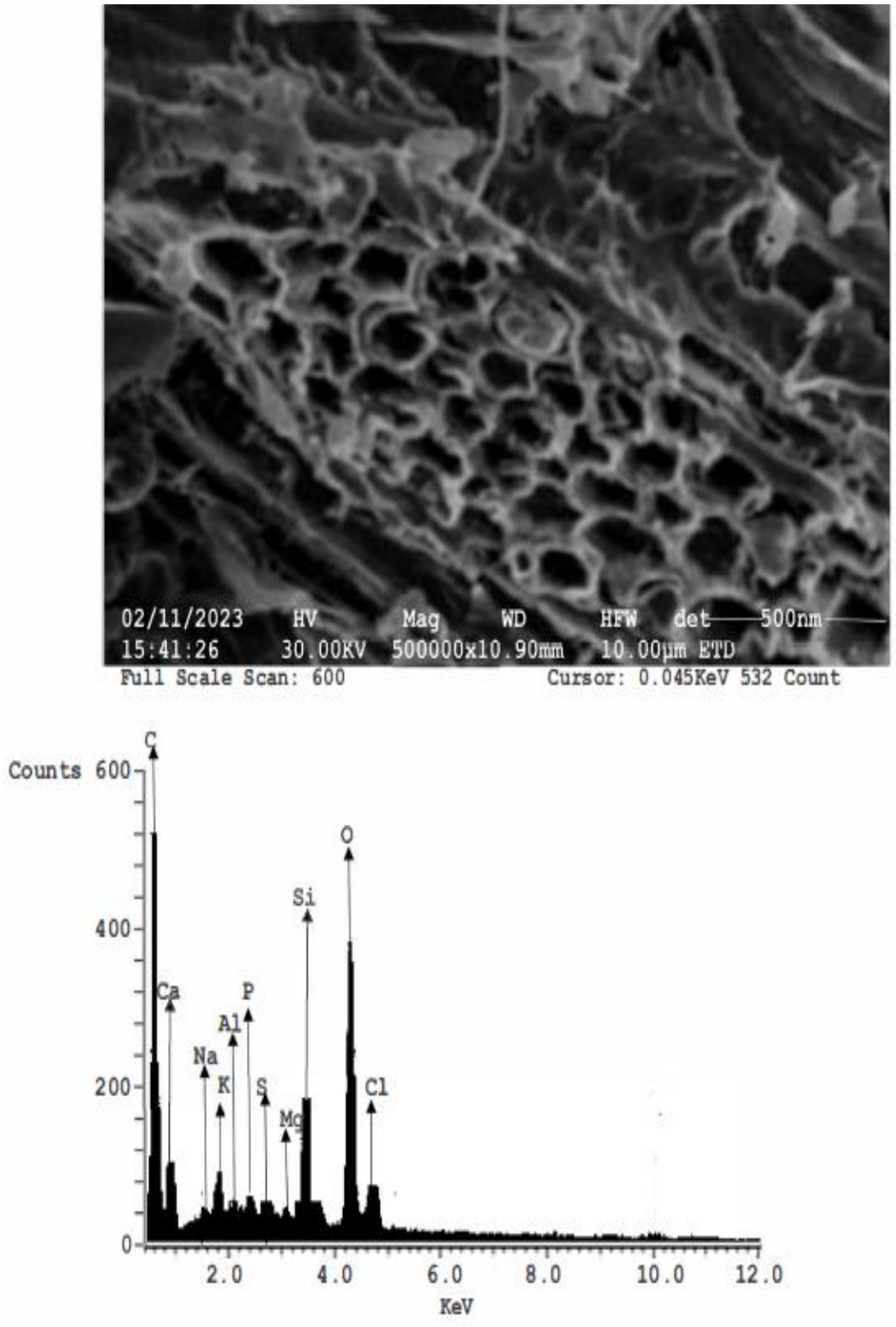

Elements	Composition (%)
C	63.11
O	24.07
Ca	1.87
Si	3.51
Al	0.49
K	2.06
Na	1.12
Mg	0.87
P	1.24
Cl	1.49
S	0.15

Fig. 4.8: SEM/EDX of CSB400

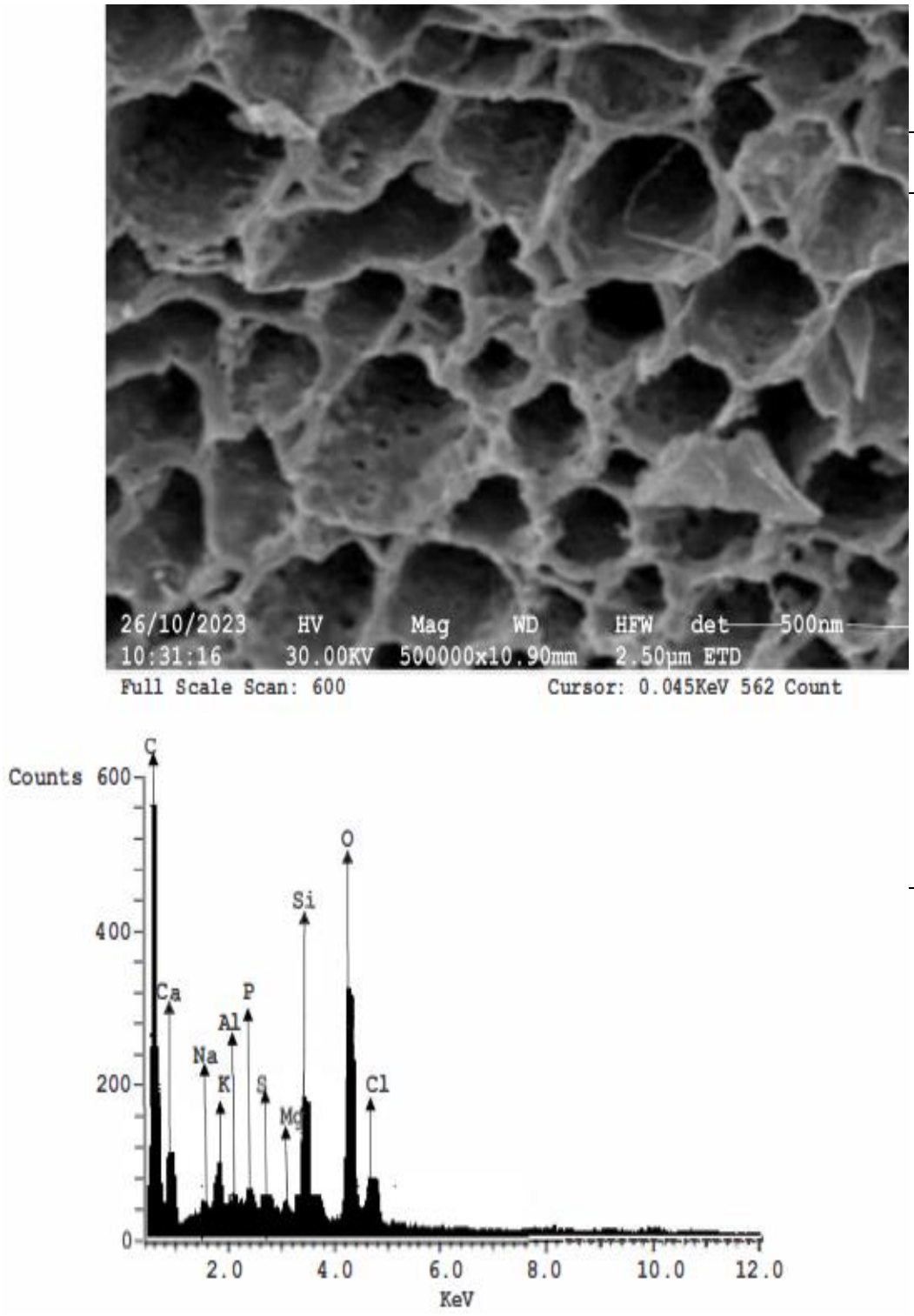

Elements	Composition (%)
C	66.03
O	18.40
Ca	2.02
Si	3.92
Al	0.91
K	2.11
Na	1.55
Mg	1.50
P	1.34
Cl	2.09
S	0.12

Fig. 4.9: SEM/EDX of CSB450

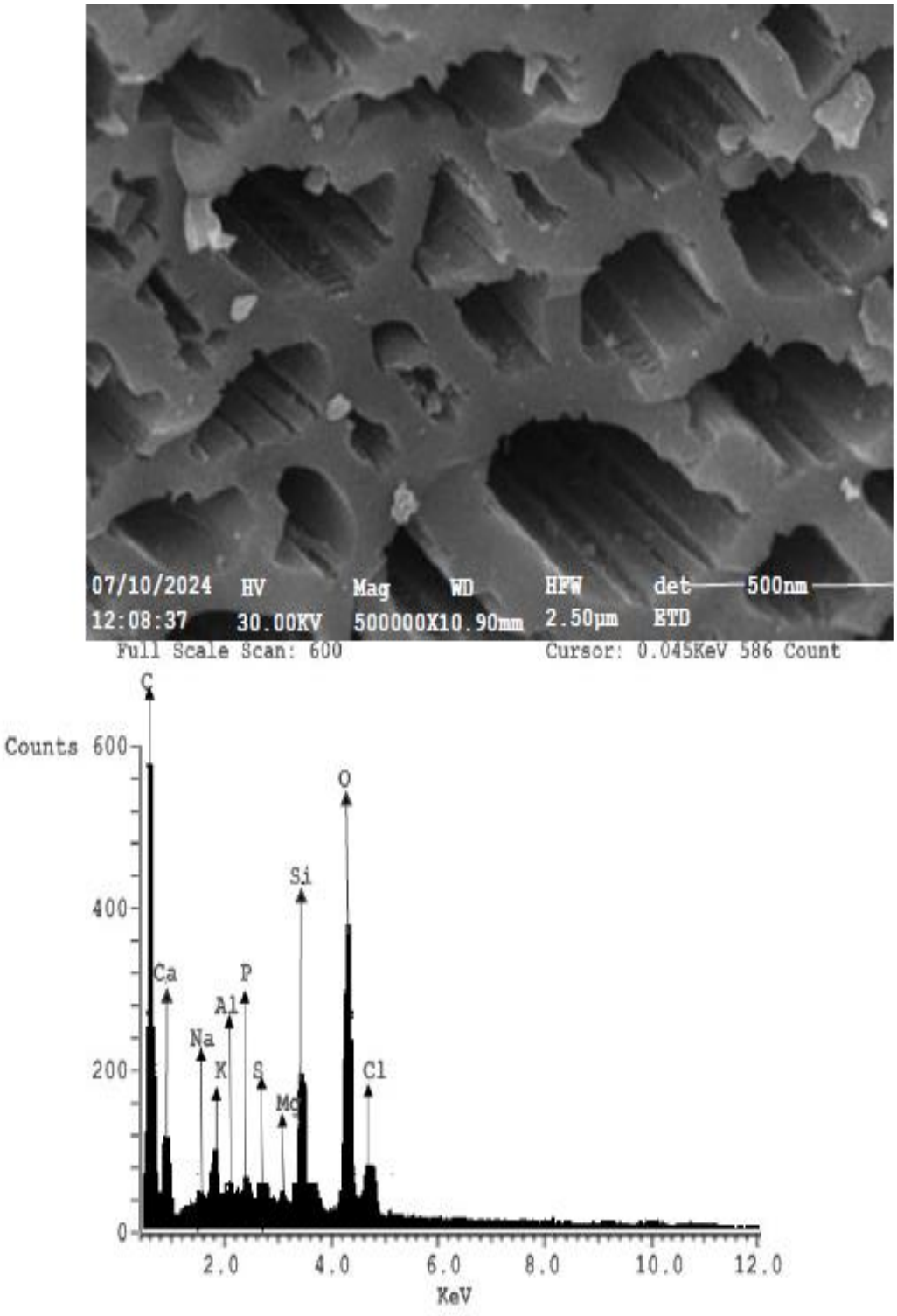

Elements	Composition (%)
C	65.15
O	17.13
Ca	1.47
Si	6.17
Al	1.11
K	2.31
Na	1.73
Mg	1.11
P	1.59
Cl	2.11
S	0.10

Fig. 4.10: SEM/EDX of CSB500

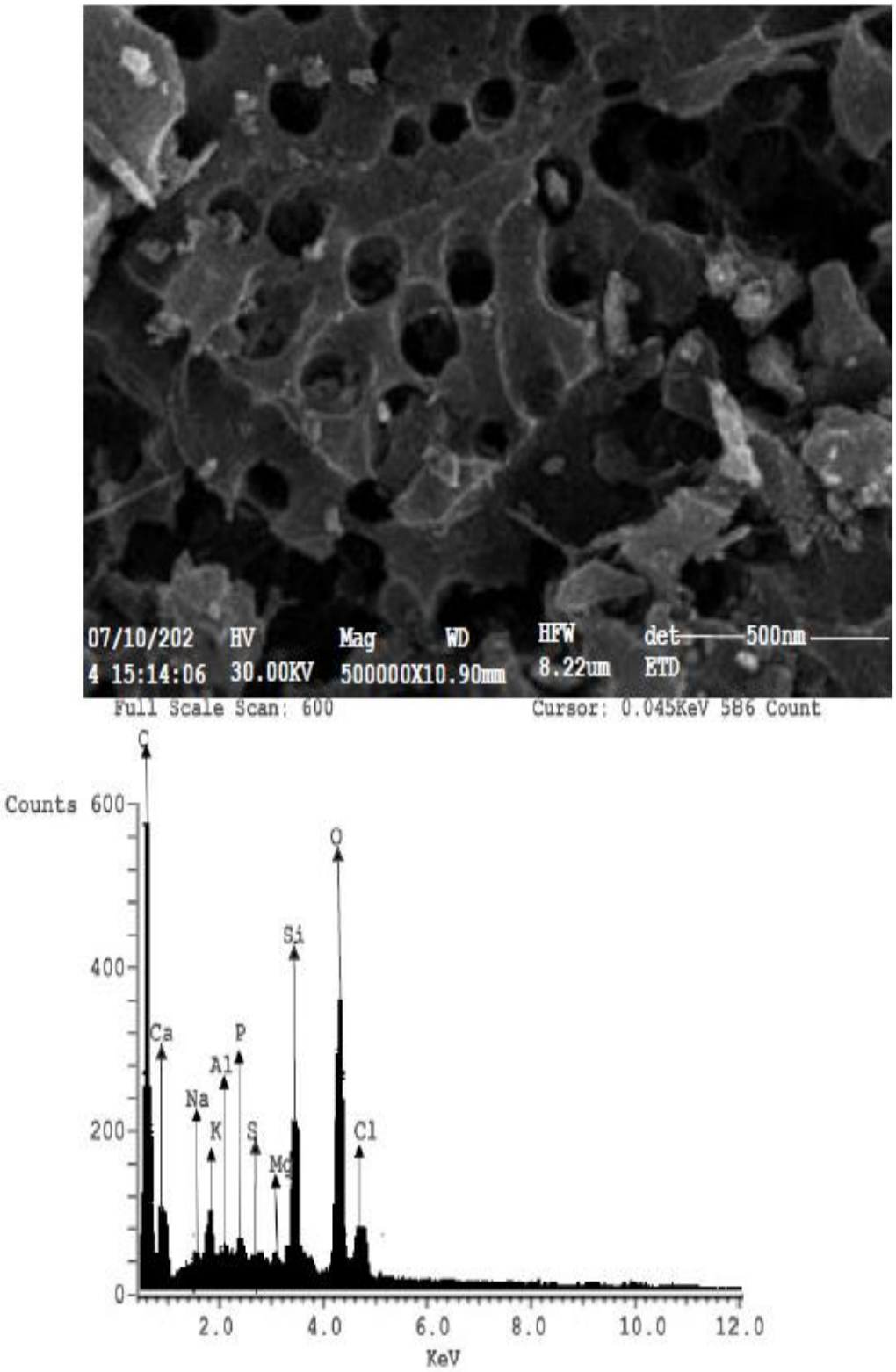

Elements	Composition (%)
C	67.07
O	18.81
Ca	1.04
Si	6.41
Al	0.23
K	2.71
Na	1.26
Mg	0.22
P	0.61
Cl	1.56
S	0.07

Fig. 4.11: SEM/EDX of CSB600

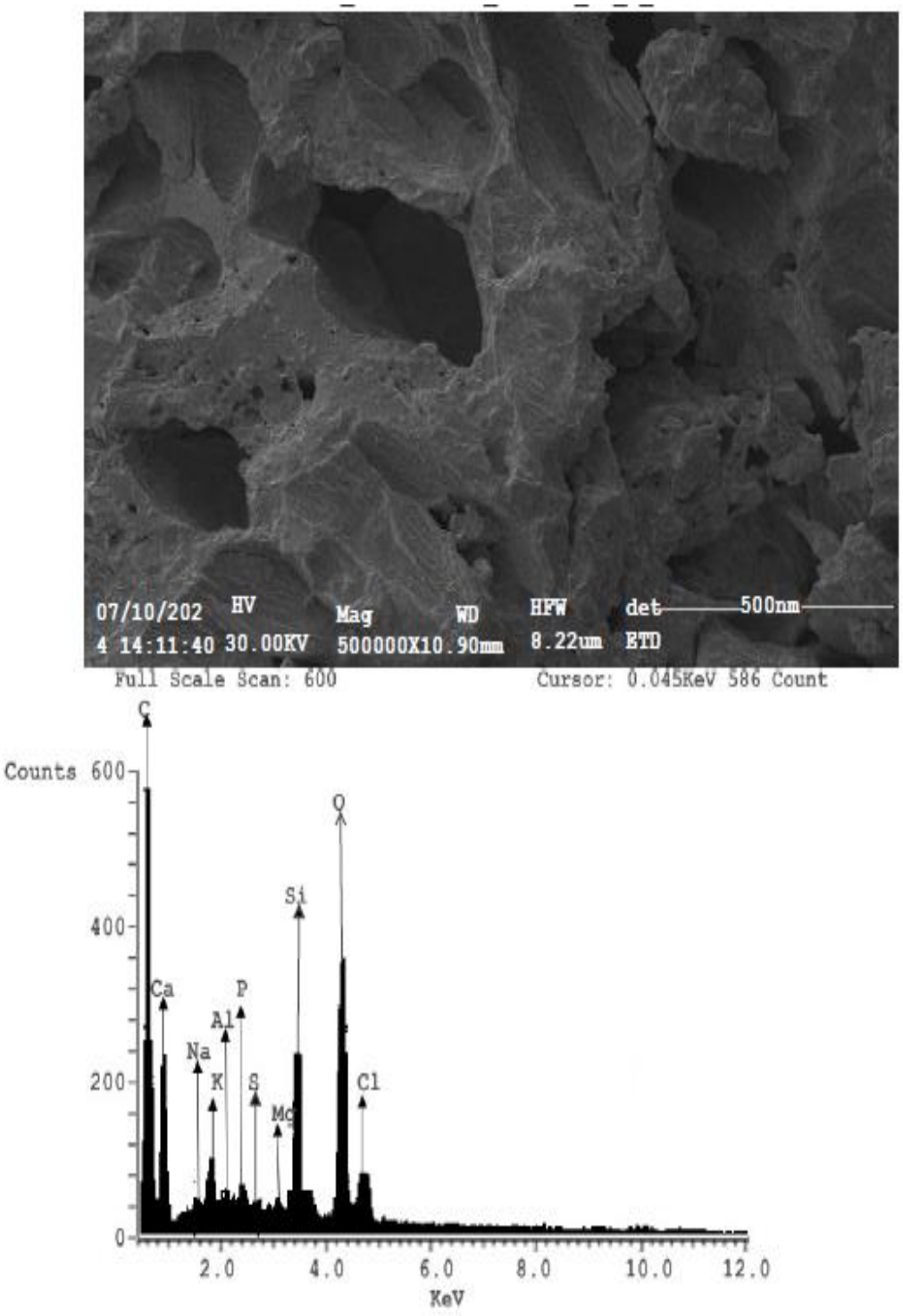

Elements	Composition (%)
C	64.66
O	15.92
Ca	1.70
Si	7.92
Al	1.50
K	2.54
Na	1.75
Mg	1.06
P	1.10
Cl	1.80
S	0.04

Fig. 4.12: SEM/EDX of CSB700

The results given in Figures 4.7 – 4.12 indicate that the coconut shell biochars obtained at the various pyrolysis temperatures were large mesoporous as shown from the porosity results. The surface elemental composition obtained from the energy dispersive x-ray (EDX) result showed that the amounts of carbon and oxygen as the dominant elements in the biochar samples varied markedly from 60.50 to 66.03% and 15.92 to 29.72% respectively.

The EDX result also showed the level of mineral nutrients (Ca, Na, K, Mg and P) in the coconut shell biochar samples. A close examination of the results showed that the total level of the mineral nutrients (Ca^{2+}, Na^{+}, K^{+} and Mg^{2+}) decreased markedly by about 35% from 8.52% at pyrolysis temperature of 350° C to 5.82% at 700°C pyrolysis temperature. These results indicate that a higher proportion of the mineral nutrient present in the biomass may be retained in the biochar obtained at moderate pyrolysis temperatures.

4.6 Ultimate Composition of Biochar Samples

The results of the ultimate (C, H, S, N, and O) analysis of the biochar samples obtained from coconut shell at the different pyrolysis temperature are given in table 4.4.

Table 4.4: Effect of Pyrolysis Temperature of Ultimate Composition of Coconut Shell Biochar.

Samples	Ultimate Composition (wt%)				
	C	H	O	N	S
CS	54.03 ± 0.00	3.22 ± 0.01	41.74 ± 0.07	0.60 ± 0.04	0.43 ± 0.01
CSB350	60.18 ± 0.02	3.03 ± 0.02	36.14 ± 0.03	0.41 ± 0.02	0.22 ± 0.02
CSB400	61.39 ± 0.02	2.99 ± 0.02	33.85 ±0.06	0.48 ± 0.00	0.24 ± 0.01
CSB450	62.92 ± 0.02	2.61 ± 0.02	33.76 ± 0.00	0.57 ± 0.02	0.14 ± 0.02
CSB500	63.95 ± 0.03	2.53 ± 0.03	33.75 ± 1.78	0.59 ± 0.00	0.40 ± 0.00
CSB600	65.01 ± 0.00	2.43 ± 0.02	33.37 ± 0.00	0.93 ± 0.01	0.083 ± 0.01
CSB700	68.63 ± 0.01	2.30 ± 0.02	27.36 ± 0.04	0.98 ± 0.03	0.037 ± 0.01

CS – Unpyrolysed Coconut Shell, CSB – Coconut Shell Biochar,

Compared to the unpyrolysed coconut shell (CS) (Table 4.4), the results showed an increase of up to 27.0% in carbon content of coconut shell biochar, while within the range of pyrolysis temperature used in this study, the biochar carbon content increases by 14.04%. Coconut shells is a hard biomass with relatively high lignin (33%) and cellulose (30%) contents. The results of Novak *et al*. (2009); and Masek *et al*. (2013) indicated that carbon content in biochars from nuts/ shell, lignin and cellulose rich materials showed remarkable increase at high pyrolysis temperatures.

The level of oxygen and hydrogen content in our biochar samples can be seen in Table 4.4 to decrease with increase in pyrolysis temperature. The value of oxygen content varied from 41.74% for the unpyrolysed coconut shell through 36.14% for CSB350 to 27.36% for CSB700 representing an overall decrease of 40.61%. An overall decrease in hydrogen content of 28.57% from the unpyrolysed coconut shell (CS) to the biochar pyrolysed at 700 °C (CSB700) can also be observed (Table 4.4). During heat treatment oxygen and hydrogen are released from biomass via low molecular weight degradation products such as H_2, CO_2, CH_4 etc. It will therefore be expected that relatively large quantities of these volatile molecules will be evolved at the highest pyrolysis temperature, resulting to the reduced levels of oxygen and hydrogen in the biochar samples. Nitrogen is an important nutrient element for growing crops. The nitrogen concentrations in the samples were generally low (below 1%), and varied from 0.60% in the unpyrolysed coconut shell, and 0.41% to 0.98% within the pyrolysis temperatures range used in this study. The low level of nitrogen in the coconut shell is consistent with the values for some lignin-rich biomass, nuts and shells (Gaskin *et al*., 2008). The more than two-folds increase in levels of nitrogen on the biochar samples associated with increase in pyrolysis temperatures of coconut shell can be attributed to the presence of nitrogen complex structure within the high-lignin component of the biomass that requires higher decomposition temperatures resulting in altered chemical structures and nitrogen (Gaskin *et al*., 2008). Generally, the biomass has low levels of sulfur, a large proportion of which is reportedly lost during pyrolysis (Chan and Xu, 2009). The sulphur content of coconut shell was 0.43% and decreased markedly with increased pyrolysis temperature to 0.037%.

4.7 Higher Heating Value of Coconut Shell Biochar

The higher heating value (HHV) refers to the ability of biochar to be used as fuel. The HHVs of the coconut shell biomass and biochars (CSB350 - CSB700) at different pyrolysis temperatures were based on ultimate analysis data of the biochar samples, and estimated using the equation generated by Cordero *et al*. (2001); Channiwala and Parikh (2002); Friedl *et al*. (2005);Tilman *et al*. (1978) for the biochar samples are giving in Table 4.5.

Table 4.5: Higher Heating Value (HHV) of coconut shell and coconut shell biochars

Samples	HHV ($MJ.kg^{-1}$)					
	Cordero *et al*. (2001)	**Channiwala and Parikh (2002)**	**Sheng and Azevedo (2005)**	**Friedl *et al*. (2005)**	**Tilman *et al*. (1978)**	**Average HHV (MJ.kg-1)**
CS	18.534	18.402	21.068	20.234	21.957	20.039
CSB350	20.962	20.758	23.072	22.128	24.647	22.313
CSB400	21.909	21.694	23.793	22.890	25.613	23.180
CSB450	21.668	21.397	23.965	22.719	25.845	23.119
CSB500	21.642	21.380	23.995	22.674	25.884	23.115
CSB600	22.257	21.935	24.646	23.312	26.759	23.782
CSB700	23.915	23.591	25.826	24.480	28.342	25.231

CS – unpyrolysed coconut shell
HHV – Higher Heating Value
CSB – coconut shell biochar

The higher heating value (HHV) of coconut shell (CS) and its derived biochars (CSB350–CSB700) showed a clear increasing trend with increase in pyrolysis temperature (Table 4.5). The raw coconut shell exhibited the lowest HHV (20.04 MJ kg^{-1}), while the biochar increases from 22.31 MJ kg^{-1} for CSB350 to 25.23 MJ kg^{-1} for CSB700, indicating an enhancement in energy density with increasing pyrolysis temperature (Qin *et al*., 2020). A plot of carbon and HHVs against pyrolysis temperatures for the coconut shell biochar samples to illustrate the relationship between carbon content and energy content is presented in Figure 4.13.

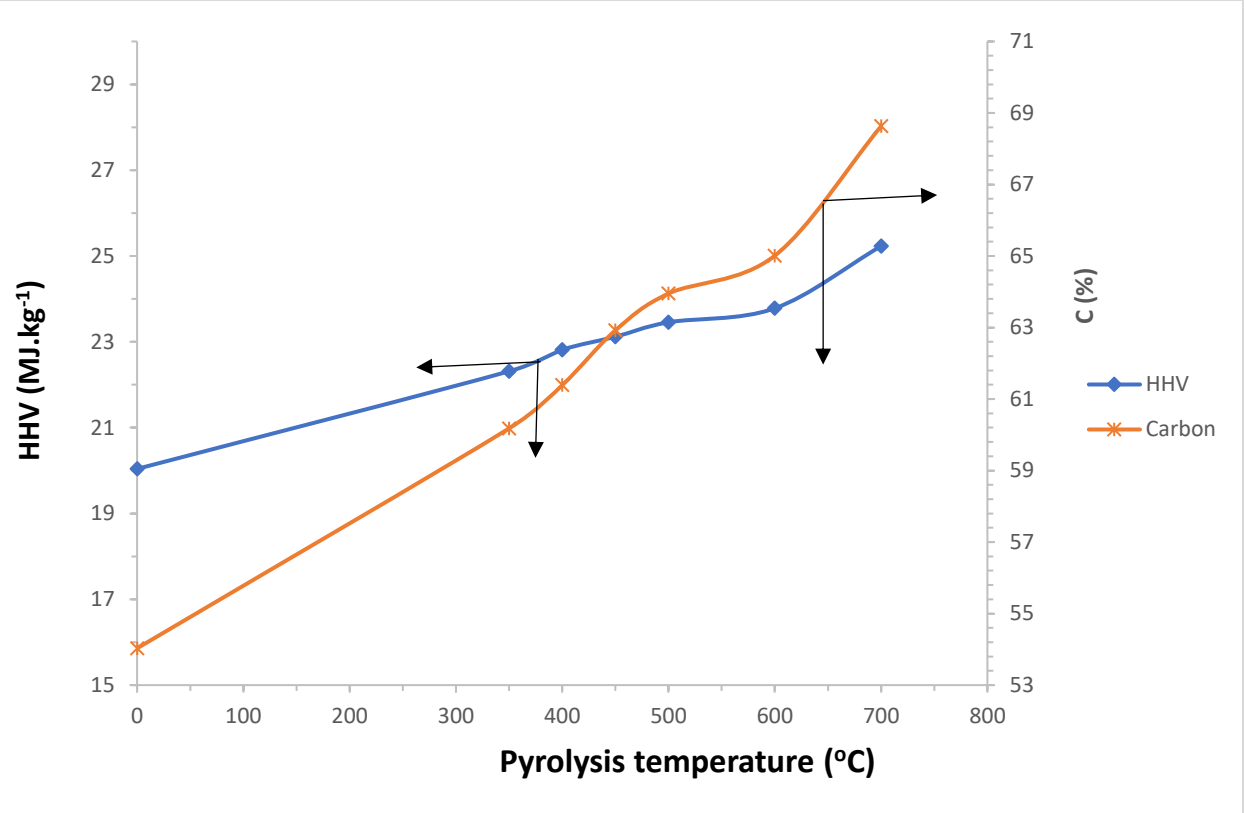

Fig. 4.13: Variation of carbon content and HHV of coconut shell biochars with pyrolysis temperature

The increase in HHV correlates strongly with the rise in carbon content of the biochar, consistent with the general understanding that higher carbon content results in greater energy content. The observed trend is attributed to the progressive thermal degradation of cellulose, hemicellulose, and lignin, which removes oxygen- and hydrogen-containing volatiles and enriches the carbon matrix (Ni *et al*., 2025).

Furthermore, the variation of HHVs with pyrolysis temperature and carbon content suggests a direct relationship between carbon conversion and heating value. This can be approximated by the dependence of carbon yield on temperature, $\alpha c(\%) = f(T)$, where αc denotes the percentage of carbon retained in the resulting biochar and T is the applied pyrolysis temperature. The relationship assumes uniform reactivity of biomass components and a simple one-step decomposition mechanism without secondary interactions (Qin *et al*., 2020). The observed trend

is in good agreement with that reported by Egbosiuba, (2022) for cassava peel with the highest HHV of 28.70 mj.kg^{-1} at a pyrolysis temperature of 600ºC suggesting that increasing pyrolysis temperature enhances the energy potential of biochars derived from lignocellulosic biomass.

4.8 Carbon Sequestration

The atomic mass ratios O/C, H/C, (O + N)/C and (O + N + S)/C in the coconut shell biochars prepared at different pyrolysis temperatures are given in Table 4.6.

Table 4.6: Atomic Mass Ratios in Coconut Shell Biochar Pyrolysed at Different Temperatures

Samples	O/C	H/C	(O + N)/C	(O + N + S)/C
CS	0.77	0.06	0.78	0.79
CSB350	0.60	0.05	0.60	0.61
CSB400	0.55	0.05	0.56	0.56
CSB450	0.54	0.04	0.54	0.55
CSB500	0.53	0.04	0.53	0.54
CSB600	0.51	0.04	0.52	0.53
CSB700	0.40	0.03	0.41	0.41

CS – unpyrolysed coconut shell
CSB – coconut shell biochar

These atomic indices are useful in assessing the stability and recalcitrance of biochar to chemical and biological degradation. The H/C index is a particularly useful indicator of the degree of aromatization in the biochar samples. The O/C and H/C indices can be seen to decrease markedly from 0.77 and 0.06 respectively for the unpyrolysed coconut shell to 0.40 and 0.03 for CSB700. This pattern of variation in the O/C and H/C atomic indices has been attributed to increasing carbonization within the biochar with increase in pyrolysis temperature (Kim *et al*., 2012). Fig. 4.14 is the plot of H/C versus O/C of coconut shell biochar samples obtained at various heat treatment temperatures (Van Krevelen plot).

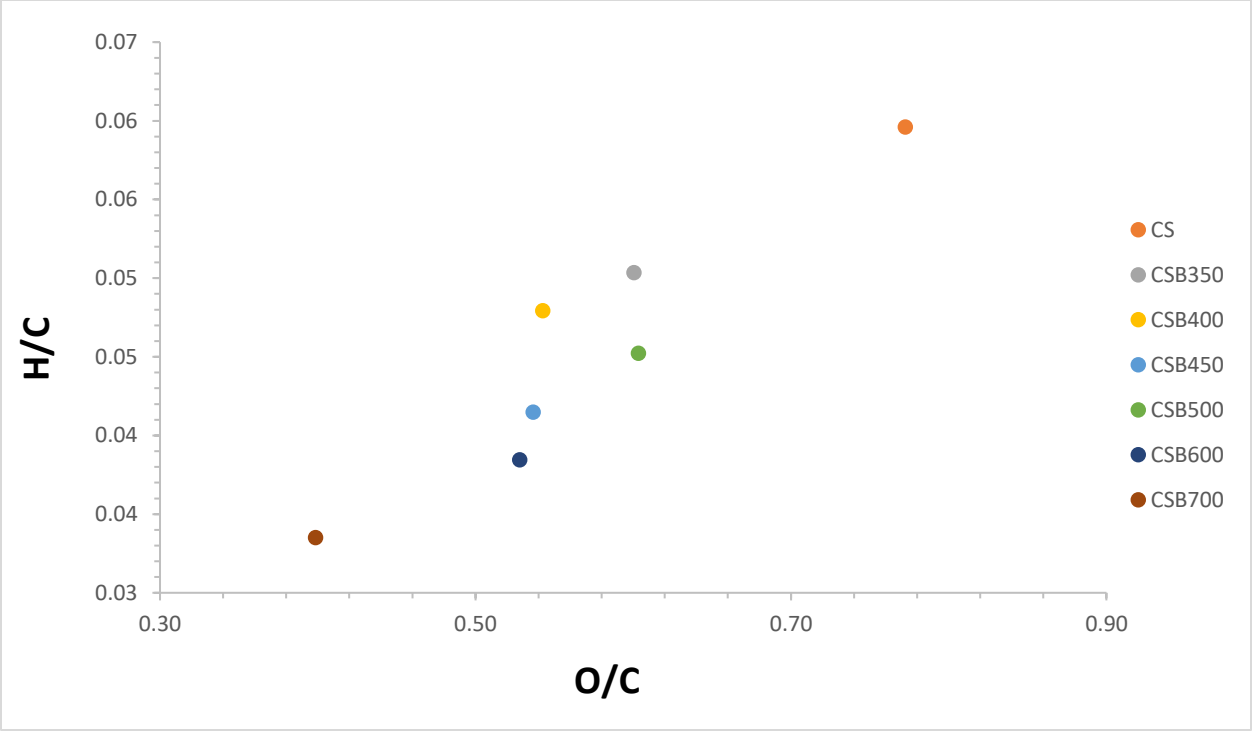

Fig. 4.14: A plot of H/C Versus O/C as a Function of Pyrolysis Temperature

The results show marked degrees in the H/C and O/C atomic ratios in the biochar samples compared with the unpyrolysed coconut shell. The general rule is that the lower these ratios, the greater the degree of aromatization and stability of the biochar. The values of (O + N + S)/C and (O + N)/C indices (Table 4.6) were highest (0.78 and 0.79) for the unpyrolysed coconut shell and decreased with increase in pyrolysis temperature to 0.61 for CSB350 and 0.41 for CSB700 respectively. These indices reflect the variation in polarity of the biochar samples (Ahmad *et al*., 2012).

4.9 Chemical Oxidation Stability of Coconut Shell biochar

The carbons in pyrolytic biochars can either be unstable/labile or stable/recalcitrant depending on the biomass source and pyrolytic temperature. The stable forms of carbon in biochar are responsible for its inherent value in carbon sequestration application. Chemical oxidation (accelerated aging) provides a direct method for the determination of the stability of biochar.

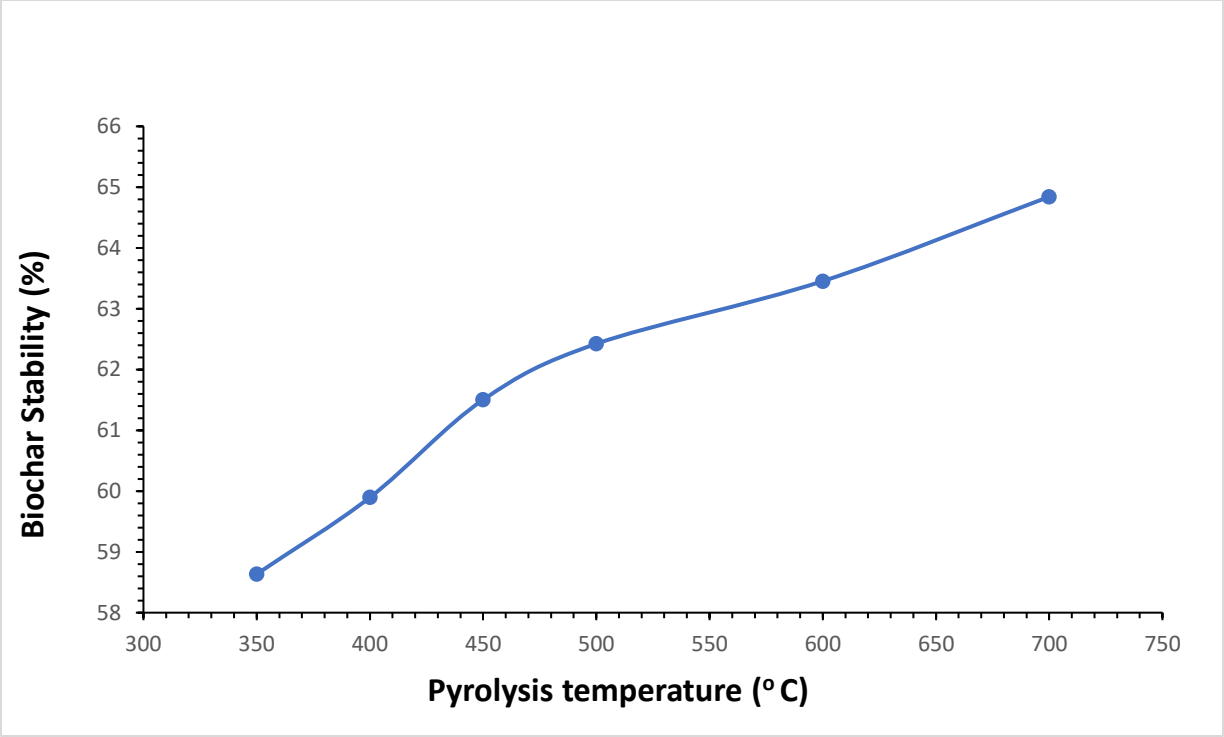

Fig 4.15: Chemical Oxidation Stability of Coconut Shell Biochar Produced at Different Pyrolysis Temperatures

Fig. 4.15 shows the effect of pyrolysis temperature on chemical oxidative stability of coconut shell biochars. It was observed that higher pyrolysis temperatures produced biochars with higher biochar stability, and corroborates the results from H:C and O:C ratios as presented in Fig 4.16. These results suggest that pyrolysis temperatures (≥ 600 °C) may be required to prepare biochars of requisite chemical oxidation stability for carbon sequestration applications.

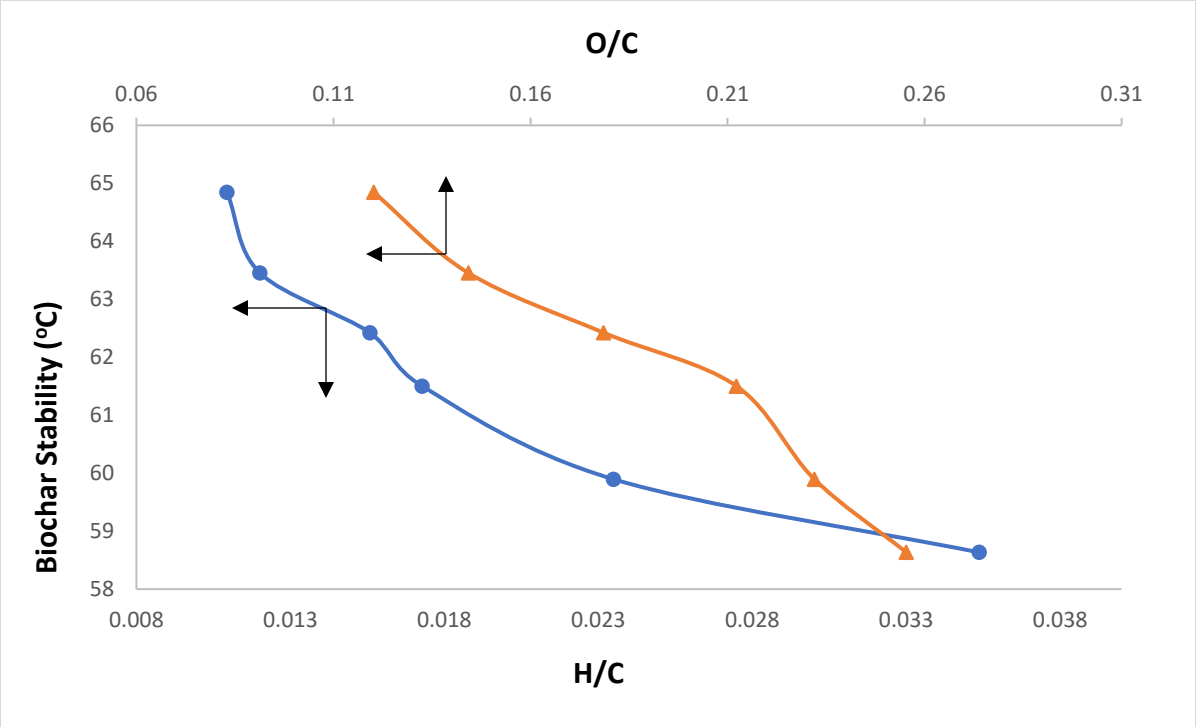

Fig. 4.16: Correlation of Indicators of Biochar Stability

Fig 4.16 illustrates the relationship between the various indices of biochar: oxidative stability and H:C and O:C atomic ratios. The higher values of biochar stability at low values of H:C and O:C ratios are consistent with the results from previous reports of Malghani *et al*. (2013), Wei *et al*. (2020) and Leng *et al*. (2019). The increase in biochar stability with increase in pyrolysis temperature can be related to the chemical composition and structure of the biomass feedstock and the changes they undergo during pyrolysis. The decomposition of cellulose and hemicellulose component of lignocellulosic materials during pyrolysis occurs more readily and at a relatively low heat treatment temperatures to produce biochar with labile C structures, that can be susceptible to further degradation at higher pyrolysis temperatures. Higher pyrolysis temperatures result in the loss of labile C structures, increase in aromaticity of the residual C structures and higher resistance to chemical oxidation (Kuryntseva *et al*., 2023; Petersen *et al*., 2023; Almutairi *et al*., 2023).

4.10 Optimization process for the preparation of Metal - Doped Coconut shell Biochar

The results of the experimental runs used in the determination of specific surface area of the metal Fe^{3+} - doped, Zn^{2+} - doped and Fe^{3+}/Zn^{2+} - doped biochar materials from the central composite design (CCD) are given in Table 4.7 - 4.9.

Table 4.7: Experimental Runs for Specific Surface Area Determination of Fe^{3+} - Doped biochar

S/N	Fe^{3+} loading (wt% CSB)	Temperature (^{o}C)	Time (hr)	Surface area ($m^2.g^{-1}$)	
				Actual	Predicted
1	1.58	301	1.6	1897.21	1775.00
2	4.57	301	1.6	1794.53	1794.96
3	1.58	449	1.6	1186.10	1183.22
4	4.57	449	1.6	705.65	634.22
5	1.58	301	3.4	1185.18	1233.65
6	4.57	301	3.4	986.37	966.29
7	1.58	449	3.4	1859.24	1835.85
8	4.57	449	3.4	900.28	999.53
9	0.56	375	2.5	1270.46	1318.86
10	5.58	375	2.5	648.31	632.39
11	3.07	250	2.5	1403.22	1447.69
12	3.07	500	2.5	990.00	978.01
13	3.07	375	1.0	1794.64	1900.17
14	3.07	375	4.0	1825.18	1752.13
15	3.07	375	2.5	1993.22	1921.31
16	3.07	375	2.5	1879.36	1921.31
17	3.07	375	2.5	1878.33	1921.31
18	3.07	375	2.5	1871.02	1921.31
19	3.07	375	2.5	1990.18	1921.31

CSB – Coconut Shell Biochar

Table 4.8: Experimental Runs for Specific Surface Area Determination of Zn^{2+} - Doped Biochar

S/N	Zn^{2+} loading (wt% CSB)	Temperature (^{o} C)	Time (hr)	Surface area ($m^2.g^{-1}$)	
				Actual	Predicted
1	1.85	301	1.6	1628.27	1775.00
2	5.35	301	1.6	1428.41	1794.96
3	1.85	449	1.6	1190.17	1183.22
4	5.35	449	1.6	972.53	634.22
5	1.85	301	3.4	1175.39	1233.65
6	5.35	301	3.4	1024.17	966.29
7	1.85	449	3.4	1598.71	1835.85
8	5.35	449	3.4	1072.53	999.53
9	0.65	375	2.5	1200.97	1318.86
10	6.54	375	2.5	824.17	632.39
11	3.60	250	2.5	1276.32	1447.69
12	3.60	500	2.5	1131.70	978.01
13	3.60	375	1.0	1500.31	1900.17
14	3.60	375	4.0	1402.71	1752.13
15	3.60	375	2.5	1703.16	1921.31
16	3.60	375	2.5	1589.30	1921.31
17	3.60	375	2.5	1588.27	1921.31
18	3.60	375	2.5	1602.27	1921.31
19	3.60	375	2.5	1700.12	1921.31

CSB – Coconut Shell Biochar

Table 4.9: Experimental runs for specific surface area determination of Fe^{3+} / Zn^{2+} - doped biochar

S/N	Fe^{3+}/Zn^{2+} (Fe^{3+} wt%, 10%wt CSB)	Temperature (^{o} C)	Time (hr)	Surface area ($m^2.g^{-1}$)	
				Actual	Predicted
1	23	301	1.6	1837.22	1790.50
2	77	301	1.6	1696.31	1628.82
3	23	449	1.6	1131.83	1141.99
4	77	449	1.6	724.17	836.95
5	23	301	3.4	995.53	928.75
6	77	301	3.4	852.74	888.58
7	23	449	3.4	1104.16	1217.64
8	77	449	3.4	941.41	1034.12
9	5	375	2.5	1197.27	1213.41
10	95	375	2.5	1004.32	923.13
11	50	250	2.5	1236.00	1344.48
12	50	500	2.5	1095.05	921.53
13	50	375	1.0	1758.05	1775.03
14	50	375	4.0	1298.22	1216.19
15	50	375	2.5	2106.54	2038.05
16	50	375	2.5	1992.68	2038.05
17	50	375	2.5	1991.65	2038.05
18	50	375	2.5	1984.34	2038.05
19	50	375	2.5	2103.86	2038.05

CSB – Coconut Shell Biochar

The maximum specific surface area of the metal - doped biochar materials was attained irrespective of the metal type was attained at the same pyrolysis temperature of 375° C and pyrolysis time of 2.5hr. The metal loading that gave the apparent maximum specific surface area varied from 3.07 wt% Fe^{3+} for Fe^{3+} - doped biochar, 3.60 wt% Zn^{2+} for Zn^{2+} - doped biochar and 50 wt% Fe^{3+} for Fe^{3+}/Zn^{2+} at a total metal loading of 2g with apparent maximum specific surface area ($m^2.g^{-1}$) of 1993.22, 1703.16 and 2106.54 $m^2.g^{-1}$ Fe^{3+} - doped, Zn^{2+} - doped and Fe^{3+}/Zn^{2+} - doped biochars.

Figs. 4.17 - 4.19 showed the correlation between the actual and predicted values of the specific surface area for the Fe^{3+} - doped, Zn^{2+} - doped and $Fe^{3+/}Zn^{2+}$ - doped biochar samples.

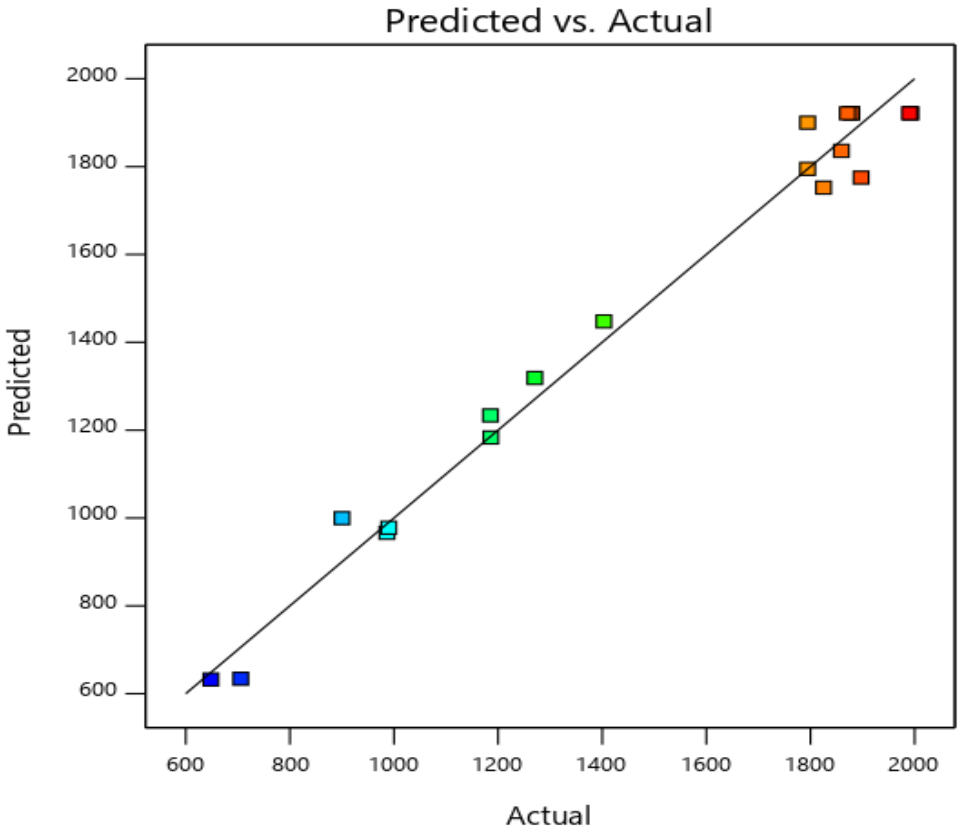

Fig. 4.17: Line Plot of the Actual and Predicted Value of Fe^{3+} - Doped Biochar

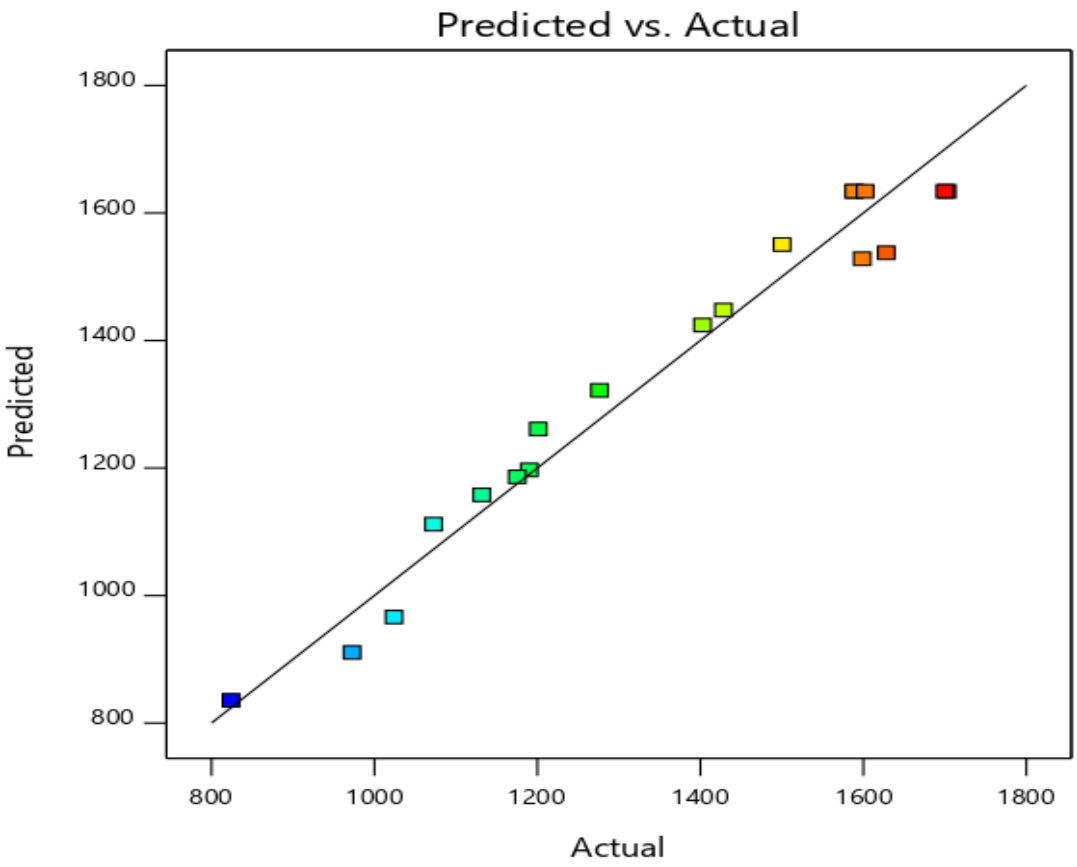

Fig. 4.18: Line Plot of the Actual and Predicted Value of Zn^{2+} - Doped Biochar

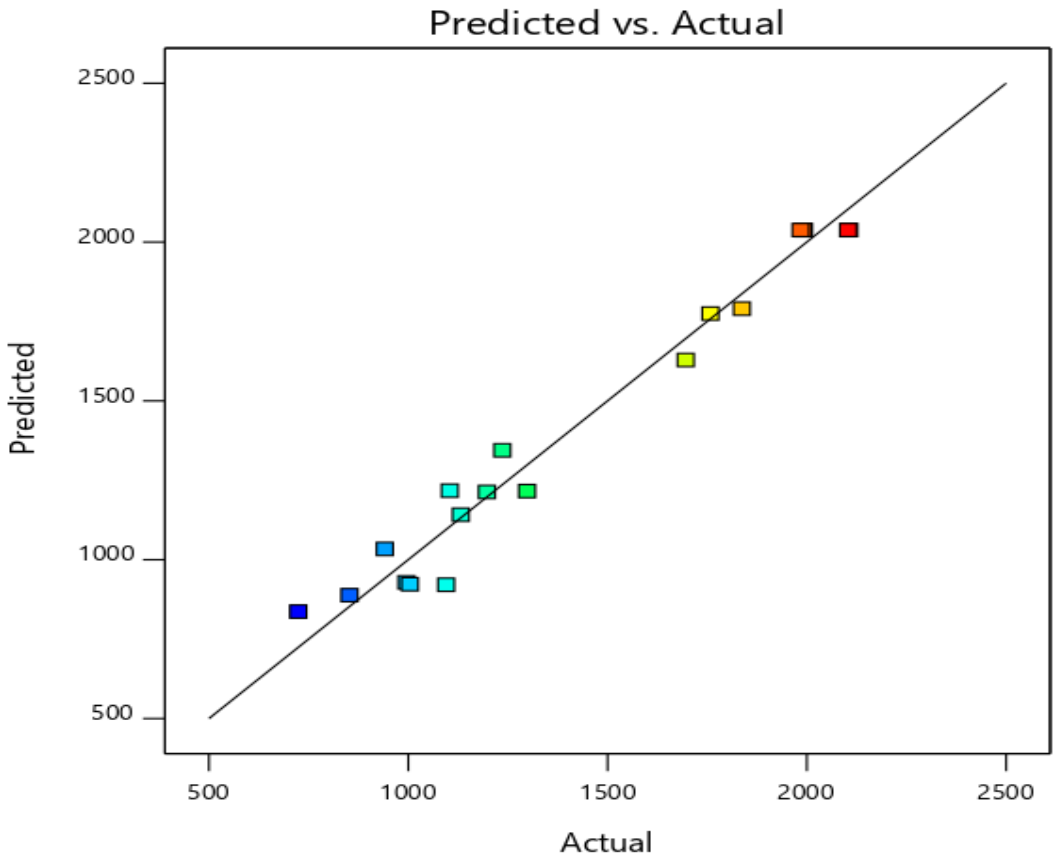

Fig. 4.19: Line Plot of the Actual and Predicted Value of Fe^{3+}/Zn^{2+} - Doped Biochar

The figs. demonstrate a strong positive correlation between the predicted and actual values of the specific surface areas which was also revealed by the high R^2 values (Table 4.10) of 0.9822, 0.9653, and 0.9707 for the Fe^{3+} - doped, Zn^{2+} - doped and Fe^{3+}/Zn^{2+} - doped biochars respectively.

From the Fit Statistics (Table 4.10), The values of adequate precision of between 14.42 – 20.08, are markedly higher than 4, the threshold for adequate signal; and indicate that the models can be used to navigate the design space (Adamu *et al*., 2022). The R^2 values of 0.9822 for Fe^{3+} - doped biochar, 0.9653 for Zn^{2+} - doped biochar and 0.9707 for Fe^{3+}/Zn^{2+}

- doped biochars explained that only 1.78, 3.47 and 2.93% of the total experimental data, respectively, were not accounted for by the developed models (Adamu *et al*., 2022).

Table 4.10: Fit Statistics for Metal and Bimetallic-Doped Biochar

Parameter	Fe^{3+}-Based Biochar	Zn^{2+}-Based Biochar	Fe^{3+}/Zn^{2+}-Based Biochar
Std. Dev.	88.47	71.63	114.82
Mean	1476.76	1347.87	1423.76
C.V. %	5.99	5.31	8.06
R^2	0.9822	0.9653	0.9707
Adeq Precision	20.0830	15.3665	14.4197

The coefficients of variation (CVs), ranging from 5.31 – 8.06%, further demonstrate the reproducibility of the experimental results. CV is a measure of the relative variability, expressed as the standard deviation as a percentage of the mean. A low CV indicates that the measurements are consistent and reproducible, while a high CV reflects greater variation relative to the mean, which may compromise the development of an adequate predictive model (Liyana-Pathirana and Shahidi, 2005; Daniel, 1991). Coefficient of variation values of between 5.31 and 8.06 are within the acceptable range (Kalu *et al*., 2021).

The model statistics for the specific surface area of the Fe^{3+}- doped, Zn^{2+}- doped, and Fe^{3+}/Zn^{2+}- doped biochars are summarized in Tables 4.11 – 4.13.

Table 4.11: Summary of Model Statistics of Specific Surface Area of Fe^{3+} - Doped Biochar

Source	Sequential p-value	Lack of Fit p-value	Adjusted R^2	Predicted R^2	
Linear	0.2847	0.0005	0.0608	-0.2659	
2FI	0.2248	0.0005	0.1727	-0.2069	
Quadratic	**< 0.0001**	**0.1776**	**0.9645**	**0.8822**	**Suggested**
Cubic	0.1029	0.4624	0.9830	0.8466	Aliased

Table 4.12: Summary of Model Statistics of Specifics Surface Area of Zn^{2+} - Doped Biochar

Source	Sequential p-value	Lack of Fit p-value	Adjusted R^2	Predicted R^2	
Linear	0.3180	0.0031	0.0442	-0.2392	
2FI	0.3172	0.0031	0.0996	-0.2258	
Quadratic	**< 0.0001**	**0.2947**	**0.9305**	**0.7823**	**Suggested**
Cubic	0.5387	0.1289	0.9264	-1.1649	Aliased

Table 4.13: Summary of Model Statistics of Specifics Surface Area of Fe^{3+}/Zn^{2+} - Doped Biochar

Source	Sequential p-value	Lack of Fit p-value	Adjusted R^2	Predicted R^2	
Linear	0.4055	0.0004	0.0058	-0.1971	
2FI	0.6092	0.0003	-0.0736	-0.8909	
Quadratic	**< 0.0001**	**0.0699**	**0.9414**	**0.7987**	**Suggested**
Cubic	0.0705	0.1798	0.9763	0.4167	Aliased

Based on the regression coefficients from the Tables, the quadratic model with highest regression values was considered a suitable model to describe the experimental result except for the cubic model which was aliased. In addition, the difference between the adjusted and predicted values were less than 20%, indicating that the adjusted R^2s were in reasonable agreement with the predicted R^2s (Rai *et al.,* 2016).

Analysis of variance (ANOVA) was performed on the response (specific surface area of the metal - doped biochar materials) to determine the accuracy and significance of the model, and the results are presented in Tables 4.14 – 4.16 . Furthermore, the significance of linear, interaction and quadratic model terms were also determined using the analysis of variance (ANOVA). The Fisher variation ratio (*F*-value), probability of error value (*p*-value), lack of fit and adequate precision were all evidence of ANOVA. Generally, the *p*-value (probability of error value) less than 0.05 suggested that terms of the model were significant (Bayuo *et al*., 2020; Alman-Abad *et al*., 2020).

Any model term with a P-value < 0.05 is considered statistically significant, indicating that variations in the factor have a measurable effect on the specific surface area of the metal - doped biochar materials.

Table 4.14: Anova of Specific Surface Area of Fe^{3+} - Doped Biochar

Source	Sum of Squares	df	Mean Square	F-value	P-value	
Model	3.893E+06	9	4.326E+05	55.27	< 0.0001*	**Significant**
A- Fe^{3+} loading	5.688E+05	1	5.688E+05	72.68	< 0.0001*	
B-Temp.	2.663E+05	1	2.663E+05	34.02	0.0002*	
C-Time	26453.44	1	26453.44	3.38	0.0991	
AB	1.619E+05	1	1.619E+05	20.68	0.0014*	
AC	41276.39	1	41276.39	5.27	0.0473*	
BC	7.128E+05	1	7.128E+05	91.08	< 0.0001*	
A^2	1.526E+06	1	1.526E+06	194.98	< 0.0001*	
B^2	8.564E+05	1	8.564E+05	109.43	< 0.0001*	
C^2	15450.40	1	15450.40	1.97	0.1936	
Residual	70435.64	9	7826.18			
Lack of Fit	54391.53	5	10878.31	2.71	0.1776	**not significant**
Pure Error	16044.11	4	4011.03			
Cor Total	3.964E+06	18				

*** – Statistically Significant**

Table 4.15: Anova of Specific Surface Area of Zn^{2+} - Doped Biochar

Source	Sum of Squares	Df	Mean Square	F-value	p-value	
Model	1.283E+06	9	1.426E+05	27.78	< 0.0001*	**Significant**
A - Zn^{2+} loading	2.188E+05	1	2.188E+05	42.64	0.0001*	
B-Temp.	32431.92	1	32431.92	6.32	0.0331*	
C-Time	19249.30	1	19249.30	3.75	0.0847	
AB	19280.59	1	19280.59	3.76	0.0845	
AC	8443.50	1	8443.50	1.65	0.2316	
BC	2.331E+05	1	2.331E+05	45.44	< 0.0001*	
A^2	5.852E+05	1	5.852E+05	114.06	< 0.0001*	
B^2	2.652E+05	1	2.652E+05	51.68	< 0.0001*	
C^2	36723.85	1	36723.85	7.16	0.0254*	
Residual	46176.04	9	5130.67			
Lack of Fit	31959.39	5	6391.88	1.80	0.2947	**not significant**
Pure Error	14216.65	4	3554.16			
Cor Total	1.329E+06	18				

*** – Statistically Significant**

Table 4.16: Anova of Specific Surface Area of Fe^{3+}/Zn^{2+} - Doped Biochar

Source	Sum of Squares	df	Mean Square	F-value	p-value	
Model	3.933E+06	9	4.370E+05	33.15	< 0.0001*	**Significant**
A - Fe^{3+}/Zn^{2+} Loading (% Fe^{3+})	1.017E+05	1	1.017E+05	7.72	0.0215*	
B-Temp.	2.159E+05	1	2.159E+05	16.38	0.0029*	
C-Time	3.770E+05	1	3.770E+05	28.60	0.0005*	
AB	10275.33	1	10275.33	0.7795	0.4003	
AC	7382.95	1	7382.95	0.5601	0.4733	
BC	4.394E+05	1	4.394E+05	33.33	0.0003*	
A^2	1.605E+06	1	1.605E+06	121.73	< 0.0001*	
B^2	1.398E+06	1	1.398E+06	106.02	< 0.0001*	
C^2	5.020E+05	1	5.020E+05	38.08	0.0002*	
Residual	1.186E+05	9	13182.54			
Lack of Fit	1.025E+05	5	20509.98	5.10	0.0699	**not significant**
Pure Error	16093.00	4	4023.25			
Cor Total	4.051E+06	18				

*** – Statistically Significant**

The ANOVA results in Table 4.14 – 4.16 show that the quadratic models for the three catalysts (Fe^{3+} - doped, Zn^{2+} - doped and Fe^{3+}/Zn^{2+} - doped biochars) were statistically significant ($p < 0.05$), indicating the model was appropriate for predicting the specific surface area within the range of process factors studied. The non-significant lack-of-fit in all the three catalysts also confirm the suitability of the models. The coded factors (A, B and C) represent metal loading, pyrolysis temperature, and pyrolysis time.

For Table 4.14, the linear term of Fe^{3+} loading (A), pyrolysis temperature (B), interaction term of AB, AC and BC and quadratic term of A^2 and B^2 had significant influence on the specific surface area as evidenced by their p-values (< 0.05). The model terms that significantly influenced the specific surface area of the Zn^{2+}-doped biochar (Table 4.15) include the linear effects of Zn^{2+} loading (A) and pyrolysis temperature (B), the interaction term BC, as well as all the quadratic terms (A^2, B^2, and C^2), as indicated by their p-values (< 0.05). The specific surface area of the Fe^{3+}/Zn^{2+}-doped biochar was significantly influenced by all the linear terms (A, B, and C), the BC interaction term, and all the quadratic terms (A^2, B^2, and C^2), as shown by their p-values (< 0.05).

4.10.1 Regression Analysis

A regression analysis was performed to fit the response function and predict the outcome of specific surface area with a simple equation . The model is expressed by Eq. (4.1 – 4.3).

For Fe^{3+}- doped biochar

Specific Surface Area = +1921.31 -204.09A -139.63B -44.01C -142.24AB -71.83AC +298.50BC -334.35A^2 -250.48B^2 -33.64C^2 (Eqn 4.1)

For Zn^{2+} - doped biochar

Specific Surface Area = +1634.16 -126.57A -48.73B -37.54C -49.09AB -32.49AC +170.71BC -207.06A^2 -139.37B^2 -51.87C^2 (Eqn 4.2)

For Fe^{3+}/Zn^{2+} - doped biochar

Specific Surface Area = +2038.046 -86.30A -125.74B -166.14C +35.84AB +30.38AC +234.35BC -342.87A^2 -319.98B^2 -191.78C^2 (Eqn 4.3)

The regression analysis produced predictive models for the specific (BET) surface area (SSA) of Fe^{3+}-, Zn^{2+}-, and Fe^{3+}/Zn^{2+}-doped biochars, expressed as coded equations (Eqns. 4.1–4.3). These equations reveal both the magnitude and direction of influence of each process variable metal loading (A), pyrolysis temperature (B), and pyrolysis time (C) on BET surface area, as well as their interactions and quadratic effects. Here, A represents the coded value of metal loading, B represents the coded value of pyrolysis temperature, and C represents the coded value of pyrolysis time.

In these equations, the coefficients of single factors represent the individual effect of each variable, while the coefficients of interaction terms represent the combined effect of the respective variables. A positive coefficient indicates that an increase in the corresponding factor or interaction leads to a corresponding increase in the BET surface area, whereas a negative coefficient indicates that an increase in the factor or interaction results in a corresponding decrease in BET surface area. Therefore, the determination of the optimized parameters to produced metal - doped biochar materials with a high BET surface area depends on the magnitude of the coefficients.

Fig. 4.20A – 4.20C shows the response surface, 3D and contour plots of the interaction between (A) metal, Fe^{3+} - loading and pyrolysis temperature at a constant pyrolysis time (2.5hr), (B) Fe^{3+} - loading and pyrolysis time at a constant pyrolysis temperature (375° C), and (C) pyrolysis temperature and pyrolysis time at a constant Fe^{3+} - loading (3.07 wt%), on the specific surface area of the Fe^{3+} - doped biochar material.

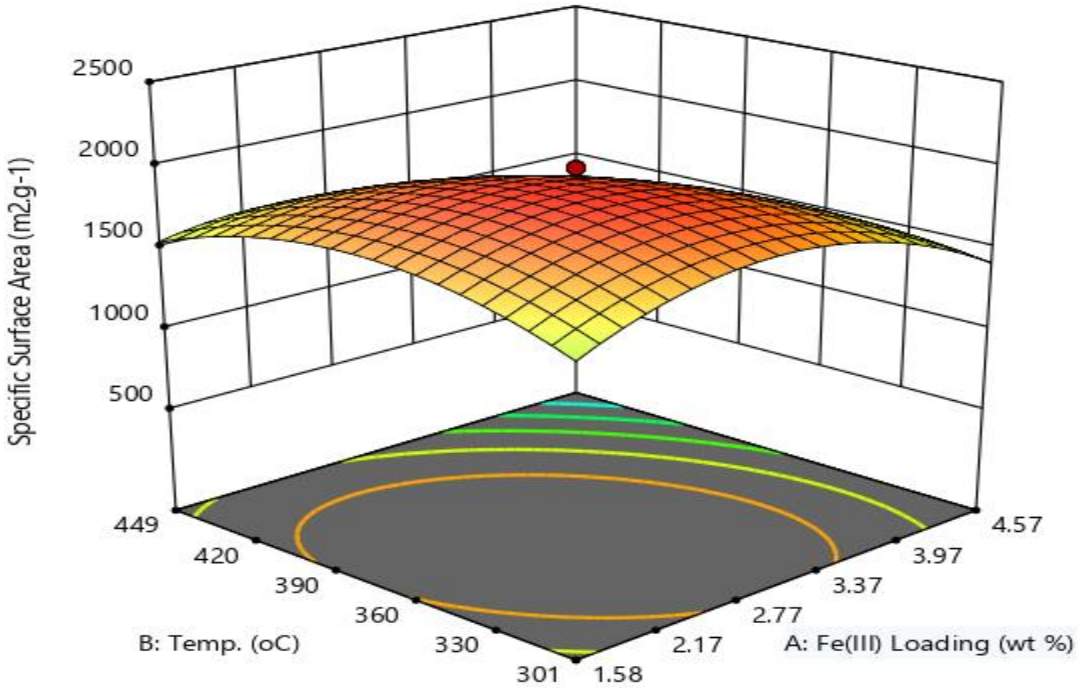

(i)

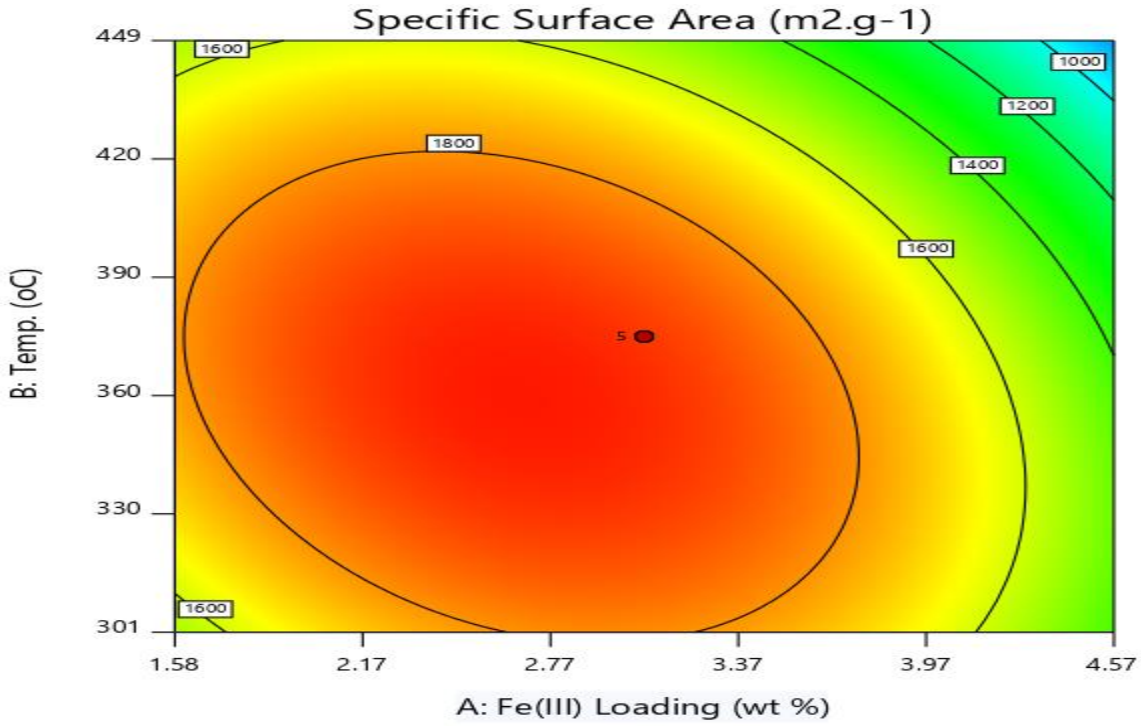

(ii)

Fig. 4.20A: Three - dimensional 3D (i) and Contour Plots (ii) of the Interaction of Fe^{3+} - Loading and Pyrolysis Temperature on the Specific Surface Area of the Fe^{3+} - Doped Biochar

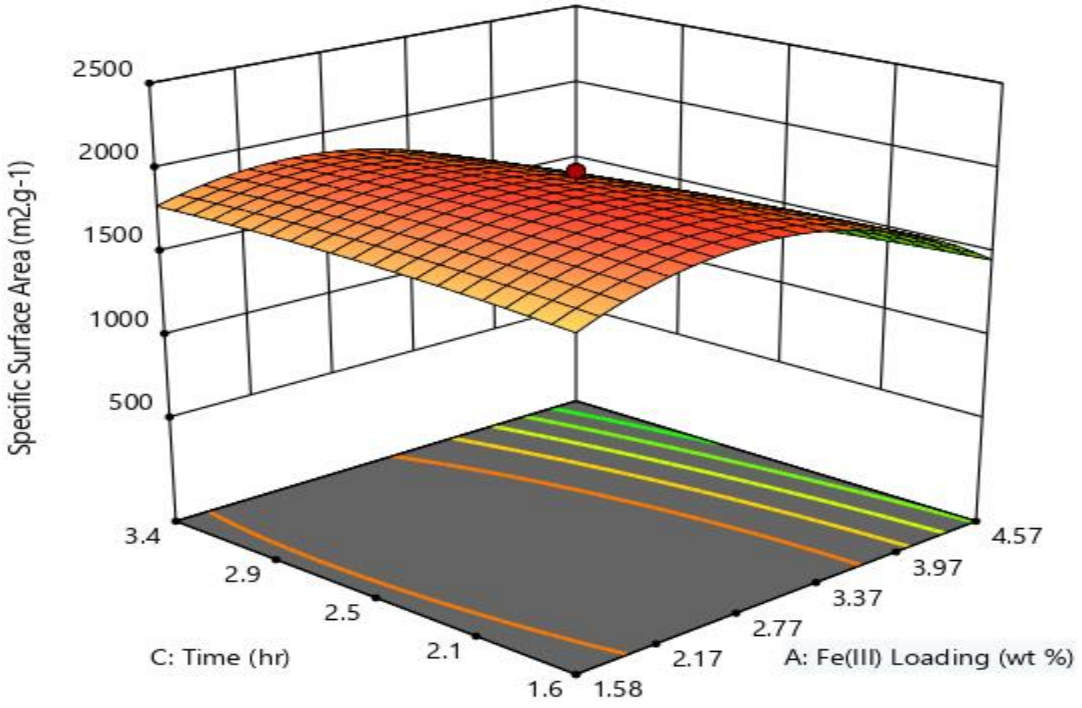

(i)

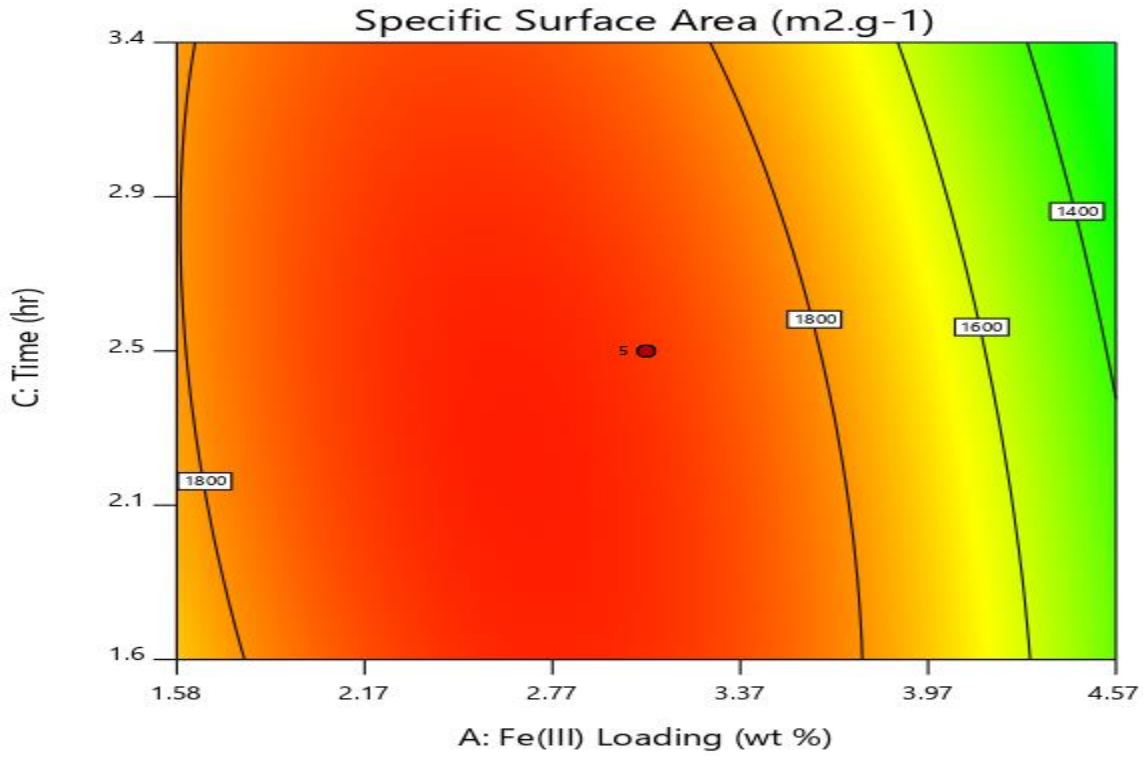

(ii)

Fig. 4.20B: Three - dimensional 3D (i) and Contour Plots (ii) of the Interaction of Fe^{3+} - Loading and Pyrolysis Time on the Specific Surface Area of the Fe^{3+} - Doped Biochar

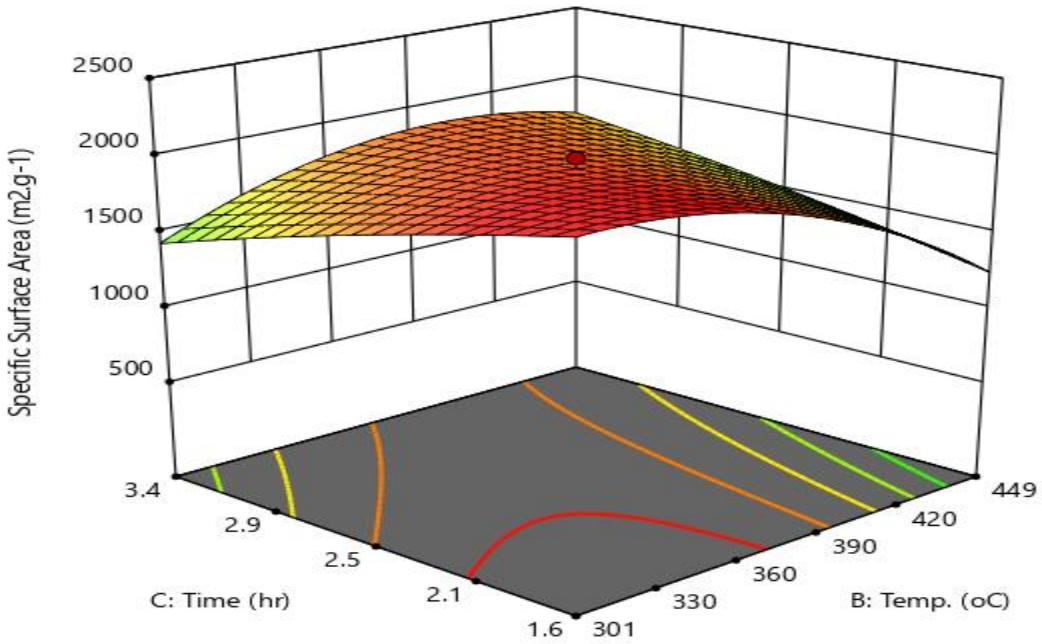

(i)

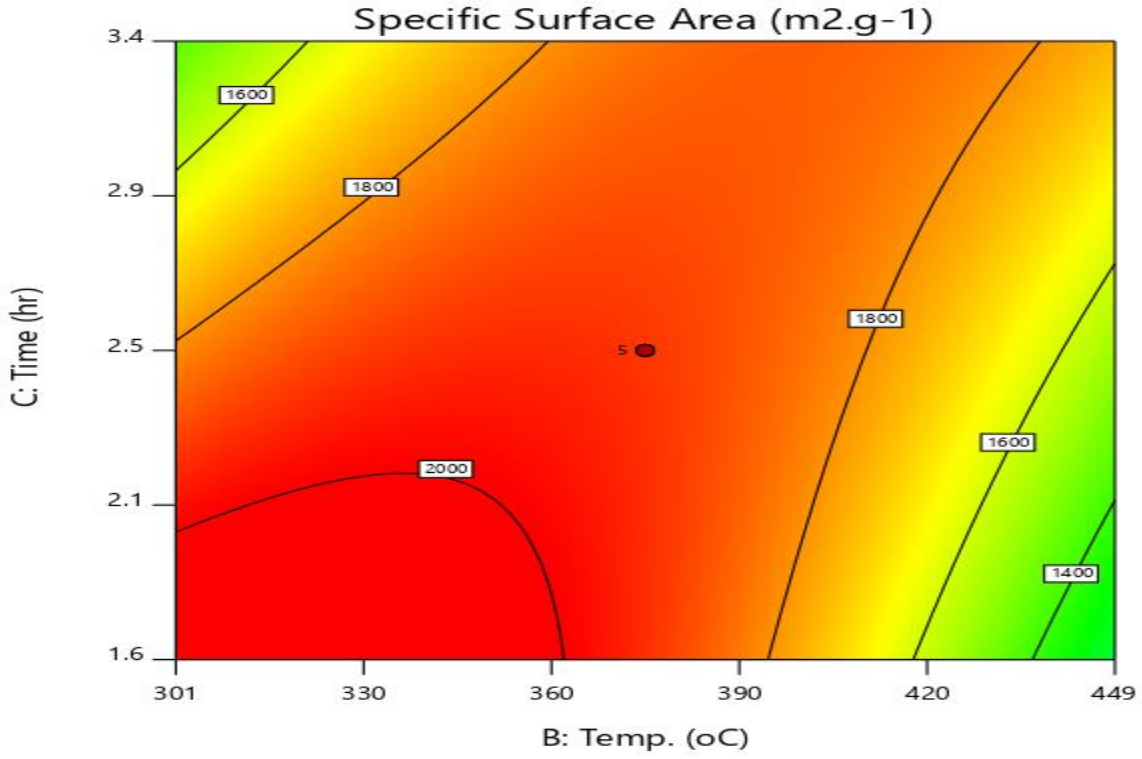

(ii)

Fig. 4.20C: Three - dimensional 3D (i) and Contour Plots (ii) of the Interaction of Pyrolysis Temperature and Pyrolysis Time on the Specific Surface Area of the Fe^{3+} - Doped Biochar

It can be observed (Fig. 4.20A) that simultaneous increase in Fe^{3+} -loading and heat treatment temperature was accompanied with a decrease in BET surface area of the Fe^{3+} - based magnetic carbon-rich material with maximum BET surface area (1865.76 $m^2.g^{-1}$) at Fe^{3+} loading (3.47 wt%) and heat treatment temperature (362^o C). The combined effect of Fe3+ loading and duration of heat treatment lead to an increase in BET surface area (1817.4 – 1956.08 $m^2.g^{-1}$) when the Fe^{3+} loading increase from 1.58 – 2.65 wt% and duration of heat treatment increase from 1.6 – 2.5 hr (Fig 4.20B). In addition, maximum BET surface area of 2099.88 $m^2.g^{-1}$ was achieved at the heat treatment temperature at 301^o C and duration of heat treatment of 1.6 hr for the combined effect of heat treatment temperature and duration of heat treatment, beyond which no significant increase was observed (Fig. 4.20C).

During co-pyrolysis, metal particles interact in a complex process with biochar, bonding to the surface or embedding within the biochar structure leading to etching or restructuring that sometimes influences the development of additional pores resulting to a potential increase in surface area and porosity (Kim *et al*., 2019).

Fig. 4.21A – 4.21C showed the 3D surface response and contour plots for the interaction between (A) metal, Zn^{2+} loading and pyrolysis temperature (B) at a fixed pyrolysis time (2.5 hr) (C), metal loading (A) and pyrolysis time (C) at a fixed pyrolysis temperature (373^o C) (B), and pyrolysis temperature (B) and pyrolysis time (C) at constant metal loading (A) (3.60 wt %) on the specific surface area of Zn^{2+} - doped biochar.

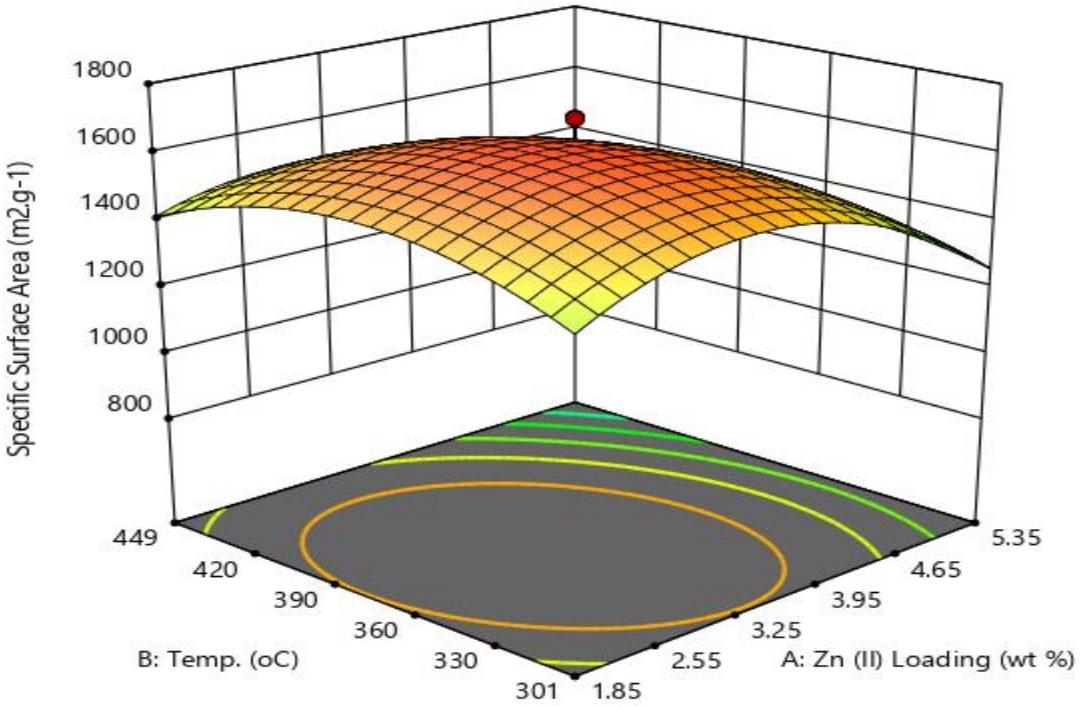

(i)

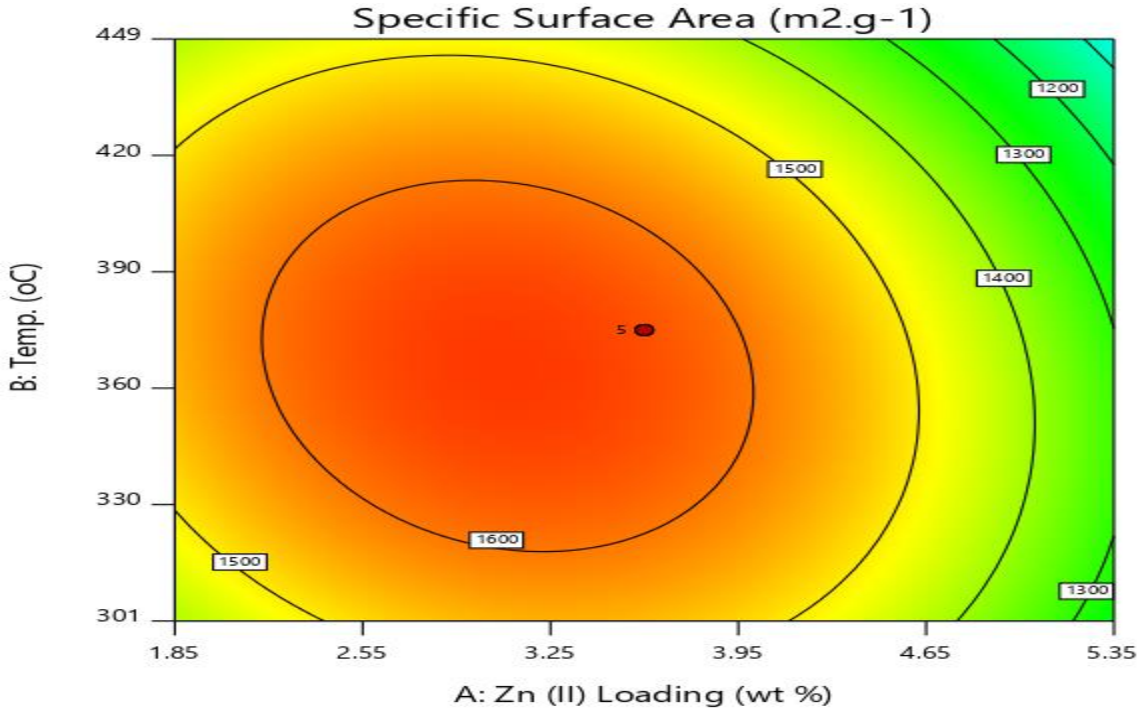

(ii)

Fig. 4.21A: Three - dimensional 3D (i) and Contour Plots (ii) of the Interaction of Zn^{2+} - Loading and Pyrolysis Temperature on the Specific Surface Area of the Zn^{2+} - Doped Biochar

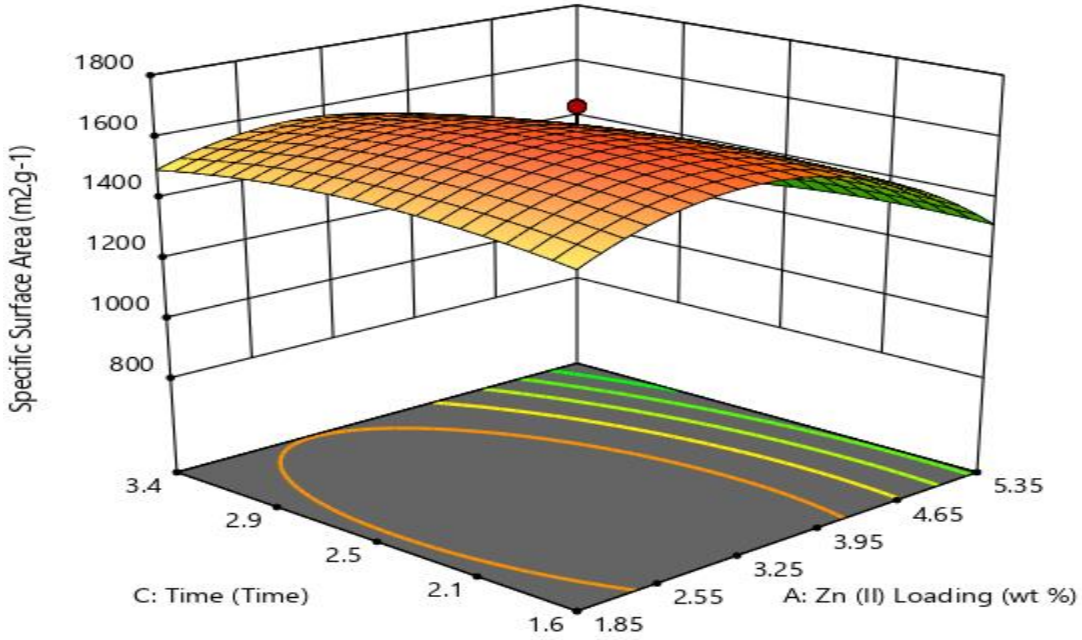

(i)

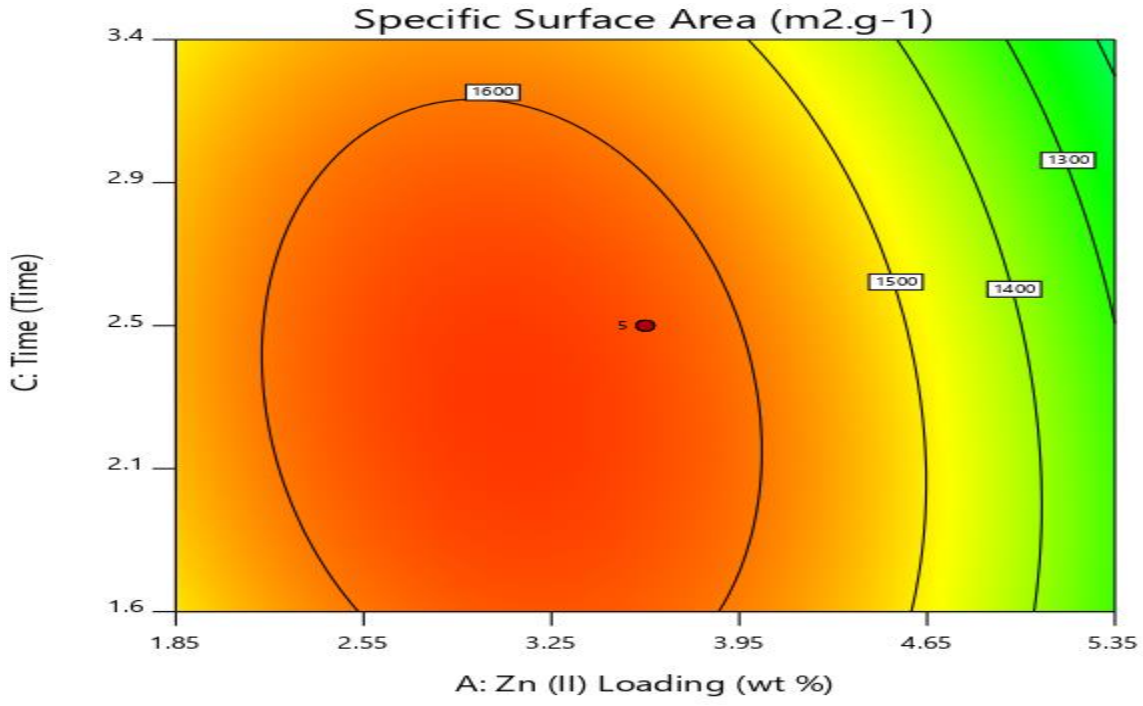

(ii)

Fig. 4.21B: Three - dimensional 3D (i) and Contour Plots (ii) of the Interaction of Zn^{2+} - Loading and Pyrolysis Time on the Specific Surface Area of the Zn^{2+} - Doped Biochar

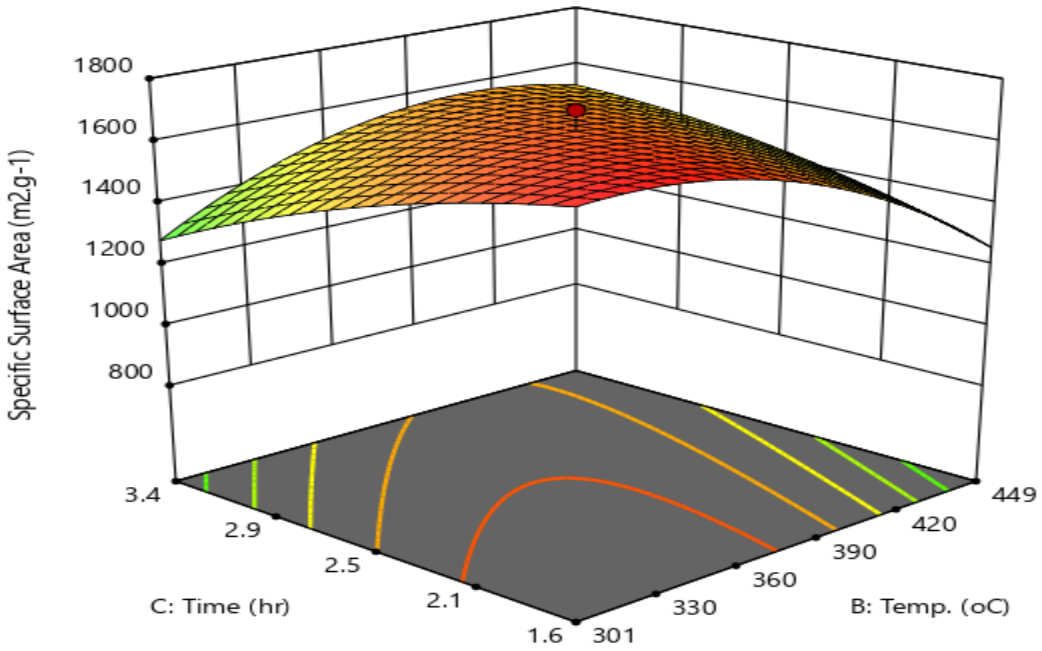

(i)

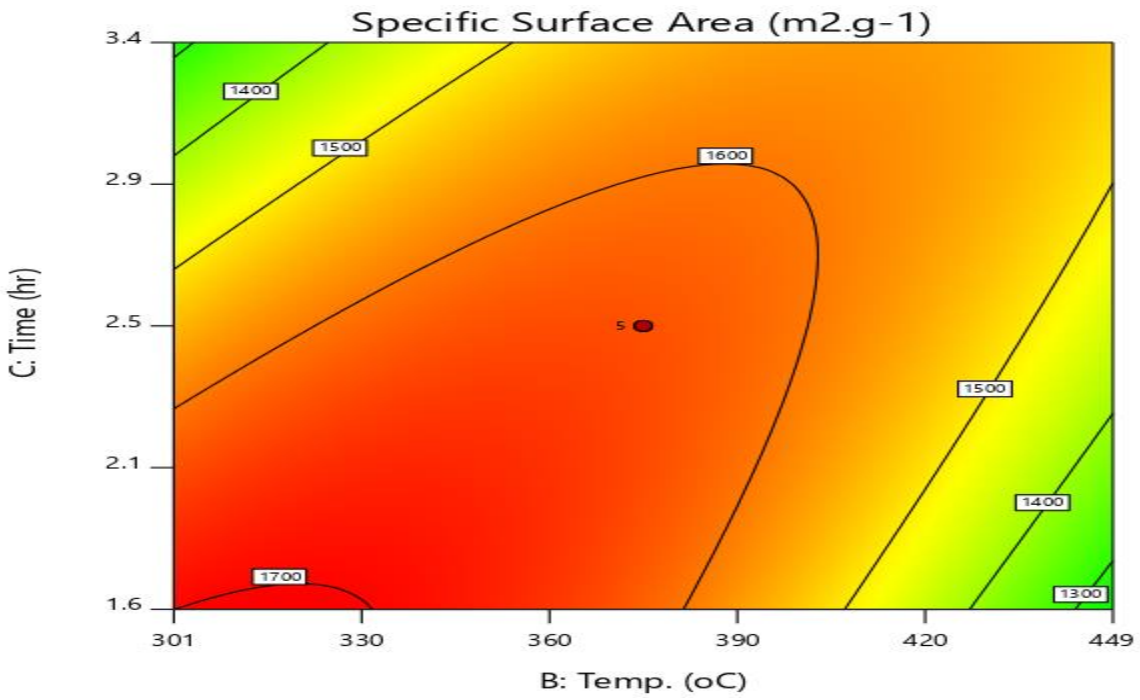

(ii)

Fig. 4.21C: Three - dimensional 3D (i) and Contour Plots (ii) of the Interaction of Pyrolysis Temperature and Pyrolysis Time on the Specific Surface Area of the Zn^{2+} - Doped Biochar

It can be seen, in Fig. 4.21A, that the combined effect of Zn^{2+} loading and heat treatment temperature resulted to a maximum BET surface area 1612.35 $m^2.g^{-1}$ for the Zn^{2+} - based magnetic carbon-rich material at a Zn^{2+} loading (3.38 wt%) and heat treatment temperature (402^o C) and beyond this a slight decrease in the BET surface area was observed. The maximum BET surface area of 1643.18 $m^2.g^{-1}$ was also recorded at Zn^{2+} loading and duration of heat treatment of 2.88 wt% and 2.70 hr respectively (Fig. 4.21B). In addition, approximately 1696.29 $m^2.g^{-1}$ of BET surface was obtained for the combined effect of heat treatment temperature of 304^o C and duration of heat treatment of 1.6hr (Fig. 4.21C).

Fig 4.22A – 4.22C showed the 3D surface response and contour plots showing the interactions of the process variables (A) increase in relative amount of Fe^{3+} in the Fe^{3+}/Zn^{2+} loading and pyrolysis temperature at a constant pyrolysis time of 2.5 hr, (B) increase in relative amount of Fe^{3+} in the Fe^{3+}/Zn^{2+} metal loading and pyrolysis time at a fixed pyrolysis temperature of 375^o C, and (C) increase in pyrolysis temperature and pyrolysis time at a fixed relative amount of Fe^{3+} in the Fe^{3+}/Zn^{2+} metal loading (50% of a total of 10 wt % biochar) on the specific surface area of the metal - doped biochar material.

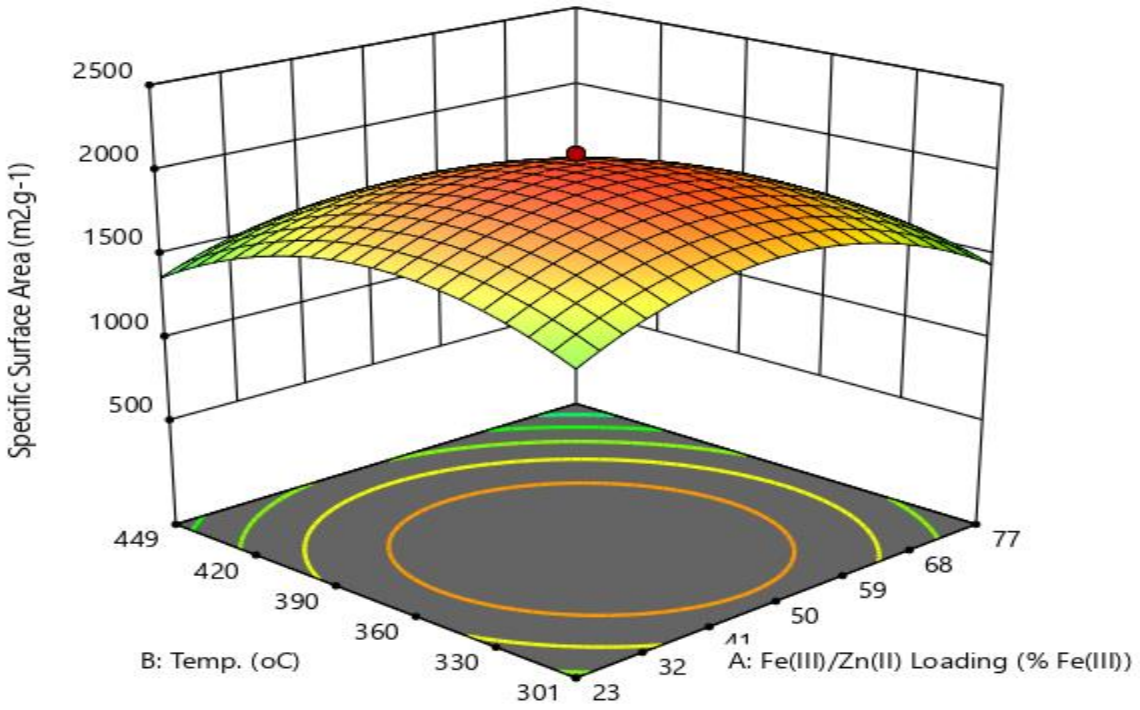

(i)

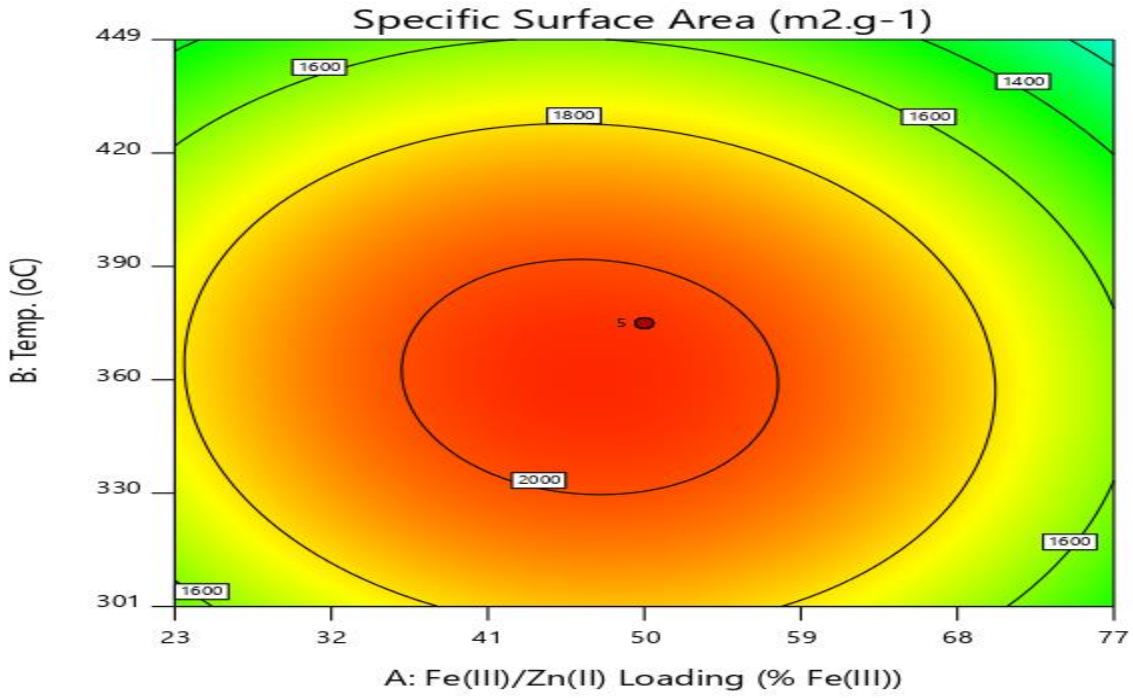

(ii)

Fig. 4.22A: Three - dimensional 3D (i) and Contour Plots (ii) of the Interaction of Fe^{3+}/Zn^{2+} - Loading and Pyrolysis Temperature on the Specific Surface Area of the Fe^{3+}/Zn^{2+} - Doped Biochar

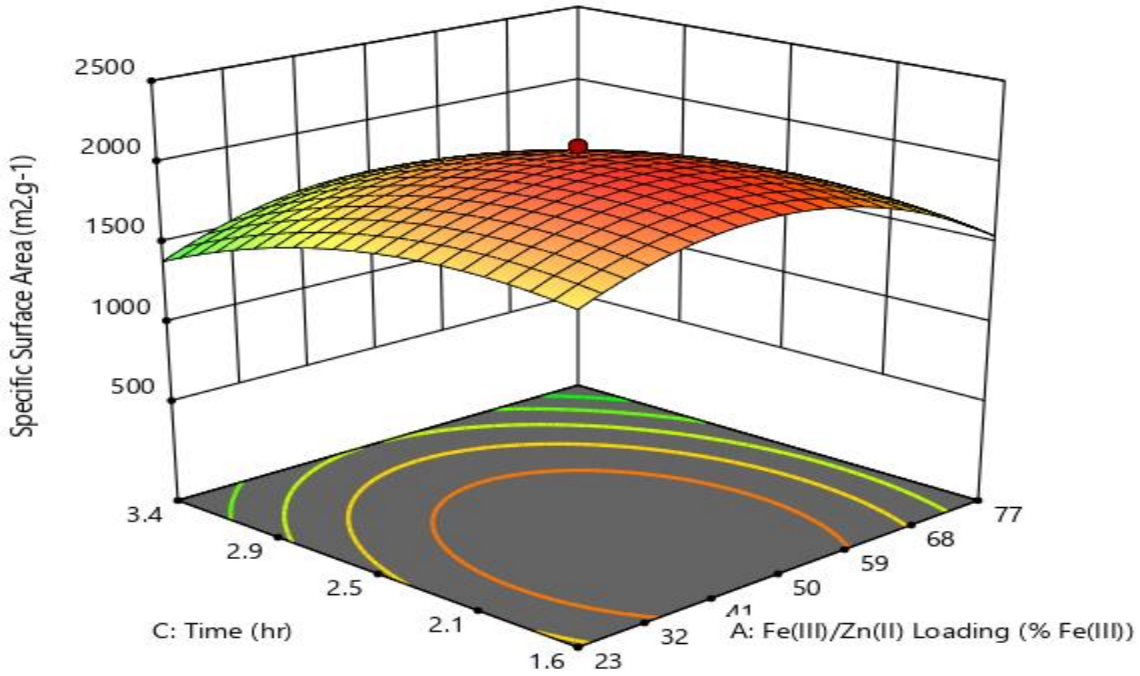

(i)

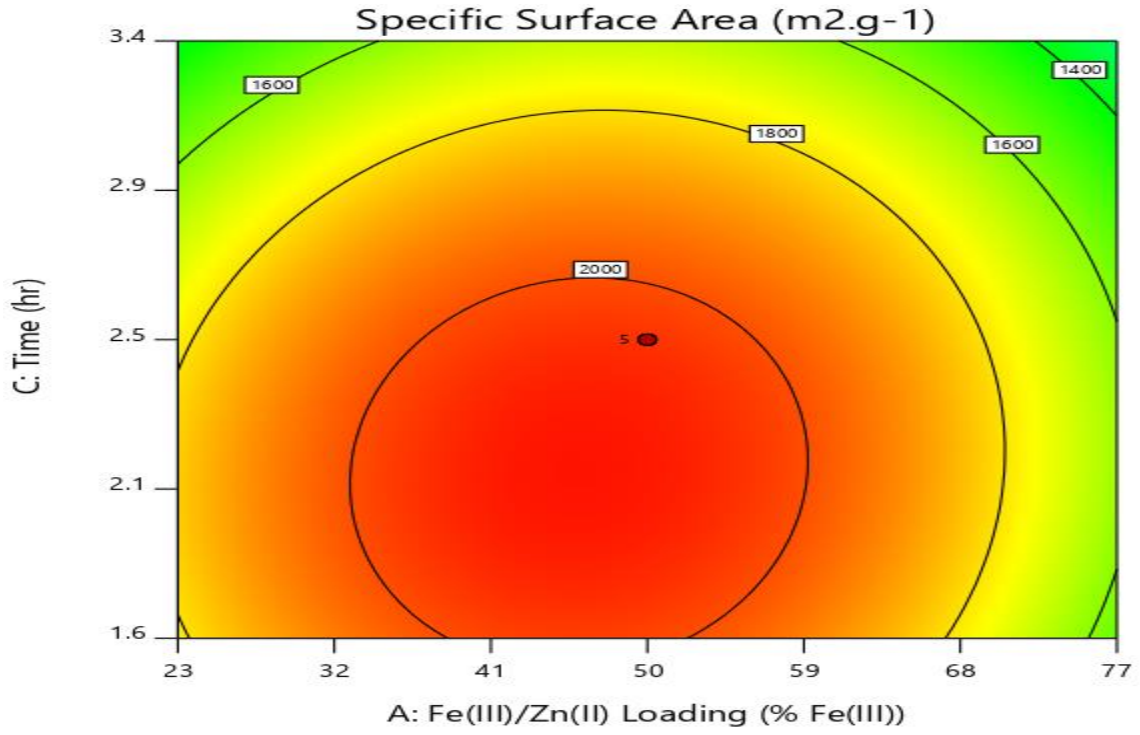

(ii)

Fig. 4.22B: Three - dimensional 3D (i) and Contour Plots (ii) of the Interaction of Fe^{3+}/Zn^{2+} - Loading and Pyrolysis Time on the Specific Surface Area of the Fe^{3+}/Zn^{2+} - Doped Biochar

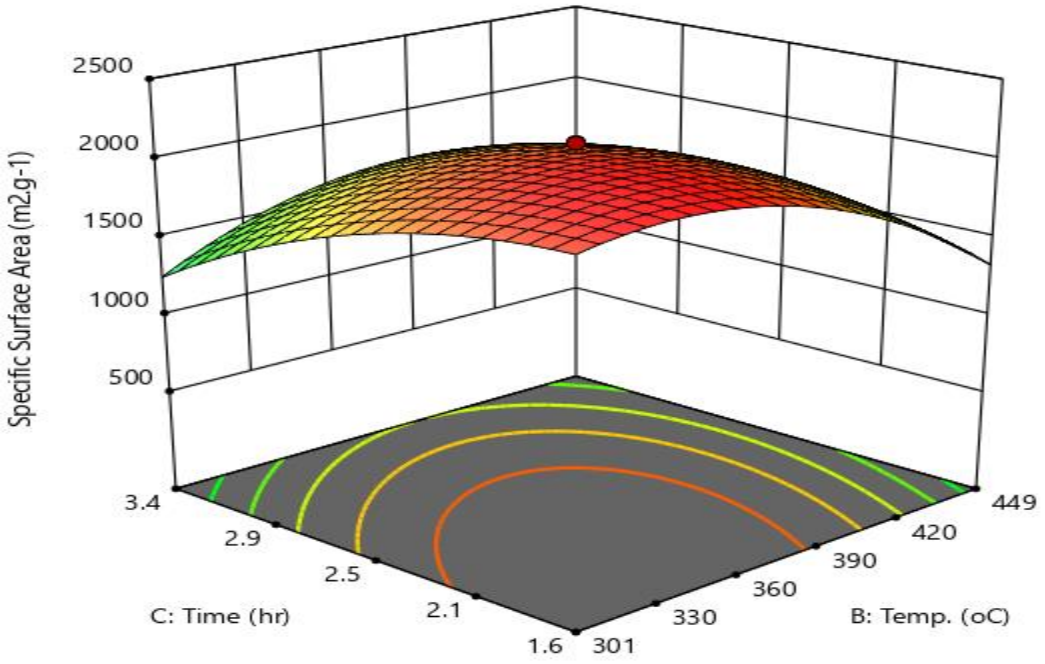

(i)

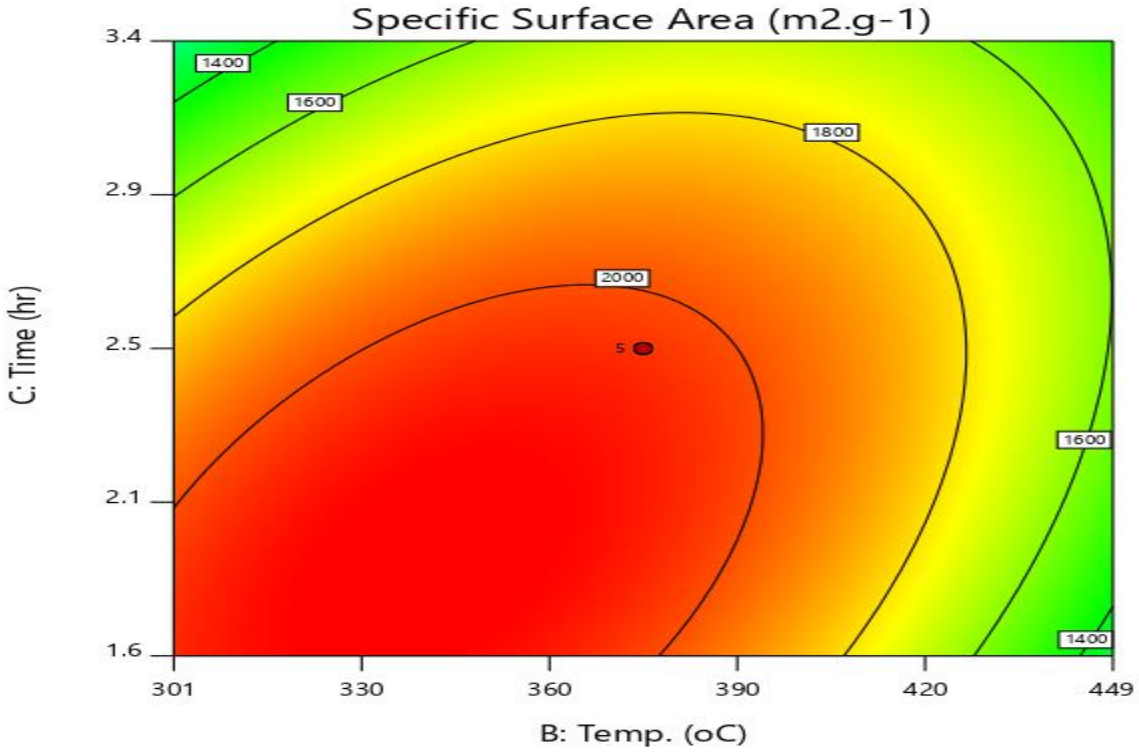

(ii)

Fig. 4.22C: Three - dimensional 3D (i) and Contour Plots (ii) of the Interaction of Pyrolysis Temperature and Pyrolysis Time on the Specific Surface Area of the Fe^{3+}/Zn^{2+} - Doped Biochar

The results from Fig. 4.22 (A – B) suggest that the initial increase in BET surface area of the magnetic biochar with combined increase in the process variables, tended to decrease with increase in the values of the process variables. Maximum BET surface areas of 2020.26, 2080.56, and 2126 $m^2\ g^{-1}$ were obtained for the combined effects of Fe^{3+}/Zn^{2+} loading (38% Fe^{3+}) and heat-treatment temperature (361 °C), Fe^{3+}/Zn^{2+} loading (47% Fe^{3+}) and heat-treatment duration (2.1 h), and heat-treatment temperature (340 °C) an d duration of heat treatment (1.9 h), respectively. Table 4.17 gives the design software predicted process variables for the optimized specific surface area of Fe^{3+}, Zn^{2+} and Fe^{3+}/Zn^{2+} - doped biochar materials.

4.10.2 Optimization of Process Parameters

Table 4.17: Optimization of Process Parameters for Single and Bimetallic-Doped Biochar

Metal System	Metal Loading	Temp. (°C)	Time (hr)	SSA ($m^2 \cdot g^{-1}$)	Desirability
Fe^{3+} loading (wt %)	3.01	327.87	1.63	2106.42	1.00
Zn^{2+} loading (wt %)	2.90	318.91	1.61	1709.55	1.00
Fe^{3+} / Zn^{2+} (% Fe^{3+}, 10 wt%)	46.73	336.86	1.88	2130.37	1.00

SSA – Specific Surface Area

The optimized conditions for the metal - doped biochars are presented in Table 4.17. The results show that under similar process conditions, the specific surface area of Fe^{3+} - doped biochar material has a 23% higher specific surface area than of Zn^{2+} - doped biochar; and that Fe^{3+}/Zn^{2+} - doped biochar material gave the highest optimum surface area of 2131.85 $m^2.g^{-1}$. The observed higher specific surface area of Fe^{3+} - based biochar in comparison with Zn^{2+} - rich biochar may be explain in terms of the difference between the ionic size

of Fe^{3+} (0.064nm) and that of Zn^{2+} ion (0.074nm) that would lead to Fe^{3+} producing smaller pore sizes in the biochar and hence to higher specific surface area (Oliveira *et al*., 2009).

4.10.3 Validation of the Model

Table 4.18 gives the textural properties of the magnetic carbon rich materials prepared using the optimum process condition of the model; in comparison with the model-derived data.

Table 4.18: Validation of Model Equation: Comparison of the Values of Surface Area Predicted from the Model Equation with Values from Samples Prepared using the Optimum Process Condition

Metal System	Specific surface area ($m^2.g^{-1}$)
Fe^{3+} - doped biochar	2098.04 (2106.42)
Zn^{2+} - doped biochar	1721.40 (1709.55)
Fe^{3+}/ Zn^{2+} - doped biochar	2124.48 (2130.31)

Values in parentheses are predicted from the model

It was observed from Table 4.18 that the values of specific surface area predicted by the model are in good agreement with the experimental. Such good agreement between the predicted and experimentally determined values of specific surface area sufficiently validates the model for projecting surface area in metal (Fe^{3+}, Zn^{2+} and Fe^{3+}/ Zn^{2+}) coconut shell based biochar materials.

4.11 PHYSICOCHEMICAL PROPERTIES OF THE METAL - DOPED COCONUT SHELL BIOCHAR MATERIALS.

Table 4.19: Physicochemical Properties of Metal - Doped Coconut Shell Biochars

Parameters	Metal - Doped Biochar		
	Fe^{3+}	Zn^{2+}	Fe^{3+} / Zn^{2+}
pH	5.43 ± 1.11	6.11 ± 0.83	5.18 ± 1.09
Electrical Conductivity (ms.cm^{-1})	37.34 ± 1.15	25.88 ± 1.22	56.60 ± 1.76
Bulk Density (g.cm^{-3})	0.94 ± 0.22	0.97 ± 0.11	0.98 ± 0.15
Cation Exchange Capacity (cmol.kg^{-1})	35.33 ± 0.84	21.81 ± 1.22	29.14 ± 1. 29

The physicochemical properties of the metal - doped biochar is presented in Table 4.19. It can be observed that the metal - doped biochar exhibited a slightly acidic pH, with Fe^{3+}/Zn^{2+}- based biochar showing the highest acidic pH. The lower pH values observed may be attributed to the hydrolysis of Fe^{3+} salts during co-pyrolysis, releasing more acidic functional groups onto the carbon surface (Zhang *et al*., 2021).

A clear variation was observed in EC values of the metal - doped biochar, with Fe^{3+}/Zn^{2+} - doped biochar showing the highest conductivity (56.60 ± 1.76 mS·cm^{-1}), followed by Fe – doped biochar (37.34 ± 1.15 mS·cm^{-1}) and Zn^{2+} – doped biochar (25.88 ± 1.22 mS·cm. The higher EC values observed in the metal-doped biochars relative to the untreated biochar can be attributed to the introduction of charged metal species (Fe^{3+} and Zn^{2+}) during the co-pyrolysis process.

The bulk densities of all metal - doped biochar samples were relatively similar, ranging from 0.94 to 0.98 g·cm^{-3} (Table 4.19), suggesting that metal doping did not cause significant structural collapse or compaction of the carbon matrix.

Fe^{3+}- doped biochar exhibited the highest CEC (35.33 ± 0.84 cmol·kg⁻¹), followed by Fe^{3+}/Zn^{2+} - doped biochar (29.14 ± 1.29 cmol·kg⁻¹), while Zn^{2+}- doped biochar had the lowest (21.81 ± 1.22 cmol·kg⁻¹). This value tend to be higher than those of the untreated biochar CSB450 (0.91 ± 0.18)(Table 4.1). This indicates that the metal (Fe and/or Zn) incorporation on biochar surface significantly enhances the amount of exchangeable cations, likely due to formation of active site metal–oxygen (M–O) functional moieties, thus facilitate cation retention (Li *et al.,* 2019).

4.12 SURFACE OXYGEN FUNCTIONAL GROUP

The functional groups on the metal - doped biochars surface were quantitatively analyzed by the Boehm titration method, and the results are summarized in Table 4.20.

Table 4.20: Surface Oxygen Functional Groups of Metal - Doped Biochars

Functional Groups	**MBC**		
	Fe^{3+}	**Zn^{2+}**	**Fe^{3+} / Zn^{2+}**
Phenolic (mmol.g^{-1})	0.79	0.40	0.48
Lactonic (mmol.g^{-1})	0.34	0.29	0.23
Carboxylic (mmol.g^{-1})	1.04	1.11	0.76
Total (mmol.g^{-1})	2.17	1.80	1.47

MBC - Metal - Doped Biochar Samples

The total surface oxygen functional groups for the metal - doped biochars (Fe^{3+}, Zn^{2+} and Fe^{3+}/Zn^{2+}) were observed to be lower (Table 4.20) than that of untreated biochar (CSB450) (Table 4.2), which had a value of 3.47 mmol·g⁻¹ . The total surface oxygen functional groups followed the order: Fe^{3+}- CSB > Zn^{2+}- CSB > Fe^{3+}/Zn^{2+}- CSB. This confirms that metal doping may result in the decomposition of surface groups during surface modification.

4.13 FUNCTIONAL GROUP

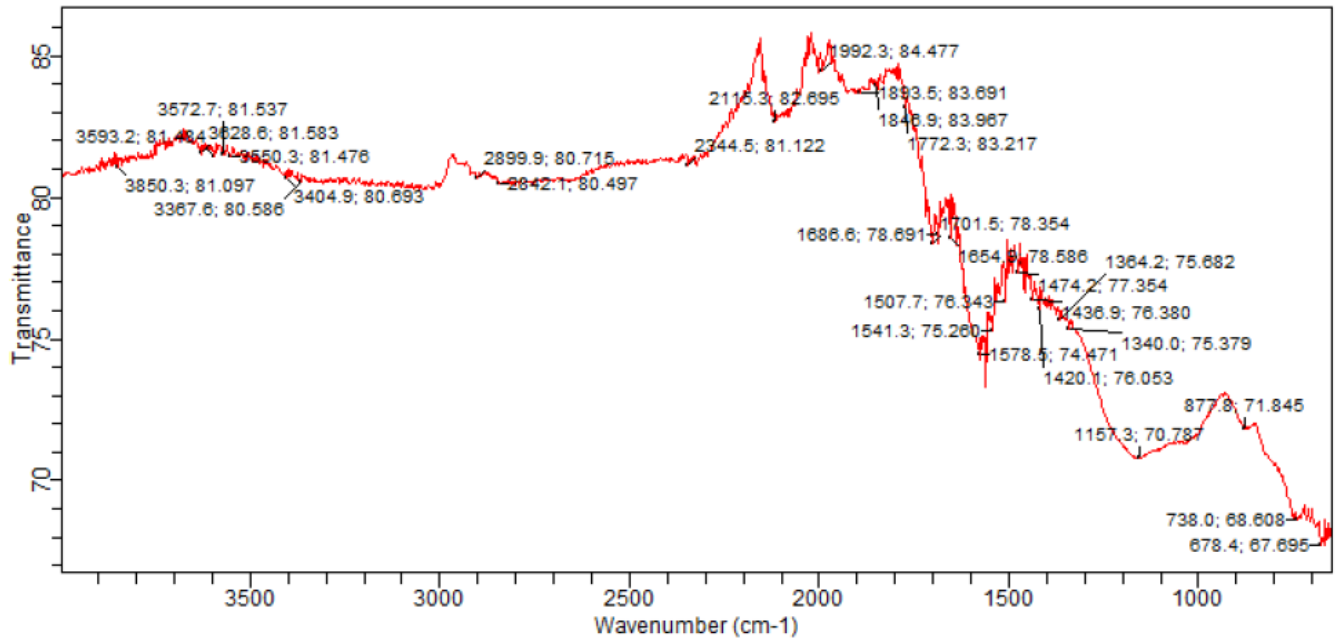

Fig. 4.23: FTIR of Fe^{3+} -Doped Biochar

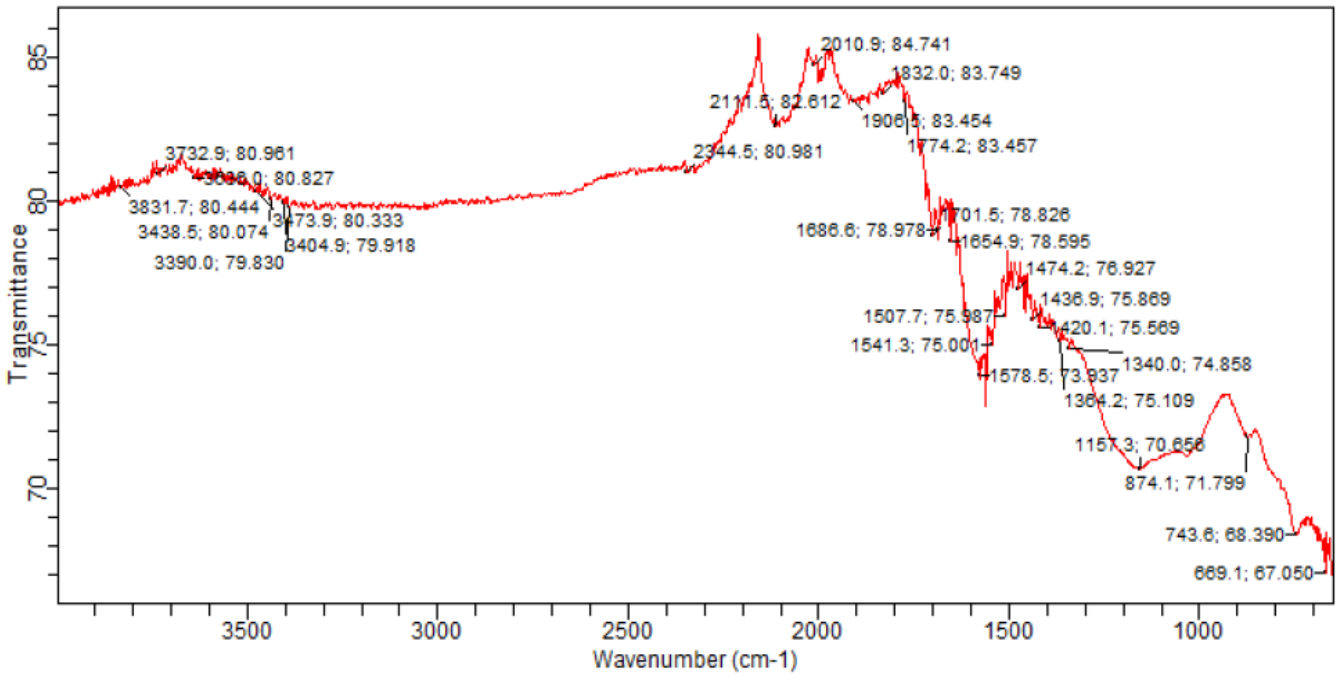

Fig. 4.24: FTIR of Zn^{2+} -Doped Biochar

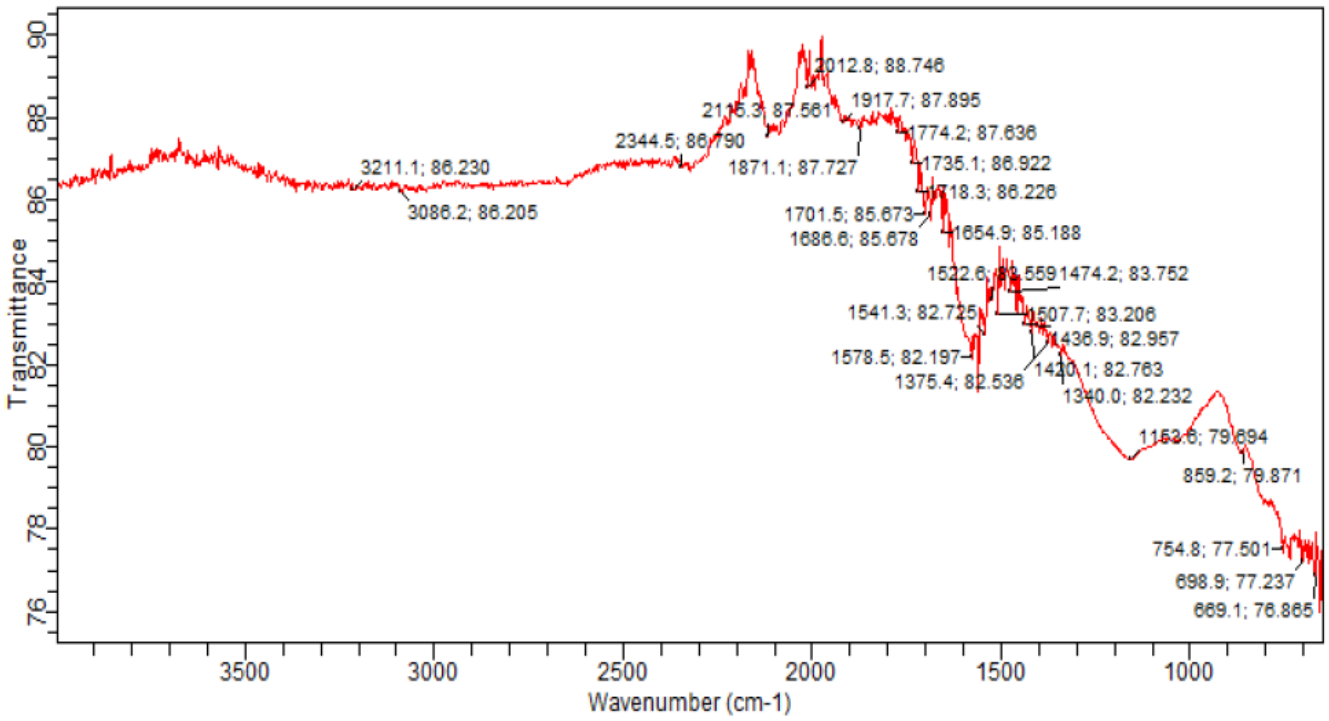

Fig. 4.25: FTIR of Fe^{3+}/Zn^{2+} -Doped Biochar

The functional groups present on the surface of the biochar after the metal incorporation were analysed using the FTIR and their spectra are presented in Fig. 4.23 – 4.25. From the figures, it can be seen that the band of interest appeared at the region of 600 – 800 cm^{-1} corresponding to the metal oxygen bond stretching vibrations (Fe-O, Zn-O and Zn-O-Fe) indicating that metals were successfully incorporated onto the biochars surface (Sybounya and Nitisoravut *et al.,* 2021).

4.14 SCANNING ELECTRON MICROSCOPY

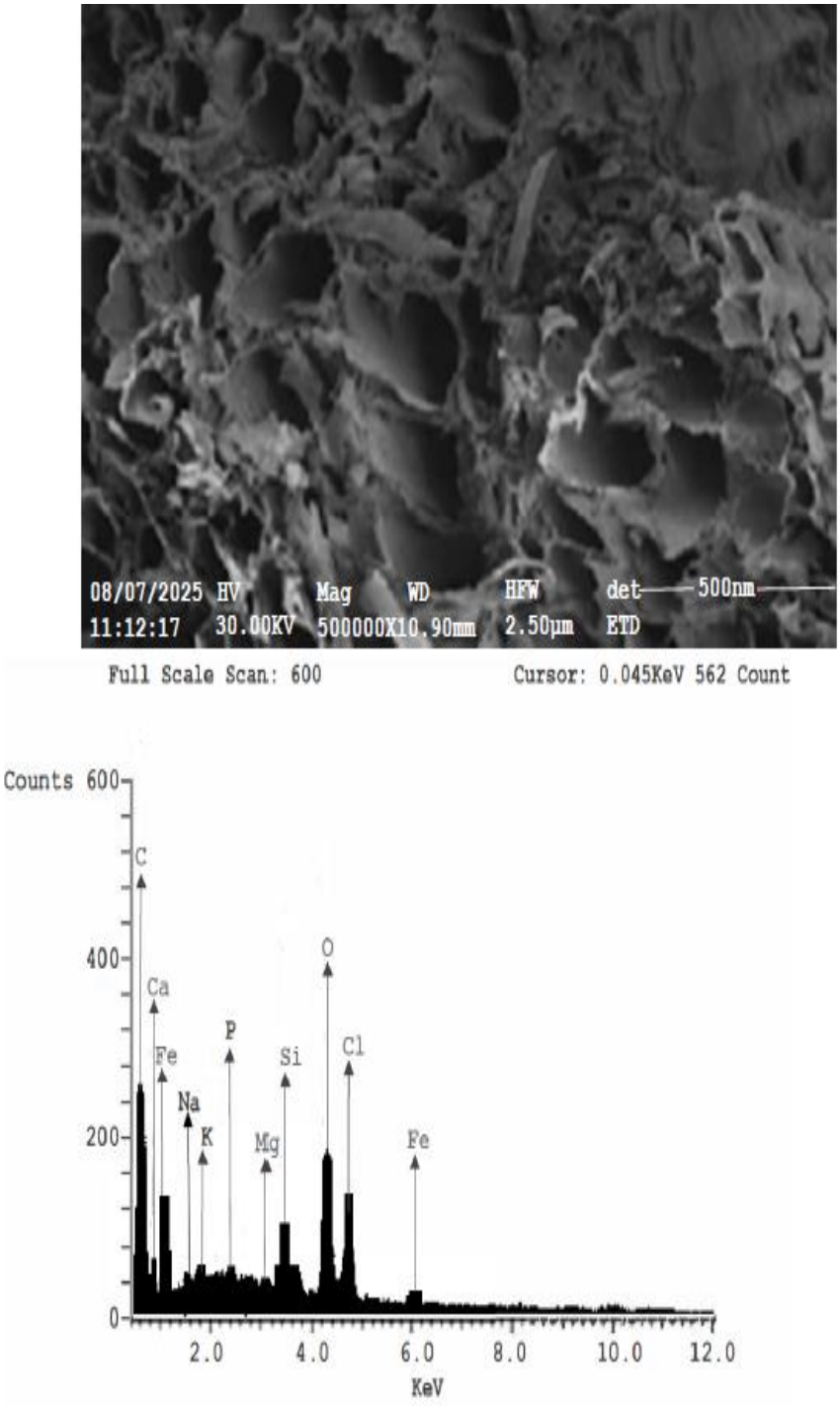

Elements	Composition (%)
C	58.11
O	13.61
Ca	1.36
Si	3.11
K	1.18
Na	1.15
Mg	1.23
P	0.52
Cl	9.63
Fe	10.09

Fig. 4.26: SEM/EDX of Fe^{3+}-Doped Biochar

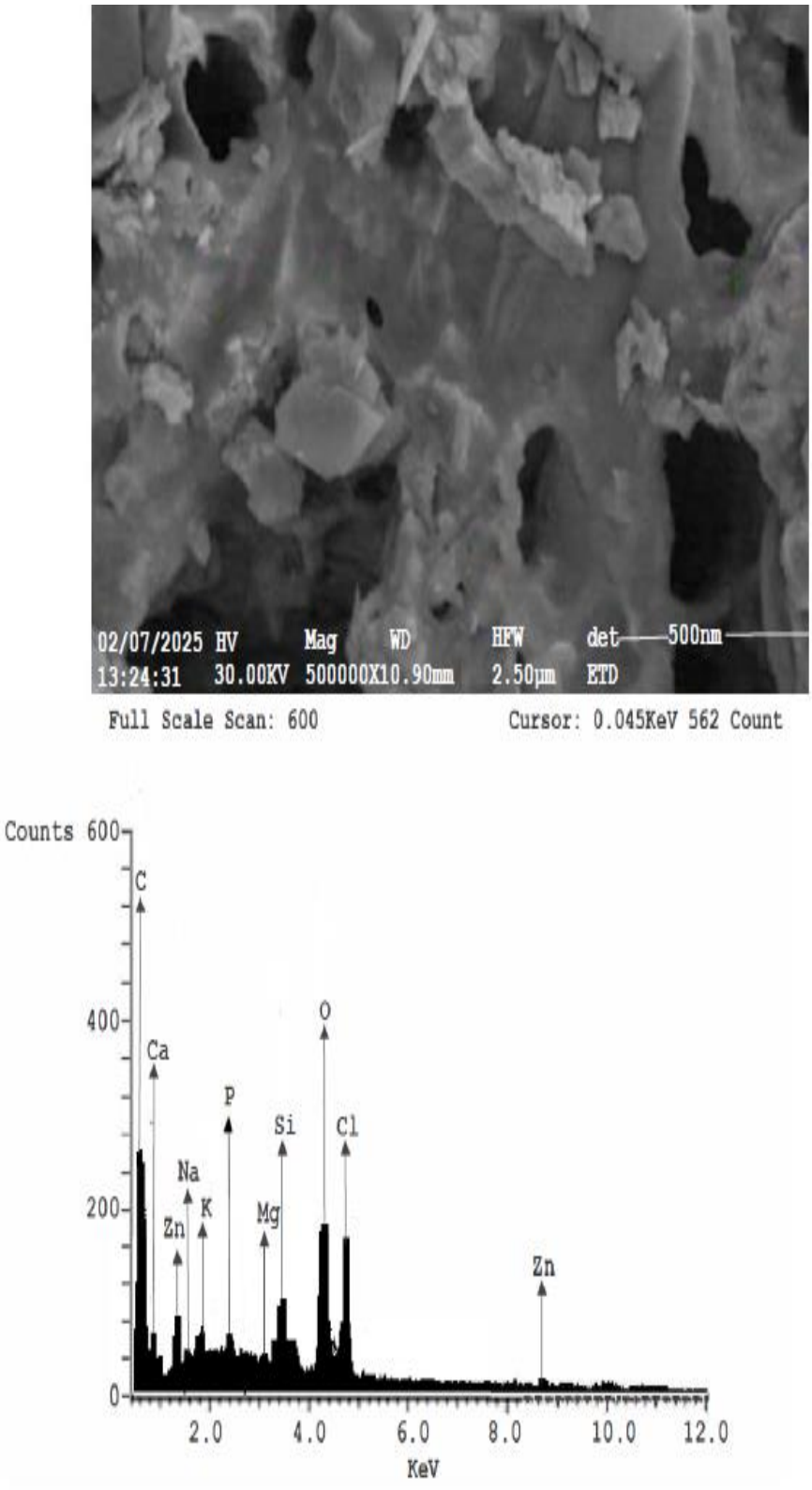

Elements	Composition (%)
C	60.09
O	14.05
Ca	1.63
Si	2.21
K	1.64
Na	1.07
Mg	1.27
P	0.64
Cl	12.22
Zn	5.17

Fig. 4.27: SEM/EDX of Zn^{2+}-Doped Biochar

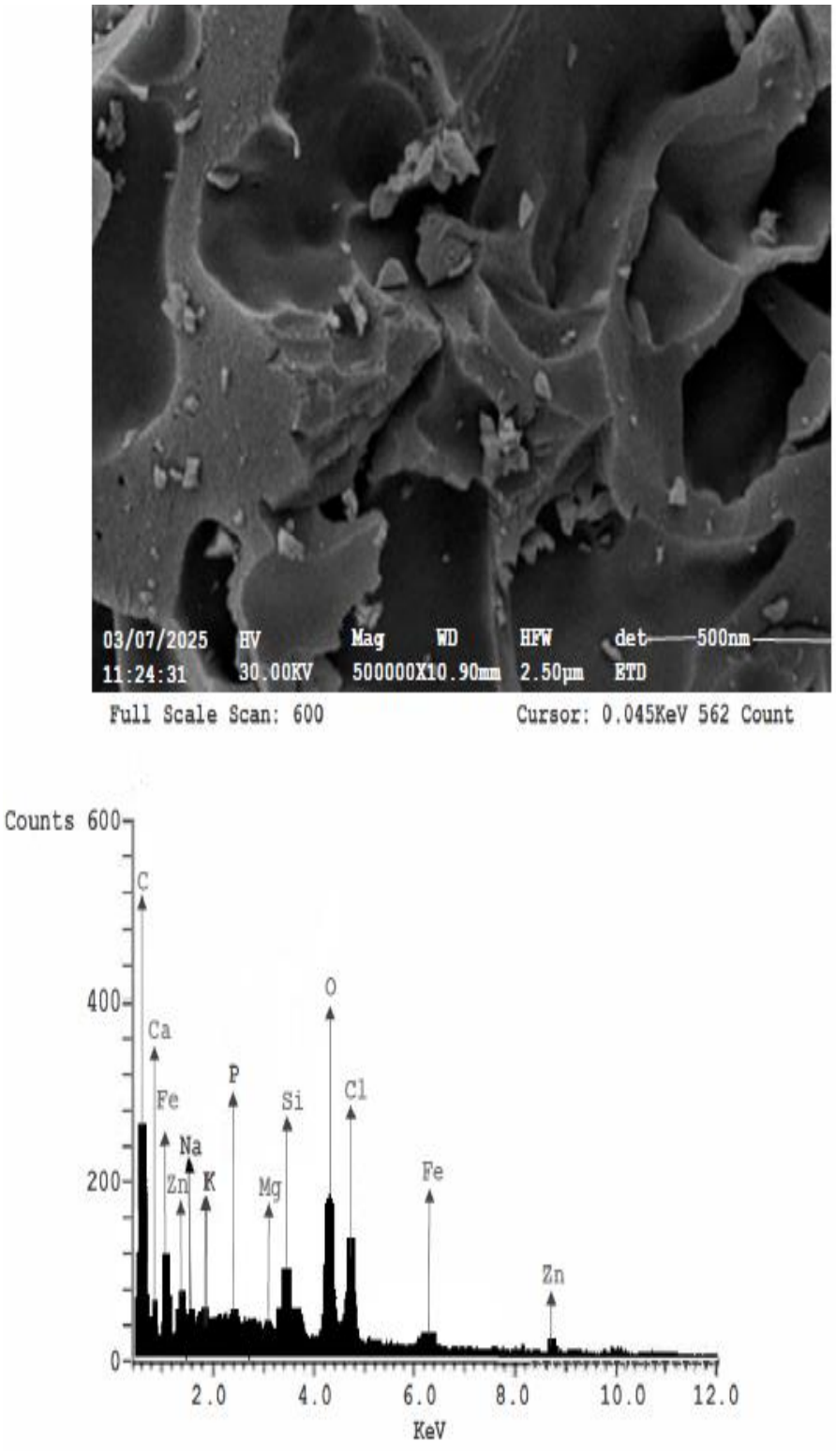

Elements	Composition (%)
C	50.32
O	11.94
Ca	1.44
Si	2.06
K	1.31
Na	1.11
Mg	1.17
P	0.45
Cl	14.25
Fe	9.44
Zn	6.51

Fig. 4.28: SEM/EDX of Fe^{3+}/Zn^{2+}- Doped Biochar

Morphological changes among the Fe^{3+}- doped coconut shell biochar (Fe-CSB), Zn^{2+} - doped coconut shell biochar (Zn-CSB) and Fe^{3+}/Zn^{2+} - doped coconut shell biochar (Fe/Zn-CSB) were investigated using the SEM images, and are presented in Fig. 4.26 – 4.28. The surface of the metal-doped coconut shell biochars (MCSB) after the co-pyrolysis process displayed numerous honeycomb-like cavities, and the inner surfaces showed a significant mesoporous structure. In addition, fine particles were observed to be evenly distributed across the surface of the MCSB. These particles were most likely iron oxides or zinc oxides generated during the co-pyrolysis process (Wang *et al*., 2017), indicating the successful preparation of the MCSB. The presence of these metal oxide particles may have contributed to the improvement of the textural properties of the biochars.

The surface elemental composition of Zn-CSB, Fe-CSB and Fe/Zn-CSB were further analyzed by energy dispersive x-ray (EDX). The EDX spectra and their corresponding elemental composition of the metal - doped biochars are provided in Fig. 4.26 – 4.28. The clear detection of Zn and Fe elements confirms the successful incorporation of these metals into the biochar matrix. In addition, the results also highlighted other elements including C and O which were predominantly present in the biochar samples while Cl, Si, Ca, K, Na, Mg were observed in trace amount.

4.15 TEXTURAL PROPERTIES

Table 4.21: Textural Properties of Metal - Doped Biochar Samples

Properties	**MBC**		
	Fe^{3+}	**Zn^{2+}**	**Fe^{3+} / Zn^{2+}**
S_{BET} ($m^2.g^{-1}$)	2098.04	1721.40	2124.48
Pore diameter (nm)	2.34	2.21	2.47
Pore volume ($cm^3.g^{-1}$)	0.91	0.72	0.77

MBC - Metal - Doped Biochar Samples
S_{BET} – Specific Surface Area

Table 4.21 summarizes the textural properties (BET surface area, pore diameter, and pore volume) of the different metal-doped biochars (MBCs). As shown in the result, the BET surface area was observed to be highest in the Fe^{3+}/Zn^{2+} co-doped biochar (2124.48 $m^2.g^{-1}$), followed closely by the Fe-doped sample (2098.04 $m^2.g^{-1}$). The Zn^{2+}-doped biochar (1721.40 $m^2.g^{-1}$) also showed a significantly high BET surface area. Importantly, all MBCs displayed markedly higher BET surface areas compared to the untreated biochar prepared at 450 °C (CSB450, 712.00 $m^2.g^{-1}$). This suggests that the presence of Fe^{3+}, particularly when combined with Zn^{2+}, is highly effective in creating additional surface sites and opening the biochar's pore structure.

In terms of pore diameter, CSB450 exhibited the smallest value (2.11 nm). Metal incorporation led to a slight increase in the pore diameter, with Fe^{3+}/Zn^{2+} co-doped biochar recording the highest value (2.47 nm). This moderate enlargement indicates that doping not only develops new micropores but also broadens existing pores into the mesopore range.

The pore volume followed a similar trend, increasing from 0.36 cm^3/g in CSB450 to 0.91, 0.72, and 0.77 cm^3/g for Fe^{3+}-, Zn^{2+}-, and Fe^{3+}/Zn^{2+} co-doped biochars, respectively. These enhancements highlight the role of metal salts in promoting pore development during pyrolysis, likely through chemical activation and modification of the carbon matrix structure.

4.16 CATALYTIC PERFORMANCE OF METAL-DOPED BIOCHAR IN FRIEDEL CRAFTS BENZYLATION REACTION

The metal-doped biochars were evaluated for their catalytic efficiency in the Friedel–Crafts benzylation reaction, using toluene (T) as the excess reactant and benzyl chloride (BC) as the limiting reactant. Reaction parameters such as mole ratio (toluene to benzyl chloride), reaction temperature, and reaction time were systematically varied to determine their effects on benzyl chloride conversion and overall catalytic performance.

4.16.1 Effect of Mole Ratio of Reactants

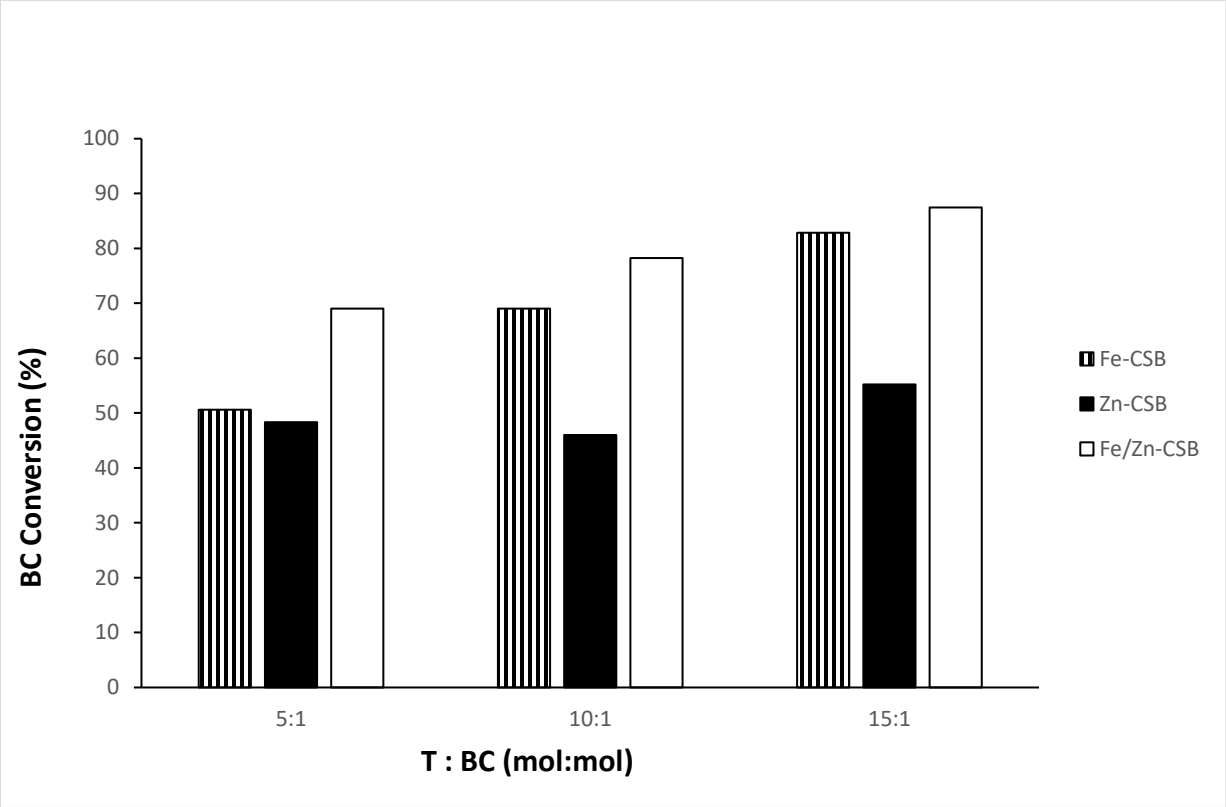

Fig. 4.29: Effect of Mole Ratio of T:BC on Benzylation of Toluene over Metal - Doped Catalyst (Catalyst Loading 8.2 wt% BC, Temperature 70ºC, Time, 180 min)

Fig. 4.29 shows the variation of benzyl chloride conversion at various benzyl chloride to toluene ratios at a fixed catalyst dose and reaction temperature of 8.2 wt% BC and 70^{o} C, respectively. The conversion of benzyl chloride increased with increase T:BC mole ratio for all catalysts, indicating the availability of aromatic sites for electrophilic substitution. The reaction conditions also prevented the reactant and products from being strongly adsorbed on the surface of the catalyst (Nandiwale *et al*., 2015). Enhanced Fe^{3+} -doped biochar showed conversion from 50.63% to 82.85%, Zn^{2+} -doped biochar demonstrated weak activity with values of 48.33–55.24% possibly due to lower Lewis acidity, hence fewer active sites on the Zn^{2+} -doped biochar surface (Liu *et al.,* 2015). The Fe/Zn co-

doped biochar exhibited the highest activity, with conversion improving from 69.04% to 87.46%, and this is attributed to the synergistic interaction between Fe^{3+} and Zn^{2+}, which enhanced active site distribution and electron transfer.

4.16.2 Effect of Temperature

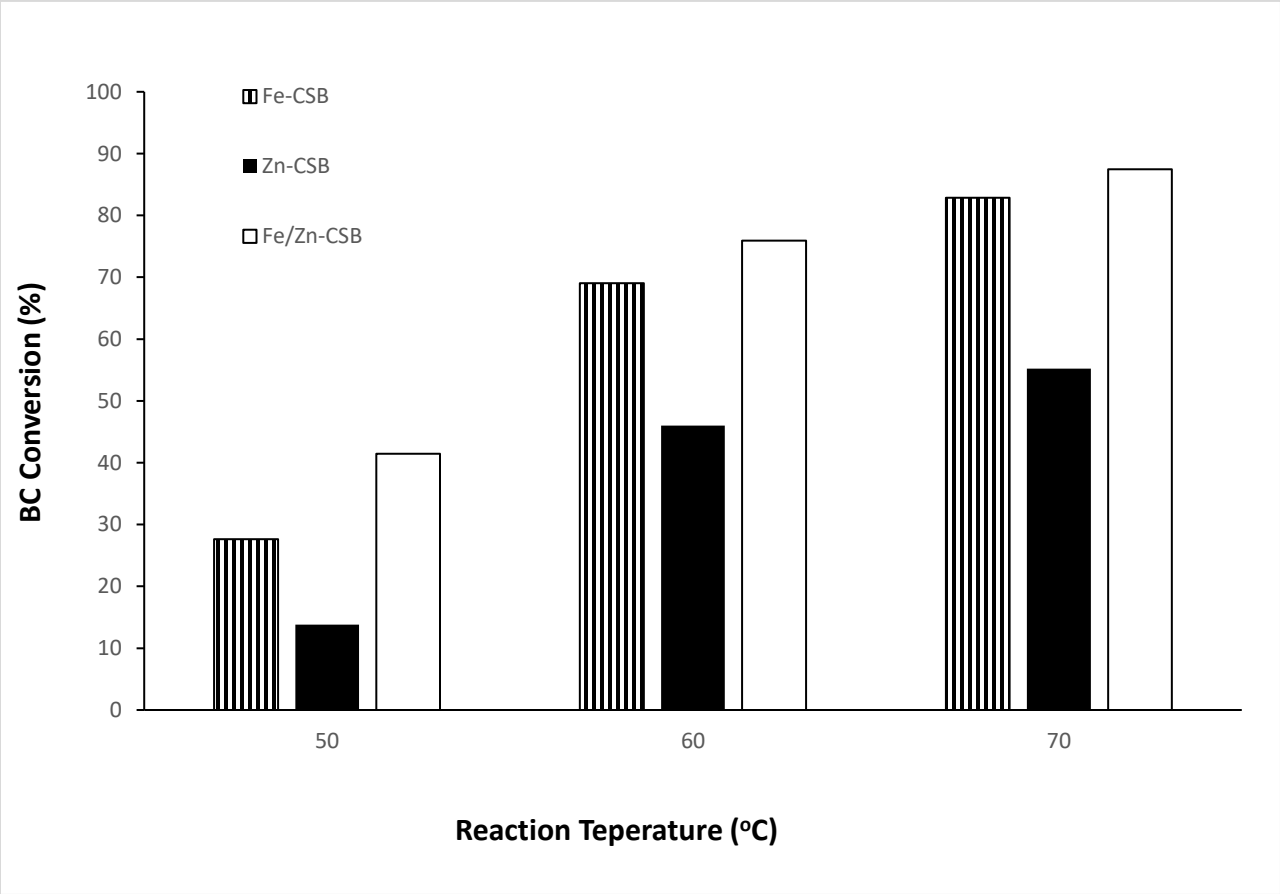

Fig. 4.30: Effect of Reaction Temperature on Benzylation of Toluene over Metal - Doped Catalyst (catalyst loading 8.2 wt% CSB, mole ratio T:BC, 15:1, Time, 180 min)

The effect of temperature on the conversion of benzyl chloride over the metal-doped biochar catalyst was studied at 50, 60 and 70° C as shown in Fig. 4.30. The catalyst loading was kept constant at 8.2 wt% benzyl chloride (BC) and mole ratio benzyl chloride to toluene (T:BC) of 15:1. It was observed that at lower temperatures (50 °C), the catalytic

activity was relatively low, suggesting insufficient thermal energy for effective activation of the reactants and catalytic sites (Yang *et al.,* 2023). As the temperature increased to 70 °C, a marked increase in conversion was observed, particularly for the Fe/Zn-doped biochar, which exhibited the highest BC conversion of 87.46% which may be linked to the cooperative interaction between Fe^{3+} and Zn^{2+} ions on the surface of the catalyst material (Nabi *et al.,* 2025).

4.16.3 Effect of Catalyst Loading

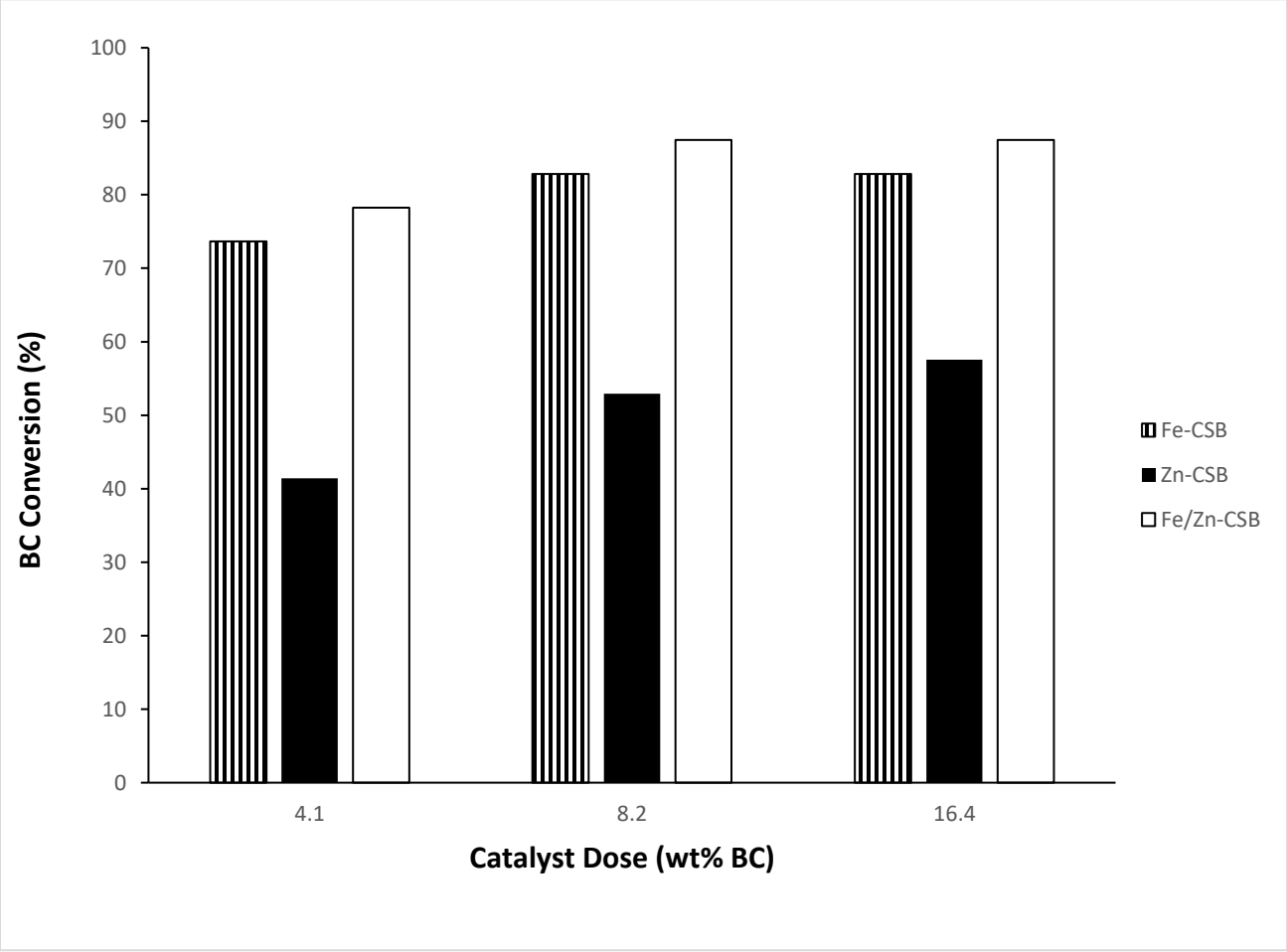

Fig. 4.31: Effect of Catalyst Dose on Benzylation of Toluene over Metal - Doped Catalyst (Mole Ratio, T:BC, 10:1, Reaction Temperature, 70° C, Time, 180 min)

The effect of catalyst dose on the conversion of benzyl chloride (BC) using metal-doped biochars is presented in Fig. 4.31. The reaction temperature was kept constant at 70° C and a mole ratio toluene to benzyl chloride (T:BC) of 10:1. An increase in catalyst loading from 4.1 wt% to 8.2 wt% led to a noticeable improvement in BC conversion in all the catalysts; beyond 8.2 wt%, no significant increase in conversion was observed, suggesting the reaction proceeds through heterogeneous mechanism (Kakasaheb *et al*., 2015). Among the catalysts, the Fe^{3+}/Zn^{2+} - doped biochar consistently showed the highest BC conversion (78.35% at 4.1 wt % to 87.46% at 16.4 wt % of benzyl chloride).

4.17 Kinetic Study

The kinetic data of the Friedel Crafts benzylation of toluene (in excess) (see appendix) and benzyl chloride (limiting) (stoichiometric ratio T:BC = 15:1) over the metal-doped biochar was fitted into a pseudo-first-order rate law:

$$log\frac{1}{1-x} = \frac{kt}{2.303(t-to)} \qquad (4.7)$$

Where kt is the pseudo-first-order rate constant, x is the conversion of benzyl chloride, t is the reaction time and t_o is the induction period. A plot of log $(\frac{1}{1-x})$ versus time gives a linear plot from which the values of the rate constant at the various reaction temperature (Table 4.22) were obtained.

Table 4.22: Variation of First-Order Rate Constant and Half-Life with Reaction Temperature for Metal-Doped Biochar Catalysts

Reaction temperature (°C)	First order rate constant (min^{-1} x 10^3)			Half life $t_{\frac{1}{2}}$ (min)		
	Fe^{3+} - doped biochar	Zn^{2+} - doped biochar	Fe^{3+}/Zn^{2+} -doped biochar	Fe^{3+} - doped biochar	Zn^{2+} - doped biochar	Fe^{3+}/Zn^{2+} -doped biochar
50	6.45	2.99	9.00	107.4	231.4	77.0
60	10.59	4.83	12.43	65.4	143.3	55.70
70	16.12	9.67	21.41	43.0	71.6	32.35

These values are comparable with the value of 29.1 x 10^{-3} min^{-1} reported for benzylation of benzene over iron mesoporous molecular sieves (Bachari *et al*., 2004) and 33.40 min^{-1} reported for nickel containing mesoporous silica (Laribi *et al*., 2012).

The results in Table 4.22 indicate that the rate of benzyl chloride conversion by the metal-doped biochars catalysts increased markedly with increase in the temperature of reaction and was an order of magnitude higher for Fe^{3+}/Zn^{2+} - doped biochar 9.00 x 10^{-3} – 21.41 x 10^{-3} min^{-1} than for Fe^{3+}- doped biochar 6.45 x 10^{-3} - 16.12 x10^{-3} min^{-1} than for Zn^{2+}- doped biochar 2.99 x 10^{-3} – 9.67 x 10^{-3} min^{-1} respectively. The values obtained are lower than the benzene benzylation rates reported by Bachari *et al.* (2004) for iron mesoporous molecular sieve catalysts, which ranged from 121 to 318 × 10^{-4} at 373–383 K. The kinetics of the benzylation reaction over the mesoporous metal-doped carbon-rich materials may be controlled either by reaction occurring on the surface of the catalyst material (surface reaction) or by intra-particulate diffusion of reactants.

The decrease in the estimated half-life of the metal- doped biochar mediated Friedel Crafts benzylation reaction of 77.0 – 32.35 min for Fe^{3+}/Zn^{2+} - doped biochar, 107.4 - 43.0 min for Fe^{3+}- doped biochar and 231.4 – 71.6 min for Zn^{2+}- doped biochar are consistent with

the observed increase in the rate of toluene benzylation over the metal-doped coconut shell biochar samples.

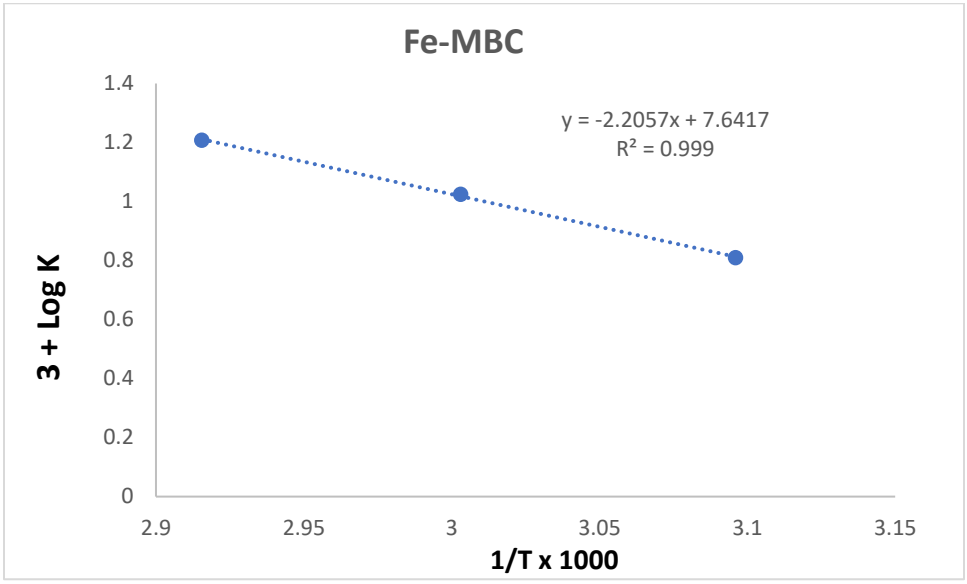

(a)

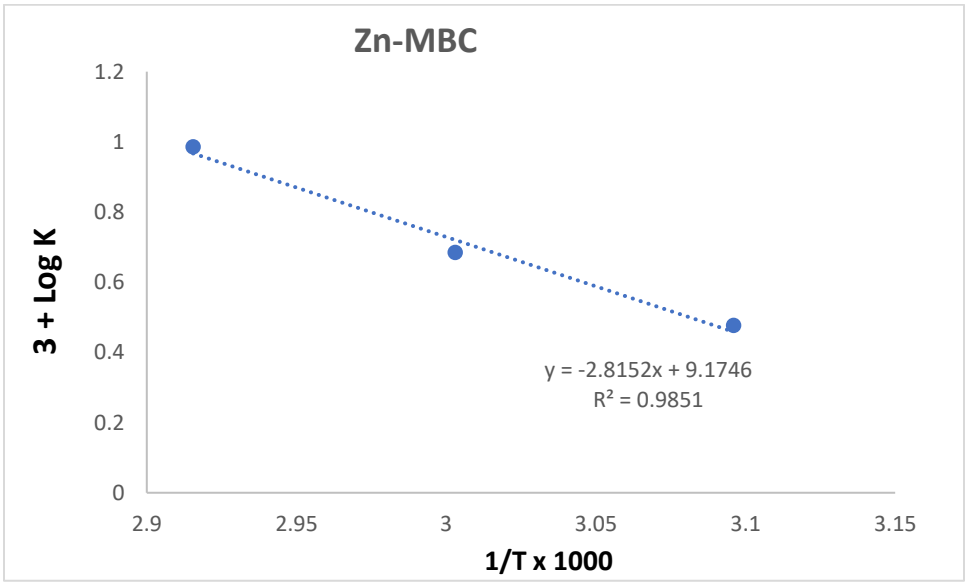

(b)

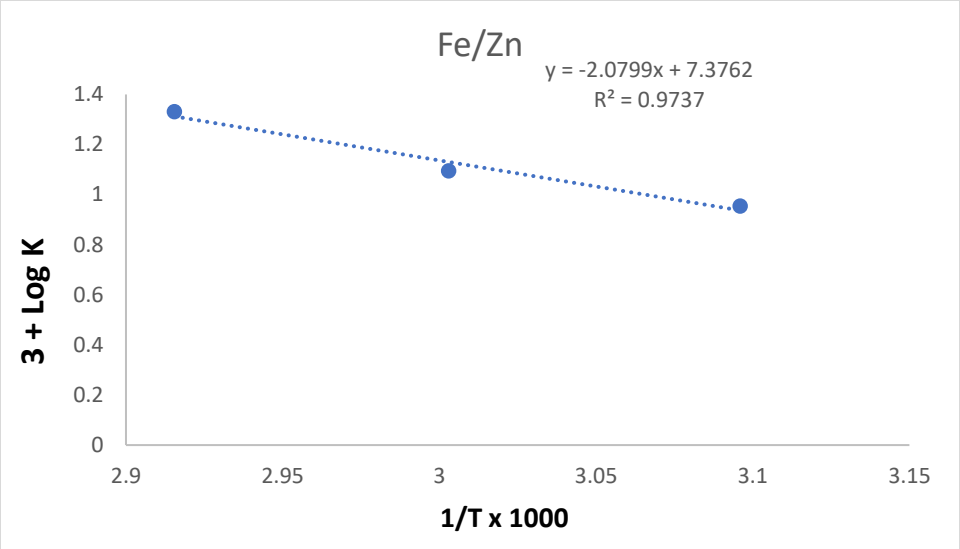

(c)

Fig. 4.32: Arrhenius plot of the Friedel Crafts benzylation reaction on (a) Fe^{3+}- doped biochar, (b) Zn^{2+}- doped biochar and (c) Fe^{3+}/Zn^{2+} - doped biochar

The variation in the observed rate of toluene benzylation with temperature of reaction was fitted using an Arrhenius plot (Fig. 4.32), from which values of activation energy for toluene benzylation of 42.23 $kcalmol^{-1}$, 53.90 $kcalmol^{-1}$ and 38.82 $kcalmol^{-1}$ were obtained for the Fe^{3+}- doped, Zn^{2+}- doped, and Fe^{3+}/Zn^{2+} -doped coconut shell biochar respectively. The values are higher than the values of activation energy (about 20 $kcalmol^{-1}$) reported by Koyande *et al.* (1998) for benzene benzylation over sulfate-treated metal oxide; however, it remains lower than the value 97 kcal mol^{-1} reported by Bachari *et al.* (2004) for iron mesoporous molecular sieve catalysts.

Notably, reactions on heterogeneous solid acid catalysts (metal-doped biochars) have been assumed by Ghodke *et al*. (2015) and Iqbal *et al*. (2020) to follow a similar mechanism to that of homogeneous Lewis acid-catalyzed systems. Typically, the benzylation reaction proceeds via electrophilic aromatic substitution. It is initiated when benzyl chloride interacts with the metal-doped biochar surface to form a charged complex. The interaction between the metal center and the chlorine atom of benzyl chloride is believed to be weak,

thereby weakening the C–Cl bond and promoting the generation of the benzyl carbocation intermediate. This positively charged species then reacts with toluene, a weak nucleophile, to form benzylated toluene and hydrochloric acid (HCl) as a by-product. Based on this mechanism, the benzylation of toluene using metal-doped biochar catalysts in this study is proposed as shown in Schemes 4.1.

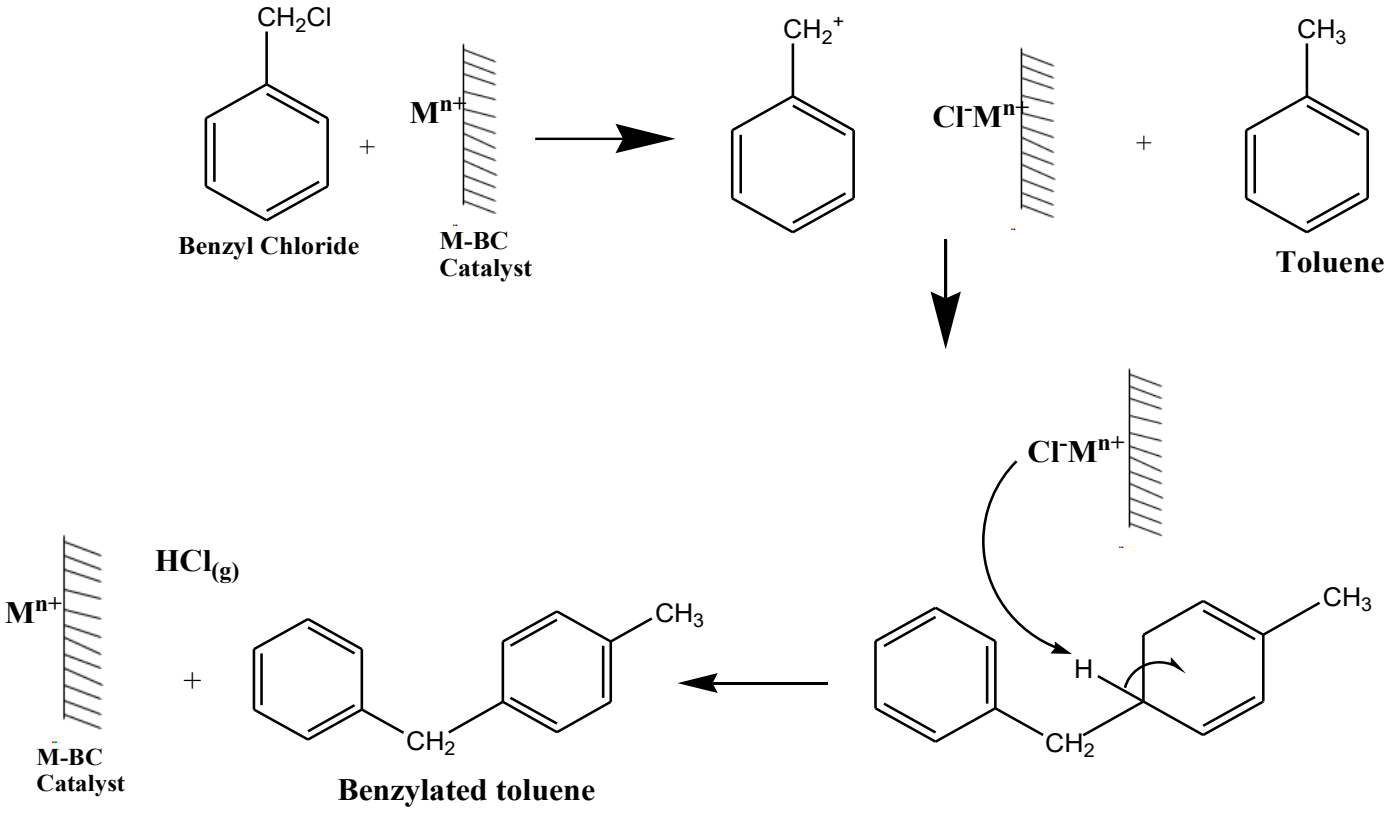

Scheme 4.1: Reaction Mechanism of the Benzylation of Toluene using Metal - Doped Biochar as Catalyst

According to Dung *et al*. (2017), the whole benzylation process consists of five steps, schematically illustrated in Fig. 4.33: (i) diffusion of reactant A (benzyl chloride) from the bulk solution to the catalyst external surface, (ii) diffusion of reactant A from the catalyst external surface to its internal reactional surface, (iii) chemical reaction between reactants A and B (toluene) on the catalyst internal surface to produce product (P) (mainly including monobenzyl toluene and dibenzyl toluene), (iv) desorption of P from the catalyst internal

surface, (v) diffusion of P away from the surface to the bulk solution. The first step, which is generally considered as the external diffusion, can be characterized by the mass transfer coefficient (k_1). The second step is considered as the internal diffusion and it can be determined by the adsorption equilibrium constant (k_2). The third step reflects the surface reaction which is controlled by the reaction rate constant. The fourth and fifth steps have negligible effects on the reaction process. Thus, the steps (i), (ii) and (iii) are systematically investigated to find out the controlling step of this catalytic reaction process.

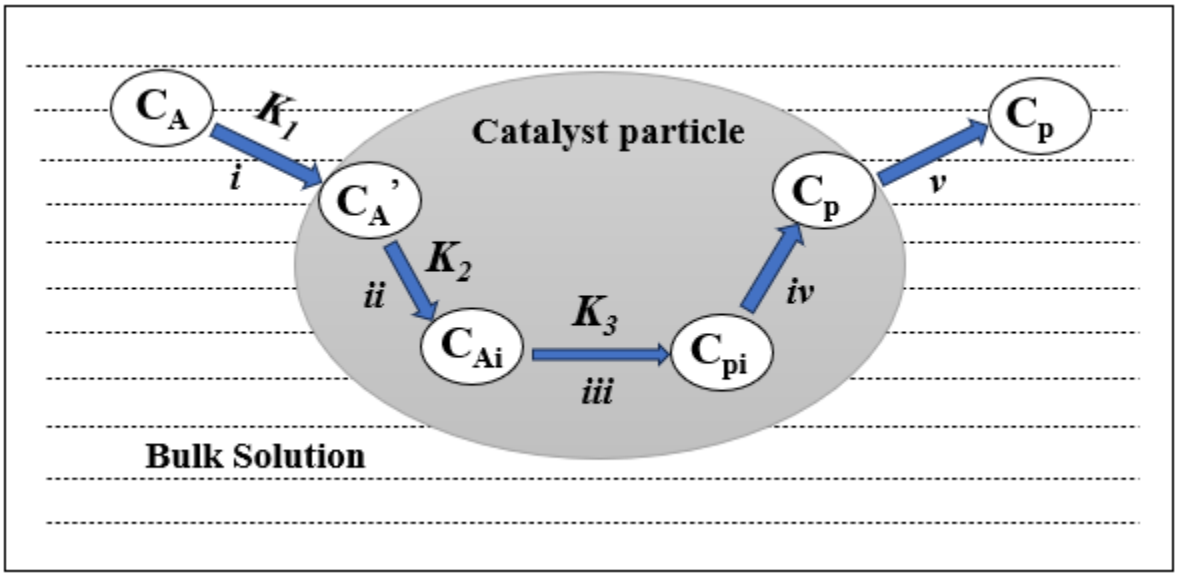

Figure 4.33: Schematic Diagram of Main Steps of Reaction in Heterogeneous Catalyst

4.18 OPTIMIZATION OF PROCESS PARAMETERS FOR FRIEDEL CRAFTS BENZYLATION REACTION

The reaction between benzyl chloride (BC)(limiting), and toluene (in excess) in the presence of the metal - doped biochar as catalyst was further optimized using the Center Composite Design (CCD) of the Response Surface Methodology (RSM). The results of the experimental runs are given in Table 4.23 – 4.25.

Table 4.23: Experimental Runs for Friedel–Crafts Benzylation Reaction over Fe^{3+}-Doped Biochar

S/N	Mole Ratio of T:BC (mol/mol)	Temperature (^{o} C)	Time (min)	BC Conversion (%)	
				Actual	Predicted
1	8.0/1.0	60.1	60.4	55	52
2	17.0/1.0	60.1	60.4	60	59
3	8.0/1.0	74.9	60.4	61	60
4	17.0/1.0	74.9	60.4	70	71
5	8.0/1.0	60.1	149.6	74	71
6	17.0/1.0	60.1	149.6	76	76
7	8.0/1.0	74.9	149.6	76	76
8	17.0/1.0	74.9	149.6	83	84
9	5.0/1.0	67.5	105.0	64	68
10	20.0/1.0	67.5	105.0	82	81
11	12.5/1.0	55.0	105.0	62	66
12	12.5/1.0	80.0	105.0	81	80
13	12.5/1.0	67.5	30.0	43	45
14	12.5/1.0	67.5	180.0	72	72
15	12.5/1.0	67.5	105.0	69	69
16	12.5/1.0	67.5	105.0	67	69
17	12.5/1.0	67.5	105.0	72	69
18	12.5/1.0	67.5	105.0	69	69
19	12.5/1.0	67.5	105.0	71	69
20	12.5/1.0	67.5	105.0	68	69

BC – Benzyl Chloride
T – Toluene

Table 4.24: Experimental Runs for Friedel–Crafts Benzylation Reaction over Zn^{2+}-Doped Biochar

S/N	Mole Ratio of T:BC (mol/mol)	Temperature (^{o} C)	Time (min)	BC Conversion (%)	
				Actual	Predicted
1	8.0/1.0	60.1	60.4	47	43
2	17.0/1.0	60.1	60.4	52	52
3	8.0/1.0	74.9	60.4	53	52
4	17.0/1.0	74.9	60.4	62	63
5	8.0/1.0	60.1	149.6	66	64
6	17.0/1.0	60.1	149.6	68	68
7	8.0/1.0	74.9	149.6	68	67
8	17.0/1.0	74.9	149.6	72	74
9	5.0/1.0	67.5	105.0	56	60
10	20.0/1.0	67.5	105.0	76	74
11	12.5/1.0	55.0	105.0	56	59
12	12.5/1.0	80.0	105.0	73	72
13	12.5/1.0	67.5	30.0	35	37
14	12.5/1.0	67.5	180.0	64	64
15	12.5/1.0	67.5	105.0	70	71
16	12.5/1.0	67.5	105.0	69	71
17	12.5/1.0	67.5	105.0	65	71
18	12.5/1.0	67.5	105.0	74	71
19	12.5/1.0	67.5	105.0	75	71
20	12.5/1.0	67.5	105.0	72	71

BC – Benzyl Chloride
T – Toluene

Table 4.25: Experimental Runs for Friedel–Crafts Benzylation Reaction over Fe^{3+} / Zn^{2+} - Doped Biochar

S/N	Mole Ratio of T:BC (mol/mol)	Temperature (^{o} C)	Time (min)	BC Conversion (%)	
				Actual	Predicted
1	8.0/1.0	60.1	60.4	56	54
2	17.0/1.0	60.1	60.4	72	68
3	8.0/1.0	74.9	60.4	75	72
4	17.0/1.0	74.9	60.4	78	78
5	8.0/1.0	60.1	149.6	67	65
6	17.0/1.0	60.1	149.6	85	86
7	8.0/1.0	74.9	149.6	74	76
8	17.0/1.0	74.9	149.6	88	89
9	5.0/1.0	67.5	105.0	65	67
10	20.0/1.0	67.5	105.0	90	90
11	12.5/1.0	55.0	105.0	67	70
12	12.5/1.0	80.0	105.0	89	88
13	12.5/1.0	67.5	30.0	52	56
14	12.5/1.0	67.5	180.0	77	75
15	12.5/1.0	67.5	105.0	85	85
16	12.5/1.0	67.5	105.0	84	85
17	12.5/1.0	67.5	105.0	86	85
18	12.5/1.0	67.5	105.0	87	85
19	12.5/1.0	67.5	105.0	89	85
20	12.5/1.0	67.5	105.0	82	85

BC – Benzyl Chloride
T – Toluene

The results indicate that maximum conversion of benzyl chloride for Fe^{3+}-doped biochar, was 83% at a mole ratio (T:BC) of 17:1, temperature 74.9° C and reaction time 149.6 min; Zn^{2+} -doped biochar was found to be 76% at a mole ratio (T:BC) of 20:1, temperature 67.5°C and reaction time 105 min. The highest maximum conversion of benzyl chloride (89%) was observed for Fe^{3+}/Zn^{2+}-based biochar catalyst at a mole ratio (T:BC) of 12:1, temperature 67.5 °C and reaction time 105 min.

Figures 4.30, 4.31 and 4.32 show the correlation between the actual and predicted values of the response, BC conversion for the Fe^{3+} - doped, Zn^{2+} - doped and Fe^{3+}/Zn^{2+} - doped biochar samples respectively.

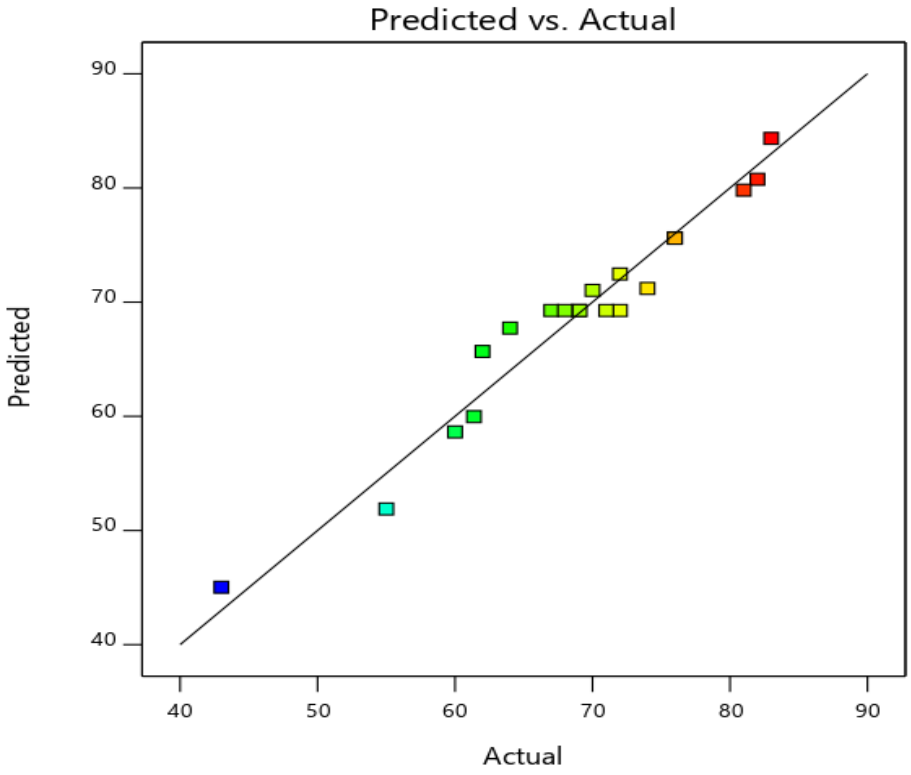

Fig. 4.34: Line Plot of the Actual and Predicted Values of Benzyl Chloride Conversion over of Fe^{3+} - Doped Biochar

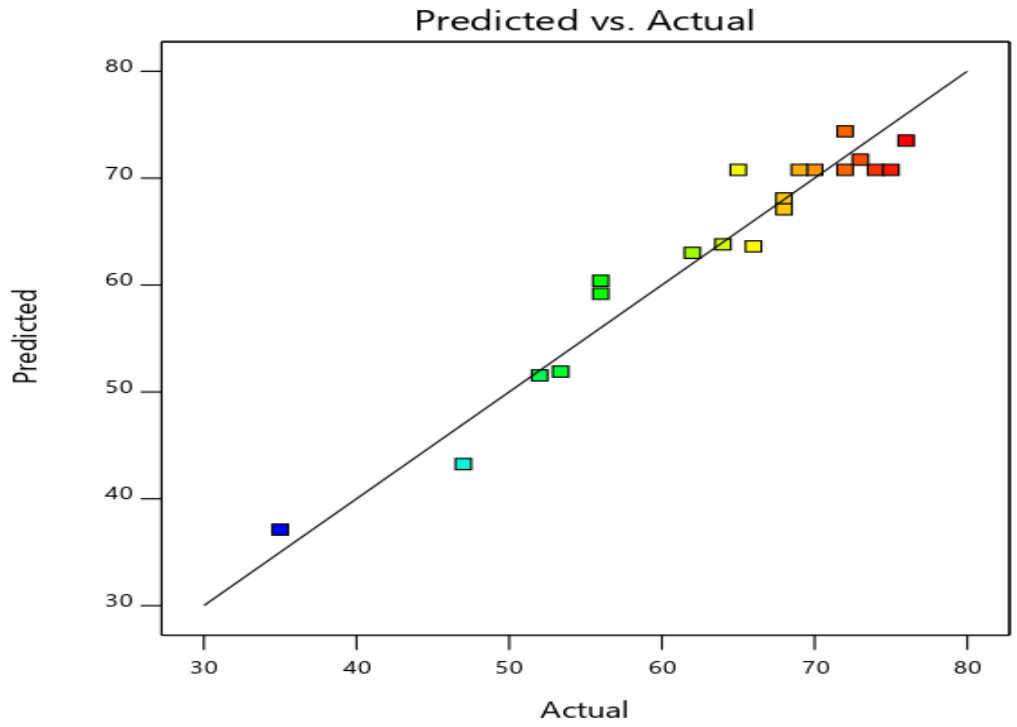

Fig. 4.35: Line Plot of the Actual and Predicted Values of Benzyl Chloride Conversion over Zn^{2+} - Doped Biochar

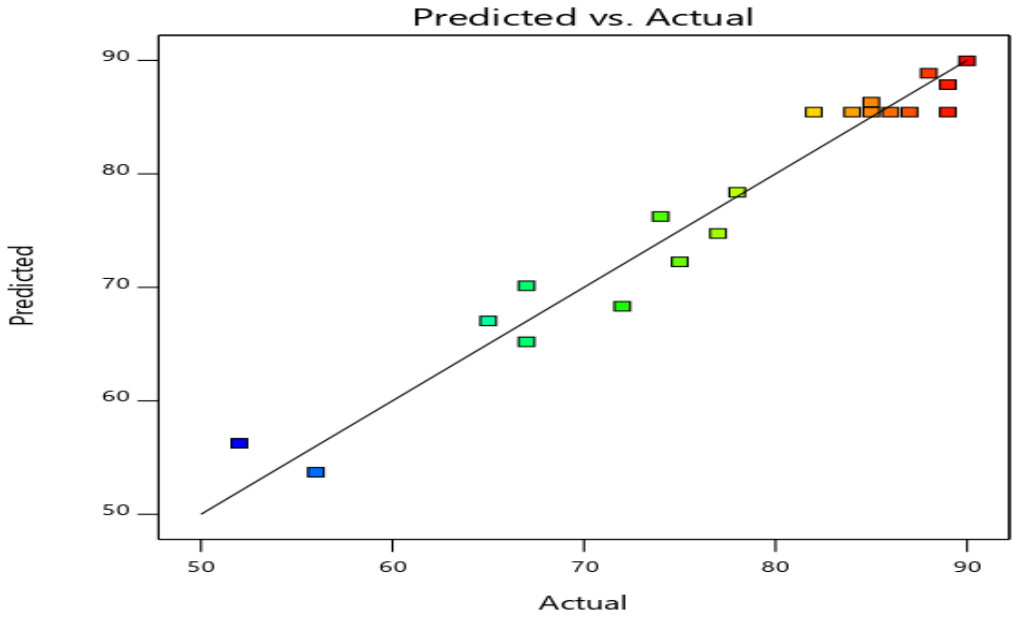

Fig. 4.36: Line Plot of the Actual and Predicted Values of Benzyl Chloride Conversion over Fe^{3+}/Zn^{2+} - Doped Biochar

The observed positive correlation between the predicted and actual response values as shown in Fig. 4.34 – 4.36 indicate the close agreement between the actual and predicted BC conversion values which is evidenced by their R^2 value that varied from 0.8800 – 0.9163. In addition, the data points were uniformly distributed near or on a straight line, confirming the goodness of fit of the mode (Parmar *et al.,* 2020).

The Fit Statistics for benzyl chloride conversion on metal - doped biochar catalysts are shown in Table 4.26. The values of adequate precision given of between 14.17 and 20.08, are markedly higher than 4 the value designated as threshold for adequate signal; and indicate that the models can be used to navigate the design space.

Table 4.26: Fit Statistics for Benzyl Chloride Conversion on Metal - Doped Biochar

Parameter	Fe^{3+}-doped Biochar	Zn^{2+}-doped Biochar	Fe^{3+}/Zn^{2+}-doped Biochar
Std. Dev.	2.77	3.72	3.24
Mean	68.77	63.67	77.40
C.V. %	4.03	5.84	4.19
R^2	0.9560	0.9368	0.9563
Adeq Precision	20.0821	14.1759	15.8043

The R^2 values of 0.9560, 0.9368, and 0.9563 for benzyl chloride conversion on the Fe^{3+}-, Zn^{2+}-, and Fe^{3+}/Zn^{2+}-doped biochars, respectively, indicate that only 4.40%, 6.32%, and 4.37% of the experimental variability was not captured by the developed models (Adamu *et al*., 2022). Coefficient of Variation (CV) as a measure of expressing standard deviation as a percentage of the mean, a small value of CV indicates better reproducibility. A high CV is an indication that variation in the mean value is high and may not lead to the development of adequate response model (Liyana-Pathurana and Shahidi, 2005; Daniel, 1991). Coefficient of variation values of between 4.03 and 5.84 are within the acceptable

range (Kalu *et al*., 2021). The model summary statistics of Benzyl Chloride (BC) conversion on the three metal - doped biochar catalysts are presented in Tables 4.27 – 4.29.

Table 4.27: Summary of Model Statistics of Benzyl Chloride Conversion Using Fe^{3+} - Doped Biochar

Source	Sequential p-value	Lack of Fit p-value	Adjusted R^2	Predicted R^2	
Linear	< 0.0001	0.0104	0.7345	0.6012	
2FI	0.8814	0.0061	0.6890	0.5464	
Quadratic	**0.0009**	**0.1010**	**0.9165**	**0.7274**	**Suggested**
Cubic	0.2145	0.0870	0.9403	-0.9872	Aliased

Table 4.28: Summary of Model Statistic of Benzyl Chloride Conversion Using Zn^{2+} - Doped Biochar

Source	Sequential p-value	Lack of Fit p-value	Adjusted R^2	Predicted R^2	
Linear	0.0028	0.0317	0.4952	0.3472	
2FI	0.9479	0.0182	0.3952	0.1448	
Quadratic	**0.0002**	**0.4717**	**0.8800**	**0.7080**	**Suggested**
Cubic	0.3916	0.4428	0.8899	0.0218	Aliased

Table 4.29: Summary of Model Statistic of Benzyl Chloride Conversion Using Fe^{3+}/Zn^{2+} - Doped Biochar

Source	Sequential p-value	Lack of Fit p-value	Adjusted R^2	Predicted R^2	
Linear	0.0020	0.0041	0.5160	0.3803	
2FI	0.7464	0.0026	0.4562	0.1797	
Quadratic	**< 0.0001**	**0.1620**	**0.9169**	**0.7369**	**Suggested**
Cubic	0.1531	0.2473	0.9479	0.0559	Aliased

Based on their maximum respective R^2 values of the adjusted and the predicted of (0.9165, 0.7274) for BC conversion on Fe^{3+} - doped Biochar, (0.8800, 0.7080) for BC conversion on Zn^{2+} - doped Biochar and (0.9169, 0.7369) for BC conversion on Fe^{3+}/Zn^{2+} - doped Biochar, the quadratic model was considered a suitable model for all to describe the experimental results, except for the cubic model which was aliased. In addition, for a suitable model, it must have a nonsignificant lack of fit (Moradi *et al*., 2023). The lack of fit *p*-values for the quadratic models were > 0.05 (Table 4.27 – 4.29), implying that the model was suitable for representing the experimental data in this research. Furthermore, the difference between the adjusted and predicted values in all the quadratic model was less than 20%, indicating that the adjusted R^2 was in reasonable agreement with the predicted (Rai *et al.,* 2016). Consequently, the quadratic model was selected for the further analysis.

The analysis of variance (ANOVA) of the response benzyl chloride (BC) conversion by the metal - doped biochar catalyst at the 5% significant level (< 0.05) are given in Tables 4.30 – 4.32. P-values less than 0.05 indicate model terms/factors are significant i.e change in the factor results to a corresponding change in BC conversion.

Table 4.30: Anova of Benzyl Chloride Conversion Using Fe^{3+}- Doped Biochar

Source	Sum of Squares	Df	Mean Square	F-value	P-value	
Model	1667.43	9	185.27	24.17	< 0.0001*	Significant
A-Mole ratio	204.87	1	204.87	26.73	0.0004*	
B-Temp.	240.67	1	240.67	31.40	0.0002*	
C-Time	908.62	1	908.62	118.54	< 0.0001*	
AB	9.30	1	9.30	1.21	0.2966	
AC	2.67	1	2.67	0.3486	0.5680	
BC	6.80	1	6.80	0.8874	0.3684	
A^2	44.58	1	44.58	5.82	0.0366*	
B^2	21.75	1	21.75	2.84	0.1230	
C^2	199.57	1	199.57	26.04	0.0005*	
Residual	76.65	10	7.67			
Lack of Fit	59.36	5	11.87	3.43	0.1010	not significant
Pure Error	17.29	5	3.46			
Cor Total	1744.08	19				

*** - Significant**

Table 4.31: Anova of Benzyl Chloride Conversion Using Zn^{2+} - Doped Biochar

Source	Sum of Squares	Df	Mean Square	F-value	P-value	
Model	2050.38	9	227.82	16.48	< 0.0001*	Significant
A-Mole ratio	207.70	1	207.70	15.02	0.0031*	
B-Temp.	190.21	1	190.21	13.76	0.0040*	
C-Time	860.34	1	860.34	62.22	< 0.0001*	
AB	3.95	1	3.95	0.2858	0.6046	
AC	7.26	1	7.26	0.5253	0.4852	
BC	13.46	1	13.46	0.9734	0.3471	
A^2	26.23	1	26.23	1.90	0.1984	
B^2	50.91	1	50.91	3.68	0.0840	
C^2	743.52	1	743.52	53.77	< 0.0001*	
Residual	138.28	10	13.83			
Lack of Fit	71.45	5	14.29	1.07	0.4717	not significant
Pure Error	66.83	5	13.37			
Cor Total	2188.66	19				

*** - Significant**

Table 4.32: Anova of Benzyl Chloride Conversion Using Fe^{3+}/Zn^{2+} - Doped Biochar

Source	Sum of Squares	Df	Mean Square	F-value	P-value	
Model	2301.56	9	255.73	24.30	< 0.0001*	Significant
A-Mole ratio	633.92	1	633.92	60.24	< 0.0001*	
B-Temp.	379.58	1	379.58	36.07	0.0001*	
C-Time	412.37	1	412.37	39.18	< 0.0001*	
AB	36.13	1	36.13	3.43	0.0936	
AC	21.13	1	21.13	2.01	0.1869	
BC	28.13	1	28.13	2.67	0.1331	
A^2	86.71	1	86.71	8.24	0.0167*	
B^2	74.66	1	74.66	7.09	0.0238*	
C^2	716.09	1	716.09	68.04	< 0.0001*	
Residual	105.24	10	10.52			
Lack of Fit	75.74	5	15.15	2.57	0.1620	not significant
Pure Error	29.50	5	5.90			
Cor Total	2406.80	19				

*** - Significant**

According to the ANOVA results presented in Table 4.30 – 4.32, all the model reliably predicts benzyl chloride conversion across the examined range of variables, which is supported by the significant p-value (< 0.05). The non-significant (> 0.05) lack-of-fit in

all cases also confirm the suitability of the models. In Table 4.30, Benzyl chloride conversion over the Fe^{3+}-doped biochar catalyst was influence by the linear effects of mole ratio of toluene to benzyl chloride (T:BC) (A), temperature (B), and reaction time (C), as well as the quadratic terms A^2 and C^2. Among these variables, reaction time (C) exerted the greatest influence, as reflected by its highest F-value (F = 118.54). The most influential factor among the linear terms that influenced the benzyl chloride conversion over the Zn^{2+}-doped biochar catalyst (Table 4.31) was the reaction time (C), as evidenced by its highest F-value (F = 62.22). The mole ratio of T:BC (A), reaction temperature (B), and the quadratic term C^2 also contributed significantly. The benzyl chloride conversion over the Fe^{3+}/Zn^{2+}-doped biochar catalyst (Table 4.32) was significantly affected by the linear terms: mole ratio (T:BC) (A), reaction temperature (B), reaction time (C) and quadratic terms (A^2, B^2, C^2), with the mole ratio of T:BC (A) exerting the greatest influence (F = 60.24).

4.18.1 Regression Analysis

The quadratic equations describing the effects of mole ratio (A), reaction temperature (B), and reaction time (C) on benzyl chloride (BC) conversion using Fe^{3+}-, Zn^{2+}-, and Fe^{3+}/Zn^{2+}-metal - doped biochars are presented in Eqs. (4.4 – 4.6).

For Fe^{3+}- Doped Biochar

$$\text{Benzyl Chloride Conversion} = 69.27 + 3.87A + 4.20B + 8.16C + 1.08AB - 0.5779AC - 0.9221BC + 1.76A^2 + 1.23B^2 - 3.72C^2 \quad (4.4)$$

For Zn^{2+} - Doped Biochar

$$\text{Benzyl Chloride Conversion} = 70.78 + 3.90A + 3.73B + 7.94C + 0.7029AB - 0.9529AC - 1.30BC - 1.35A^2 - 1.88B^2 - 7.18C^2 \quad (4.5)$$

For Fe^{3+}/Zn^{2+} - Doped Biochar

$$\text{Benzyl Chloride Conversion} = 85.44 + 6.81A + 5.27B + 5.50C - 2.13AB + 1.62AC - 1.88BC - 2.45A^2 - 2.28B^2 - 7.05C^2 \quad (4.6)$$

Where, A represents the coded value of the mole ratio of benzyl chloride to toluene, B represents the coded value of reaction temperature, and C represents the coded value of reaction time. The coefficients of the single-factor terms indicate the individual effect of each factor, while the coefficients of the two-factor interaction terms represent the combined effect of the respective factors. A positive coefficient in all the metal - doped biochars catalysts denote a positive effect, meaning that an increase in the factor leads to a corresponding increase in benzyl chloride conversion, whereas a negative coefficient indicates a negative effect, where an increase in the factor results in a decrease in conversion. The magnitude and sign of these coefficients are crucial for determining the optimal parameters for benzyl chloride conversion using the metal-doped biochar catalysts.

To demonstrate the effect of interactions between variables on the benzylation of toluene in the presence of the metal-doped biochar as a heterogeneous catalyst, a 3D response surface and contour plots (2-dimensional representations of 3D response surfaces) were generated, as shown in Figures 4.37 - 4.39. The regression equation obtained from the model was used to construct these 3D surface plots, which illustrate the relationship between the conversion of benzyl chloride (BC) and the input factors including: the mole ratio of benzyl chloride to toluene (T:BC) (A), reaction temperature (B), and reaction time (C). In preparing these plots, two variables were varied within their experimental ranges, and the third variable was considered to be constant, in order to visualize how the interaction of each pair of factors influences the overall catalytic performance.

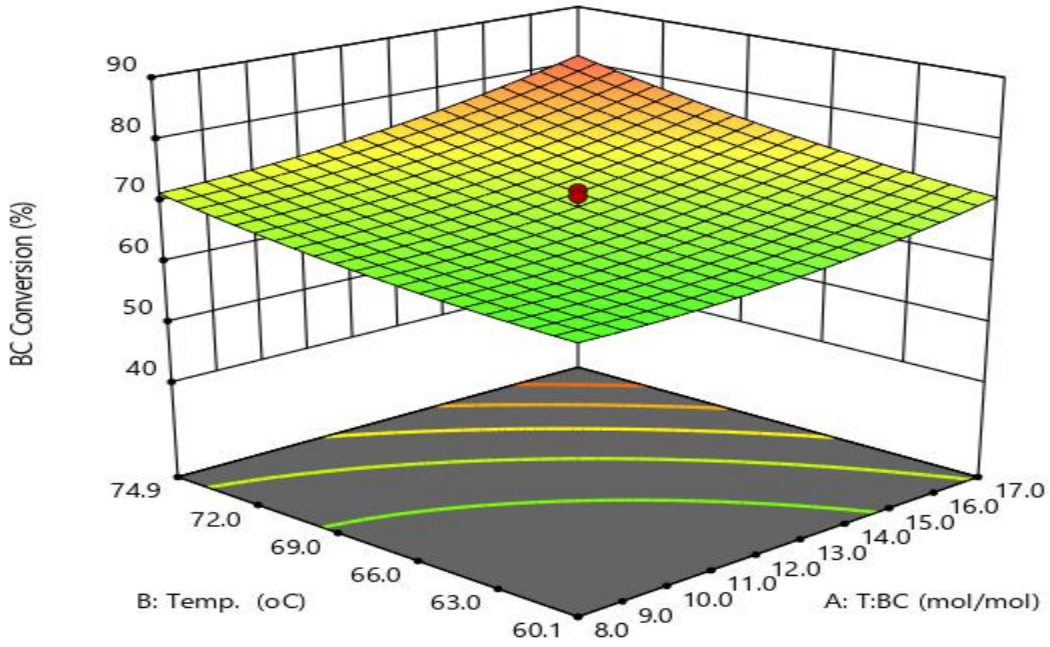

(i)

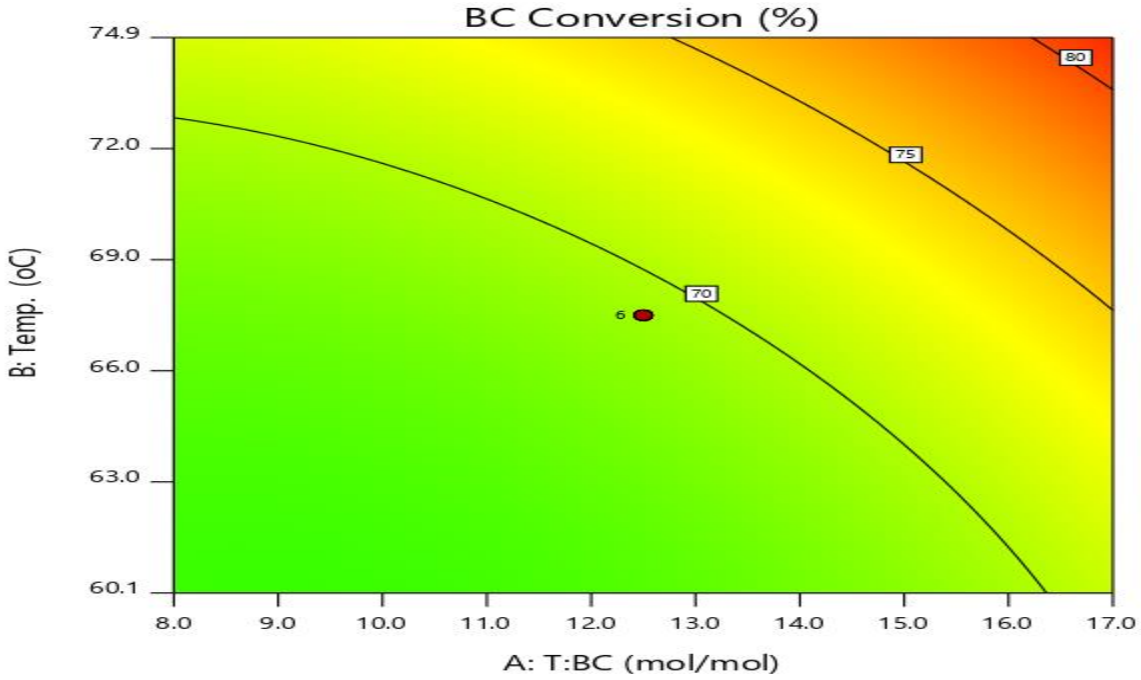

(ii)

Fig. 4.37A: Three - dimensional 3D (i) and Contour Plots (ii) of the Interaction of Mole Ratio and Temperature on BC conversion over Fe^{3+} - doped biochar

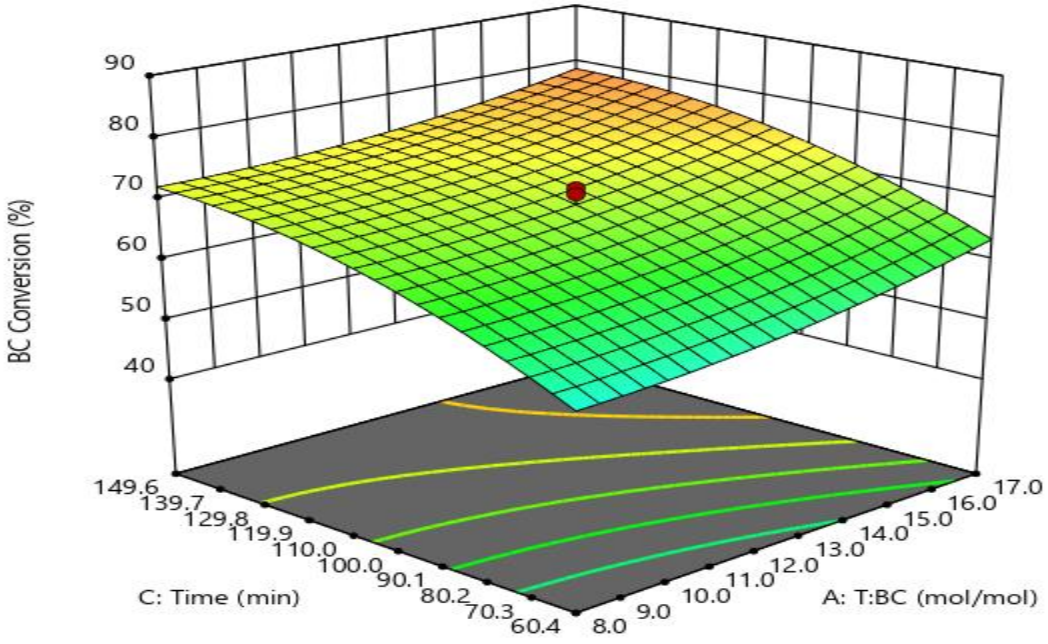

(i)

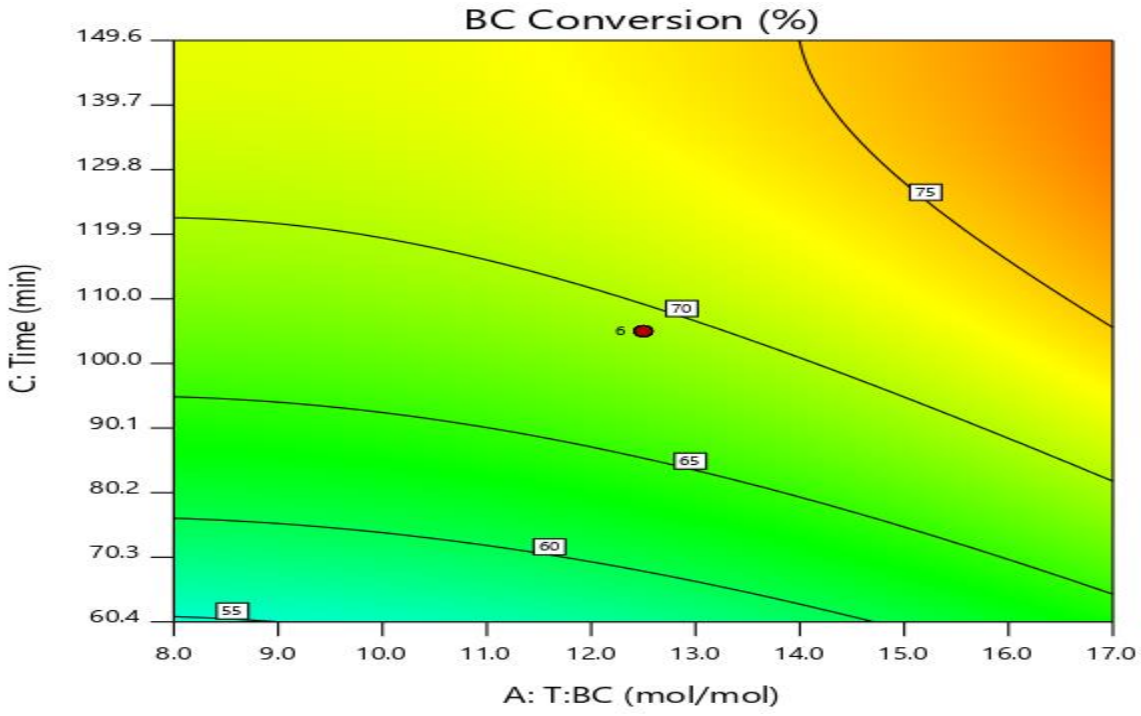

(ii)

Fig. 4.37B: Three - dimensional 3D (i) and Contour Plots (ii) of the Interaction of Mole Ratio and Time on BC conversion over Fe^{3+} - doped biochar

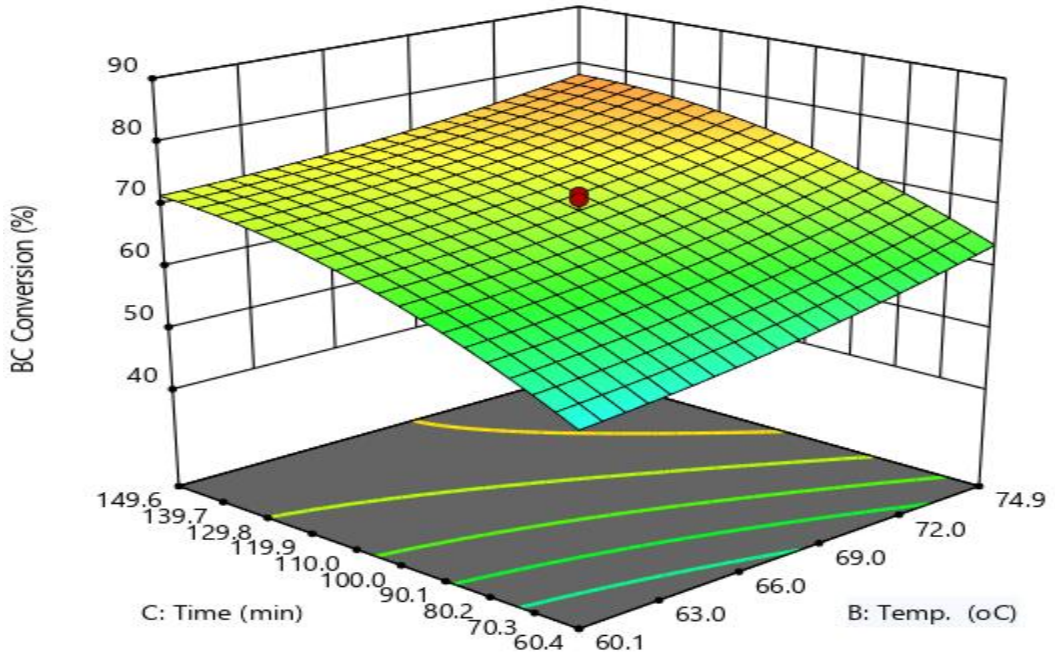

(i)

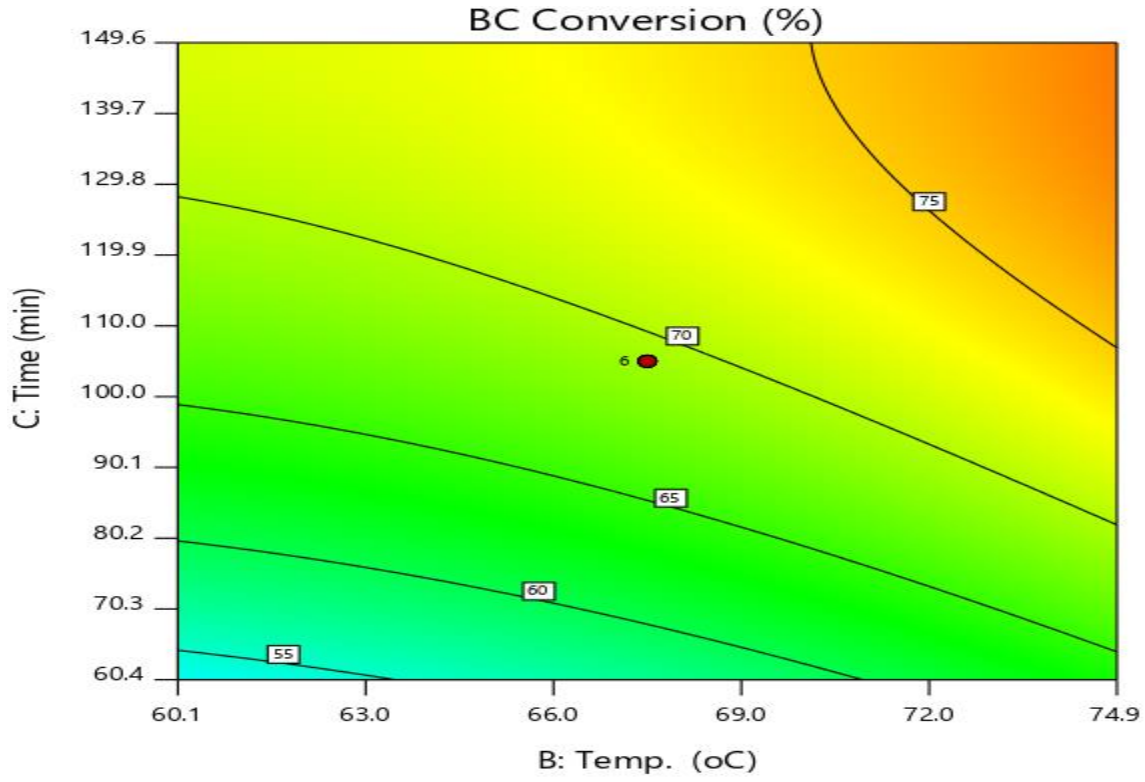

(ii)

Fig. 4.37C: Three - dimensional 3D (i) and Contour Plots (ii) of the Interaction of Temperature and Time on BC conversion over Fe^{3+} - doped biochar

Fig. 4.37A (i) and (ii) show the combined influence of the mole ratio of toluene to benzyl chloride (T:BC) and reaction temperature (A×B) on the conversion of benzyl chloride (BC) at a fixed reaction time of 105 min. It can be observed that BC conversion was maximum at approximately 81% with an increase in mole ratio of T:BC from 8:1 – 17:1 and reaction temperature from 60 - 75° C. A similar trend was observed in case of Fig. 4.37B (i) and (ii) for the combined effect of mole ratio (T:BC) and reaction time (A×C) at a constant temperature of 67.5°C. The increase in the mole ratio (T:BC) (8:1 – 17:1) and reaction time (60.4 – 149.6 min) resulted in an increase in BC conversion of up to 78.7%. Likewise Fig. 4.37C (i) and (ii), the combined effect of reaction temperature and reaction time (B×C) at constant mole ratio (T:BC) (12.5:1) followed a similar trend, leading to an increase in BC conversion of approximately 78%.

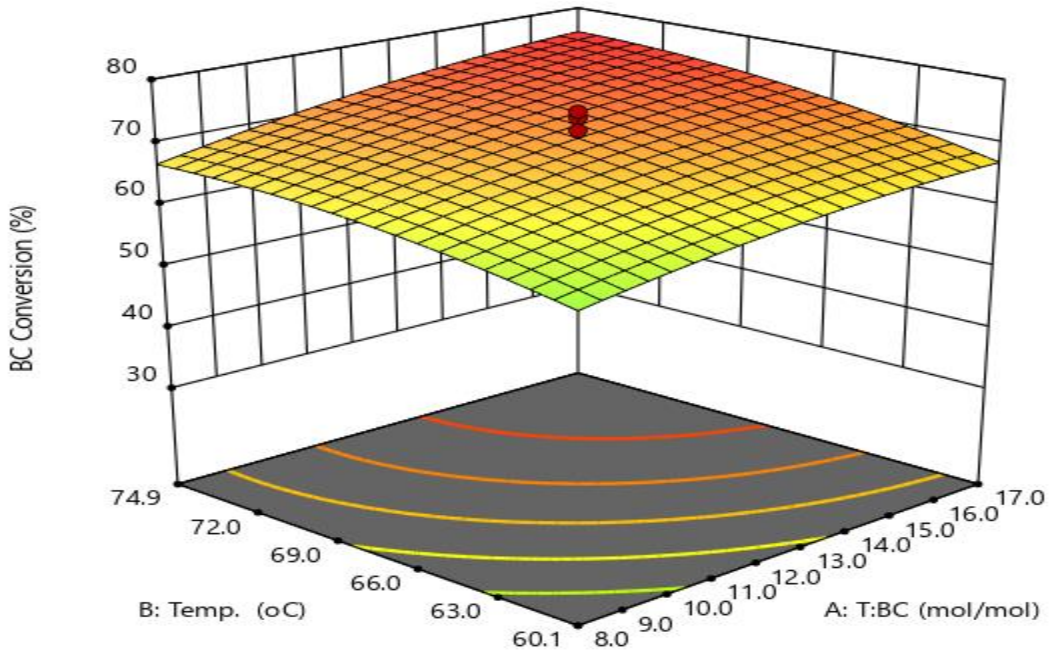

(i)

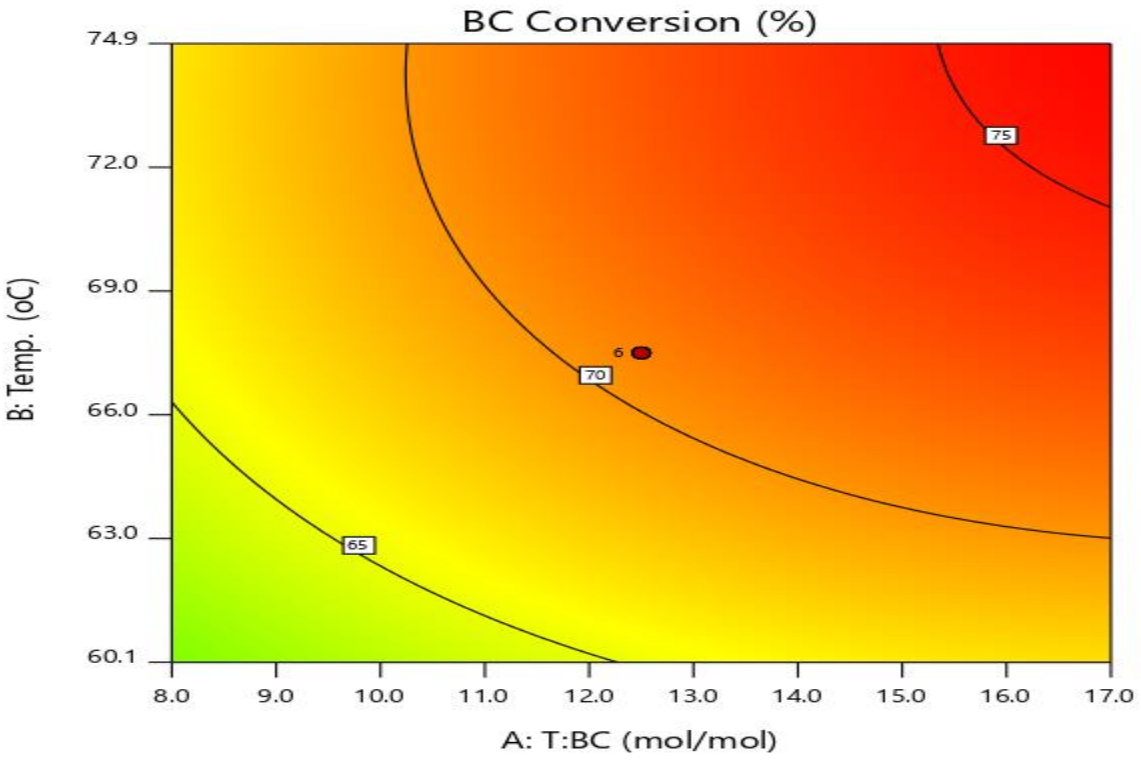

(ii)

Fig. 4.38A: Three - dimensional 3D (i) and Contour Plots (ii) of the Interaction of Mole Ratio and Temperature on BC conversion over Zn^{2+} - doped biochar

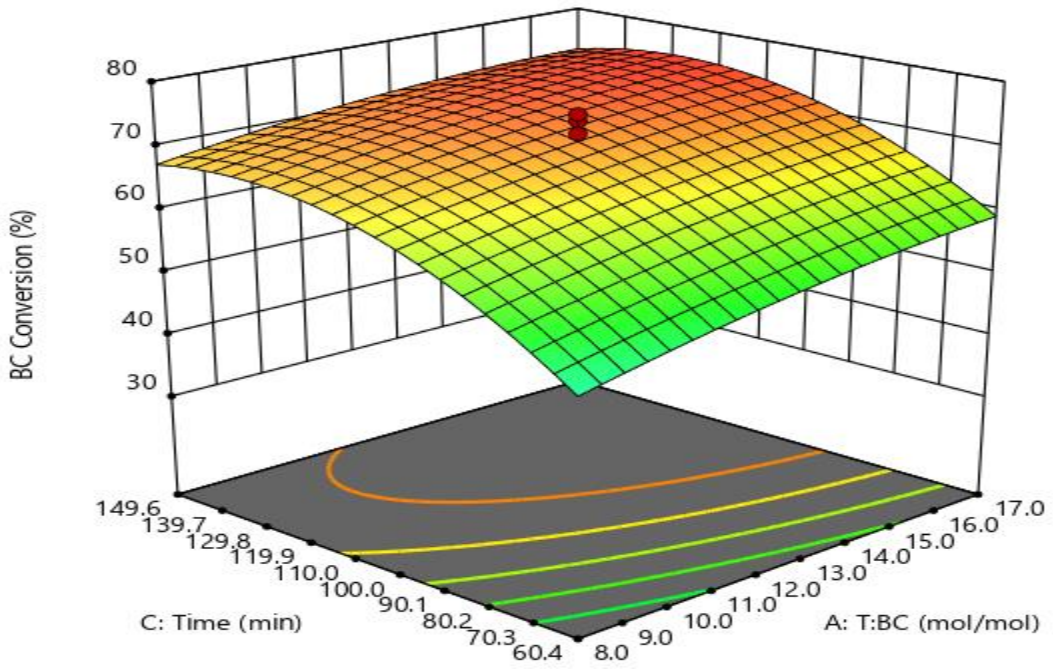

(i)

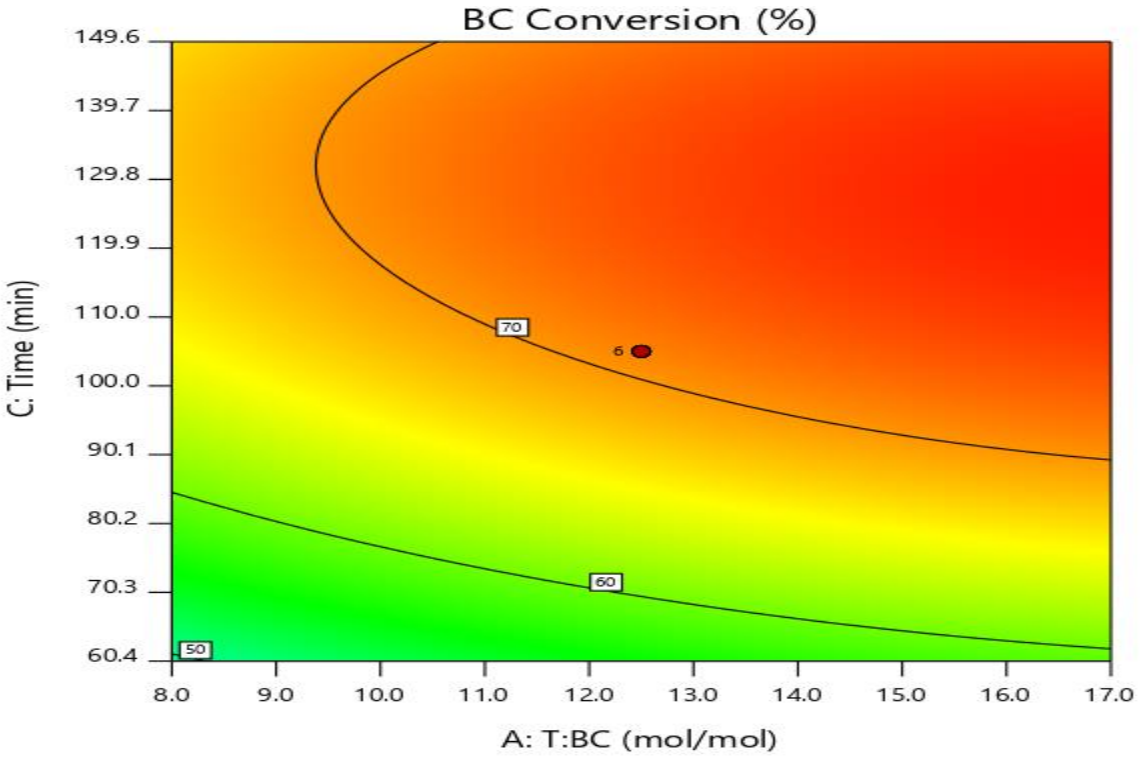

(ii)

Fig. 4.38B: Three - dimensional 3D (i) and Contour Plots (ii) of the Interaction of Mole Ratio and Time on BC conversion over Zn^{2+} - doped biochar

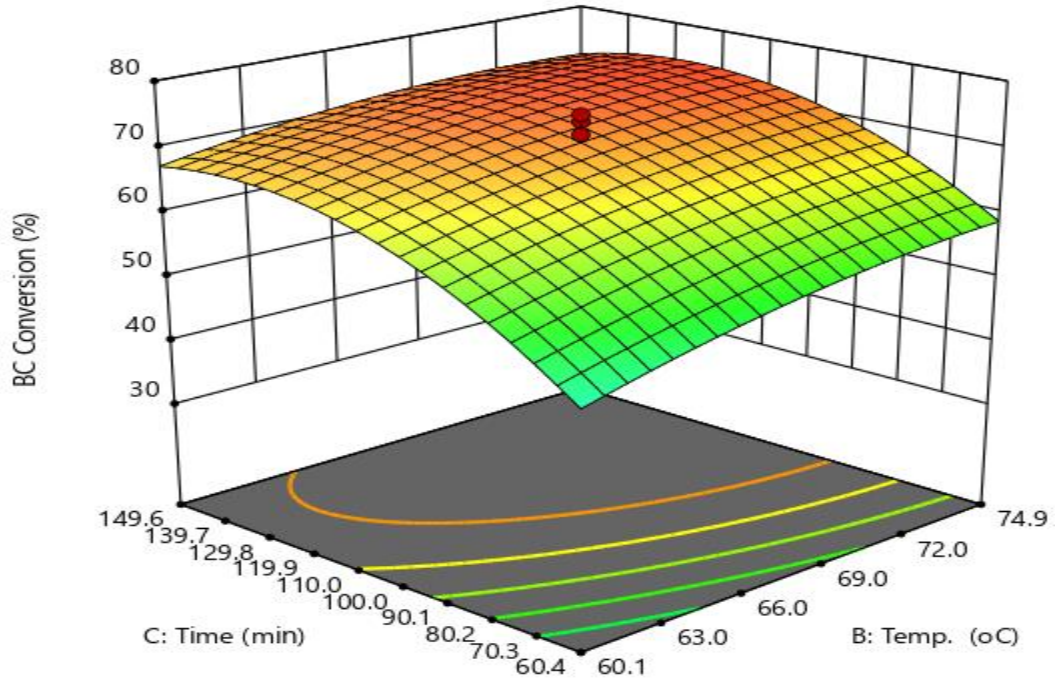

(i)

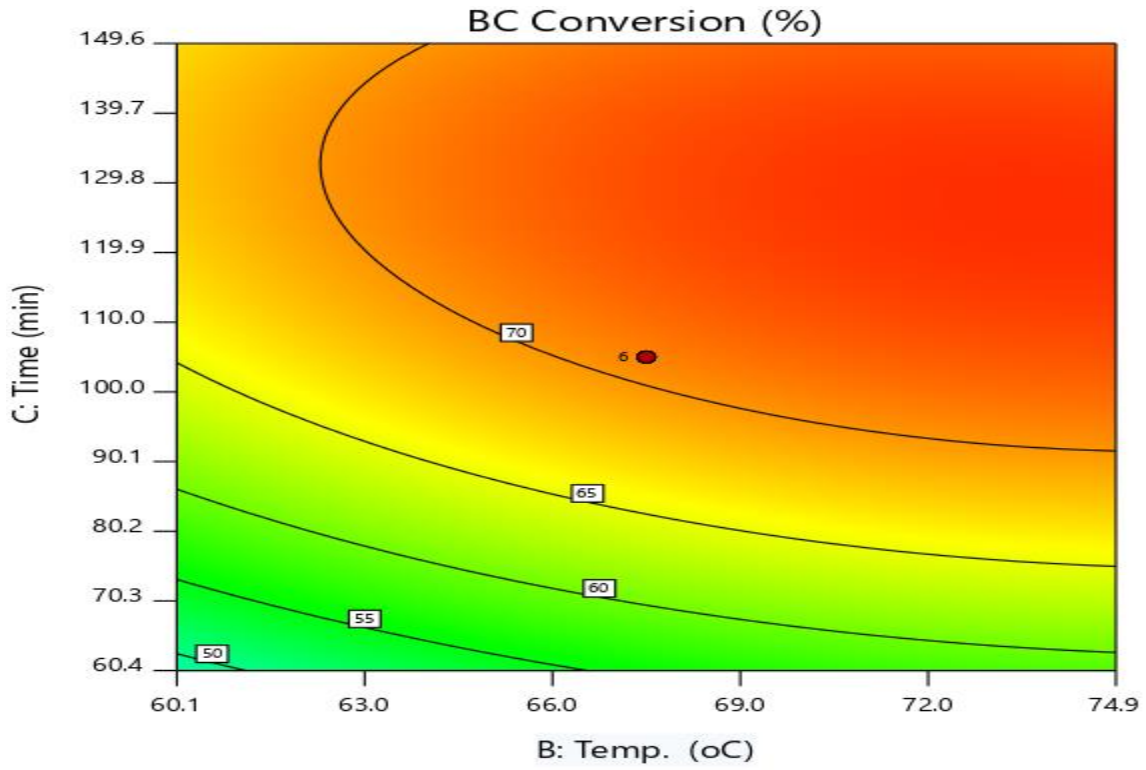

(ii)

Fig. 4.38C: Three - dimensional 3D (i) and Contour Plots (ii) of the Interaction of Temperature and Time on BC conversion over Zn^{2+} - doped biochar

Fig. 4.38 (A – C) display the interaction effect of the process variables (mole ratio (A), reaction temperature (B), and reaction time (C)) on the response, benzylation of toluene using Zn^{2+}-doped biochar as heterogenous catalyst. For the interaction between the mole ratio (T:BC) and reaction temperature (A×B) at a constant reaction time (105 min) (Fig. 4.38A (i) and (ii), it was observed that increasing the mole ratio (T:BC) from 8:1 to 17:1 and the reaction temperature from 60.1 to 74.9 °C resulted in a BC conversion of approximately 75.8%. Fig. 4.38B (i and ii) show the interaction effect between mole ratio (T:BC) and reaction time (A x C) and at fixed reaction temperature (67.5^{o}C), an increase in both factors up to 16.9:1 and 127.9 min, respectively, resulted to a maximum BC conversion of 74.2%. A similar trend was observed in Fig. 4.38C (i) and (ii) for the combined effect of reaction temperature and reaction time (B×C) at a constant T:BC mole

ratio of 12.5:1, where the BC conversion of approximately 74.2% was attained at reaction temperature of 74 °C and reaction time of 126 min.

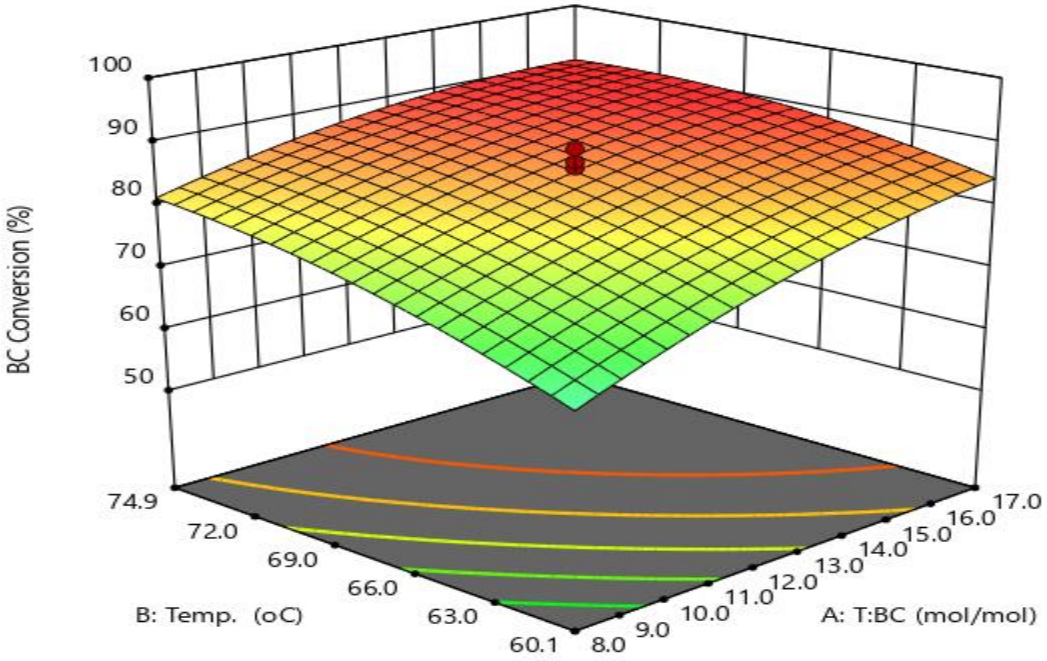

(i)

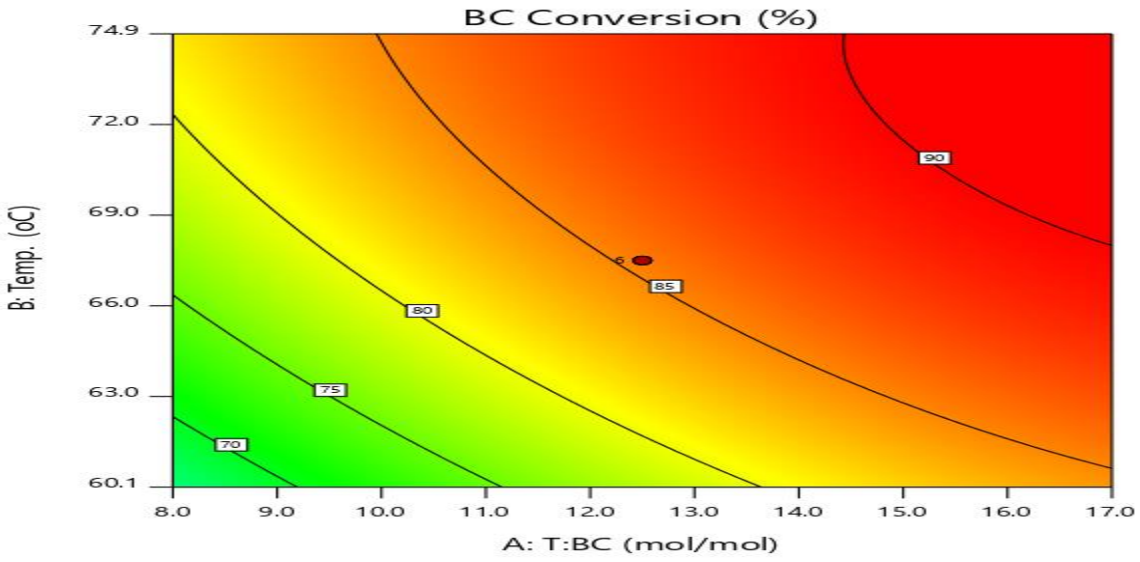

(ii)

Fig. 4.39A: Three - dimensional 3D (i) and Contour Plots (ii) of the Interaction of Mole Ratio and Temperature on BC conversion over Fe^{3+}/Zn^{2+} - doped biochar

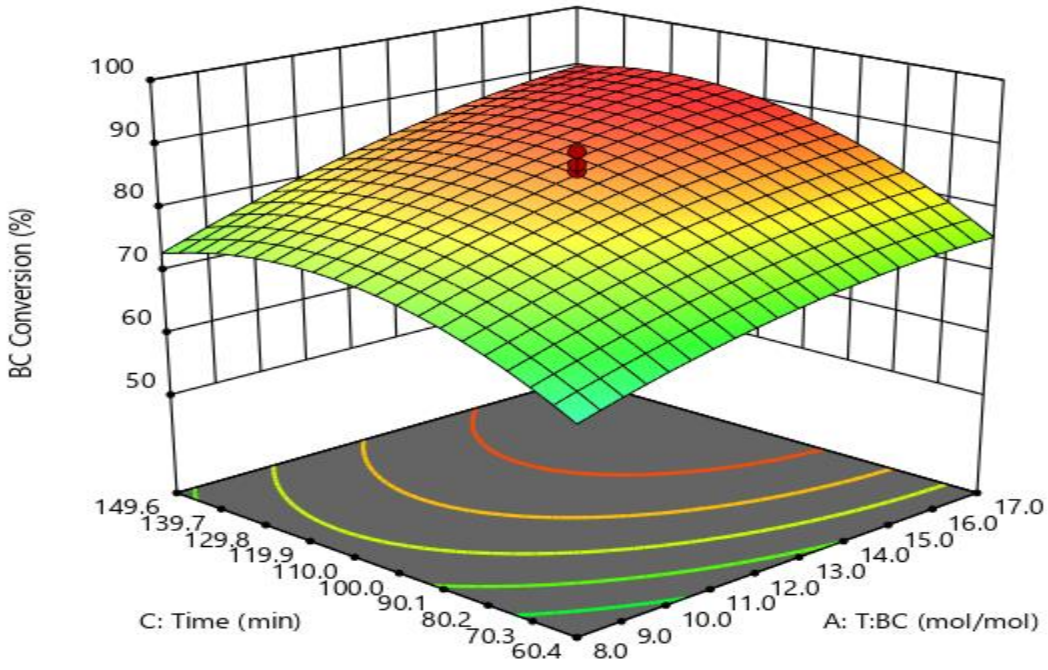

(i)

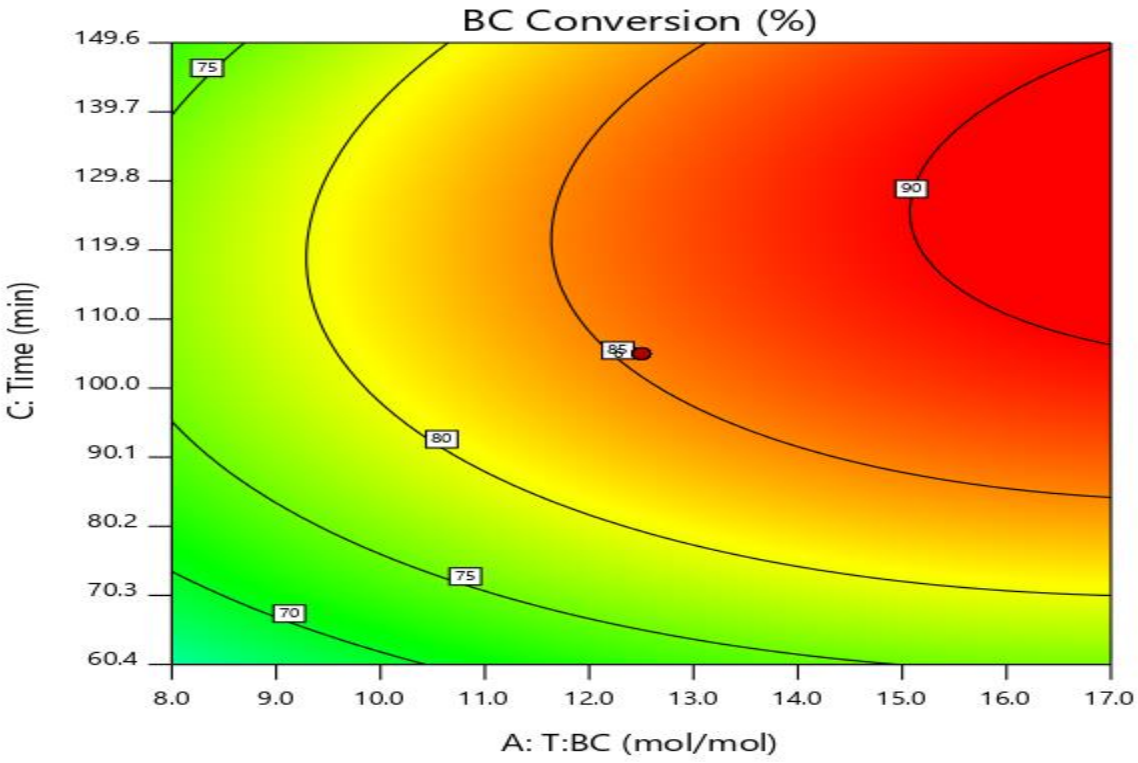

(ii)

Fig. 4.39B: Three - dimensional 3D (i) and Contour Plots (ii) of the Interaction of Mole Ratio and Time on BC conversion over Fe^{3+}/Zn^{2+} - doped biochar

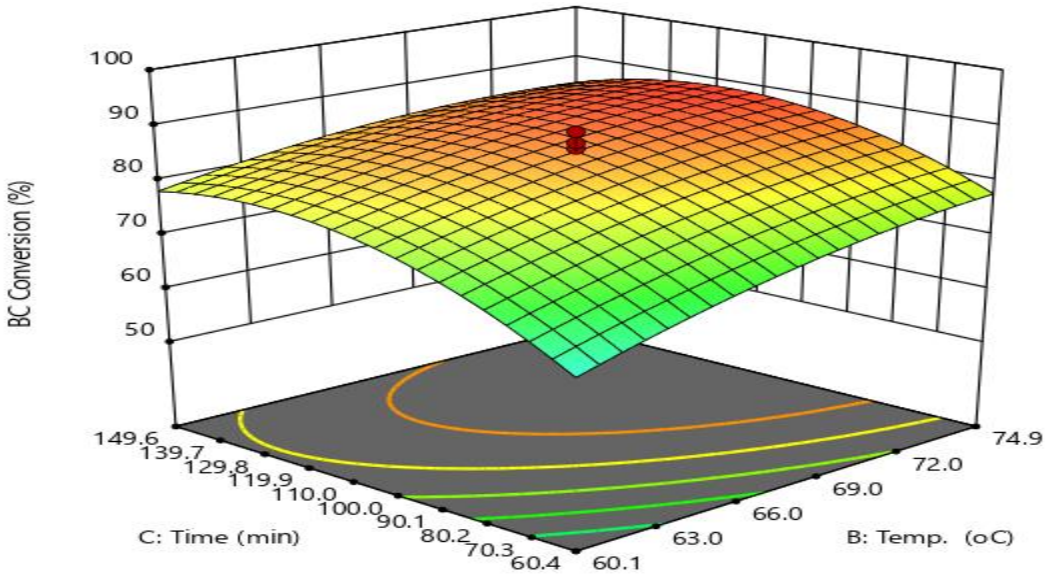

(i)

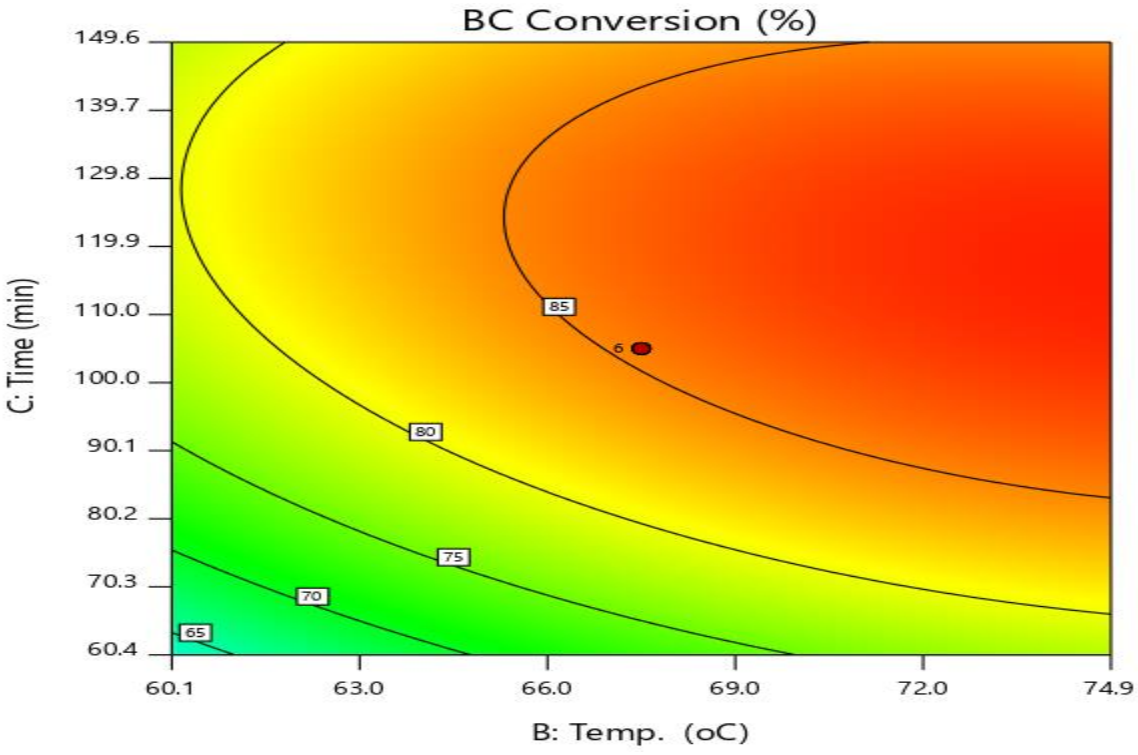

(ii)

Fig. 4.39C: Three - dimensional 3D (i) and Contour Plots (ii) of the Interaction of Temperature and Time on BC conversion over Fe^{3+}/Zn^{2+} - doped biochar

Fig. 4.39 (A -C) illustrate the interaction effects of the process variables on the benzylation of toluene using Fe^{3+}/Zn^{2+}-doped biochar as a heterogeneous catalyst. Fig. 4.39A (i) and (ii) show the combined effects of mole ratio (A), reaction temperature (B) at a constant reaction time (C) (105 min) on benzyl chloride (BC) conversion. The highest BC conversion obtained with the Fe^{3+}/Zn^{2+}-doped biochar catalyst was observed in the red region (representing the end of the process), indicating a more pronounced catalytic activity compared to the individual Fe^{3+}- and Zn^{2+}-doped biochars. The maximum BC conversion of 90.75% was achieved at the combined maximum values of mole ratio (T:BC = 16.7:1) and reaction temperature (74.4°C). Fig. 4.39B (i) and (ii) depict the interaction between mole ratio (T:BC) and reaction time (A×C) at a constant reaction temperature(67°C). The plot reveals an approximately maximum BC conversion of 91.5% at a mole ratio of 16.8:1 at a reaction time of 127.1 min. Fig. 4.39C (i) and (ii) present the interaction between reaction temperature (B) and reaction time (C) at a constant mole ratio (T:BC = 12.5:1). A similar trend was observed, with a maximum BC conversion of 88.86% recorded at maximum reaction temperature (75°C) and reaction time (119.5 min).

The high catalytic activity of the metal-doped biochar catalysts are attributed to the abundance of active sites, increased Lewis acidity, enhanced electron transfer capability, and improved substrate catalyst interactions. These properties collectively enhanced the activation of benzyl chloride and facilitated efficient electrophilic substitution on the aromatic ring of toluene. Among the metal-doped biochars (Fe^{3+}-, Zn^{2+}-, and Fe^{3+}/Zn^{2+}-doped) investigated, the Fe^{3+}/Zn^{2+}-doped biochar achieved the highest benzyl chloride (BC) conversion, indicating the synergistic interaction between Fe^{3+} and Zn^{2+} active sites on the biochar matrix, and facilitated more efficient benzyl chloride activation during the Friedel Crafts benzylation reaction.

4.18.2 Optimization of Process Parameters

Table 4.33: Optimization of Process Parameters for the Friedel Crafts benzylation Reaction

Catalyst	Mole ratio (T:BC)	Temperature (°C)	Time (min)	BC Conversion (%)	Desirability
Fe^{3+}- doped biochar	16.96:1	74.9	149.6	84	1.000
Zn^{2+}- doped biochar	16.95:1	74.8	123.1	77	1.000
Fe^{3+} / Zn^{2+}- doped biochar	16.80:1	69.1	134.57	91	1.000

BC – Benzyl Chloride
T - Toluene

The numerical optimization shown in Table 4.33, was conducted to determine the optimum condition for conversion of benzyl chloride using the metal - doped biochars as catalyst. A set of ranges was selected for all controlling parameters (mole ratio of toluene to benzyl chloride, reaction temperature and reaction time) to achieve maximum BC conversion, where the higher the desirability of the function, the better the model's accuracy. The optimum conditions forecast that the Fe^{3+}/Zn^{2+}-doped biochar catalyst gave the highest BC conversion of 91.63% at mole ratio (T:BC) ($mol.mol^{-1}$) of 16.80:1, reaction temperature of 69.1 °C, and reaction time of 134.57 min, with a desirability value of 1.000.

The Fe^{3+}-doped biochar and Zn^{2+}-doped biochar also demonstrated high conversions of 84% and 77%, respectively, at mole ratio (T:BC) of 16.96:1, 16.95:1, reaction temperature of 74.9, 74.8 °C, and reaction time of 14.6, 123.1 respectively.

The mole ratio (BC:T), reaction temperature, and reaction time significantly influenced benzyl chloride conversion, as evident from the 3D surface and contour plots. High reaction temperatures, appropriate mole ratios, and sufficient reaction times provided the thermal energy required to activate the metal ion sites (Fe^{3+}, Zn^{2+}, Fe^{3+}/Zn^{2+}) for effective catalysis. An optimal substrate ratio ensures adequate molecular contact, while longer reaction times

allow complete substrate utilization. However, excessively long reaction times may lead to catalyst fouling or active site blockage, consequently reducing conversion efficiency.

4.18.3 Validation of the Model

Table 4.34 gives the textural properties of the magnetic carbon rich materials prepared using the optimum process condition of the model; in comparison with the model-derived data.

Table 4.34: Validation of model equation

Catalyst	BC conversion (%)
Fe^{3+}- doped biochar	87 (84)
Zn^{2+}- doped biochar	81 (77)
Fe^{3+} / Zn^{2+}- doped biochar	93 (91)

Values in parentheses are predicted from the model

BC – Benzyl Chloride

As shown in Table 4.34, to validate the predicted model, experiments were carried out under the optimum conditions obtained from the numerical optimization. This produced BC conversion values of 87%, 81%, and 93% for Fe^{3+}-, Zn^{2+}-, and Fe^{3+}/Zn^{2+}-doped biochars, respectively. The experimental results were found to be in close agreement with the predicted values, confirming the accuracy and reliability of the developed model. Among the three catalysts, the Fe^{3+}/Zn^{2+}-doped biochar exhibited the highest BC conversion of 93%, indicating its superior catalytic efficiency.

CHAPTER FIVE

5.0 SUMMARY AND CONCLUSION

Metal-doped coconut-shell biochars (Fe^{3+}-, Zn^{2+}- and Fe^{3+}/Zn^{2+}-doped) were successfully prepared, characterized, optimized using the center composite design, and applied as heterogeneous catalysts for the Friedel–Crafts benzylation of toluene. Characterization confirmed that metal incorporation markedly improved textural properties (BET surface area, pore volume and pore diameter) and altered surface chemistry compared with untreated biochar (CSB450). Among the optimized metal - doped biochars prepared, Fe^{3+}/Zn^{2+}-doped biochar exhibited the highest surface area (2130.4 $m^2 \cdot g^{-1}$ validated value $\approx$ 2124.5 $m^2 \cdot g^{-1}$) at the optimum conditions (46.7% Fe wt % (of a 2g total metal), 336.9 °C and 1.89 h) which may be attributed to the combined effect of Fe^{3+} and Zn^{2+} species, which enhanced pore development and structural activation during pyrolysis. The optimized materials were further evaluated for their catalytic performance in the Friedel–Crafts benzylation reaction. Optimization studies also using the center composite design (CCD) revealed that reaction temperature, mole ratio (benzyl chloride : toluene), and reaction time had significant effects on benzyl chloride conversion. Among all catalysts, the Fe^{3+}/Zn^{2+}-doped biochar achieved the highest conversion of 91.5% , indicating the combined effect of Fe^{3+} and Zn^{2+} on the biochar matrix. The high catalytic activity of the metal-doped biochars is attributed to the abundance of active sites, increased Lewis acidity, enhanced electron transfer capability, and improved substrate–catalyst interactions. This study demonstrates that biochar can serve as an efficient, low-cost, and environmentally benign support for heterogeneous catalysis in organic transformations.

At the model predicted optimized process condition, optimum benzyl chloride conversion 93% was found for Fe^{3+}/Zn^{2+} , with values of 87 and 81% found for the Fe^{3+} - doped and Zn^{2+} - doped biochar respectively.

5.2 FINDINGS

The coconut shell biochars (CSBs) produced at different pyrolysis temperatures were found to: (i) be alkaline in nature; (ii) exhibit high electrical conductivity (EC) and cation exchange capacity (CEC), along with diverse surface functional groups; (iii) reveal CSB450 with a high specific surface area; and (iv) display mesoporous structures.

Response Surface Methodology (RSM) optimized specific surface area of metal-doped biochars prepared by the co-pyrolysis method were 2098.04 $m^2.g$, 1721.40 $m^2.g^{-1}$, and 2124.48 $m^2.g^{-1}$ respectively for Fe^{3+}-doped biochar, Zn^{2+}-doped biochar, Fe^{3+}/Zn^{2+}-doped biochar.

The prepared metal-doped biochar were found to: (i) exhibit acidic pH, with EC and CEC values higher that the pristine (undoped) biochar (CSB450); (ii) retain their mesoporous structures, with elemental analysis confirming successful metal incorporation at 10.09%, 5.17%, and 9.44/6.51% for the Fe^{3+}-, Zn^{2+}-, and Fe^{3+}/Zn^{2+}-doped materials, respectively; and (iii) show reduced surface functional group intensities as a result of the co-pyrolysis and metal-doping processes.

Furthermore, RSM optimization of the catalytic reaction indicated maximum benzyl chloride conversions of 87% (Fe^{3+}-doped), 81% (Zn^{2+}-doped), and 93% (Fe^{3+}/Zn^{2+}-doped) biochars.

5.3 CONTRIBUTION TO KNOWLEDGE

The study has contributed to knowledge in the following ways:

1. Provided data and information on the effect of pyrolysis temperature on coconut shell biochar's properties to reveal their potential for environmental and agronomic benefits;
2. For the first time, models have been developed for the preparation of metal (Fe^{3+}, Zn^{2+} and Fe^{3+}/Zn^{2+}) doped CSB using the co-pyrolysis method with enhanced textural properties;
3. The application of metal (Fe^{3+}, Zn^{2+} and Fe^{3+}/Zn^{2+}) doped coconut shell biochar in the Friedel Crafts benzylation reaction was described for the first time.

5.4 RECOMMENDATION FOR FURTHER STUDIES

Future research could focus on evaluating the recovery and reusability of the metal-doped biochar in Friedel Crafts benzylation reactions and in environmental remediation

LIST OF PUBLICATIONS

1. **Ejimadu, C.M.,** Okuo, J.M. & Okieimen, F.E. (2025). Evolution of functionalities and structure of biochar in pyrolysis of coconut shell at different temperatures. *Acta Chemica Malaysia,* 9(2):122-130
2. **Chima Maximus Ejimadu,** James Majebi Okuo, and Felix Ebhodaghe Okieimen (2025). Optimization of High Surface Area Magnetic Biochar Production from Coconut (Cocos nucifera L.) Shell with $FeCl_3$ using Response Surface Methodology. *ChemClass Journal, 9(4):76 – 91*
3. **Ejimadu, C.M.,** Okuo, J.M. & Okieimen, F.E. (2025). Carbon sequestration potential of coconut shell biochar produced by slow pyrolysis. *Nigerian Research Journal of Engineering and Environmental Sciences,* 10(2):297-304
4. **Ejimadu, C.M.,** Okuo, J.M., Okieimen, F.E. (2026). Chemical oxidation stability of coconut shell biochar. *Singapore Journal of Scientific Research,* 16(1):1-7
5. **Ejimadu, C.M.,** Okuo, J.M. & Okieimen, F.E. (2026). Optimisation of Process Variables for Preparation of Magnetic Carbon-Rich Materials using Response Surface Methodology. *Chemical Papers,* - In press (Accepted)

REFERENCES

Adamu, M., Trabanpruek, P., Limwibul, V., Jongvivatsakul, P., Iwanami, M. and Likitlersuang, S. (2022). Compressive behavior and durability performance of high-volume fly-ash concrete with plastic waste and graphene nanoplatelets by using response-surface methodology. Journal of Materials in Civil Engineering, 34:04022222.

Agegnehu G., Srivastava, A.K., Bird, M.I. (2017). The role of biochar and biochar-compost in improving soil quality and crop performance: A review. Applied Soil Ecology 119:156-170

Ahmad, M., Lee, S.S., Dou, X., Mohan, D., Sung, J.-K., Yang, J.E. and Ok, Y.S. (2012). Effects of pyrolysis temperature on soybean stover- and peanut shell-derived biochar properties and TCE adsorption in water. *Bioresour. Technol.*, 118: 536–544. https://doi.org/10.1016/j.biortech.2012.05.042.

Ahmedna, M., Johns, M.M., Clarke, S.J., Marshall, W.E. and Rao, R.M. (1997). Potential of agricultural by-product-based activated carbons for use in raw sugar decolourisation. *J. Sci. Food Agric.*, 75(1): 117–124. https://doi.org/10.1002/(SICI)1097-0010(199709)75:1<117::AID-JSFA850>3.0.CO;2-M.

Aimikhe, V.J., Anyebe, M.S. and Ibezim-Ezeani, M. (2022). Development of composite activated carbon from mango and almond seed shells for CO_2 capture. *Biomass Convers. Biorefin.*, 14: 4645–4659.

Ajien, A., Idris, J., Md-Sofwan, N., Husen, R. and Seli, H. (2022). Coconut shell and husk biochar: A review of production and activation technology, economic, financial

aspect and application. *Waste Manag. Res.*, 41(1): 37–45. https://doi.org/10.1177/0734242X221127167.

Akinwunmi, B., Hirvi, J.T., Kasa, S. and Pakkanen, T.A. (2020). Swelling pressure of Na- and Ca-montmorillonites in saline environments: A molecular dynamics study. Chemical Physics, 528, 110511. https://doi.org/10.1016/j.chemphys.2019.110511

Al Mamari, H.H. (2023). Developments and uses of Lewis acids: From conventional catalysts to modern green catalysts. In: Akitsu, T. (ed.) Electrophile and Lewis acid. IntechOpen, Chapter 3, pp. 1.21. http://dx.doi.org/10.5772/intechopen.1001154

Alchouron, J., Navarathna, C., Chludil, H.D., Dewage, N.B., Perez, F., Hassan, E.B., Pittman, C.U., Vegas, A.S. and Mlsna, T.E. (2020). Assessing South American *Guadua chacoensis* bamboo biochar and Fe_3O_4 nanoparticle dispersed analogues for aqueous arsenic(V) remediation. *Sci. Total Environ.*, 706: 135943.

Alman-Abad, Z.S., Pirkharrati, H., Asadzadeh, F. and Maleki-Kakelar, M. (2020). Application of response surface methodology for optimization of zinc elimination from a polluted soil using tartaric acid. *Adsorpt. Sci. Technol.*, 38(3–4): 79–93.

Almutairi, A.A., Ahmad, M., Rafique, M.I. and Al-Wabel, M.I. (2023). Variations in composition and stability of biochars derived from different feedstock types at varying pyrolysis temperature. *J. Saudi Soc. Agric. Sci.*, 22(1): 25–34. https://doi.org/10.1016/j.jssas.2020.07.005.

Alotaibi, A. M. (2025). An Overview of Zeolites: From Historical Background to Diverse Applications. Molecules, 30(20):4036. https://doi.org/10.3390/molecules30204036

Alzeer, M.I.M. & MacKenzie, K.J.D. (2022). Alkali-activated materials as catalysts in chemical processes. In: Alkali-Activated Materials in Environmental Technology Applications. Woodhead Publishing Series in Civil and Structural Engineering, pp. 355–379. https://doi.org/10.1016/B978-0-323-88438-9.00016-8

Amalina, F., Abd Razak, A.S., Krishnan, S., Sulaiman, H., Zularisam, A.W. and Nasrullah, M. (2022). Advanced techniques in the production of biochar from lignocellulosic biomass and environmental applications. *Cleaner Materials*, 6: 100137. https://doi.org/10.1016/j.clema.2022.100137.

Amalina, F., Razak, A.S.A., Krishnan, S., Sulaiman, H., Zularisam, A.W. and Nasrullah, M. (2022). Biochar production techniques utilizing biomass waste-derived materials and environmental applications – A review. *J. Hazard. Mater. Adv.*, 7: 100134. https://doi.org/10.1016/j.hazadv.2022.100134.

Amenaghawon, A.N., Anyalewechi, C.L., Okieimen, C.O. and Kusuma, H.S. (2021). Biomass pyrolysis technologies for value-added products: A state-of-the-art review. *Environ. Dev. Sustain.*, 23: 14324–14378.

Anekwe, I.M.S., Akpasi, S.O., Tetteh, E.K., Joel, A.S., Mustapha, S.I. and Isa, Y.M. (2025). Progress in heterogeneous catalysis for renewable energy and petrochemical production from biomass. Fuel Processing Technology, 276:108267.

Azeta, O., Ayeni, A.O., Agboola, O. and Elehinafe, F.B. (2021). A review on the sustainable energy generation from the pyrolysis of coconut biomass. *Sci. Afr.*, 13: e00909. https://doi.org/10.1016/j.sciaf.2021.e00909.

Babu, B.V. and Chaurasia, A.S. (2003). Modeling, simulation and estimation of optimum parameters in pyrolysis of biomass. *Energy Convers. Manag.*, 44: 2135–2158.

Babu, K.K.B.S., Nataraj, M., Tayappa, M., Vyas, Y., Mishra, R.K. and Acharya, B. (2024). Production of biochar from waste biomass using slow pyrolysis: Studies of the effect of pyrolysis temperature and holding time on biochar yield and properties. *Mater. Sci. Energy Technol.*, 7: 318–334.

Bachari, K., Millet, J.M.M., Benaïchouba, B., Cherifi, O. and Figueras, F. (2004). Benzylation of benzene by benzyl chloride over iron mesoporous molecular sieves materials. Journal of Catalysis, 221:55-61.

Bakraoui, M., Karouach, F., Ouhammou, B., Aggour, M., Essamri, A. and El Bari, H. (2020). Biogas production from recycled paper mill wastewater by UASB digester: optimal and mesophilic conditions. *Biotechnol. Rep.*, 25: e00402.

Banik, C., Lawrinenko, M., Bakshi, S. and Laird, D.A. (2018). Impact of pyrolysis temperature and feedstock on surface charge and functional group chemistry of biochars. *J. Environ. Qual.*, 47(3): 1–10. https://doi.org/10.2134/jeq2017.11.0432.

Bas, D. and Boyacı, I.H. (2007). Modeling and optimization I: Usability of response surface methodology. *J. Food Eng.*, 78: 836–845.

Basu, P. (2013). Biomass characteristics. In: *Biomass Gasification, Pyrolysis and Torrefaction*. Elsevier Inc., pp. 47–86.

Bayuo, J., Abukari, M.A. and Pelig-Ba, K.B. (2020). Optimization using central composite design (CCD) of response surface methodology (RSM) for biosorption of hexavalent chromium from aqueous media. *Appl. Water Sci.*, 10(6): 1–12.

Berrazoum, A., Marouf, R., Ouadjenia, F. and Schott, J. (2015). Bioadsorption of a reactive dye from aqueous solution by municipal solid waste. *Biotechnol. Rep.*, 7: 44–50.

Bhure, M.H., Rode, C.V., Chikate, R.C., Patwardhan, N. and Patil, S. (2007). Phosphotungstic acid as an efficient solid catalyst for intramolecular rearrangement of benzyl phenyl ether to 2-benzyl phenol. Catalysis Communications, 8(2):139–144.

Bombuwala Dewage, N., Liyanage, A.S., Smith, Q., Pittman, C.U., Perez, F., Hassan, E.B., Mohan, D. and Mlsna, T. (2019). Fast aniline and nitrobenzene remediation from

water on magnetized and nonmagnetized Douglas fir biochar. *Chemosphere*, 225: 943–953.

Boonmee, A. (2012). Hydrolysis of various Thai agricultural biomasses using the crude enzyme from *Aspergillus aculeatus* Iizuka Fr60 isolated from soil. *Braz. J. Microbiol.*, 43: 456–466.

Brahmi, L., Ali-Dahmane, T., Hamacha, R. and Hacini, S. (2016). Catalytic performance of Al-MCM-41 catalyst for the allylation of aromatic aldehydes with allyltrimethylsilane: Comparison with $TiCl_4$ as Lewis acid. Journal of Molecular Catalysis A: Chemical, 423:31–40.

Brewer, C.E., Chuang, V.J., Masiello, C.A., Gonnermann, H., Gao, X., Dugan, B., Driver, L.E., Panzacchi, P., Zygourakis, K. and Davies, C.A. (2014). New approaches to measuring biochar density and porosity. *Biomass Bioenergy*, 66: 176–185.

Brown, R.A., Kercher, A.K., Nguyen, T.H., Nagle, D.C. and Ball, W.P. (2006). Production and characterization of synthetic wood chars for use as surrogates for natural sorbents. *Org. Geochem.*, 37(3): 321–333. https://doi.org/10.1016/j.orggeochem.2005.10.008.

Bushra, B. and Remya, N. (2020). Biochar from pyrolysis of rice husk biomass – Characteristics, modification and environmental application. *Biomass Convers. Biorefin.*, in press.

Cai, R., Pei, X., Pan, H., Wan, K., Chen, H., Zhang, Z. and Zhang, Y. (2020). Biomass catalytic pyrolysis over zeolite catalysts with an emphasis on porosity and acidity: A state-of-the-art review. Energy & Fuels, 34(10):11771–11790. https://doi.org/10.1021/acs.energyfuels.0c02147

Cai, Y., Qi, H., Liu, Y. and He, X. (2016). Sorption/desorption behavior and mechanism of NH_4^+ by biochar as a nitrogen fertilizer sustained-release material. *J. Agric. Food Chem.*, 64(24): 4958–4964.

Candu, N., Florea, M., Coman, S.M. and Pârvulescu, V.I. (2011). Benzylation of benzene with benzyl alcohol on zeolite catalysts. Applied Catalysis A: General, 393(1.2), pp. 206.214. https://doi.org/10.1016/j.apcata.2010.11.044

Cazetta, A.L., Vargas, A.M.M., Nogami, E.M., Kunita, M.H., Guilherme, M.R., Martins, A.C., Silva, T.L., Moraes, J.C.G. and Almeida, V.C. (2011). NaOH-activated carbon of high surface area produced from coconut shell: kinetics and equilibrium studies from the methylene blue adsorption. *Chem. Eng. J.*, 174: 117–125.

Chan, K.Y. and Xu, Z. (2009). Biochar: Nutrient properties and their enhancement. In: Lehmann, J. and Joseph, S. (eds.), *Biochar for Environmental Management: Science and Technology*. Eastern Publishers, London, pp. 67–84.

Channiwala, S.A. and Parikh, P.P. (2002). A unified correlation for estimating HHV of solid, liquid and gaseous fuels. *Fuel*, 81(8): 1051–1063.

Chary, K.V.R., Naresh, D., Vishwanathan, V., Sadakane, M. and Ueda, W. (2007). Vapour phase hydrogenation of phenol over Pd/C catalysts: A relationship between dispersion, metal area and hydrogenation activity. *Catal. Commun.*, 8(3): 471–477. https://doi.org/10.1016/j.catcom.2006.07.029.

Chellappan, S., Nair, V., Sajith, V. and Aparna, K. (2018). Synthesis, optimization and characterization of biochar-based catalyst from sawdust for simultaneous esterification and transesterification. *Chin. J. Chem. Eng.*, 26(12): 2654–2663.

Chen, D., Zhou, J. and Zhang, Q. (2014). Effects of heating rate on slow pyrolysis behavior, kinetic parameters and products properties of moso bamboo. *Bioresour. Technol.*, 169: 313–319. https://doi.org/10.1016/j.biortech.2014.07.009.

Chen, X., Yan, H., Ma, L., Fang, Q., Deng, S., Wang, X. and Yin, C. (2023). Moisture content effects on self-heating in stored biomass: An experimental study. *Energy*, 285: 129391. https://doi.org/10.1016/j.energy.2023.129391.

Chen, Y., Zhang, X. and Zhou, Z. (2019). Carbon-based substrates for highly dispersed nanoparticle and even single-atom electrocatalysts. *Small Methods*, 3: 1900050.

Chevella, D., Mameda, N., Kodumuri, S., Banothu, R., Gajula, K.S., Kutepov, B.I. and Namaa, N. (2018). Catalytic performance of supported catalysts for selective reactions. *Catal. Commun.*, 105: 20–25. https://doi.org/10.1016/j.catcom.2017.11.002.

Chi, S., Yu, G., Zhang, X., Zhang, Y., Liu, C., Li, Z., Li, B. and Cui, Q. (2019). Response surface optimization of ammonium sulfite pretreatment for fermentable sugar production from wheat straw. *Bioresources*, 14(2): 4603–4622.

Chintala, V., Kumar, S., Pandey, J.K., Sharma, A.K. and Kumar, S. (2017). Solar thermal pyrolysis of non-edible seeds to biofuels and their feasibility assessment. *Energy Convers. Manag.*, 153: 482–492.

Choudhary, V.R., Jana, S.K. and Kiran, B.P. (1999). Alkylation of benzene by benzyl chloride over H-ZSM-5 zeolite with its framework Al completely or partially substituted by Fe or Ga. *Catal. Lett.*, 59: 217–219.

Choudhary, V.R., Jana, S.K. and Mamman, A.S. (2002). Benzylation of benzene by benzyl chloride over Fe-modified ZSM-5 and H-β zeolites and Fe_2O_3 or $FeCl_3$ deposited on micro-, meso- and macro-porous supports. *Microporous Mesoporous Mater.*, 56: 65–71.

Claoston, N., Samsuri, A., Ahmad Husni, M. and Mohd Amran, M. (2014). Effects of pyrolysis temperature on the physicochemical properties of empty fruit bunch and

rice husk biochars. *Waste Manag. Res.*, 32(4): 331–339. https://doi.org/10.1177/0734242X14525822.

Collard, F.X., Blin, J., Bensakhria, A. and Valette, J. (2012). Influence of impregnated metal on the pyrolysis conversion of biomass constituents. *J. Anal. Appl. Pyrolysis*, 95: 213–226.

Cordero, T., Márquez, F., Rodríguez-Mirasol, J. and Rodríguez, J.J. (2001). Predicting heating values of lignocellulosic and carbonaceous materials from proximate analysis. *Fuel*, 80: 1567–1571.

Cornish-Bowden, A. (1999). Enzyme kinetics from a metabolic perspective. *Biochem. Soc. Trans.*, 27: 281–284.

Couto, N., Rouboa, A., Silva, V., Monteiro, E. and Bouziane, K. (2013). Influence of the biomass gasification processes on the final composition of syngas. *Energy Procedia*, 36: 596–606. https://doi.org/10.1016/j.egypro.2013.07.068.

Creamer, A.E., Gao, B. and Zhang, M. (2014). Carbon dioxide capture using biochar produced from sugarcane bagasse and hickory wood. *Chem. Eng. J.*, 249: 174–179. https://doi.org/10.1016/j.cej.2014.03.105.

Cross, A. and Sohi, S.P. (2013). A method for screening the relative long-term stability of biochar. GCB Bioenergy, 5:215-220.

Cuong, N.D., Hoa, N.D., Hoa, T.T., Khieu, D.Q., Quang, D.T., Quang, V.V. and Hieu, N.V. (2014). Nanoporous hematite nanoparticles: Synthesis and applications for benzylation of benzene and aromatic compounds. *J. Alloys Compd.*, 582: 83–87.

Daniel, W.W. (1991). *Biostatistics: A foundation for analysis in health sciences*, 5th edn. Wiley, New York.

Dehkhoda, A.M. and Ellis, N. (2013). Biochar-based catalyst for simultaneous reactions of esterification and transesterification. *Catal. Today*, 207: 86–92. https://doi.org/10.1016/j.cattod.2011.12.005.

Dehkhoda, A.M., West, A.H. and Ellis, N. (2010). Biochar-based solid acid catalyst for biodiesel production. *Appl. Catal. A: Gen.*, 382: 197–204.

Deng, Y., Zhang, T. and Wang, Q. (2017). Biochar adsorption treatment for typical pollutants removal in livestock wastewater: A review. *Eng. Appl. Biochar*, 5: 72–79.

Dev, A., Srivastava, A.K. and Karmakar, S. (2018). New generation hybrid nanobiocatalysts: the catalysis redefined. In: Hussain, C.M. (ed.) Handbook of Nanomaterials for Industrial Applications. Elsevier Inc., pp. 217–231.

Devi, B.L.A.P., Reddy, T.V.K., Lakshmi, K.V. and Prasad, R.B.N. (2014). A green recyclable SO_3H-carbon catalyst derived from glycerol for the production of biodiesel from FFA-containing karanja (Pongamia glabra) oil in a single step. Bioresource Technology, 153:370–373.

Dhyani, V. and Bhaskar, T. (2018). A comprehensive review on the pyrolysis of lignocellulosic biomass. *Renew. Energy*, 129: 695–716.

Diallo, I., Thiam, A., Diop, B., Mbow, B., Fofana, M., Faye, F.D., Fall, E.H.A. and Sene, A. (2025). Brief review on the evolution of catalysis in chemistry. American Journal of Chemistry, 15(2):25–42.

Dougherty, M.J., Tran, H., Stavila, V., Hadi, M.Z., et al. (2014). Cellulosic biomass pretreatment and sugar yields as a function of biomass particle size. *PLOS ONE*, 9(6): e100836. https://doi.org/10.1371/journal.pone.0100836.

Du, C., Song, Y., Shi, S., Jiang, B., Yang, J. and Xiao, S. (2020). Preparation and characterization of a novel Fe_3O_4–graphene–biochar composite for crystal violet adsorption. *Sci. Total Environ.*, 711: 134662.

Dung, P.D., Babick, F., Nguyen Minh, T., Wessely, B. and Stintz, M. (2017). Modelling the influence of mass transfer on fixed-bed photocatalytic membrane reactors. *Chem. Eng. Sci.*, 173: 242–252.

Duwiejuah, A.B., Abubakari, A.H., Quainoo, A.K. and Amadu, Y. (2020). Review of biochar properties and remediation of metal pollution of water and soil. *J. Health Pollut.*, 10(27): 200902. https://doi.org/10.5696/2156-9614-10.27.200902.

Egbosiuba, T.C. (2022). Biochar and bio-oil fuel properties from nickel nanoparticles assisted pyrolysis of cassava peel. *Heliyon*, 8(8): e10114. https://doi.org/10.1016/j.heliyon.2022.e10114.

Elkhalifa, S., Al-Ansari, T., Mackey, H.R. and McKay, G. (2019). Food waste to biochars through pyrolysis: A review. *Resour. Conserv. Recycl.*, 144: 310–320.

Elnour, A.Y., Alghyamah, A.A., Shaikh, H.M., Poulose, A.M., Al-Zahrani, S.M., Anis, A. and Al-Wabel, M.I. (2019). Effect of pyrolysis temperature on biochar microstructural evolution, physicochemical characteristics, and its influence on biochar/polypropylene composites. *Appl. Sci.*, 9(6): 1149. https://doi.org/10.3390/app9061149.

Elnour, A.Y., Alghyamah, A.A., Shaikh, H.M., Poulose, A.M., Al-Zahrani, S.M., Anis, A. and Al-Wabel, M.I. (2019). Effect of pyrolysis temperature on biochar microstructural evolution, physicochemical characteristics, and its influence on biochar/polypropylene composites. *Appl. Sci.*, 9(6): 1149. https://doi.org/10.3390/app9061149.

Emojevwe, V. (2013). *Cocos nucifera* (coconut) fruit: A review of its medical properties. *Adv. Agric. Sci. Eng. Res.*, 3(3): 718–723.

Erdem, A. and Dogru, M. (2021). Process intensification: Activated carbon production from biochar produced by gasification highly porous carbon substances with low production costs. *Johnson Matthey Technol. Rev.*, 65: 352–365.

Fajrina, N., Tahir, M. (2019). 2D-montmorillonite-dispersed g-C3N4/TiO2 2D/0D nanocomposite for enhanced photo-induced H2 evolution from glycerol-water mixture. Appl. Surf. Sci. 471:1053-1064.

Fan, Y., Wang, B., Yuan, S., Wu, X., Chen, J. and Wang, L. (2010). Adsorptive removal of chloramphenicol from wastewater by NaOH-modified bamboo charcoal. *Bioresour. Technol.*, 101: 7661–7664.

Fang, J., Zhan, L., Ok, Y.S. and Gao, B. (2018). Mini review of potential applications of hydrochar derived from hydrothermal carbonization of biomass. *J. Ind. Eng. Chem.*, 57: 15–21.

Fellet, G., Marmiroli, M. and Marchiol, L. (2014). Elements uptake by metal accumulator species grown on mine tailings amended with three types of biochar. *Sci. Total Environ.*, 468–469: 598–608.

Feng, Z.J. and Zhu, L.Z. (2018). Sorption of phenanthrene to biochar modified by base. *Front. Environ. Sci. Eng.*, 12: 1. https://doi.org/10.1007/s11783-017-0978-7.

Ferreiro, A.I., Ferreira, A.F., Fernandes, E.C. and Coelho, P. (2024). Influence of process parameters on biomass gasification: A review of experimental studies in entrained flow reactors and drop-tube furnaces. *Biomass Bioenergy*, 185: 107217. https://doi.org/10.1016/j.biombioe.2024.107217.

Fidel, R.B., Laird, D.A., Thompson, M.L. and Lawrinenko, M. (2017). Characterization and quantification of biochar alkalinity. Chemosphere, 167:367-373.

Fogler, H.S. (2016). Elements of Chemical REACTION Engineering. 5th ed. International Series in the Physical and Chemical Engineering Sciences. Upper Saddle River, NJ: Prentice Hall, PP. 31-32.

Friedl, A.P., Elias, R.H. and Varmuza, K. (2005). Prediction of heating values of biomass fuel from elemental composition. *Anal. Chim. Acta*, 544(1–2): 191–198.

Gan, Q., Hou, H., Liang, S., Qiu, J., Tao, S., Yang, L., Yu, W., Xiao, K., Liu, B., Hu, J., Wang, Y. and Yang, J. (2020). Sludge-derived biochar with multivalent iron as an efficient Fenton catalyst for degradation of 4-chlorophenol. *Sci. Total Environ.*, 725: 138299.

Gao, S. and DeLuca, T.H. (2016). Influence of biochar on soil nutrient transformations, nutrient leaching, and crop yield. *Adv. Plants Agric. Res.*, 4(5): 00150.

Gaskin, J., Steiner, C., Harris, K., Das, K.C. and Bibens, B. (2008). Effect of low-temperature pyrolysis conditions on biochar for agricultural use. *Trans. ASABE*, 51(6): 2061–2069. https://doi.org/10.13031/2013.25409.

Gawande, M.B., Fornasiero, P. and Zbořil, R. (2020). Carbon-based single-atom catalysts for advanced applications. *ACS Catal.*, 10: 2231–2259.

Gazulla, M. F., Rodrigo, M., Orduña, M., and Ventura, M. J., 2016. Determination of organic oxygen in petroleum cokes an coals. Microchemical Journal, 126:538– 544. doi:10.1016/j.microc.2016.01.018

Geetha, T., Smitha, J.K., Sebastian, M., Litty, M.I., Joseph, B., Joseph, J. and Nisha, T.S. (2024). Synthesis and characterization of nano iron oxide biochar composite for

efficient removal of crystal violet from water. *Heliyon*, 10(21): e39450. https://doi.org/10.1016/j.heliyon.2024.e39450.

Ghodke, S.V. and Chudasama, U.V. (2015). Friedel–Crafts alkylation and acylation of aromatic compounds under solvent-free conditions using solid acid catalysts. *Int. J. Chem. Stud.*, 2(5): 27–34.

González Martínez, M., Couce, A.A., Dupont, C., da Silva Perez, D., Thiéry, S., Meyer, X. and Gourdon, C. (2022). Torrefaction of cellulose, hemicelluloses and lignin extracted from woody and agricultural biomass in TGA-GC/MS: Linking production profiles of volatile species to biomass type and macromolecular composition. *Ind. Crops Prod.*, 176: 114350.

Guel-Nájar, N.A., Rios-Hurtado, J.C., Muzquiz-Ramos, E.M., Dávila-Pulido, G.I., González-Ibarra, A.A. and Pat-Espadas, A.M. (2023). Magnetic biochar obtained by chemical coprecipitation and pyrolysis of corn cob residues: Characterization and methylene blue adsorption. *Materials*, 16(8): 3127. https://doi.org/10.3390/ma16083127.

Guo, F., Peng, K., Liang, S., Jia, X., Jiang, X. and Qian, L. (2019). Evaluation of the catalytic performance of different activated biochar catalysts for removal of tar from biomass pyrolysis. *Fuel*, 258: 116204.

Gupta, S., Kua, H.W. and Koh, H.J. (2018). Application of biochar from food and wood waste as green admixture for cement mortar. *Sci. Total Environ.*, 619: 419–435.

Hardwick, C. (2011). *Practical Design of Experiment: DOE Made Easy*. Minitab Statistical Software, Minitab Inc., USA.

Heravi, M.M. and Zadsirjan, V. (2021). Recent advances in applications of Friedel–Crafts reactions in total synthesis of alkaloids. In: *Recent Applications of Selected Name*

Reactions in the Total Synthesis of Alkaloids, pp. 59–105. https://doi.org/10.1016/B978-0-12-824021-2.00009-1.

Heravi, M.M., Zadsirjan, V., Saedi, P. and Momeni, T. (2018). Applications of Friedel–Crafts reactions in total synthesis of natural products. *RSC Adv.*, 8: 40061–40163.

Hervy, M., Berhanu, S., Weiss-Hortala, E., Chesnaud, A., Gérente, C., Villot, A., Pham, M.D., Thorel, A., Le, C.L. and Nzihou, A. (2017). Multi-scale characterisation of chars mineral species for tar cracking. *Fuel*, 189: 88–97.

Houben, D., Evrard, L. and Sonnet, P. (2012). Mobility, bioavailability and pH-dependent leaching of cadmium, zinc and lead in a contaminated soil amended with biochar. *Chemosphere*, 92: 1450–1457.

Hu, Y., Zhu, Y., Zhang, Y., Lin, T., Zeng, G., Zhang, S., Wang, Y., He, W., Zhang, M. and Long, H. (2019). An efficient adsorbent: Simultaneous activated and magnetic ZnO doped biochar derived from camphor leaves for ciprofloxacin adsorption. *Bioresour. Technol.*, 288: 121511.

Huff, M.D. and Lee, J.W. (2016). Biochar-surface oxygenation with hydrogen peroxide. *J. Environ. Manage.*, 165: 17–21. https://doi.org/10.1016/j.jenvman.2015.08.046.

Igalavithana, A.D., Mandal, S., Niazi, N.K., Vithanage, M., Parikh, S.J., Mukome, F.N.D., Rizwan, M., Oleszczuk, P., Al-Wabel, M. and Bolan, N. (2017). Advances and future directions of biochar characterization methods and applications. *Crit. Rev. Environ. Sci. Technol.*, 47: 2275–2330.

Iqbal, A., Tan, K.-H., Shaari, U.S., Ahmad, N.I.N.B., Adam, F., Lee, H.V., Yusop, R.M., Abu Bakar, N.H.H., Lee, H.L., Pauzi, H., Abd Malik, M.F.I., Jusoh, A.F., Wilson, L.D., Ahmad, M.N., Hussain, M.H. and Mohamad Ibrahim, M.N. (2020). Friedel–Crafts benzylation of toluene catalyzed by $ZnCl_2/SiO_2$ heterogeneous catalyst to

para- and ortho-mono-benzylated toluene. *J. Iranian Chem. Soc.*, 17(7): 1615–1626. https://doi.org/10.1007/s13738-020-01888-0.

Ivanovski, M., Goricanec, D., Krope, J. and Urbancl, D. (2022). Torrefaction pretreatment of lignocellulosic biomass for sustainable solid biofuel production. *Energy*, 240: 122483.

Jacobsson, S. and Johnson, A. (2000). The diffusion of renewable energy technology: an analytical framework and key issues for research. *Energy Policy*, 28(9): 625–640.

Jafri, N., Wong, W.Y., Doshi, V., Yoon, L.W. and Cheah, K.H. (2018). A review on production and characterization of biochars for application in direct carbon fuel cells. *Process Saf. Environ. Prot.*, 118: 152–166. https://doi.org/10.1016/j.psep.2018.06.036.

Jain, A., Balasubramanian, R. and Srinivasan, M.P. (2016). Hydrothermal conversion of biomass waste to activated carbon with high porosity: a review. *Chem. Eng. J.*, 283: 789–805.

Janu, R., Mrlik, V., Ribitsch, D., Hofman, J., Sedláček, P., Bielská, L. and Soja, G. (2021). Biochar surface functional groups as affected by biomass feedstock, biochar composition and pyrolysis temperature. *Carbon Res. Convers.*, 4(5): 1–10. https://doi.org/10.1016/j.crcon.2021.01.003.

Jha, S., Gaur, R., Shahabuddin, S. and Tyagi, I. (2023). Biochar as sustainable alternative and green adsorbent for the remediation of noxious pollutants: A comprehensive review. *Toxics*, 11(2): 117. https://doi.org/10.3390/toxics11020117.

Jiang, S.-F., Ling, L.-L., Chen, W.-J., Liu, W.J., Li, D.C. and Jiang, H. (2019). High efficient removal of bisphenol A in a peroxymonosulfate/iron functionalized biochar system: Mechanistic elucidation and quantification of the contributors. *Chem. Eng. J.*, 359: 572–583.

Jin, H., Capareda, S., Chang, Z., Gao, J., Xu, Y. and Zhang, J. (2014). Biochar pyrolytically produced from municipal solid wastes for aqueous As(V) removal: adsorption property and its improvement with KOH activation. *Bioresour. Technol.*, 169: 622–629.

Jitjamnong, J., Thunyaratchatanon, C., Luengnaruemitchai, A., Kongrit, N., Kasetsomboon, N., Sopajarn, A., Chuaykarn, N. and Khantikulanon, N. (2021). Response surface optimization of biodiesel synthesis over a novel biochar-based heterogeneous catalyst from cultivated (Musa sapientum) banana peels. *Biomass Conv. Bioref.*, 11(6): 2795–2811.

Jose, L.G.-E., Tom, S., Chris, D.C. and Mark, E.H. (2011). Effects of biochar and the earthworm *Eisenia fetida* on the bioavailability of polycyclic aromatic hydrocarbons and potentially toxic elements. *Environ. Pollut.*, 159(2): 616–622.

Joseph, S., Cowie, A.L., Van Zwieten, L., Bolan, N., Budai, A., Buss, W., Cayuela, M.L., Graber, E.R., Ippolito, J.A., Kuzyakov, Y., Luo, Y., Ok, Y.S., Palansooriya, K.N., Shepherd, J., Stephens, S., Weng, Z.H. and Lehmann, J. (2021). How biochar works, and when it doesn't: A review of mechanisms controlling soil and plant responses to biochar. *Glob. Change Biol. Bioenergy*, 13(11): 1731–1764. https://doi.org/10.1111/gcbb.12885.

Jung, K.W., Choi, B.H., Jeong, T.U. and Ahn, K.H. (2016). Facile synthesis of magnetic biochar/Fe3O4 nanocomposites using electro-magnetization technique and its application on the removal of acid orange 7 from aqueous media. *Bioresour. Technol.*, 220: 672–676.

Jurado-Alameda, E., Bravo-Rodríguez, V., Bailón-Moreno, R., Nuñez-Olea, J. and Altmajer, V.D. (2003). Bath-substrate-flow method for evaluating the detersive and dispersant performance of hard-surface detergents. *Ind. Eng. Chem. Res.*, 42: 4303–4310.

Kakasaheb, Y., Pratika, T. and Vijay, V. (2015). Environmentally benign process for benzylation of toluene to mono-benzylated toluene over highly active and stable hierarchical zeolite catalyst. Applied Petrochemical Research, 5:113-119.

Kalu, A.M., Edore, B.E., Madojemu, G.O., Ejimadu, C.M., Idode, V.O. and Okieimen, F.E. (2021). Total hydrocarbon degradation of crude oil contaminated soil using mixture of poultry manure and biochar: Optimization of amendment process variables. *Int. J. Res. Chem. Environ.*, 11(1): 1–8.

Karimi, A., Moezzi, A., Chorom, M. and Enayatizamir, N. (2020). Application of biochar changed the status of nutrients and biological activity in a calcareous soil. *J. Soil Sci. Plant Nutr.*, 20: 450–459.

Kastner, J.R., Miller, J., Geller, D.P., Locklin, J., Keith, L.H. and Johnson, T. (2012). Catalytic esterification of fatty acids using solid acid catalysts generated from biochar and activated carbon. *Catal. Today*, 190: 122–132.

Khan, M.H., Akash, N.M., Akter, S., Rukh, M., Nzediegwu, C. and Islam, M.S. (2023). A comprehensive review of coconut-based porous materials for wastewater treatment and CO_2 capture. *J. Environ. Manag.*, 338: 117825. https://doi.org/10.1016/j.jenvman.2023.117825.

Khorram, M.S., Zhang, Q., Lin, D., Zheng, Y., Fang, H. and Yu, Y. (2016). Biochar: a review of its impact on pesticide behavior in soil environments and its potential applications. *J. Environ. Sci. (China)*, 44: 269–279.

Kim, C., Zhu, C., Aoki, Y. and Habazaki, H. (2019). Heteroatom-doped porous carbon with tunable pore structure and high specific surface area for high performance supercapacitors. *Electrochim. Acta*, 314: 173–187.

Kim, K.H., Cho, T.-S. and Choi, J.W. (2012). Influence of pyrolysis temperature on physicochemical properties of biochar obtained from the fast pyrolysis of pitch pine

(Pinus rigida). *Bioresour. Technol.*, 118: 158–162. doi:10.1016/j.biortech.2012.04.094.

Kim, P., Johnson, A., Edmunds, C.W., Radosevich, M., Vogt, F., Rials, T.G. and Labbé, N. (2011). Surface functionality and carbon structures in lignocellulosic-derived biochars produced by fast pyrolysis. *Energy Fuels*, 25: 4693–4703.

Kitano, M., Yamaguchi, D., Suganuma, S., Nakajima, K., Kato, H., Hayashi, S., Hara, M. (2009). Adsorption-enhanced hydrolysis of β-1,4-glucan on graphene-based amorphous carbon bearing SO3H, COOH, and OH groups. Langmuir. 25:5068-5075.

Klasson, K.T. (2017). Biochar characterization and a method for estimating biochar quality from proximate analysis results. *Biomass and Bioenergy*, 96: 50–58.

Kokel, A., Schäfer, C. and Török, B. (2019). Organic synthesis using environmentally benign acid catalysis. Current Organic Synthesis, 16(4):615–649. https://doi.org/10.2174/1570179416666190206141028

Kordala, N. and Wyszkowski, M. (2024). Zeolite properties, methods of synthesis, and selected applications. Molecules, 29(5):1069.

Koyande, S.N., Jaiswal, R.G. and Jayaram, R.V. (1998). Reaction kinetics of benzylation of benzene with benzyl chloride on sulfate-treated metal oxide catalysts. Industrial & Engineering Chemistry Research, 37:908-913.

Králik, M., Koóš, P., Markovič, M. and Lopatka, P. (2025). Research and Developments of Heterogeneous Catalytic Technologies. *Molecules*, 30(15): 3279. https://doi.org/10.3390/molecules30153279

Kumar, M., Ambika, S., Hassani, A. and Nidheesh, P.V. (2023). Waste to catalyst: Role of agricultural waste in water and wastewater treatment. *Science of The Total Environment*, 858(1):159762.

Kumar, P., Barrett, P., Delwiche, M.J. and Stroeve, P. (2009). Methods for pre-treatment of lignocellulosic biomass for efficient hydrolysis and biofuel production. *Ind. Eng. Chem. Res.*, 48(8): 3713–3729.

Kuryntseva, P., Karamova, K., Galitskaya, P., Selivanovskaya, S. and Evtugyn, G. (2023). Biochar functions in soil depending on feedstock and pyrolyzation properties with particular emphasis on biological properties. *Agriculture*, 13(10). https://doi.org/10.3390/agriculture13102003

Lachter, E.R., San Gil, R.A.S. and Valdivieso, L.G. (2024). Friedel–Crafts reactions revisited: Some applications in heterogeneous catalysis. *Curr. Org. Chem.*, 28: 1060–1068.

Lachter, E.R., San Gil, R.A.S. and Valdivieso, L.G. (2024). Friedel–Crafts reactions revisited: Some applications in heterogeneous catalysis. Current Organic Chemistry, 28(14), pp. 1060–1068.

Lam, S.S., Lee, X.Y., Nam, W.L., Phang, X.Y., Liew, R.K., Yek, P.N., Ho, Y.L., Ma, N.L. and Rosli, M.H. (2019). Microwave vacuum pyrolysis conversion of waste mushroom substrate into biochar for use as growth medium in mushroom cultivation. *J. Chem. Technol. Biotechnol.*, 94: 1406–1415.

Lamberti, E., Viscusi, G., Kiani, A. and Boumezough, Y. (2024). Efficiency of dye adsorption of modified biochar: A comparison between chemical modification and ball milling assisted treatment. *Biomass and Bioenergy*, 185: 107247. https://doi.org/10.1016/j.biombioe.2024.107247

Laribi, M., Bachari, K., Chebout, R. and Touati, M. (2012). Synthesis, characterization and catalytic application of the nickel containing mesoporous silica. *J. Assoc. Arab Univ. Basic Appl. Sci.*, 12(1): 42–47.

Lee, J., Lee, K., Sohn, D., Kim, Y.M. and Park, K.Y. (2018). Hydrothermal carbonization of lipid extracted algae for hydrochar production and feasibility of using hydrochar as a solid fuel. *Energy*, 153: 913–920.

Lee, J., Sarmah, A.K. and Kwon, E.E. (2019). Production and formation of biochar. In: Y.S. Ok, D.C.W. Tsang, N. Bolan and J.M. Novak (Eds.) *Biochar from Biomass and Waste*, Elsevier; Chapter 1, pp. 3–18.

Lee, Y., Kim, Y.T., Kwon, E.E. and Lee, J. (2020). Biochar as a catalytic material for the production of 1,4-butanediol and tetrahydrofuran from furan. *Environ. Res.*, 184: 109325. https://doi.org/10.1016/j.envres.2020.109325

Lehmann, J. and Joseph, S. (2015). Biochar for Environmental Management: An Introduction. In: *Biochar for Environmental Management*, 2nd Edition, Routledge, London, Chapter 1, pp. 1–13.

Lehmann, J. and Joseph, S. (2015). Biochar for Environmental Management: An Introduction. In: *Biochar for Environmental Management*, 2nd Edition, Routledge, London, Chapter 1, pp. 1–13.

Lei, Z., Bai, S., Dang, L., Xia, H., Xu, Q., Cao, Y., An, L., Zhao, M., Lo, A.-Y. and Liu, S.-B. (2009). Fe2O3/SBA-15 catalyst synthesized by chemical vapor infiltration for Friedel–Crafts alkylation reaction. *Microporous and Mesoporous Mater.*, 123: 306–313.

Lei, Z., Bai, S., Dang, L., Xia, H., Xu, Q., Cao, Y., An, L., Zhao, M., Lo, A.-Y. and Liu, S.-B. (2009). Fe2O3/SBA-15 catalyst synthesized by chemical vapor infiltration for

Friedel–Crafts alkylation reaction. *Microporous and Mesoporous Mater.*, 123: 306–313.

Leng, K., Ren, Y., Wang, W., Wang, R., Gao, K. and Li, X. (2022). Evaluation of catalytic performance of hierarchical zeolites in Friedel-Crafts fixed-bed alkylation. ChemistrySelect, 7(41):e202201405. https://doi.org/10.1002/slct.202201405

Leng, L., Huang, H., Li, H., Li, J. and Zhou, W. (2019). Biochar stability assessment methods: A review. *Sci. Total Environ.*, 647: 210–222. doi:10.1016/j.scitotenv.2018.07.402

Li, C., Huang, Q., Zhang, H., Wang, Q., Xue, R., Guo, G., Hu, J., Li, T., Wang, J. and Hu, S. (2021). Characterization of biochars produced by co-pyrolysis of hami melon (cantaloupes) straw mixed with polypropylene and their adsorption properties of cadmium. *Int. J. Environ. Res. Public Health*, 18: 11413. doi:10.3390/ijerph182111413

Li, H., Dong, X., da Silva, E.B., de Oliveira, L.M., Chen, Y. and Ma, L.Q. (2017). Mechanisms of metal sorption by biochars: biochar characteristics and modifications. *Chemosphere*, 178: 466–478.

Li, J.C., Wei, Z., Liu, D., Du, D., Lin, Y. and Shao, M. (2019). Dispersive single-atom metals anchored on functionalized nanocarbons for electrochemical reactions. *Top. Curr. Chem.*, 377: 4.

Li, M., Zheng, Y., Chen, Y. and Zhu, X. (2014). Biodiesel production from waste cooking oil using a heterogeneous catalyst from pyrolyzed rice husk. Bioresource Technology, 154, pp. 345–348.

Li, R., Shahbazi, A., Wang, L., Zhang, B., Chung, C.-C., Dayton, D. and Yan, Q. (2018). Nanostructured molybdenum carbide on biochar for CO_2 reforming of CH4. *Fuel*, 225: 403–410.

Li, Y., Shao, J., Wang, X., Deng, Y., Yang, H. and Chen, H. (2014). Characterization of modified biochars derived from bamboo pyrolysis and their utilization for target component (furfural) adsorption. *Energy Fuels*, 28(8): 5119–5127.

Li, Z., Yuqing, S., Yang, Y., Han, Y., Wang, T., Chen, J. and Tsang, D. (2019). Biochar-supported nanoscale zero-valent iron as an efficient catalyst for organic degradation in groundwater. *J. Hazard. Mater.*, 383: 121240. doi:10.1016/j.jhazmat.2019.121240

Liang, B., Lehmann, J., Solomon, D., Kinyangi, J., Grossman, J., O'Neill, B., Skjemstad, J.O., Thies, J., Luizão, F.J., Petersen, J. and Neves, E.G. (2006). Black carbon increases cation exchange capacity in soils. *Soil Sci. Soc. Am. J.*, 70: 1719–1730.

Liang, C., Gasco, G., Fu, S., Mendez, A. and Paz-Ferreiro, J. (2016). Biochar from pruning residues as a soil amendment: effects of pyrolysis temperature and particle size. *Soil Tillage Res.*, 164: 3–10.

Liang, J., Li, X., Yu, Z., Zeng, G., Luo, Y., Jiang, L., Yang, Z., Qian, Y. and Wu, H. (2017). Amorphous MnO_2 modified biochar derived from aerobically composted swine manure for adsorption of Pb (II) and Cd (II). *ACS Sustain. Chem. Eng.*, 5: 5049–5058.

Liu, C., Chen, T., Zhang, F., Han, H., Yi, B., Meng, J., Chi, D. and Ok, Y.S. (2025). Engineered biochar effects on methane emissions and rice yield under alternate wetting and drying in paddy soils. Environmental Technology & Innovation, 38:104133.

Liu, Q.-Y., Yang, F., Liu, Z.-H. and Li, G. (2015). Preparation of SnO_2–Co_3O_4/C biochar catalyst as a Lewis acid for corncob hydrolysis into furfural in water medium. *J. Ind. Eng. Chem.*, 26: 46–54.

Liu, W.J., Jiang, H. and Yu, H.Q. (2015). Development of biochar-based functional materials: toward a sustainable platform carbon material. *Chem. Rev.*, 115: 12251–12285.

Liu, X., Zhang, Y., Li, Z., Feng, R. and Zhang, Y. (2014). Characterization of corncob-derived biochar and pyrolysis kinetics in comparison with corn stalk and sawdust. *Bioresour. Technol.*, 170: 76–82.

Liu, Y., Sohi, S.P., Liu, S., Guan, J., Zhou, J. and Chen, J. (2019). Adsorption and reductive degradation of Cr(VI) and TCE by a simply synthesized zero valent iron magnetic biochar. *J. Environ. Manage.*, 235: 276–281.

Liu, Y.-L., Liu, L., Wang, Y.-L., Han, Y.-C., Wang, D. and Chen, Y.-J. (2008). Calix[n]arene sulfonic acids bearing pendant aliphatic chains as recyclable surfactant-type Brønsted acid catalysts for allylic alkylation with allyl alcohols in water. Green Chem., 10:635–640 https://doi.org/10.1039/b719278a

Liyana-Pathirana, C. and Shahidi, F. (2005). Optimization of extraction of phenolic compounds from wheat using response surface methodology. *Food Chem.*, 93(1): 47–56. https://doi.org/10.1016/j.foodchem.2004.08.050

Longo, L., Baldassin, D., Di Michele, A., Bittencourt, C., Menegazzo, F. and Signoretto, M. (2025). Activation strategies for rice husk biochar: Enhancing porosity and performance as a support for Pd catalysts in hydrogenation reactions. *Catal. Sci. Technol.*, 15: 5101–5115. https://doi.org/10.1039/D5CY00242G

Luo, B., Huang, G., Yao, Y., An, C., Zhang, P. and Zhao, K. (2021). Investigation into the influencing factors and adsorption characteristics in the removal of sulfonamide antibiotics by carbonaceous materials. *J. Clean. Prod.*, 319: 128692. https://doi.org/10.1016/j.jclepro.2021.128692

Luo, X., Wu, H., Li, C., Li, Z., Li, H., Zhang, H., Li, Y., Su, Y. and Yang, S. (2020). Heteropoly acid-based catalysts for hydrolytic depolymerization of cellulosic biomass. Frontiers in Chemistry, 8:580146. https://doi.org/10.3389/fchem.2020.580146

Luque, R., Budarin, V., Clark, J.H., Shuttleworth, P. and White, R.J. (2011). Starbon® acids in alkylation and acetylation reactions: Effect of the Brönsted-Lewis acidity. *Catal. Commun.*, 12: 1471–1476.

Ma, Y., Li, P., Yang, L., Wu, L., He, L., Gao, F., Qi, X. and Zhang, Z. (2020). Iron/zinc and phosphoric acid modified sludge biochar as an efficient adsorbent for fluoroquinolone antibiotics removal. *Ecotoxicol. Environ. Saf.*, 196: 110550.

Mahmoud, E.R.I., Aly, H.M., Hassan, N.A., Aljabri, A., Khan, A.L. and El-Labban, H.F. (2024). Biochar from date palm waste via two-step pyrolysis: A modified approach for Cu (II) removal from aqueous solutions. *Processes*, 12(6): 1189. https://doi.org/10.3390/pr12061189

Malghani, S., Gleixner, G. and Trumbore, S.E. (2013). Chars produced by slow pyrolysis and hydrothermal carbonization vary in carbon sequestration potential and greenhouse gases emissions. *Soil Biol. Biochem.*, 62: 137–146. https://doi.org/10.1016/j.soilbio.2013.03.013

Mani, S., Kastner, J.R. and Juneja, A. (2013). Catalytic decomposition of toluene using a biomass derived catalyst. *Fuel Process. Technol.*, 114: 118–125.

Masek, O., Brownsort, P., Cross, A. and Sohi, S. (2013). Influence of production conditions on the yield and environmental stability of biochar. *Fuel*, 103: 151–155. https://doi.org/10.1016/j.fuel.2011.08.044

Masoumifard, N., Guillet-Nicolas, R. & Kleitz, F. (2018). Synthesis of engineered zeolitic materials: From classical zeolites to hierarchical core–shell materials. Advanced Materials, 30, 1704439. https://doi.org/10.1002/adma.201704439

Masud, M.A.A., Samaraweera, H., Mondol, M.M.H., Zhang, Y., Liu, Y. and Terry, L.G. (2025). Iron biochar synergy in aquatic systems through surface functionalities, electron transfer and reactive species dynamics. *npj Clean Water*, 8(1): 46. https://doi.org/10.1038/s41545-025-00471-5

McKendry, P. (2002a). Energy production from biomass (Part 1): Overview of biomass. *Bioresour. Technol.*, 83: 7–46.

McKendry, P. (2002b). Energy production from biomass (Part 2): Conversion technologies. *Bioresour. Technol.*, 83(1): 47–54.

Meacham, S.G. and Taylor, R.A. (2023). Selective alkylation of mandelic acid to diarylacetic acids over a commercial zeolite. *Chem. Commun.*, 59: 9243–9246. https://doi.org/10.1039/D3CC01444D

Mimmo, T., Panzacchi, P., Baratieri, M., Davies, C.A. and Tonon, G. (2014). Effect of pyrolysis temperature on miscanthus (Miscanthus × giganteus) biochar physical, chemical and functional properties. *Biomass Bioenergy*, 62: 149–157. https://doi.org/10.1016/j.biombioe.2014.01.004

Mishra, R.K., Lu, Q. and Mohanty, K. (2020). Thermal behaviour, kinetics and fast pyrolysis of Cynodon dactylon grass using Py-GC/MS and Py-FTIR analyser. *J. Anal. Appl. Pyrolysis*, 150: 104871.

Mohamed Noor, N., Shariff, A. and Abdullah, N. (2012). Slow pyrolysis of cassava wastes for biochar production and characterization. *Iranica J. Energy Environ.*, 3: 60–65.

Mohan, D., Singh, P., Sarswat, A., Steele, P.H. and Pittman, C.U. (2015). Lead sorptive removal using magnetic and nonmagnetic fast pyrolysis energy cane biochars. *J. Colloid Interface Sci.*, 448: 238–250.

Montgomery, D.C. (2001). *Design and Analysis of Experiments*, 5th ed. New York: John Wiley and Sons.

Moradi, M., Rezayat, M., Meiabadi, S., Karamimoghadam, M., Hillyard, S., Mateo, A., Casalino, G., Tanveer, Z., Adnan Manzoor, M., Iqbal, M.A. and Razmkhah, O. (2023). Capability enhancing of CO_2 laser cutting for PMMA sheet using statistical modeling and optimization. Applied Sciences, 13(23), 12601. https://doi.org/10.3390/app132312601

Mourabet, M., El Rhilassi, A., El Boujaady, H., Bennani-Ziatni, M. and Taitai, A. (2014). Use of response surface methodology for optimization of fluoride adsorption in an aqueous solution by Brushite. *Arab. J. Chem.*, 10: S3292–S3302. http://dx.doi.org/10.1016/j.arabjc.2013.12.028

Mukherjee, A., Zimmerman, A. R., and Harris, W. (2011). Surface chemistry variations among a series of laboratory-produced biochars. Geoderma, 163(3-4):247–255. doi:10.1016/j.geoderma.2011.04.021.

Myers, R.H. and Montgomery, D.C. (1995). *Response surface methodology: Process and product optimization using designed experiments*. New York: John Wiley and Sons, Inc.

Nabi, F., Kama, R., Sajid, S., Qadir, M., Kanwal, R., Memon, F.U., Ma, C. and Li, H. (2025). Synergistic effects of Mg and Fe-modified bimetallic biochar for immobilization of As and Cd in agricultural soils. *Environmental Chemistry and Ecotoxicology*, 7: 1059–1071. https://doi.org/10.1016/j.enceco.2025.1059

Nandiwale, K.Y., Thakur, P. and Bokade, V.V. (2015). Environmentally benign process for benzylation of toluene to mono-benzylated toluene over highly active and stable hierarchical zeolite catalyst. *Appl. Petrochem. Res.*, 5: 113–119. https://doi.org/10.1007/s13203-014-0096-4

Ni, X., Cen, K., Li, X., Cui, D., Liu, M., Zhu, L. and Chen, D. (2025). Cellulose upgradation by torrefaction pretreatment and effect of torrefaction severity on the quality of pyrolysis products. *Ind. Crops Prod.*, 225: 120516.

Noman, M., Yu, G., Awugichew, D.T. and Li, X. (2024). Synthesis of surficial-modified green biochar catalyst generated by biogas residue biochar and potential application for catalytic ozonation degradation of ciprofloxacin. *Environ. Res.*, 257: 119314. https://doi.org/10.1016/j.envres.2024.119314

Noor, N.M., Shariff, A., Abdullah, N. and Aziz, S. (2019). Temperature effect on biochar properties from slow pyrolysis of coconut flesh waste. *Malays. J. Fundam. Appl. Sci.*, 15(2): 153–158. https://doi.org/10.11113/mjfas.v15n2.1015

Novak, J.M., Lima, I., Xing, B., Gaskin, J.W., Steiner, C., Das, K.C., Ahmedna, M., Rehrah, D., Watts, D.W., Busscher, W.J. and Schomberg, H. (2009). Characterization of designer biochar produced at different temperatures and their effects on a loamy sand. *Ann. Environ. Sci.*, 3: 195–206.

Novotný, M., Marković, M., Raček, J., Šipka, M., Chorazy, T., Tošić, I. and Hlavínek, P. (2023). The use of biochar made from biomass and biosolids as a substrate for green infrastructure: A review. *Sustain. Chem. Pharm.*, 32: 100999.

Ogede, L.O., Ejimadu, C.M. and Okieimen, F.E. (2024). Chemical and textural properties of melon seed shell-derived biochar relevant to their application in the remediation of contaminated soil. *Niger. Res. J. Eng. Environ. Sci.*, 9(2): 681–688.

Ohata, J. (2024). Friedel–Crafts reactions for biomolecular chemistry. *Org. Biomol. Chem.*, 22: 3544–3558. https://doi.org/10.1039/D4OB00406J

Oliveira, L.C.A., Pereira, E., Guimaraes, I.R., Vallone, A., Pereira, M., Mesquita, J.P. and Sapag, K. (2009). Preparation of activated carbons from coffee husks utilizing $FeCl_3$ and $ZnCl_2$ as activating agents. *J. Hazard. Mater.*, 165(1–3): 87–94

Othugile, L.E., Lekgoba, T. and Ntuli, F. (2022). Sequestration of heavy metals from coal wash water using biochar from pyrolysis of Morula shells. *Eur. J. Sustain. Dev. Res.*, 6(1): em0173. https://doi.org/10.21601/ejosdr/11377

Owoyemi, J.M., Akinwamide, T.O. and Ibidokun, A.O. (2022). Development of coconut plantation in Nigeria: Problems and prospects. *Int. J. Agric. Plant Sci.*, 4(1): 58–66

Pandit, C., Pandit, S., Pant, M., Ghosh, D., Agarwal, D., Lahiri, D., Nag, M. and Ray, R.R. (2023). A concise review on the synthesis and characterization of the pyrolytic lignocellulosic biomass for oil, char and gas production: Recent advances and its environmental application. *Chemistry Africa*, 6: 2237–2263. https://doi.org/10.1007/s42250-022-00523-4

Parmar, K. (2017). Biomass – An overview on composition, characteristics and properties. *IRA-Int. J. Appl. Sci.*, 7(1): 42. https://doi.org/10.21013/jas.v7.n1.p4

Parmar, P., Shukla, A., Goswami, D., Patel, B. and Saraf, M. (2020). Optimization of cadmium and lead biosorption onto marine Vibrio alginolyticus PBR1 employing a Box-Behnken design. Chemical Engineering Journal Advances, 4:100043.

Peňa, M.A. and Fierro, J.L.G. (2001). Chemical Structures and Performance of Perovskite Oxides. Chemical Reviews, 101:1981-2017. http://dx.doi.org/10.1016/j.apsusc.2014.10.168

Peng, P., Lang, Y.H. and Wang, X.M. (2016). Adsorption behavior and mechanism of pentachlorophenol on reed biochars: pH effect, pyrolysis temperature, hydrochloric acid treatment and isotherms. *Ecol. Eng.*, 90: 225–233

Penny, D.J. and Lindfield, G. (1999). *Numerical Methods Using MATLAB*. New Jersey: Prentice-Hall Inc.

Pérez-Mayoral, E., Calvino-Casilda, V. and Soriano, E. (2016). Metal-supported carbon-based materials: opportunities and challenges in the synthesis of valuable products. *Catal. Sci. Technol.*, 6: 1265–1291. https://doi.org/10.1039/c5cy01437a

Pertile, E., Dvorský, T., Václavík, V., Berkyová, L. and Balvín, P. (2025). Almond shell-derived biochar for lead adsorption: Comparative study of pyrolysis techniques and sorption capacities. *Molecules*, 30(20): 4121. https://doi.org/10.3390/molecules30204121

Petersen, H.I., Lassen, L., Rudra, A., Nguyen, L.X., Do, P.T.M. and Sanei, H. (2023). Carbon stability and morphotype composition of biochars from feedstocks in the Mekong Delta, Vietnam. *Int. J. Coal Geol.*, 271: 104233. https://doi.org/10.1016/j.coal.2023.104233

Pirkanniemi K, Sillanpaa M. (2002). Heterogeneous water phase catalysis as an environmental application: a review. Chemosphere, 48:1047-1060, DOI: 10.1016/S0045-6535(02)00168-6.

Prabakar, D., Manimudi, V.T., Suvetha, S., Sampath, S., Mahapatra, D.M., Rajendran, K. and Pugazhendhi, A. (2018). Advanced biohydrogen production using pretreated industrial waste: outlook and prospects. *Renew. Sust. Energy Rev.*, 96: 306–324.

Prajapati, S., Mishra, A.P. and Srivastava, A. (2012). Friedel–Crafts reaction: a review. *Int. J. Pharm. Chem. Biol. Sci.*, 2(1): 52–62.

Qambrani, N.A., Rahman, M.M., Won, S., Shim, S. and Ra, C. (2017). Biochar properties and eco-friendly applications for climate change mitigation, waste management, and wastewater treatment: A review. *Renew. Sust. Energy Rev.*, 79: 255–273.

Qian, C., Li, Q., Zhang, Z., Wang, X., Hu, J. and Cao, W. (2020). Prediction of higher heating values of biochar from proximate and ultimate analysis. *Fuel*, 265: 116925.

Qian, K. and Kumar, A. (2015). Reforming of lignin-derived tars over char-based catalyst using Py-GC/MS. *Fuel*, 162: 47–54.

Qin, L., Wu, Y., Hou, Z. and Jiang, E. (2020). Influence of biomass components, temperature and pressure on the pyrolysis behavior and biochar properties of pine nut shells. *Bioresour. Technol.*, 313: 123682.

Qu, J., Chu, H., Wang, M., Yu, R., Wang, S., Liu, T., Tao, Y., Han, S. and Zhang, Y. (2025). Synthesis, mechanism, and application of element-doped biochar for heavy metal contamination in agricultural soils. *Adv. Environ. Eng.*, 1: e002.

Rai, A., Mohanty, B. and Bhargava, R. (2016). Supercritical extraction of sunflower oil: A central composite design for extraction variables. *Food Chem.*, 192: 647–659.

Rajapaksha, A.U., Chen, S.S., Tsang, D.C., Zhang, M., Vithanage, M., Mandal, S., Gao, B., Bolan, N.S. and Ok, Y.S. (2016). Engineered/designer biochar for contaminant removal/immobilization from soil and water: potential and implication of biochar modification. *Chemosphere*, 148: 276–291.

Rangabhashiyam, S. and Balasubramanian, P. (2019). The potential of lignocellulosic biomass precursors for biochar production: Performance, mechanism and wastewater application: A review. *Ind. Crops Prod.*, 128: 405–423.

Reddy, N. and Yang, Y. (2015). Coconut husk fibers. In: Reddy, N. and Yang, Y. (eds.) *Innovative Biofibers from Renewable Resources.* Berlin, Heidelberg: Springer, Chapter 9: 31–34. https://doi.org/10.1007/978-3-662-45136-6_9

Ren, H., Cunha, E., Sun, Q., Li, Z., Kinloch, I.A., Young, R.J. and Fan, Z. (2019). Surface functionality analysis by Boehm titration of graphene nanoplatelets functionalized via a solvent-free cycloaddition reaction. *Nanoscale Adv.*, 1: 1432–1441.

Richard, I.M. (2001). *Chemical Kinetics and Catalysis.* New York: Wiley-Interscience. ISBN 0-471-24197-0.

Robertson, G.P., Sollins, P., Ellis, B.G. and Lajtha, K. (1999). Exchangeable ions, pH, and cation exchange capacity. In: Robertson, G. (ed.) *Standard Soil Methods for Long-Term Ecological Research.* New York: Oxford University Press, pp. 106–114.

Roshan, A., Ghosh, D. and Maiti, S.K. (2023). How temperature affects biochar properties for application in coal mine spoils? A meta-analysis. *Carbon Res.*, 2: 3.

Rueping, M. and Nachtsheim, B.J. (2010). A review of new developments in the Friedel–Crafts alkylation – from green chemistry to asymmetric catalysis. *Beilstein J. Org. Chem.*, 6: 1–31. https://doi.org/10.3762/bjoc.6.6

Saber, A., Smahi, A., Solhy, A., Nazih, R., Elaabar, B., Maizi, M. and Sebti, S. (2003). Heterogeneous catalysis of Friedel–Crafts alkylation by the fluorapatite alone and doped with metal halides. *J. Mol. Catal. A: Chem.*, 202: 229–237.

Sajjadi, B., Chen, W.-Y. and Egiebor, N.O. (2019). A comprehensive review on physical activation of biochar for energy and environmental applications. *Rev. Chem. Eng.*, 35: 735–776.

Sakhiya, A.K., Anand, A. and Kaushal, P. (2020). Production, activation, and applications of biochar in recent times. *Biochar*, 2: 253–285.

Samsuri, A.W., Sadegh-Zadeh, F. and Seh-Bardan, B.J. (2013). Adsorption of As(III) and As(V) by Fe coated biochars and biochars produced from empty fruit bunch and rice husk. *J. Environ. Chem. Eng.*, 1: 981–988.

Sepehri, A. and Sarrafzadeh, M.H. (2018). Effect of nitrifiers community on fouling mitigation and nitrification efficiency in a membrane bioreactor. *Chem. Eng. Process. – Process Intensif.*, 128: 10–18. https://doi.org/10.1016/j.cep.2018.04.006

Shadle, L.J., Indrawan, N., Breault, R.W. and Bennett, J. (2025). Gasification technology. In: *Handbook of Climate Change Mitigation and Adaptation*, pp. 793–882.

Sharma, A., Pareek, V. and Zhang, D. (2015). Biomass pyrolysis—A review of modelling, process parameters and catalytic studies. *Renew. Sust. Energy Rev.*, 50: 1081–1096.

Shen, Y. and Zhang, N. (2019). Facile synthesis of porous carbons from silica-rich rice husk char for volatile organic compounds (VOCs) sorption. *Bioresour. Technol.*, 282: 294–300.

Shen, Y., Areeprasert, C., Prabowo, B., Takahashi, F. and Yoshikawa, K. (2014). Metal nickel nanoparticles in-situ generated in rice husk char for catalytic reformation of tar and syngas from biomass pyrolytic gasification. *RSC Adv.*, 4(77): 41019–41027. https://doi.org/10.1039/C4RA07760A

Sheng, C. and Azevedo, J.L.T. (2005). Estimating the higher heating value of biomass fuels from basic analysis data. *Biomass Bioenergy*, 28(5): 499–507.

Shetty, A., Molahalli, V., Sharma, A. and Hegde, G. (2023). Biomass-derived carbon materials in heterogeneous catalysis: A step towards sustainable future. *Catalysts*, 13(1): 20. https://doi.org/10.3390/catal13010020

Shi, Z., Yang, W., Gu, Y., Liao, T. and Sun, Z. (2020). Metal-nitrogen-doped carbon materials as highly efficient catalysts: Progress and rational design. *Adv. Sci.*, 7(15): 2001069. https://doi.org/10.1002/advs.202001069

Shoaib, A.G.M., El-Sikaily, A., El Nemr, A. *et al.* (2022). Preparation and characterization of highly surface area activated carbons followed type IV from marine red alga (Pterocladia capillacea) by zinc chloride activation. *Biomass Conversion and Biorefinery*, 12:2253-2265. https://doi.org/10.1007/s13399-020-00760-8

Shoudho, K.N., Khan, T.H., Ara, U.R., Khan, M.R., Shawon, Z.B.Z. and Hoque, M.E. (2024). Biochar in global carbon cycle: Towards sustainable development goals. *Curr. Res. Green Sustain. Chem.*, 8: 100409. https://doi.org/10.1016/j.crgsc.2024.100409

Sikarwar, V.S., Zhao, M., Fennell, P.S., Shah, N. and Anthony, E.J. (2017). Progress in biofuel production from gasification. Progress in Energy and Combustion Science, 61:189–248.

Silveira, E.A., Santanna Chaves, B., Macedo, L., Ghesti, G.F., Evaristo, R.B.W., Cruz Lamas, G., Luz, S.M., Protásio, T.P. and Rousset, P. (2023). A hybrid optimization approach towards energy recovery from torrefied waste blends. *Renew. Energy*, 212: 151–165.

Singh, B., Dolk, M.M., Shen, Q. and Camps-Arbestain, M. (2017). Biochar pH, electrical conductivity and liming potential. In: *Biochar: A Guide to Analytical Methods*, pp. 23–38.

Smith, M.B. and March, J. (2007). *March's Advanced Organic Chemistry: Reactions, Mechanisms, and Structure*. 6th edn. Hoboken, NJ: John Wiley & Sons, Chapter 11, pp. 657–751.

Sohi, S.P., Krull, E., Lopez-Capel, E. and Bol, R. (2010). A review of biochar and its use and function in soil. *Adv. Agron.*, 105: 47–82.

Spokas, K.A. (2010). Review of the stability of biochar in soils: Predictability of O:C molar ratios. *Carbon Manage.*, 1: 289–303.

Sun, B., Khan, F.-A., Süss-Fink, G. and Therrien, B. (2017). Metal catalysts intercalated in smectite clays. In: *Encapsulated Catalysts*, Elsevier, pp. 387–441. https://doi.org/10.1016/B978-0-12-803836-9.00012-2

Sun, J., He, F., Pan, Y. and Zhang, Z. (2017). Effects of pyrolysis temperature and residence time on physicochemical properties of different biochar types. *Acta Agric. Scand., Section B – Soil Plant Sci.*, 67(1): 1–11. https://doi.org/10.1080/09064710.2016.1214745

Sun, K., Tang, J., Gong, Y. and Zhang, H. (2015). Characterization of potassium hydroxide (KOH) modified hydrochars from different feedstocks for enhanced removal of heavy metals from water. *Environ. Sci. Pollut. Res.*, 22: 16640–16651.

Sybounya, S. and Nitisoravit, R. (2021). Hybrid composite of modified commercial activated carbon and Zn–Ni hydrotalcite for fermentative hydrogen production. *J. Environ. Chem. Eng.*, 9(1): 104801.

Taha, S.M., Amer, M.E., Elmarsafy, A.E. and Elkady, M.Y. (2014). Adsorption of 15 different pesticides on untreated and phosphoric acid treated biochar and charcoal from water. *J. Environ. Chem. Eng.*, 2(4): 2013–2025.

Tan, X.F., Liu, Y.G., Gu, Y.L., Xu, Y., Zeng, G.M., Hu, X.J., Liu, S.B., Wang, X., Liu, S.M. and Li, J. (2016). Biochar-based nano-composites for the decontamination of wastewater: a review. *Bioresour. Technol.*, 212: 318–333.

Tan, Z.Q., Qiu, J.R., Zeng, H.C. et al. (2011). Removal of elemental mercury by bamboo charcoal impregnated with H_2O_2. *Fuel*, 90(4): 1471–1475. https://doi.org/10.1016/j.fuel.2010.12.004

Theivandran, G., Ibrahim, S.M. and Murugan, M. (2015). Fourier transform infrared (FT-IR) spectroscopic analysis of *Spirulina fusiformis*. *J. Med. Plants Stud.*, 3: 30–32.

Tilman, D.A. (1978). *Wood as energy resource*. New York: Academic Press.

Timur, S., Kantarli, I.C., Ikizoglu, E. and Yanik, J. (2006). Preparation of activated carbons from Oreganum stalks by chemical activation. *Energy Fuels*, 20: 2636–2641.

Tirol-Padre, A. and Ladha, J.K. (2004). Assessing the reliability of permanganate-oxidizable carbon as an index of soil labile carbon. Soil Science Society of America Journal, 68:969-978.

Tomczyk, A., Kondracki, B. and Szewczuk-Karpisz, K. (2023). Chemical modification of biochars as a method to improve its surface properties and efficiency in removing xenobiotics from aqueous media. *Chemosphere*, 312: 137238. https://doi.org/10.1016/j.chemosphere.2022.137238

Tomczyk, A., Sokołowska, Z. and Boguta, P. (2020). Biochar physicochemical properties: pyrolysis temperature and feedstock kind effects. *Rev. Environ. Sci. Biotechnol.*, 19: 191–215. https://doi.org/10.1007/s11157-020-09523-3

Tomin, O. and Yazdani, M.R. (2022). Production and characterization of porous magnetic biochar: before and after phosphate adsorption insights. *J. Porous Mater.*, 29: 849–859. https://doi.org/10.1007/s10934-022-01217-1

Tong, M., He, L., Rong, H., Li, M. and Kim, H. (2020). Transport behaviors of plastic particles in saturated quartz sand without and with biochar/Fe_3O_4-biochar amendment. *Water Res.*, 169: 115284.

Torri, I.D.V., Paasikallio, V., Faccini, C.S., Huff, R., Caramão, E.B., Sacon, V., Oasmaa, A. and Zini, C.A. (2016). Bio-oil production of softwood and hardwood forest industry residues through fast and intermediate pyrolysis and its chromatographic characterization. *Bioresour. Technol.*, 200: 680–690. https://doi.org/10.1016/j.biortech.2015.10.086

Tripathi, M., Sahu, J.N. and Ganesan, P. (2016). Effect of process parameters on production of biochar from biomass waste through pyrolysis: a review. *Renew. Sust. Energy Rev.*, 55: 467–481. https://doi.org/10.1016/j.rser.2015.10.122

Upadhyay, P.R. and Srivastava, V. (2016). Clays: An encouraging catalytic support. Current Catalysis, 5(3):162–181. https://doi.org/10.2174/2211544705666160624082343

Uraguchi, D., Sorimachi, K. and Terada, M. (2004). Organocatalytic asymmetric aza-Friedel–Crafts alkylation of furan. Journal of the American Chemical Society, 126(38):11804–11805. https://doi.org/10.1021/ja046185h

Varjani, S., Kumar, G. and Rene, E.R. (2019). Developments in biochar application for pesticide remediation: current knowledge and future research directions. *J. Environ. Manage.*, 232: 505–513.

Varkolu, M., Gundekari, S., Omvesh, Palla, V.C.S., Kumar, P., Bhattacharjee, S. and Vinodkumar, T. (2025). Recent advances in biochar production, characterization, and environmental applications. *Catalysts*, 15(3): 243. https://doi.org/10.3390/catal15030243

Vinu, A., Sawant, D.P., Ariga, K., Hartmann, M. and Halligudi, S.B. (2005). Benzylation of benzene and other aromatics by benzyl chloride over mesoporous AlSBA-15 catalysts. Microporous and Mesoporous Materials, 80(1–3), pp. 195–203.

Wang, H., Gao, B., Wang, S., Fang, J., Xue, Y. and Yang, K. (2015). Removal of Pb(II), Cu(II), and Cd(II) from aqueous solutions by biochar derived from $KMnO_4$-treated hickory wood. *Bioresour. Technol.*, 197: 356–362.

Wang, J., Liao, Z.W., Ifthikar, J., Shi, L.R., Chen, Z.Q. and Chen, Z.L. (2017). One-step preparation and application of magnetic sludge-derived bio-char on acid orange 7 removal via both adsorption and persulfate-based oxidation. *RSC Adv.*, 7(30): 18696–18706.

Wang, J.L. and Wang, S.Z. (2018). Activation of persulfate (PS) and peroxymonosulfate (PMS) and application for the degradation of emerging contaminants. *Chem. Eng. J.*, 334: 1502–1517.

Wang, L., Ok, Y.S., Tsang, D.C.W., Alessi, D.S., Rinklebe, J., Wang, H., Mašek, O., Hou, R., O'Connor, D. and Hou, D. (2020). New trends in biochar pyrolysis and modification strategies: feedstock, pyrolysis conditions, sustainability concerns and implications for soil amendment. *Crit. Rev. Environ. Sci. Technol.*, 36(3): 358–386.

Wang, P., Tang, L., Wei, X., Zeng, G., Zhou, Y., Deng, Y., Wang, J., Xie, Z. and Fang, W. (2017). Synthesis and application of iron and zinc doped biochar for removal of p-nitrophenol in wastewater and assessment of the influence of co-existed Pb(II). *Appl. Surf. Sci.*, 392: 391–401.

Wang, S., Ai, S., Nzediegwu, C., Kwak, J.-H., Islam, M.S., Li, Y. et al. (2020). Carboxyl and hydroxyl groups enhance ammonium adsorption capacity of iron (III) chloride and hydrochloric acid modified biochars. *Bioresour. Technol.*, 309: 123390.

Wang, S., Gao, B., Li, Y., Wan, Y. and Creamer, A.E. (2015). Sorption of arsenate onto magnetic iron-manganese (Fe-Mn) biochar composites. *RSC Adv.*, 5: 67971–67978.

Wang, S., Li, H. and Wu, M. (2021). Advances in metal/biochar catalysts for biomass hydro-upgrading: A review. *J. Cleaner Prod.*, 303: 126825. https://doi.org/10.1016/j.jclepro.2021.126825

Wang, S., Zhao, M., Zhou, M., Zhao, Y., Li, Y.C., Gao, B., Feng, K., Yin, W., Ok, Y.S. and Wang, X. (2019). Biomass facilitated phase transformation of natural hematite at high temperatures and sorption of Cd^{2+} and Cu^{2+}. *Environ. Int.*, 124: 473–481.

Wang, X., Jin, H., Zhang, J., Yang, H., Wang, J., Dong, C., Li, G., Tang, Y., Liu, H. and Ye, C. (2025). Synthesis of iron-cobalt-loaded biochar catalyst using CO_2-activated goat manure for the enhanced catalytic cracking of toluene. *J. Anal. Appl. Pyrolysis*, 186: 106920. https://doi.org/10.1016/j.jaap.2024.106920

Weber, K. and Quicker, P. (2018). Properties of biochar. *Fuel*, 217: 240–261. https://doi.org/10.1016/j.fuel.2017.12.054

Wei, J., Tu, C., Yuan, G., Liu, Y., Bi, D., Xiao, L., Lu, J., Theng, B.K.G., Wang, H., Zhang, L. and Zhang, X. (2019). Assessing the effect of pyrolysis temperature on the molecular properties and copper sorption capacity of a halophyte biochar. *Environ. Pollut.*, 251: 56–65.

Wei, L., Huang, Y., Huang, L., Li, Y., Huang, Q., Xu, G., Müller, K., Wang, H., Ok, Y.S. and Liu, Z. (2020). The ratio of H/C is a useful parameter to predict adsorption of the herbicide metolachlor to biochars. *Environ. Res.*, 184: 109324.

Wijitkosum, S. and Sriburi, T. (2023). Aromaticity, polarity, and longevity of biochar derived from disposable bamboo chopsticks waste for environmental application. *Heliyon*, 9(9): e19831.

Wu, J., Huang, D., Liu, X., Meng, J., Tang, C. and Xu, J. (2018). Remediation of As(III) and Cd(II) co-contamination and its mechanism in aqueous systems by a novel calcium-based magnetic biochar. *J. Hazard. Mater.*, 348: 10–19.

Xiao, B., Jia, J., Wang, W., Zhang, B., Ming, H., Ma, S., Kang, Y. and Zhao, M. (2023). A review on magnetic biochar for the removal of heavy metals from contaminated soils: Preparation, application, and microbial response. *Hazard. Mater. Adv.*, 10: 100254. https://doi.org/10.1016/j.hazadv.2023.100254

Xiao, X., Chen, Z. and Chen, B. (2016). H/C atomic ratio as a smart linkage between pyrolytic temperatures, aromatic clusters and sorption properties of biochars derived from diverse precursory materials. *Sci. Rep.*, 6: 22644.

Xie, Y., Wang, L., Li, H., Westholm, L.J., Carvalho, L., Thorin, E., Yu, Z., Yu, X. and Skreiberg, Ø. (2022). A critical review on production, modification and utilization of biochar. *J. Anal. Appl. Pyrolysis*, 161: 105405.

Xiong, X., Yu, I.-K.M., Cao, L., Tsang, D.-C.W., Zhang, S. and Ok, Y.S. (2017). A review of biochar-based catalysts for chemical synthesis, biofuel production, and pollution control. *Bioresour. Technol.*, 246: 254–270.

Xu, D., Cao, J., Li, Y., Howard, A. and Yu, K. (2019). Effect of pyrolysis temperature on characteristics of biochars derived from different feedstocks: A case study on ammonium adsorption capacity. *Waste Manag.*, 87: 652–660. https://doi.org/10.1016/j.wasman.2019.02.049

Xue, Y., Gao, B., Yao, Y., Inyang, M., Zhang, M., Zimmerman, A.R. and Ro, K.S. (2012). Hydrogen peroxide modification enhances the ability of biochar (hydrochar) produced from hydrothermal carbonization of peanut hull to remove aqueous heavy metals: batch and column tests. *Chem. Eng. J.*, (200–202): 673–680.

Yaashikaa, P.R., Kumar, P.S., Varjani, S. and Saravanan, A. (2020). A critical review on the biochar production techniques, characterization, stability and applications for circular bioeconomy. *Biotechnol. Rep.*, 28: e00570. https://doi.org/10.1016/j.btre.2020.e00570

Yakout, S.M., Daifullah, A.E.H.M. and El-Reefy, S.A. (2015). Pore structure characterization of chemically modified biochar derived from rice straw. *Environ. Eng. Manage. J.*, 14: 473–480.

Yan, J., Lu, H., Gao, W., Song, X. and Chen, M. (2015). Biochar supported nanoscale zerovalent iron composite used as persulfate activator for removing trichloroethylene. *Bioresour. Technol.*, 175: 269–274.

Yang, F., Zhao, L., Gao, B., Xu, X. and Cao, X. (2016). The interfacial behavior between biochar and soil minerals and its effect on biochar stability. *Environ. Sci. Technol.*, 50(5): 2264–2271. https://doi.org/10.1021/acs.est.5b03656

Yang, G. and Zhou, L. (2017). Active sites of M(IV)-incorporated zeolites (M = Sn, Ti, Ge, Zr). Scientific Reports, 7:16113.

Yang, H. and Sheng, K. (2012). Characterization of biochar properties affected by different pyrolysis temperatures using visible-near-infrared spectroscopy. *ISRN Sci. Technol.*, 2012: 1–7. https://doi.org/10.5402/2012/712837

Yang, H., Yan, R., Chin, T., Liang, D.T., Chen, H. and Zheng, C. (2004). Thermogravimetric analysis–Fourier transform infrared analysis of palm oil waste pyrolysis. *Energy Fuels*, 18(6): 1814–1821. https://doi.org/10.1021/ef030193m

Yang, X., Ng, W., Wong, B.S.E., Baeg, G.H., Wang, C.-H. and Ok, Y.S. (2019). Characterization and ecotoxicological investigation of biochar produced via slow pyrolysis: Effect of feedstock composition and pyrolysis conditions. *J. Hazard. Mater.*, 365: 178–185.

Yang, Y., Zhao, S., Cui, L., Bi, F., Zhang, Y., Liu, N., Wang, Y., Liu, F., He, C. and Zhang, X. (2023). Recent advancement and future challenges of photothermal catalysis for VOCs elimination: From catalyst design to applications. *Green Energy Environ.*, 8(3): 654–672. https://doi.org/10.1016/j.gee.2022.02.006

Yeboah, M.L., Li, X. and Zhou, S. (2020). Facile fabrication of biochar from palm kernel shell waste and its novel application to magnesium-based materials for hydrogen storage. *Materials*, 13(3): 625. https://doi.org/10.3390/ma13030625

Yi, Y., Huang, Z., Lu, B., Xian, J., Tsang, E.P., Cheng, W., Fang, J. and Fang, Z. (2020). Magnetic biochar for environmental remediation: A review. *Bioresour. Technol.*, 298: 122468.

You, S., Ok, Y.S., Tsang, D.C.W., Kwon, E.E. and Wang, C.-H. (2018). Towards practical application of gasification: a critical review from syngas and biochar perspectives. *Crit. Rev. Environ. Sci. Technol.*, 48: 1165–1213.

You, S.-L., Cai, Q. and Zeng, M. (2009). Chiral Brønsted acid catalyzed Friedel–Crafts alkylation reactions. Chemical Society Reviews, 38:2190–2201.

Yu, K.L., Lau, B.F., Show, P.L., Ong, H.C., Ling, T.C., Chen, W.-H. and Ng, E.P., Chang, J.-S. (2017). Recent developments on algal biochar production and characterization. *Bioresour. Technol.*, 246: 2–11.

Yu, L., Shang, X., Chen, H., Xiao, L., Zhu, Y. and Fan, J. (2019). A tightly-bonded and flexible mesoporous zeolite-cotton hybrid hemostat. Nature Communications, 10:1932.

Yuan, J.-H., Xu, R.-K. and Zhang, H. (2011). The forms of alkalis in the biochar produced from crop residues at different temperatures. *Bioresour. Technol.*, 102(3): 3488–3497. https://doi.org/10.1016/j.biortech.2010.11.018

Yunes, S., Kenvin, J. and Gil, A. (2023). On the genesis of a catalyst: A brief review with an experimental case study. *Eng.*, 4(3): 2375–2406. https://doi.org/10.3390/eng4030136

Zaitun, Z., Halim, A., Sa'dah, Y. and Cahyadi, R. (2022). Surface morphology properties of biochar feedstock for soil amendment. *IOP Conf. Ser.: Earth Environ. Sci.*, 951(1): 012034. https://doi.org/10.1088/1755-1315/951/1/012034

Zarate-Guzman, A., Gutierrez, L., Ocampo, R., Carrasco-Marin, F. and Romero-Cano, L. (2020). Iron precursor salt effect on the generation of OH radicals and sulfamethoxazole degradation through a heterogeneous Fenton process using Carbon-Fe catalysts. *J. Water Process Eng.*, 36: 101273.

Zhang, J., Shao, J., Jin, Q., Li, Z., Zhang, X., Chen, Y., Zhang, S. and Chen, H. (2019). Sludge-based biochar activation to enhance Pb(II) adsorption. *Fuel*, 252: 101–108.

Zhang, L. and Sun, X. (2014). Changes in physical, chemical, and microbiological properties during the two-stage co-composting of green waste with spent mushroom compost and biochar. *Bioresour. Technol.*, 171: 274–284.

Zhang, L., Dong, Y., Sun, R., Liu, J., Wang, Q. and Lin, H. (2021). The effect of co-pyrolysis temperature for iron–biochar composites on their adsorption behavior of antimonite and antimonate in aqueous solution. *Bioresour. Technol.*, 347: 126362. https://doi.org/10.1016/j.biortech.2021.126362

Zhang, L., Larsson, A., Moldin, A. and Edlund, U. (2022). Comparison of lignin distribution, structure, and morphology in wheat straw and wood. *Ind. Crops Prod.*, 187: 115432. https://doi.org/10.1016/j.indcrop.2022.115432

Zhang, Q., Li, Q., Zhang, L., Yu, Z., Jing, X., Wang, Z., Fang, Y. and Huang, W. (2017). Experimental study on co-pyrolysis and gasification of biomass with deoiled asphalt. *Energy*, 134: 301–310.

Zhang, X., Kong, G., Zhang, X., Wang, K., Liu, Q., Shi, S., and Han, L. (2023). Gasification integrated with steam co-reforming of agricultural waste biomass over its derived CO_2/O_2/steam-mediated porous biochar for boosting H_2-rich syngas

production. *J. Environ. Chem. Eng.*, 11(2): 109556. https://doi.org/10.1016/j.jece.2023.109556

Zhang, X., Zhang, P., Yuan, X., Li, Y. and Han, L. (2020). Effect of pyrolysis temperature and correlation analysis on the yield and physicochemical properties of crop residue biochar. *Bioresour. Technol.*, 296: 122318.

Zhang, Y., Chen, H. and Islam, S. (2025a). Advances in biochar modification for environmental remediation with emphasis on iron functionalization. *Biochar X*, 1: e009. https://doi.org/10.48130/bchax-0025-0010

Zhang, Y., Xia, Z., Nafsun, A.I. and Feng, W. (2025b). Preparation of nitrogen-doped biochar and its adsorption performance for Cr^{6+} and Pb^{2+} in aqueous systems. *Toxics*, 13(5): 402. https://doi.org/10.3390/toxics13050402

Zhang, Z., Zhu, Z., Shen, B. and Liu, L. (2019). Insights into biochar and hydrochar production and applications: a review. *Energy*, 171: 581–598.

Zhou, N., Wang, Y., Yao, D., Li, S., Tang, J., Shen, D., Zhu, X., Huang, L., Zhong, M. and Zhou, Z. (2019). Novel wet pyrolysis providing simultaneous conversion and activation to produce surface-functionalized biochars for cadmium remediation. *J. Clean. Prod.*, 221: 63–72.

Zhu, C., Wang, H., Li, H., Cai, B., Lv, W., Cai, C., Wang, C., Yan, L., Liu, Q. and Ma, L. (2019). Selective hydrodeoxygenation of 5-hydroxymethylfurfural to 2,5-dimethylfuran over alloyed Cu−Ni encapsulated in biochar catalysts. *ACS Sustain. Chem. Eng.*, 7: 19556–19569.

Zormpa, F., Treu, P. & Saraçi, E. (2025). Advancing biomass valorization with zeolite catalysts: Focus on oxidative transformations. Sustainable Chemistry for the Environment, 10:100249.

APPENDIX I : Kinetic Data for the Friedel Crafts Benzylation of Toluene at 70° C over the three Catalyst Materials

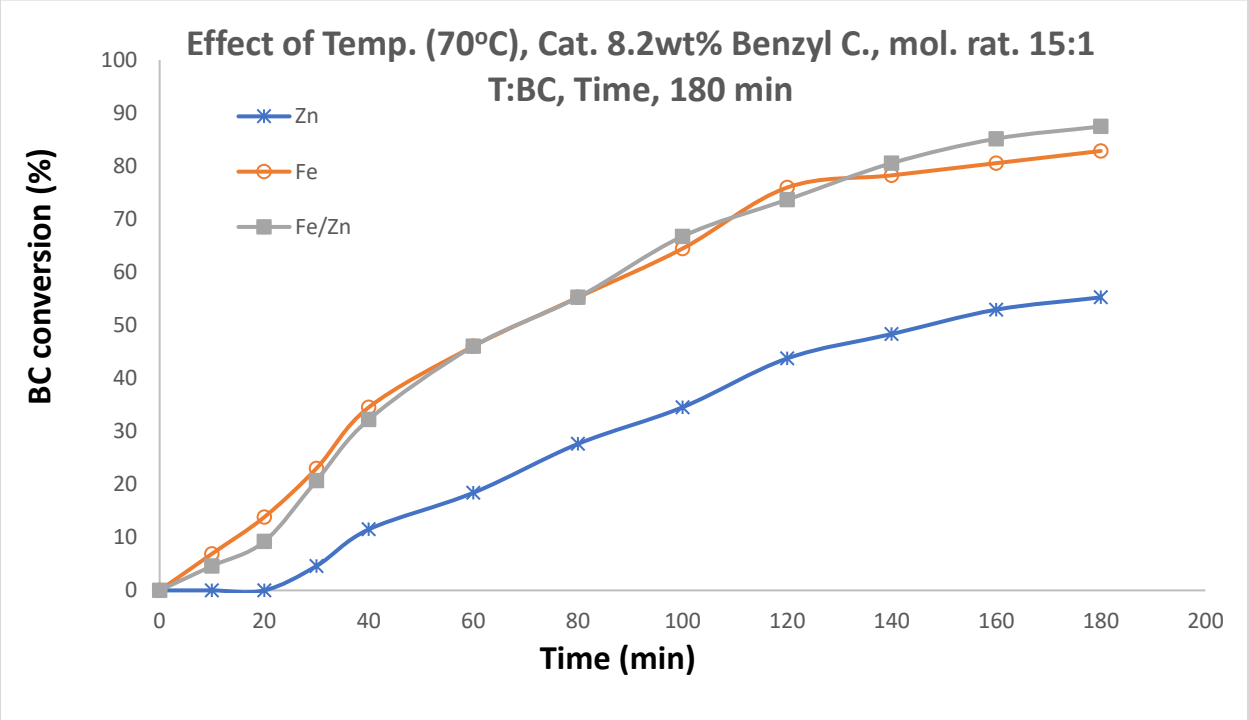

APPENDIX II : Kinetic Data for the Friedel Crafts Benzylation of Toluene at 60º C over the three Catalyst Materials

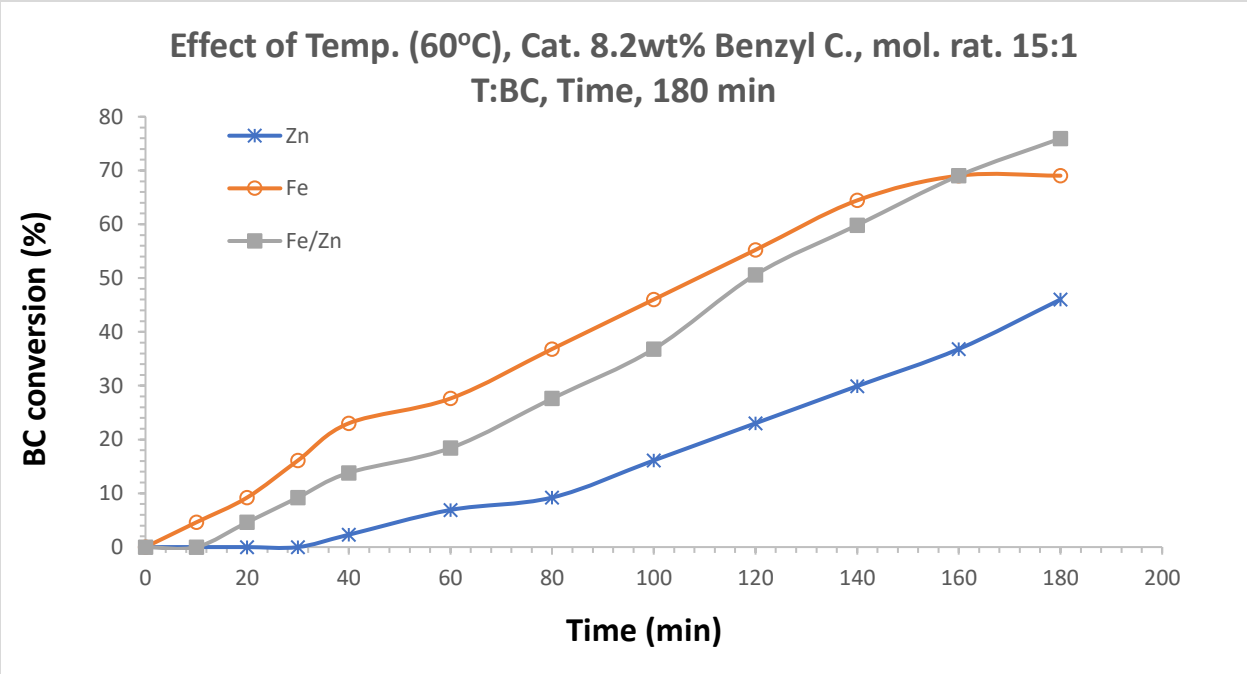

APPENDIX III : Kinetic Data for the Friedel Crafts Benzylation of Toluene at 50º C over the three Catalyst Materials